

BREAST CANCER DETECTION WITH DIFFUSE OPTICAL TOMOGRAPHY

By

CHANGQING LI

A DISSERTATION PRESENTED TO THE GRADUATE SCHOOL
OF THE UNIVERSITY OF FLORIDA IN PARTIAL FULFILLMENT
OF THE REQUIREMENTS FOR THE DEGREE OF
DOCTOR OF PHILOSOPHY

UNIVERSITY OF FLORIDA

2006

Copyright 2006

by

Changqing Li

ACKNOWLEDGMENTS

First, I would like to thank Professor Huabei Jiang, for his continuous support, trusts and precious advice during my study for the Ph.D. Professor Jiang is well-known in the field of optical tomography. His views and understandings on the research subjects are exceptional. As a professor, although his schedule is very tight, he is always available to help me on my research whenever I have frustrations. What I have learned and experienced in Professor Jiang's lab will definitely benefit my future career and life.

Secondly, my thanks go to my academic committee members: Dr. William Ditto, Dr. Mingzhou Ding, Dr. Sihong Song. Their comments and suggestions were very helpful to my study and research. Their valuable time spent on reading my dissertation is highly appreciated.

Thirdly, I would like to thank Dr. Steven Grobmyer, an assistant professor in the surgery department of University of Florida. As our clinical research partner, Dr. Grobmyer helps us to recruit many breast cancer patients. And I would like to thank the research scientist in our lab, Dr. Qizhi Zhang, for his help on both my study and my research. I also thank Dr. Zhen Yuan for his help on the algorithm development. Dr. Qiang Wang's suggestions on the experiments were always impressive. Miss Lin Chen, a graduate student in our lab, gave me lots of help in performing the clinical trial experiments. So did Dr. Xiaoping Liang. Their help is highly appreciated.

Fourthly, thanks go to my wife, Pan Sheng, for her support. Without her support and encouragement, I could not have gotten through my graduate study. And thanks go to my lovely son, Jonathan Li, for giving me so many excellent memories and happiness.

At last, thanks to NIH for the financial support on the breast cancer imaging project.

TABLE OF CONTENTS

	<u>page</u>
ACKNOWLEDGMENTS	3
LIST OF TABLES	7
LIST OF FIGURES	8
ABSTRACT	14
CHAPTER	
1 INTRODUCTION	16
1.1 Breast Cancer Facts	16
1.2 History of Optical Imaging	16
1.3 Optical Imaging of the Breast	17
1.4 Optical Diffusion Theory	23
1.5 DOT Reconstruction Algorithm	26
1.5.1 Forward Solution Procedure	26
1.5.2 Inverse Solution Procedure	27
2 DOT IMAGING SYSTEM AND ITS CALIBRATION	30
2.1 DOT Imaging System	30
2.1.3 Source/detector Fiber Optic Probe	31
2.1.4 Detection Unit	32
2.1.5 Gain Control	33
2.1.6 Detector Sensitivity and Dynamic Range	34
2.1.7 Stability	34
2.1.8 DC Offset/Noise Reduction	35
2.1.9 Data Acquisition Unit	35
2.1.10 System Timing	36
2.2 DOT Imaging System Operation	36
3 SYSTEM CALIBRATION AND DOT ALGORITHM REFINEMENTS	45
3.1 System Calibration	45
3.1.1 Image Reconstruction Algorithm	45
3.1.2 Calibration Method	46
3.1.3 Experimental Methods and Materials	48
3.1.4 Results and Discussion	48
3.2 Dual Mesh Method	51
3.2.1 Dual Mesh Method	51
3.2.2 Experiments	53
3.2.3 Results and Discussion	53

3.3	Source Intensity Optimization Method.....	55
3.3.1	Source Intensity Optimization Methods	56
3.3.2	Experiments.....	58
3.3.3	Results and Discussion.....	59
4	PARTICLE SIZE IMAGING: PHANTOM EXPERIMENTAL STUDIES	86
4.1	Measurement of Particle Size Distribution and Concentration in Heterogeneous Turbid Media.....	86
4.1.1	Materials and Methods	86
4.1.2	Simulations and experiments.....	89
4.1.3	Results	90
4.1.4	Discussion and Conclusions.....	92
4.2	Imaging of Particle Size Distribution and Concentration in Heterogeneous Turbid Media	93
4.2.1	Methods and materials.....	93
4.2.2	Results and discussion.....	94
4.3	Experimental Results from Concentrated Suspensions with Bi-modal Particle Size Distribution	97
4.3.1	Experimental system and materials.....	97
4.3.2	Experimental results and discussion.....	98
4.3.3	Conclusions	103
5	EX VIVO AND IN VIVO STUDY OF TUMOR CELL SIZING	119
5.1	Ex Vivo Study of Tumor Cells	119
5.2	Morphological Characteristics of Breast Tumors: In-Vivo Study with Multispectral Diffuse Optical Tomography	120
5.2.1	Methods	120
5.2.2	Results	121
5.2.2.1	Case studies: #1, 2 and 3: Infiltrating ductal carcinomas.....	121
5.2.2.2	Case studies: #4, 5 and 6: Benign nodule or mass	125
5.2.2.3	Statistical analysis and pathological co-registration	129
6	SPECTRALLY CONSTRAINED IMAGING OF ABSORPTION CHROMOPHORES AND SCATTERING CONCENTRATION	147
6.1	Introduction.....	147
6.2	Algorithms	148
6.2.1	Spectrally Constrained Reconstruction with the Method from Literature	148
6.2.2	Spectrally Constrained Reconstruction with Scatterer's Volume Fraction Method.....	150
6.3	Numerical Simulations	152
6.3.1	Reconstruction with the Method from Literature.....	152
6.3.2	Reconstruction with the Scattering Volume Fraction Method.....	153
6.4	In-Vivo Imaging with the Molar Absorption from References.....	155
6.5	Measurements of Molar Extinction Coefficients.....	156

6.6 Phantom Experiments.....	159
6.7 In-Vivo Imaging with the Measured Molar Extinction Coefficients.....	160
7 CONCLUSIONS AND FUTURE STUDIES.....	179
7.1 Conclusions.....	179
7.2 Future Studies	181
7.2.1 Imaging System and Calibrations.....	181
7.2.2 Multi-modality Imaging	182
7.2.3 Scattering Theory	182
7.2.4 Clinical Studies.....	183
LIST OF REFERENCES.....	184
BIOGRAPHICAL SKETCH	192

LIST OF TABLES

<u>Table</u>	<u>page</u>
3-1 Optical and geometric parameters used for Group 1 experiments.....	84
3-2 Optical and geometric parameters used for Group 2 experiments.....	84
3-3 Optical and geometric parameters used for Group 3 experiments.....	84
3-4 Optical properties of the phantom background and the target for all 5 cases.....	85
3-5 Optical properties of the target and background used in the six experiments performed.....	85
4-1 Reconstructed parameters from simulated data at different noise levels for simulation 1.....	116
4-2 Reconstructed parameters from simulated data at different noise levels for simulation 2.....	116
4-3 Reconstructed parameters from experimental data using the peak and average scattering spectra of the target area.....	116
4-4 Target materials of experiment set 1. The unit of volume is mL.....	117
4-5 Target materials of experiment set 2. The unit of volume is mL.....	117
4-6 Target materials of experiment set 3. The unit of volume is mL.....	117
4-7 Reconstructed results of set1.	117
4-8 Reconstructed results of set2.	118
4-9 Reconstructed results of set3.	118
5-1 Mean diameters and volume fraction of the nucleus and nucleolus found from the microscopic pictures and those of scattering particles calculated from the reconstructed images.....	146
6-1 Volume fraction of different particles in the background and the three targets for numerical simulation case 3.....	178
6-2 Concentrations of the absorption chromophores and Volume fractions particles for numerical simulation case4.....	178

LIST OF FIGURES

<u>Figure</u>	<u>page</u>
2-1 Schematic of the experimental system.....	37
2-2 Photographs of the experimental system.	38
2-3 Optical switch (a) Schematic and (b) photograph.....	39
2-4 Photographs of the ring structure.....	40
2-5 Internal and external connections of a silicon photodiode S8754.	40
2-6 Diagram of mounting configuration for one sensor.....	41
2-7 The detection board: (a) Schematic;(b) layout.....	42
2-8 Flow chart of a detector gain controller.....	43
2-9 The control panel of the DOT imaging system.....	43
2-10 The LABVIEW control panel of the DOT imaging system.	44
3-1 Geometry of the phantom configuration.....	64
3-2 Reconstructed absorption and scattering images for the 3 cases in Group 1.....	65
3-3 Reconstructed absorption and scattering images for the 3 cases in Group 2.....	66
3-4 Reconstructed absorption and scattering images for the 3 cases in Group 3.....	67
3-5 1D profile of the absorption coefficient along the transect AB (see Figure. 3-1) for the image shown in Figure. 3-2a (a) and for image shown in Figure. 3-2d (b).....	68
3-6 Four fine mesh elements generated from one coarse mesh element.....	68
3-7 Geometry of the tissue mimicking phantom.....	69
3-8 The μ_a images (a-d) and μ'_s images (e-h) reconstructed for case 1 (4:1 μ_a , 2.8:1 μ'_s contrast, 15 mm off-center) phantom experiment.....	70
3-9 The μ_a images (a-d) and μ'_s images (e-h) reconstructed for case 2 (4:1 μ_a , 2.8:1 μ'_s contrast, 10 mm off-center) phantom experiment.	71
3-10 The μ_a images (a-d) and μ'_s images (e-h) reconstructed for case 3 (4:1 μ_a , 2.8:1 μ'_s contrast, 5 mm off-center) phantom experiment.....	72

3-11	The three-dimensional views of the reconstructed absorption coefficient images (a, c, e) in mm^{-1} and the reconstructed reduced scattering coefficient images (b, d, f).....	73
3-12	Geometry of the phantom under study.....	74
3-13	The absorption images reconstructed for case 1 (2:1 μ_a contrast).....	75
3-14	The absorption images reconstructed for case 2 (4:1 μ_a contrast).....	76
3-15	Reconstructed absorption images (rows 1 and 2) and scattering images (rows 3-5) for case 3 (2:1 μ_a and μ'_s contrast)	77
3-16	The absorption images reconstructed for case 4 (4:1 μ_a and μ'_s contrast).....	79
3-17	The scattering images reconstructed for case 4 (4:1 μ_a and μ'_s contrast).....	80
3-18	Recovered μ_a values along a transect through the centers of the target and background for the images at $y=0$ mm, $z=2$ mm.....	81
3-19	The absorption images (a and b) and scattering images (c and d) reconstructed with the source optimization method for case 5 (4:1 μ_a and μ'_s contrast).....	82
3-20	The absorption images (a and b) and scattering images (c and d) reconstructed with the source optimization method for case 6.....	83
3-21	The source intensity obtained with the uniform source intensity method and the source intensity distribution obtained with the source intensity optimization method.....	83
4-1	Simulated scattering spectra obtained from Mie calculation and the fittings based on the recovered particle size distribution and concentration at different noise levels.....	104
4-2	Reconstructed scattering images for Case 2 at 10 different wavelengths.....	105
4-3	Normalized exact (solid lines) and reconstructed (dashed lines) particle size distribution from phantom measurements for Cases 1, 2 and 3.....	106
4-4	Experimental scattering spectra obtained with different methods for Case 1 (left) and Case 3 (right).....	106
4-5	Scattering spectra: (a) The spectra generated by Eq. (5) and the Mie fittings using recovered particle parameters from simulated data.....	107
4-6	The DOT reconstructed absorption images (a1 to a10) and reduced scattering images (b1 to b10) at 10 different wavelengths.....	108

4-7	Reconstructed images of mean particle size (a, c) and concentration (b, d) for the 2.06 μm (a, b) and 5.66 μm (c, d) polystyrene cases, respectively.....	109
4-8	The reduced scattering coefficient images at 9 different wavelengths for experiment set1_1.....	110
4-9	The reduced scattering coefficient images at 9 different wavelengths for experiment set1_1. The global minimum error initial value is selected.....	111
4-10	Reduced scattering coefficient at 10 wavelengths for 5 cases of experiment set1. Fixed α value was applied for each case.....	112
4-11	Reduced scattering coefficient at 10 wavelengths for 5 cases of experiment set1. The value of α corresponding to the global minimum error was applied for each case.....	112
4-12	Reduced scattering coefficient at 10 wavelengths for 4 cases of experiment set2. Fixed α value was applied for each case.....	113
4-13	Reduced scattering coefficient at 10 wavelengths for 3 cases of experiment set 3. Fixed α value was applied for each case.....	113
4-14	The reconstructed diameter versus (a) the calculated scattering coefficient ratio of 1 μm particles and 6 μm particles and (b) the volume fraction of 1 μm particles for experiment set 1.....	114
4-15	The reconstructed diameter versus (a) the calculated scattering coefficient ratio of 1 μm particles and 6 μm particles and (b) the volume fraction of 1 μm particles for experiment set 2.....	115
5-1	The microscopic picture of (a) the tumor tissue (400 time magnificent) and (b) the normal tissue (100 time magnificent).....	132
5-2	Experiment preparation: (a) the removed tissue was put inside the background phantom; (b) The tissue was covered with background phantom and examined by the system.....	132
5-3	Ex-vivo results: (a) The extracted nucleus concentration distribution in the tissue region and the intralipid concentration distribution in the background region.....	133
5-4	Mammogram films: (a) Right CC mammogram, (b) Right MLO mammogram for the right breast of a 52 years old patient (patient ID #G1).....	133
5-5	The constructed scattering images at 9 wavelengths from 638nm to 922nm (figs. a to i) of the examined breast for patient G1.....	134
5-6	The extracted images of particle diameters (a) and particle volume fraction (b) of the examined breast for patient G1.....	134

5-7	Mammogram films: (a) CC mammogram, (b) MLO mammogram for the right breast of a 50 years old patient.....	135
5-8	The reconstructed scattering images at 9 wavelengths from 638nm to 922nm (Figs. a to i) of the examined breast for patient #G2.....	136
5-9	The extracted images of particle diameters (a) and particle volume fraction (b) of the examined breast for patient #G2.....	136
5-10	The reconstructed scattering images at 4 wavelengths from 733nm to 840nm (Figs. a to d) of the examined breast for patient G8.....	137
5-11	The extracted images of particle diameters (a) and particle volume fraction (b) of the examined breast for patient G8.....	137
5-12	Mammogram films: (a) MLO and (b) CC mammography of the right breast for patient #S5.....	138
5-13	The reconstructed absorption coefficient images for the right breast of the patient #S5 at 9 wavelengths from 638nm to 922nm (a to i).....	138
5-14	The reconstructed scattering images at the right breast of the patient #S5 at 9 wavelengths from 638nm to 965nm (a to i).....	139
5-16	Mammogram films: (a) CC and (b) MLO mammography of the left breast for patient #S7.....	140
5-17	The reconstructed scattering images of the examined breast at 9 wavelengths from 638nm to 965nm (a to i) for patient #S7.....	140
5-18	The reconstructed particle diameter image (a) and the particle volume fraction image (b) of the examined breast for patient #S7.....	141
5-19	Mammogram films: (a)RMLO, (b)RML images of the patient #S9.....	141
5-20	The reconstructed scattering images of the right breast for patient #S9 at 9 wavelengths from 638nm to 965nm (a to i).....	142
5-21	The reconstructed particle diameter image (a) and the particle volume fraction image (b) of the right breast for patient #S9.....	143
5-22	Average values of recovered mean diameter and volume fraction of scattering particles for 8 benign cases and 4 malignant cases, respectively	143
5-23	The peak value of the recovered volume fraction in the target region versus the peak value of mean diameter in the target region.....	144
5-24	The pathological microscopic pictures of tumor cells for patient #G1 (shown in a), #G2 (shown in b) and #G3 (shown in c).....	145

6-1	Reconstructed concentration images of Hbo2 (a), Hb (b) and water (c) and images of equivalent diameters (d) and volume fraction (e).....	166
6-2	The exact images of volume fraction (a) and diameters (b) and the reconstructed images of volume fraction (c) and diameters (d) with the method described in subsection 6.2.1 when only the volume fraction and diameters are reconstructed.....	166
6-3	The geometry of the numerical simulations for case 3 (a) and case 4 (b), where $D=70$ mm, $d=20$ mm and $D_{\text{offset}}=40$ mm.....	167
6-4	The reconstructed volume fractions images for 150 nm particles (a, d), 1000 nm particles (b, e) and 6000 nm particles (c, f)	167
6-5	The reconstructed images of concentrations of Hbo2, Hb, water and volume fractions of 1000 nm particles and 6000 nm particles from leftmost column to rightmost column.....	168
6-6	The reconstructed concentration images of Hbo2 (a, f), Hb (b, g), water (c, h) and volume fraction images of 1000 nm particles (d, i) and 6000 nm particles (e, j) for patient 1 and for patient 2	168
6-7	The container for molar absorption measurements. The upper part is the drinking water bottle and the bottom part is composed of Cling Wrap	169
6-8	The liquid solution inside the container is ready for the measurements. The Cling Wrap contacts with fiber probes.	169
6-9	The absorption coefficients of water from the reference (triangle) and measurements of Intralipid solution (diamonds).	170
6-10	The molar absorption of oxy-hemoglobin from the reference (solid line) and measurements of blood solution with different concentrations	170
6-11	The molar absorption of deoxy-hemoglobin from the reference (solid line) and measurements of blood solution with different concentrations	171
6-12	Reconstructed images of total hemoglobin concentrations (1 st row) in unit of μM , oxygen saturation (2 nd row), water concentration (3 rd row) in percentage and scatterers volume fraction (4 th row) in percentage of phantom experiments.....	172
6-13	Chromophores concentration images and scatterers' volume fraction image in percentage (j) reconstructed with the measured molar spectra, using method 1 (1 st row), method 2 (2 nd row) and method 3 (3 rd row) for clinical case S5	173
6-14	For clinical case S5, chromophores concentration images reconstructed with the molar spectra from reference, using method 1 (1 st row) and method 2 (2 nd row) for clinical case S5.....	173

6-15	For clinical case S7, chromophores concentration images and scatterers' volume fraction image in percentage (j) reconstructed with the measured molar spectra, using method 1 (1 st row), method 2 (2 nd row) and method 3 (3 rd row)	174
6-16	For clinical case S7, chromophores concentration images reconstructed with the molar spectra from reference, using method 1 (1 st row) and method 2 (2 nd row).....	174
6-17	For clinical case S28, chromophores concentration images and scatterers' volume fraction image in percentage (j) reconstructed with the measured molar spectra, using method 1 (1 st row), method 2 (2 nd row) and method 3 (3 rd row)	175
6-18	For clinical case G1, chromophores concentration images and scatterers' volume fraction image in percentage (j) reconstructed with the measured molar spectra, using method 1 (1 st row), method 2 (2 nd row) and method 3 (3 rd row)	176
6-19	For clinical case G14, Chromophores concentration images and scatterers' volume fraction image in percentage (j) reconstructed with the measured molar spectra, using method 1 (1 st row), method 2 (2 nd row) and method 3 (3 rd row)	177

Abstract of Dissertation Presented to the Graduate School
of the University of Florida in Partial Fulfillment of the
Requirements for the Degree of Doctor of Philosophy

BREAST CANCER DETECTION WITH DIFFUSE OPTICAL TOMOGRAPHY

By

Changqing Li

December 2006

Chair: Huabei Jiang

Major Department: Biomedical Engineering

Diffuse optical tomography (DOT) is emerging as a potential imaging technique for breast cancer detection. Compared with the routine x-ray mammography which gives only the structural images of breast tissue, DOT provides not only the structural information, but also the functional images including oxyhemoglobin, deoxyhemoglobin, lipid and water content as well as the morphological images including nucleus size and volume fraction. The goal of this thesis study is to obtain these structural, functional and morphological contents of breast tissue using a multi-spectral DOT reconstruction approach. This study involves imaging hardware implementation and software development necessary for achieving the goal. The imaging system and reconstruction software implemented are tested and evaluated using extensive simulations, tissue-like phantom experiments and in vivo clinical studies.

A compact diffuse optical tomography system, specifically designed for breast imaging, is constructed. The system consists of 64 silicon photodiode detectors, 64 excitation points, and 10 diode lasers in the near-infrared region, allowing multi-spectral, three-dimensional optical imaging of breast tissue. The system performance and optimization through a calibration procedure are detailed. The system is evaluated using tissue-like phantom and clinical experiments. Quantitative 2D and 3D images of absorption and reduced scattering coefficients

are obtained from these experimental data. Two methods, dual mesh method and source intensity optimization method, are implemented for improved 3D DOT reconstructions and validated by tissue-like phantom experiments.

Reconstruction algorithms for obtaining tissue morphological images are described. Quantitative images are successfully reconstructed in terms of the size, location and tissue morphology of target from both tissue phantom and in vivo data. Initial clinical results show that the scattering particle size and volume fraction at cellular level are potential new parameters that could be used for differentiating malignant from benign lesions.

A new method, namely spectrally constrained DOT, is also developed to directly reconstruct tissue chromophore concentrations and volume fraction of scattering particles simultaneously. The absorption extinction coefficient spectra of oxy-hemoglobin, deoxy-hemoglobin as well as the absorption spectrum of water are measured using a mixture of human blood and Intralipid solution with the imaging system developed. The quality of the reconstructed images is improved substantially when the measured spectra are utilized, compared with that of the images recovered with the spectra obtained from the literature.

CHAPTER 1 INTRODUCTION

1.1 Breast Cancer Facts

The American Cancer Society estimates that 211,240 women will be diagnosed with invasive breast cancer, as well as approximately an additional 58,490 women will be diagnosed with in situ breast cancer, and 40,410 women will die of cancer of the breast in 2005. Only lung cancer accounts for more cancer deaths in women. Based on rates from 2000-2002, 13.22% of women born today will be diagnosed with cancer of the breast at some time during their lifetime. This number can also be expressed as 1 in 8 women will be diagnosed with cancer of the breast during their lifetime.¹

1.2 History of Optical Imaging

Breast cancer is caused by the cancer cells, which are characterized by the uncontrolled division and the ability to invade into the normal tissues and spread to the whole body. The stage before the spreading is called in situ, meaning that the tumor is happened locally and is not invasive. When a tumor or a lump is palpable in the breast, it is usually one centimetre in size and contains one million cells approximately. It is estimated that a lump of this size may take one to five years to be developed. The cancer may metastasize, or spread to other tissues by lymphatics or blood during the development period. The earlier the cancer is detected, the lower risk for patients to have it spread and the higher probability to have it cured. Optical imaging allows the possibility of earlier breast cancer detection due to its unique feature of functional imaging. Furthermore, the physical examination has only 20% to 30% specificity for lesion detections. And annual mammography screening provides higher specificity and sensitivity of breast lesion detection. However, the patients are under risk with exposure to x-ray radiations

frequently. The non-ionized optical imaging can be used to screen the breasts frequently without any side effects.

Earlier time, optical imaging was called transillumination or diaphanography, in which the white light cast on a breast directly and the shadow of the breast was reviewed.² This technology was further improved by using the red light and near infrared (wavelength from 600 nm to 800 nm) since the photons at these wavelengths could penetrate deeper into the breast.³ However, the clinical trial results of the improved transillumination showed that the method failed to detect tumors less than 2cm inside the breast due to the dominated scattering.⁴⁻⁵ This is unacceptable for the breast screening since the screening resolution is required to be a few millimeters at least.

The optical imaging for breast cancer detection has made substantial progress recently due to the improved mathematical models of optical transportation, much more powerful computation tools, and advanced measurement technologies. The mathematical models are introduced in subsection 1.4. The models are solved by the finite element method, differential method or other methods. All these methods need heavy computation. The powerful and cheap computer makes the heavy computation possible and feasible for many scholars. With the progress in electronics, there are many advanced optical measurement tools available, such as photomultiplier tube (PMT), photodiodes, CCD. These tools measure the photon flying time, the amplitude and phase of high frequency modulated light or the light intensity of continue-wave light. These accurate measurements allow a good quality of optical imaging.

1.3 Optical Imaging of the Breast

Optical imaging attracts more and more scholars because of its unique features. At first, it is non-ionized. There are no side effects for the optical breast imaging. So the patient can do breast screening frequently. Secondly, compared with other methods, the cost of optical imaging is lower. Thirdly, optical imaging is efficient to differentiate between the soft tissues because the

optical absorption is proportional to the concentrations of hemoglobin, water and lipid in the tissues. Finally, optical imaging is both a functional and morphological imaging method. It is able to image the concentrations of oxy-hemoglobin, deoxy-hemoglobin, water and lipid of the examined tissues using the optical absorption spectra. And it is also able to obtain the particle (such as nucleus) size distribution and density in the tissues using the scattering spectra. This special feature makes the optical imaging a possible method to detect the breast cancer earlier than other methods such as mammography, ultrasound, MRI and PET. Mammography is the most widely accepted method for breast cancer screening. Despite its advantages, mammography has a high false positive rate because it can not differentiate the benign and malignant tumors efficiently. And mammography makes the patient expose to the x-ray radiation. As an adjunct to the mammography, the breast ultrasound is used to determine whether a lump is filled with fluid or solid mass. Ultrasound works well for dense breasts. Ultrasound breast imaging is still under investigation for further improvements. Current breast MRI clinical applications include the evaluation of the extent of cancer in breast before surgery, imaging the breast with silicone augmentation and evaluating the extent of chest wall to assist the surgery. Breast MRI is more expensive than mammography, ultrasound and optical imaging. Positron emission tomography (PET) of breast can determine whether a tumor is malignant or benign. But its spatial resolution is very low. And PET is also very expensive.

Optical breast imaging method is based on the fact that the optical properties of diseased and normal breast tissues are different.⁶⁻¹⁰ At NIR wavelength, the absorption in carcinoma is significantly higher than in adjacent uninvolved tissues. The difference between diseased and normal tissues is as high as 100% in the near infrared region due to the increased hemoglobin

concentration in tumor.⁸ It was also reported that there was a four-fold increase in blood volume in diseased breast compared to the normal tissue due to the increased blood vessels and size.¹¹

Although the mechanisms of photon propagation in breast tissues have not been understood completely, pilot *in vivo* measurements of endogenous optical properties and endogenous tumor contrast have been reported.¹²⁻²³ The reported results were promising. For example, Gu et al.¹² reported that cysts ranging from 1-4 cm in diameter can be quantitatively imaged. Cysts can be differentiated from solid breast tumors because cysts generally demonstrate lower absorption and scattering coefficients compared with the surrounding normal tissue, whereas solid tumors show concurrent higher absorption and scattering related to the normal tissue. The use of exogenous contrast agents has also been studied.²³ For example, Indocyanine green (ICG) was demonstrated to enhance breast tumor contrast *in vivo*.²³ All the reported results suggest that the optical imaging is a potential diagnostic method.

So far, several groups including our own have developed reconstruction algorithms for optical image reconstructions in frequency domain²⁴⁻²⁶, time domain²⁷ and CW domain²⁸⁻³¹, or in a hybrid (frequency/continuous-wave) domain.³² We are interested in the CW domain DOT due to its simple hardware implementation compared with the frequency and time domain DOT. While we and other groups have shown that the CW method could extract the absorption coefficient and the reduced scattering coefficient images quantitatively two- and three-dimensionally using tissue mimicking phantoms and *in vivo* tissues at the specific wavelengths,^{28,30,32} it is still a very challenging problem to obtain the quantitative images at the wavelengths in the region from 600 nm to 1000 nm due to the worse signal noise ratio at both the short and long wavelengths such as 600 nm and 1000 nm. Because the spectroscopy in the whole region is needed in order to extract the optical scatterers' size and volume fraction, it is necessary

to further improve our current algorithm by using methods such as the dual mesh method,³²⁻³⁴ and source intensity optimization.³⁵

We built our first generation DOT system using single photomultiplier tube (PMT) detection.²⁸ Even though it was extremely slow, it allowed us to obtain the first successful 2D and 3D optical imaging of in vivo breast tissue based on CW approaches.³⁶⁻³⁷ Recently we developed the second generation optical imaging system using 16 PMTs and 3 wavelengths.³⁸ Significant in vivo breast imaging results have been generated from this second generation machine¹² while active clinical studies are still on-going using this system. In order to acquire the functional and morphology images, 3 wavelengths are not enough and more laser modules at different wavelengths are needed.³⁹⁻⁴⁰ A new system with 10 wavelengths which are capable of fast data collection is needed.

When light propagates through mammalian tissues, the scatterers are cell organelles of various sizes, such as nucleus and mitochondria, which have higher refractive index than the surrounding cytoplasm.⁴¹ Perelman et al. have shown that light singly backscattered from an epithelial layer of tissue such as the skin has a wavelength-dependent periodic pattern.⁴² They found that the periodicity of the pattern increased with nuclear size and the amplitude of the periodic signal was related with the density of nucleus. After analyzing the periodic pattern, the nucleus size and density could be extracted. However, the periodic pattern was overwhelmed by the diffuse background or by the multiple scattered lights since the backscattered light is only a small portion of the scattered light. One way to overcome the problem is to use a model to mathematically describe the single backscattered light. But this method has to be remodeled for different tissues under investigation which is inconvenient.⁴² Another robust approach, also proposed by Backman et al., is to use polarized light to differentiate the single scattered light

from multiple scattered light background.⁴³ It was reported that the initially polarized light lost its polarization after scattered propagation in turbid media such as biological tissues.⁴⁴⁻⁴⁶ In contrast, the single backscattered light kept its polarization.⁴⁷ After subtracting the unpolarized light, the polarized component of the backscattered light from the epithelial layer of the tissue was obtained. An alternative approach to differentiate the backscattering from background is to utilize a probe geometry that optimizes the detection of single scattered light.⁴⁸ It was demonstrated that the single optical fiber approach was highly sensitive to the light backscattered from layered superficial tissues.

Cells have complicated structures and the organelles inside a cell vary in size from a tenth of micron to 10 microns. All the organelles contribute to the scattering which complicates the cell scattering phenomena. With fiber-optic, polarized elastic-scattering spectroscopy techniques, Mourant et al. estimated that the average scatterer radius in tissue was from 0.5 to 1.0 μ m, which is much smaller than the nucleus.⁴⁹ Using the polarized light spectroscopy, the particle size distribution in mammal cells was measured and the results suggested that small particles (possibly the mitochondria) contribute most to the scattering. However, other subcellular structures, such as the nucleoli and the nucleus, may also contribute significantly.⁵⁰ Backman et al. demonstrated that the spectrum of the single backscattering component was capable of providing the cell nuclei size distribution, which means the single backscattering was dominated by the nucleus.⁵¹

Scattering spectra in multi-spectral diffuse optical tomography (MSDOT) have been relatively less explored. This is hampered largely by the strong crosstalk between absorption and scattering contrasts that occurred in earlier DOT reconstructions, which was reduced/eliminated only recently by various image enhancement schemes.^{31,52} In pure optical spectroscopy studies as

described above, it has been shown that scattering spectra are correlated with tissue morphology. These experimental studies have suggested that both nuclei and mitochondria contribute to tissue scattering significantly. On the other hand, it is well known in pathology that tumor cells/nuclei are considerably enlarged relative to normal ones.⁵³ Thus significant clinical value would be resulted from the exploration of scattering spectra in MSDOT. Thus far scattering spectra in MSDOT have been studied with a simple power law,⁵⁴⁻⁵⁵ which was originated from spectroscopy studies with homogeneous media.⁵⁶⁻⁵⁹ The advantages of the power law are its simplicity and reasonable accuracy under certain conditions. The disadvantage is that the constants in the power law have no clear physical meanings and that particle size distribution and concentration cannot be directly obtained from this empirical relationship.

Currently, two noninvasive optical imaging methods are used to measure particle size distribution. One is the light scattering spectroscopy (LSS),⁶⁰ in which polarized light was delivered to the epithelial tissue and the single backscattering light that kept the polarization was analyzed to extract the morphological features and the refractive index of the scatterers. This method is limited primarily to superficial surface imaging. The other one, which we are trying to further develop, is a tomographic imaging method based on multi-spectral diffuse optical tomography,⁶¹⁻⁶² in which the tomographic scattering images of tissue at multiple wavelengths were obtained with diffuse optical tomography and the scattering spectra were then used to extract the scatterer's size information with a Mie theory based reconstruction method. To utilize the Mie theory for particle/nucleus sizing, several assumptions are generally made: particles are spherical; no particle-particle interactions exist; and the photon diffusion equation is valid which means that light scattering is much larger than the absorption. While the reasonable results have been obtained based on above assumptions,⁶¹⁻⁶² we plan to investigate them further to see

whether better results could be extracted if more complicated models such as Wentzel-Kramers-Brillouin (WKB) model was applied.⁶³

Conventionally, two separate sequential steps are deployed to calculate the functional images. At first, the absorption images at different wavelengths are reconstructed by DOT. Then the contributions to the absorption images from each tissue chromophore are calculated.¹⁵ Recently, a new approach for extracting the tissue chromophores is that tissue chromophore concentrations and Mie scattering factors are reconstructed directly by exploiting the spectral priori information.⁵⁵ Corlu et al. show that the new method works very well in the CW domain with the linear inverse method to update the parameters iteratively. While the chromophore concentration image quality is improved substantially due to the reduction of the reconstructed parameters by exploiting a priori spectral constrained technique, the cross talk between the scattering parameters a and b limited its applications. The new method applications to our nonlinear iterative DOT algorithm will also be investigated in this dissertation to determine whether image quality could be further improved.

1.4 Optical Diffusion Theory

Boltzmann transport equation describes incoherent photon propagation through highly scattering media such as tissue. The equation in time domain is written as

$$\left(\frac{1}{c} \frac{\partial}{\partial t} + \hat{s} \cdot \nabla + \mu_{tr}(\hat{r}) \right) \phi(\hat{r}, \hat{s}, t) = \mu_s(\hat{r}) \int_{4\pi} \Theta(\hat{s}, \hat{s}') \phi(\hat{r}, \hat{s}', t) d\hat{s}' + q(\hat{r}, \hat{s}, t) \quad (3.1)$$

where $\phi(\hat{r}, \hat{s}, t)$ is the radiance [W/(cm² sr)] at position \hat{r} , at time t, propagating along the unit vector \hat{s} . $\mu_{tr}(\hat{r}) = \mu_a(\hat{r}) + \mu_s(\hat{r})$ is the transport cross section at position \hat{r} . $\mu_a(\hat{r})$ and $\mu_s(\hat{r})$, the absorption and scattering coefficients, are the inverse of the absorption and scattering mean free path respectively. c is the speed of light in the medium. The function $\Theta(\hat{s}, \hat{s}')$ is the probability

density function over all solid angles of the change in photon propagation direction from \hat{s} to \hat{s}' due to an elastic scattering event which satisfies the condition: $\int_{4\pi} \Theta(\hat{s}, \hat{s}') d\hat{s} = 1$. $q(\hat{r}, \hat{s}, t)$ is the photon power generated at position \hat{r} along direction \hat{s} . This equation reflects the energy conservation in the medium. However, the equation often must be simplified to be mathematically manageable. One way to simplify it is to expand the equation with spherical harmonics and truncate the series at the N^{th} term, namely P_N approximation. Thus the quantities in equation 3.1 can be expressed as

$$\phi(\hat{r}, \hat{s}, t) = \sum_L \sum_{m=-L}^L \left(\frac{2L+1}{4\pi} \right)^{\frac{1}{2}} \psi_{L,m}(\hat{r}, t) Y_{L,m}(\hat{s}) \quad (3.2)$$

$$q(\hat{r}, \hat{s}, t) = \sum_L \sum_{m=-L}^L \left(\frac{2L+1}{4\pi} \right)^{\frac{1}{2}} q_{L,m}(\hat{r}, t) Y_{L,m}(\hat{s}) \quad (3.3)$$

$$\Theta(\hat{s}, \hat{s}') = \sum_L \left(\frac{2L+1}{4\pi} \right)^{\frac{1}{2}} \Theta_L P_L(\cos\theta) \quad (3.4)$$

where $\left(\frac{2L+1}{4\pi} \right)^{\frac{1}{2}}$ is the normalization factor, $Y_{L,m}$ the spherical harmonic of order L at degree m , P_L Legendre polynomial of order L .

P_1 approximation is obtained when $N=1$ from the P_N approximation. After simplification, the following equations are obtained:

$$\left(\frac{1}{c} \frac{\partial}{\partial t} + \mu_{\text{tr}}(\hat{r}) \right) \Phi(\hat{r}, t) + \nabla \cdot \hat{J}(\hat{r}, t) = \mu_s(\hat{r}) \Phi(\hat{r}, t) + \Theta_0 q_{0,0}(\hat{r}, t) \quad (3.5)$$

$$\left(\frac{1}{c} \frac{\partial}{\partial t} + \mu_{\text{tr}}(\hat{r}) \right) \hat{J}(\hat{r}, t) + \frac{1}{3} \nabla \Phi(\hat{r}, t) = \Theta_1 \mu_s(\hat{r}) \hat{J}(\hat{r}, t) + \hat{q}_1(\hat{r}, t) \quad (3.6)$$

where $\Phi(\hat{r}, t) = \psi_{0,0}(\hat{r}, t)$ is the photon fluence,

$$\hat{\mathbf{J}}(\hat{r}, t) = \left[\frac{1}{\sqrt{2}} (\psi_{1,-1}(\hat{r}, t) - \psi_{1,1}(\hat{r}, t)), \frac{1}{i\sqrt{2}} (\psi_{1,-1}(\hat{r}, t) + \psi_{1,1}(\hat{r}, t)), \psi_{1,0}(\hat{r}, t) \right]^T \text{ the photon flux.}$$

The P_1 approximation can be further simplified by making the following assumptions:

$$\frac{\partial \hat{\mathbf{J}}}{\partial t} = 0, \quad \hat{q}_1 = 0. \quad (3.7)$$

The approximation, namely diffuse approximation, is usually justified only if the scattering coefficient is much larger than the absorption coefficient in order to satisfy the first assumption,

$\frac{\partial \hat{\mathbf{J}}}{\partial t} = 0$. The second assumption, $\hat{q}_1 = 0$, means that the photon source is isotropic. The diffuse

approximation leads to the following equation, namely diffusion equation, in the time domain

$$-\nabla \cdot D(\hat{r}) \nabla \Phi(\hat{r}, t) + \mu_a \Phi(\hat{r}, t) + \frac{1}{c} \frac{\partial \Phi(\hat{r}, t)}{\partial t} = q_0(\hat{r}, t), \quad (3.8)$$

or in the frequency domain

$$-\nabla \cdot D(\hat{r}) \nabla \Phi(\hat{r}, \omega) + \mu_a \Phi(\hat{r}, \omega) + \frac{i\omega}{c} \Phi(\hat{r}, \omega) = q_0(\hat{r}, \omega), \quad (3.9)$$

or in the continue wave domain

$$-\nabla \cdot D(\hat{r}) \nabla \Phi(\hat{r}) + \mu_a \Phi(\hat{r}) = q_0(\hat{r}) \quad (3.10)$$

where $D(\hat{r}) = \frac{1}{3(\mu_a + \mu'_s)}$ is the diffusion coefficient, $\mu'_s = (1 - \Theta_1)\mu_s$ the reduced scattering

coefficient and $q_0(\hat{r}) = q_{0,0}(\hat{r})$ the isotropic source.

In infinite homogeneous media, the solution to the diffusion equation can be obtained through the Green function method. However, for realistic finite homo- or hetero-geneous media such as tissue, the boundary effects/conditions must be accounted for.

1.5 DOT Reconstruction Algorithm

There are two procedures involved in the DOT image reconstruction. The first one is the forward solution procedure, in which the distribution of light in the medium of interest is predicted. The second one, the inverse solution procedure, is used to iteratively update the initially guessed optical property distribution of the medium through an optimization method such as Newton method by minimizing the squared difference between the data computed from the diffusion equation and measured around the surface of the medium.

1.5.1 Forward Solution Procedure

Since an analytical solution to the Boltzmann transport or the diffusion equation is not available in a realistic situation, numerical methods must be used for most cases. Finite element method (FEM) is a natural choice because it can be used to solve the diffusion equation in inhomogeneous media with an arbitrary geometry, although other numerical methods such as finite difference method⁶⁴, finite volume method⁶⁵ and boundary element method⁶⁶ have been used in DOT. The FEM applications in DOT have been discussed in details elsewhere⁶⁸⁻⁶⁹. Here we follow Paulsen and Jiang⁶⁹ and briefly describe the FEM method in the CW DOT.

Using the finite element discretization, the steady-state photon diffuse equation coupled with the type III boundary conditions, $-D\nabla\Phi \cdot \hat{n} = \alpha\Phi$, can be transformed into the following matrix form

$$[A]\{\Phi\} = \{b\}, \quad (3.11)$$

where α is the BC coefficient related to the internal reflection at the boundary; the elements of matrix $[A]$ are $a_{ij} = \langle -D\nabla\phi_j \cdot \nabla\phi_i - \mu_a\phi_j\phi_i \rangle$, where $\langle \rangle$ indicates integration over the problem domain; $\{b\}$ is $-\langle S\phi_i \rangle + \alpha \sum_{j=1}^M \Phi_j \oint \phi_i\phi_j ds$; $S = S_0\delta(r - r_0)$ where S_0 is the source strength and

$\delta(r - r_0)$ is the Dirac delta function for a source at r_0 ; ; M is the number of boundary nodes; ϕ_i and ϕ_j are locally spatially varying Lagrangian basis functions at nodes i and j , respectively. The vector $\{\Phi\} = [\Phi_1, \Phi_2, \dots, \Phi_N]$ is the photon density.

Four critical parameters (the BC coefficient α , the source strength S_0 , and the initial guess of D and μ_a) should be accurately determined by a preprocessing data optimization scheme for the forward computation. We assume all the source intensities are the same and equal to S_0 . The pre-processing data optimization scheme for determining the four initial parameters is discussed in detail elsewhere [Nic and Jiang, 2000]. Briefly, X-square errors, $X^2 = \sum_{i=1}^{M1} [\Phi_i^{(m)} - \tilde{\Phi}_i^{(c)}]^2$, are minimized as the function of the above four parameters, where $M1$ is the number of boundary measurements (for example, $M1=64 \times 64$), $\Phi_i^{(m)}$ is the measured photon density from a given experimental heterogeneous medium, and $\tilde{\Phi}_i^{(c)}$ is the computed photon density from a numerical simulation of a homogeneous medium with the same geometry as the experimental medium. Given reasonable ranges for the four parameters, the minimum X^2 corresponds to the best initial guess of the four parameters.

1.5.2 Inverse Solution Procedure

An example of inverse solution procedure is given here based on Taylor expansion or Newton method. We assume that the computed and/or the measured Φ are analytic functions of D and μ_a , and that D and μ_a are independent parameters. Φ then can be Taylor expanded about an assumed (D, μ_a) distribution, which is a perturbation away from some other distribution, $(\tilde{D}, \tilde{\mu}_a)$, and the expansion is expressed as,

$$\Phi(\tilde{D}, \tilde{\mu}_a) = \Phi(D, \mu_a) + \frac{\partial \Phi}{\partial D} \Delta D + \frac{\partial \Phi}{\partial \mu_a} \Delta \mu_a + \dots \quad (3.12)$$

where $\Delta D = \tilde{D} - D$ and $\Delta \mu_a = \tilde{\mu}_a - \mu_a$. If the assumed optical property distribution is close to the true one, the high order items in the expansion can be neglected and we obtain

$$J \Delta \chi = \Psi^o - \Psi^c \quad (3.13)$$

where

$$J = \begin{bmatrix} \frac{\partial \Psi_1}{\partial D_1} & \frac{\partial \Psi_1}{\partial D_2} & \dots & \frac{\partial \Psi_1}{\partial D_K} & \frac{\partial \Psi_1}{\partial \mu_{a1}} & \frac{\partial \Psi_1}{\partial \mu_{a2}} & \dots & \frac{\partial \Psi_1}{\partial \mu_{aL}} \\ \frac{\partial \Psi_2}{\partial D_1} & \frac{\partial \Psi_2}{\partial D_2} & \dots & \frac{\partial \Psi_2}{\partial D_K} & \frac{\partial \Psi_2}{\partial \mu_{a1}} & \frac{\partial \Psi_2}{\partial \mu_{a2}} & \dots & \frac{\partial \Psi_2}{\partial \mu_{aL}} \\ \dots & \dots & \ddots & \dots & \dots & \dots & \ddots & \dots \\ \frac{\partial \Psi_M}{\partial D_1} & \frac{\partial \Psi_M}{\partial D_2} & \dots & \frac{\partial \Psi_M}{\partial D_K} & \frac{\partial \Psi_M}{\partial \mu_{a1}} & \frac{\partial \Psi_M}{\partial \mu_{a2}} & \dots & \frac{\partial \Psi_M}{\partial \mu_{aL}} \end{bmatrix} \quad (3.14)$$

$$\Delta \chi = [\Delta D_1 \quad \Delta D_2 \quad \dots \quad \Delta D_K \quad \Delta \mu_{a1} \quad \Delta \mu_{a2} \quad \dots \quad \Delta \mu_{aL}]^T \quad (3.15)$$

$$\Psi^o = [\Psi_1^o \quad \Psi_2^o \quad \dots \quad \Psi_M^o]^T \quad (3.16)$$

$$\Psi^c = [\Psi_1^c \quad \Psi_2^c \quad \dots \quad \Psi_M^c]^T \quad (3.17)$$

and Ψ_i^o and Ψ_i^c are observed and calculated data for $i=1,2,\dots,M$ measurements, D_k for $k=1,2,\dots,K$ and μ_{al} for $l=1,2,\dots,L$ are the reconstruction optical parameters. In order for equation 3.13 invertible, regularization method is used and expressed as

$$(J^T J + \lambda I) \Delta \chi = J^T (\Psi^o - \Psi^c) \quad (3.18)$$

where I is the identity matrix with the size of $2N \times 2N$, N is the node number of the finite element mesh, λ is the regularization parameter, J^T is the transposed Jacobian matrix, $\Delta\chi$ is the updating vector defined by equation 3.15.

CHAPTER 2 DOT IMAGING SYSTEM AND ITS CALIBRATION

2.1 DOT Imaging System

The imaging system is schematically shown in Figure 2-1. Light beams from ten laser modules are transmitted to the optical switch, which sequentially passes one of the beams to 64 pre-selected points at the surface of the phantom or breast via source fiber bundles. The ring structure or fiber optic/tissue interface holds the 64 source and 64 detection fiber bundles. Light from the 64 detection fiber bundles are sensed by the detection units, which convert the light intensity into voltage signals. The computer collects the signals through a data acquisition board. The DC motor near the ring is used to adjust the diameter of the ring. Two CCD cameras are mounted underneath the ring to monitor the contact between the tissue and fiber optics. Figures 2-2a and 2-2b show photograph of the entire imaging system where we can see that all the optical and electronic components are housed under the exam table. The individual components are detailed below.

2.1.1 10-wavelength Laser System

10 fiber-coupled laser modules at different wavelengths are used as CW laser sources. Each laser module is a compact integrated package of laser driver, thermoelectric cooler and temperature controller. The output power can be set from zero to maximum by adjusting the output control voltage from 0 to 5 volts. The pigtail fibers are 100 μ m in diameter and have a numerical aperture (NA) of 0.22. Table 2-1 gives more detailed information about these laser modules.

2.1.2 Optical Switch

A programmable 10x64 optical switch (GP700-4-1, Dicon Fiberoptics, Richmond, CA), controlled by a LABVIEW program through RS-232 remote interface, is used to deliver light

from lasers to the source fiber bundles. The configuration diagram and photograph of the optical switch are shown in Figures 2-3a and 2-3b, respectively. Inside the optical switch, there is a dual switch that works in tandem to deliver light to the target. The function of the left switch is to choose the wavelength and the other to select the source fibers. 100 μm fibers with FC connectors inside the optical switch, connected to the pig-tail fibers from the 10 laser modules, are used for light receiving/coupling. The insertion loss and back reflection are in the range from 0.56 to 1.15 dB and from -30.20 to -23.80 dB, respectively. The maximum crosstalk between any two channels is -80 dB. The laser output passes through the optical switch via 100 μm -diameter fibers, and is then coupled to 1mm-diameter source fiber bundles.

2.1.3 Source/detector Fiber Optic Probe

Figures 2-4a and 2-4b show photographs of the source/detector fiber optic array. It consists of a diameter-adjustable cone-shaped frustum containing four planes/rings of fiber optic bundles (RoMack, Williamsburg, VA). In each plane/ring, 16 detector fiber bundles (2.0 mm in diameter) are arranged equally spaced around the annulus with another 16 source fiber bundles (1.0mm in diameter) interspersed between the detector bundles. This fiber-optic/tissue interface was custom designed and constructed with high precision. The synchronized radial motion of fibers is realized through mechanical fingers that are driven by a DC motor. The diameter of the fiber array can be adjusted between 4.0 and 15.0 cm to fit different breast sizes. The height of the four-layer fiber array covers 2.0 cm.

The fiber optic probe is mounted right below an aperture on the exam table. During a clinical imaging measurement, the patient places her breast through the aperture so that the breast comes in contact with the fiber optic array. While the four-layer fiber optics is good enough to image the tissue volume for most cases in which we are currently interested, different

vertical positioning can be realized through the vertical translation of the ring. The position of the four planes/rings of fiber optic bundles is extended up intentionally. This allows the fiber optic probe to be positioned close to the patient's chest wall if necessary.

2.1.4 Detection Unit

Low noise light sensors, silicon photodiodes (S8745, Hamamatsu, Bridgewater, NJ) are chosen for low level light measurement. Each sensor, integrated into a small package, consists of a large area silicon photodiode (D1), an operation amplifier, a feed back resistance ($R_f = 1\text{G}\Omega$) and a capacitance ($C_f = 5\text{pF}$), as shown in Figure 2-5. The external feed back resistors, R_{f1} , R_{f2} and R_{f3} , are used to adjust the feedback gain. By controlling the relay (8L02-05-01, COTO Technology) switches (switch 1, switch 2 and switch 3), the sensor gain can be set to one of four gains (gain0, gain1, gain2 and gain3). The gain switching is discussed in detail in section 4.B below.

Four detection boards are made with 16 sensors mounted on each board. There are 64 sensors totally in the detection unit, which receive light intensities delivered from the 64 detection fiber bundles simultaneously. Figure 2-6 shows the diagram of mounting configuration for one sensor as well as the coupling between the detection fiber bundle and the silicon window of the sensor. The ten pins of each sensor are easy to be bent/broken. To protect the pins, one piece of plastic is used to hold the sensor and the plastic is attached to the circuit board to insure that there is no relative movement between the plastic and the circuit board once the pins are soldered on the circuit board. The plastic also isolates the circuit board from the grounded aluminum box, which shields any external electric/magnetic noises.

Figure 2-7a shows the schematic of a circuit board we designed. The 4-16 decoder is used to select the sensors. A four-bit digital signal from the computer is sent to the decoder directly.

Once a sensor is selected, the external feedback resistors are connected with pin4 and pin6 such that the gain is adjusted by the “gain switch controller”, whose function is to reduce the gain whenever the output is saturated and to increase the gain whenever the output is below 0.2 V. The controller sends the gain status (digital signal) to the computer. The signal output from the inverting amplifier is subsequently sent to a low-pass filter with a cutoff frequency of 10 KHz. Finally, the output signal from the low-pass filter, is sent to the A/D board. The A/D board collects only one output at a time from each time. The whole detection unit has four detection boards, hence four channels of data can be acquired at the same periods and 16 times of data collection are needed for all the 64 detection channels. Figure 2.7b shows the layout of the detection board, which is designed by the ORCAD.

2.1.5 Gain Control

When all the three gain switches are off, the detector gain is set to maximum (gain0). Whenever one of the switches is on, the other two must be off. The gain ratio, gain0: gain1: gain2: gain3, is 27000:900:30:1.

Figure 2-8 is a schematic, showing how the three switches are controlled. Once the output voltage is larger than 9.9V, the controller switches the gain to next level and the voltage is reduced by a factor of 30 to the level of 0.33V, shown by arrows 2, 4, and 6. Whenever the output voltage is less than 0.2V, the gain is switched to upper level and the voltage is amplified by a factor of 30, shown by arrows 1, 3, and 5. The hysteresis loop makes the controller insensitive to small signal fluctuations.

All the detector gains are set to gain1 initially. Most signal levels are between 0.2 and 9.9V, and the signal-to-noise ratio (SNR) is as high as 200:1 since the background noise measured in dark room is around 1 mV. But for a very large size phantom or breast tissue (e.g.,

larger than 10 cm), the minimum output is as small as 20mV at gain0. The SNR is then deteriorated to 20:1 in this case.

2.1.6 Detector Sensitivity and Dynamic Range

According to the data sheet of S8745 provided by Hamamatsu, photon sensitivity (S) of the detector is 0.3V/nW at 673 nm. Using a laser module of 673 nm and neutral density (ND) filters, the photon sensitivity of a representative photodiode sensor is measured. With a power meter, optical signal directed to the sensor is measured at different levels of laser input. Photon sensitivity for one detector at gain 0 (maximum gain), gain 1, gain 2 and gain 3 (minimum gain) is 0.23V/nW, 7.7V/uW, 0.257V/uW and 8.5V/mW, respectively. At gain 0, there are no externally connected resistors and the photon sensitivity is approximately equal to that provided by the manufacture data sheet. The slight difference is due to the loss occurred in the fiber coupling.

The maximum output voltage of a detector unit is 9.9V while the minimum output voltage or the electronic noise level is 1mV. At gain 3, the maximum detectable optical intensity is

$$\frac{9.9V}{8.5V / mW} = 1.164mW . \text{ At gain 0, the noise equivalent intensity is } \frac{1mV}{0.23V / nW} = 4.34pW . \text{ Thus}$$

the dynamic range can be calculated to be 2.682×10^8 .

2.1.7 Stability

For testing the stability, one laser module and one detector are chosen randomly. Laser beam with a power of 40 mw is sent to the optical switch, then to a 5 cm diameter phantom through one source fiber bundle. The diffused light delivered by a detector fiber bundle is measured by a photodiode detector. The data points are acquired every 10 seconds and the output voltage is normalized. The measurement fluctuation is less than 0.5%.

2.1.8 DC Offset/Noise Reduction

The DC offset came from the preamplifier and the low pass filters deteriorates the system performance. Before each experiment, the DC offset of each detection channel is collected. The setup is the same as that for experiments except the laser sources were off. The maximum offset is below 1mV.

Both optical and electronic noises exist in the system. Optical noises are from the laser modules and ambient environment. Electronic noises come from the electrical power grounding, fluctuation of power supply, electromagnetic disturbance, digital grounding of the computer, preamplifier in the photodiodes, operational amplifier offset, and resistance variation in the resistors. Since the experiments are performed in a dark room, influence from environmental light can be eliminated. To remove the remaining noises, the following routine methods are applied: low pass filters at a cutoff frequency of 1 KHz, a sealed aluminum box for each detection unit, a Tantalum capacitor to remove the power supply fluctuation and other standard techniques.

2.1.9 Data Acquisition Unit

The data acquisition unit is composed of PCI-DAS6035 and PCI-DDA08/12 (Measurement Computing, Middleboro, Massachusetts). PCI-DAS6035 is a 16-bit resolution A/D board with a maximum ADC rate of 200 KS/s. It has 8 differential channels, four of them are used currently (one for each board). The digital I/O ports of PCI-DDA08/12 are configured as two 8255 mode 0 emulations, each consisting of four ports: port A (8 bits), port B (8 bits), port C high (4 bits), and port C low (4 bits). These digital I/O lines either send digital signal to the decoder or receive the gain status from the boards. A LABVIEW program controls the operation of the data acquisition unit.

2.1.10 System Timing

When the gain of a sensor is set to gain0, the cutoff frequency of operational amplifier equals 32 Hz. To increase signal quality, 150 ms settling time used before the signal is converted by the A/D board when the sensor gain is set to gain0. Most sensors need to be set at gain0 for large size phantoms or tissues due to the associated small SNR. For each illumination position, the detection unit needs 2.4 seconds to collect all the data. The optical switch operates at the speed of 330 ms per switching action. Thus for 64 illumination and 64 detection positions, the total data acquisition time is about 2.9 minutes per wavelength. For a ten-wavelength measurement, the data collection time adds up to 29 minutes.

2.2 DOT Imaging System Operation

Before the imaging experiment, the system should be powered for half an hour for warm up. Figure 2-9 shows the power buttons of the system. Usually, the optical switch is powered at first, then the computer, and at last the laser modules. The switching power supply for the computer will affect the boot of the optical switch if the computer is powered before the optical switch.

Since our imaging system can only cover 2 cm slice of a breast at one imaging time, doctor has to tell us which breast of the patient has problems and the approximate location of the abnormality in the breast from the mammography films. When the patient comes, the consent form must be read and signed by the patient. The examined breast is positioned in correct location by the operator.

Figure 2-10 shows the LABVIEW control panel of the imaging system. Operator changes the output data file names, one for voltage signals and the other for gain stages of corresponding voltage signals. Then the number of detection layers and the number of laser modules are selected from the control panel. At last, the system runs automatically for the data acquisition.

The collected data will be calibrated and then used for the DOT image reconstruction using our finite element based algorithms.

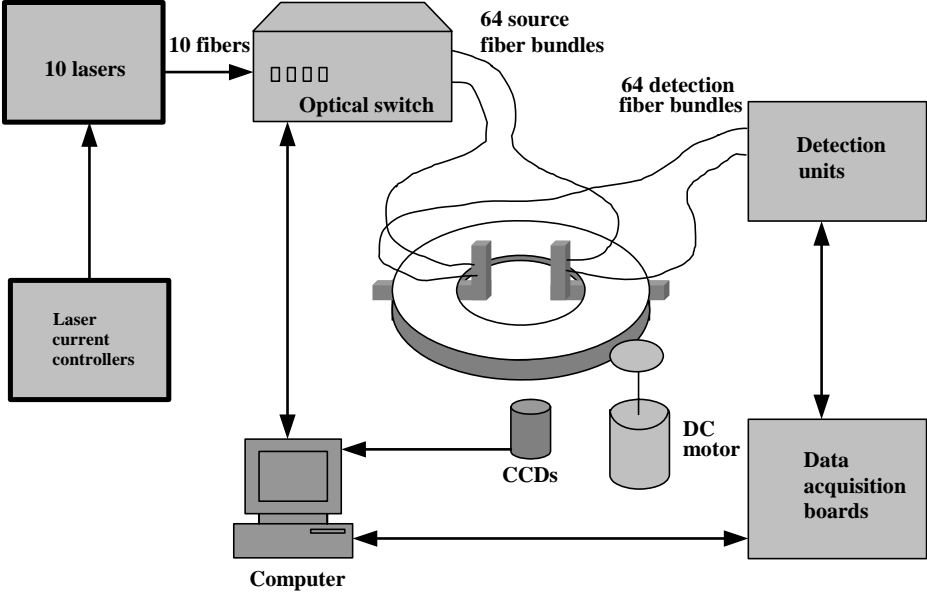
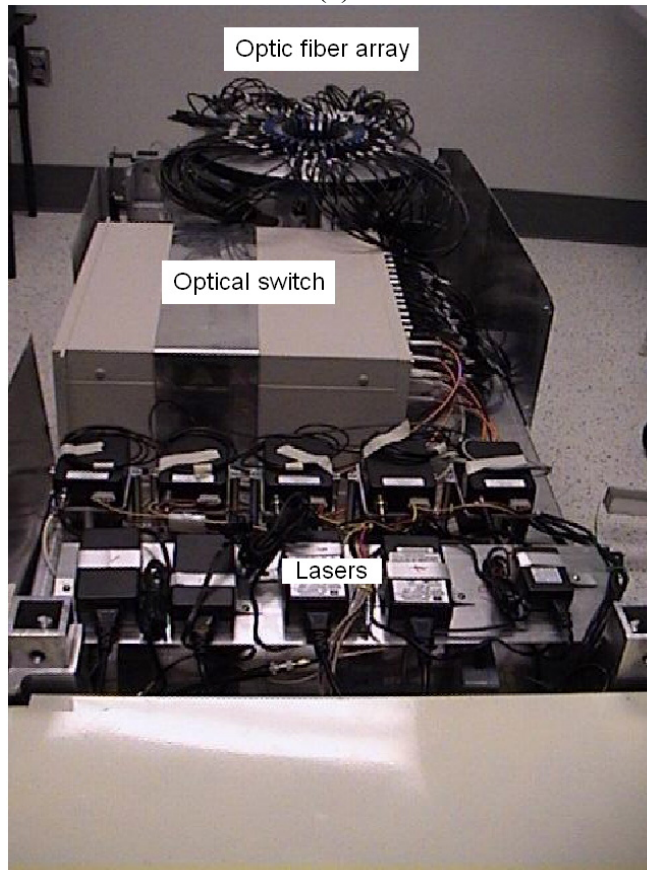


Figure 2-1. Schematic of the experimental system.

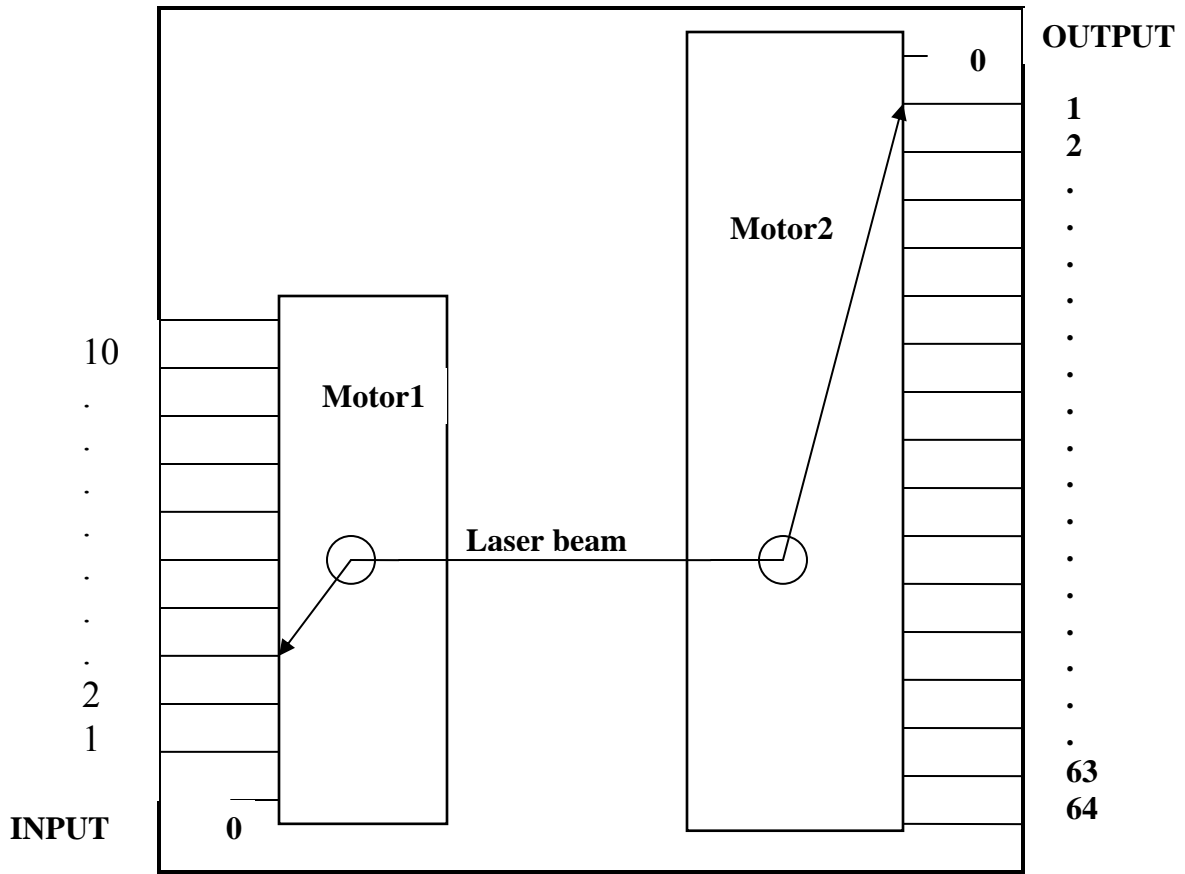


(a)

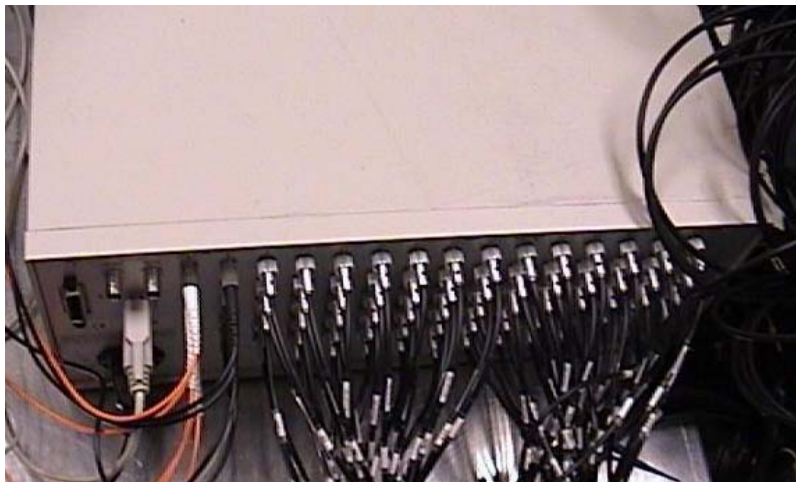


(b)

Figure 2-2. Photographs of the experimental system.

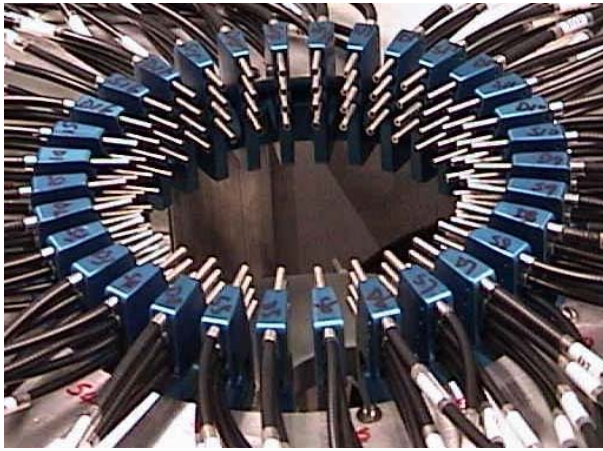


3(a)



3(b)

Figure 2-3. Optical switch (a) Schematic and (b) photograph.



(a)



(b)

Figure 2-4. Photographs of the ring structure.

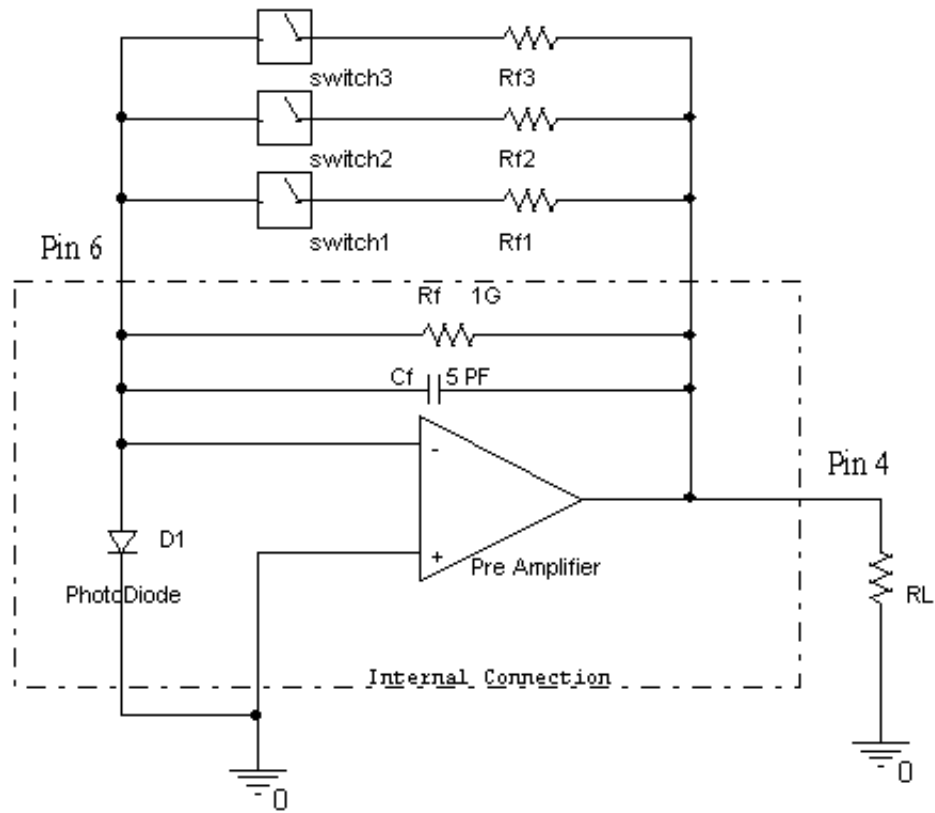


Figure 2-5. Internal and external connections of a silicon photodiode S8754.

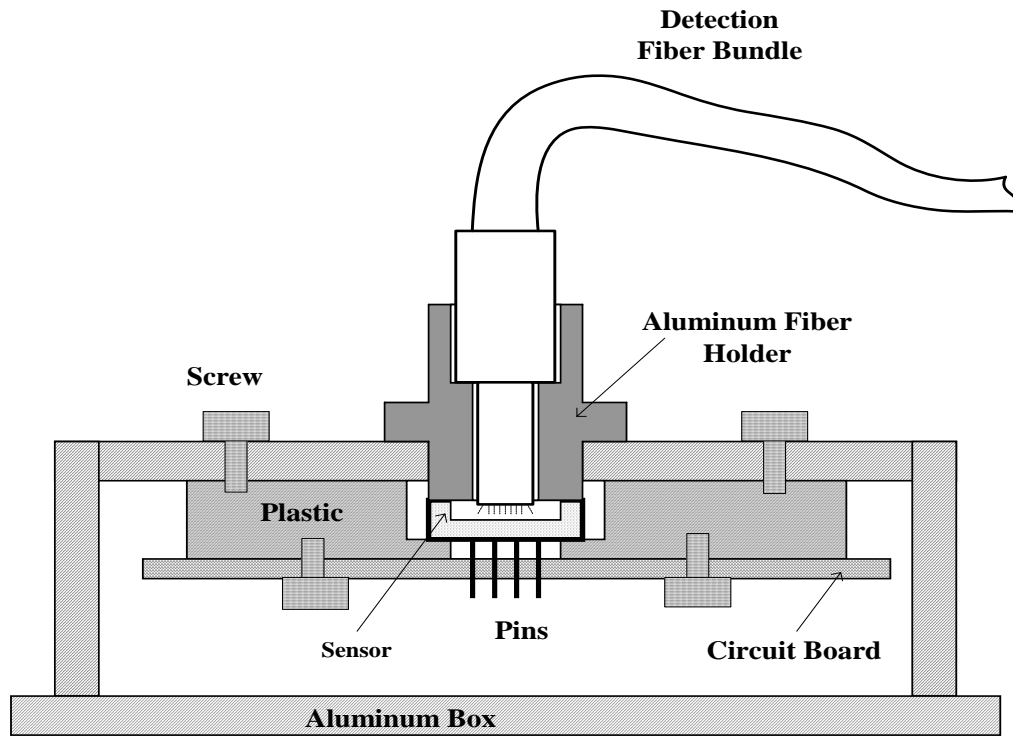
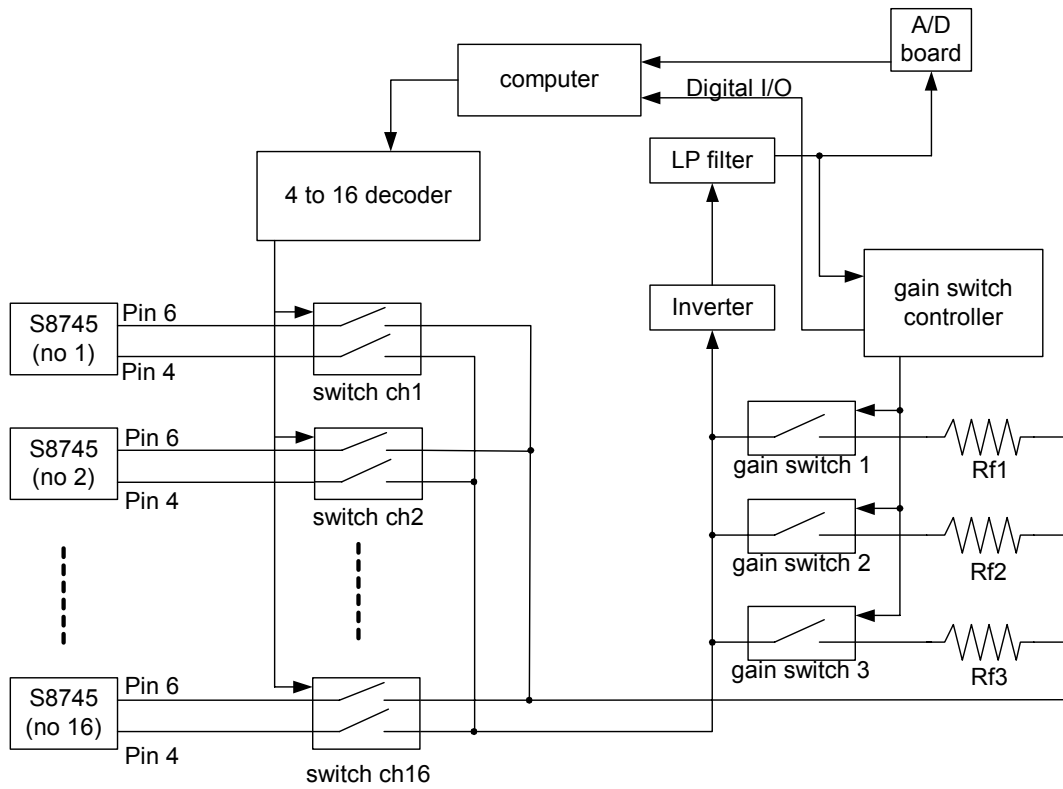
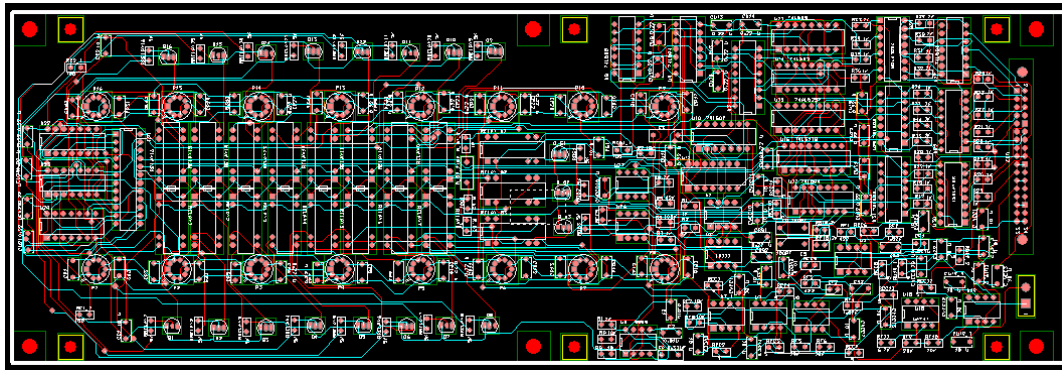


Figure 2-6. Diagram of mounting configuration for one sensor.



(a)



(b)

Figure 2-7. The detection board: (a) Schematic;(b) layout.

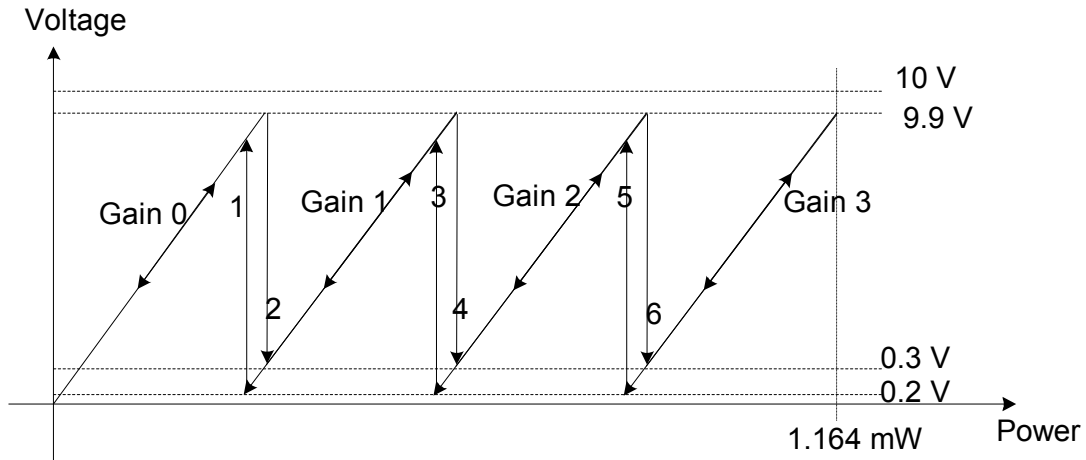


Figure 2-8. Flow chart of a detector gain controller.

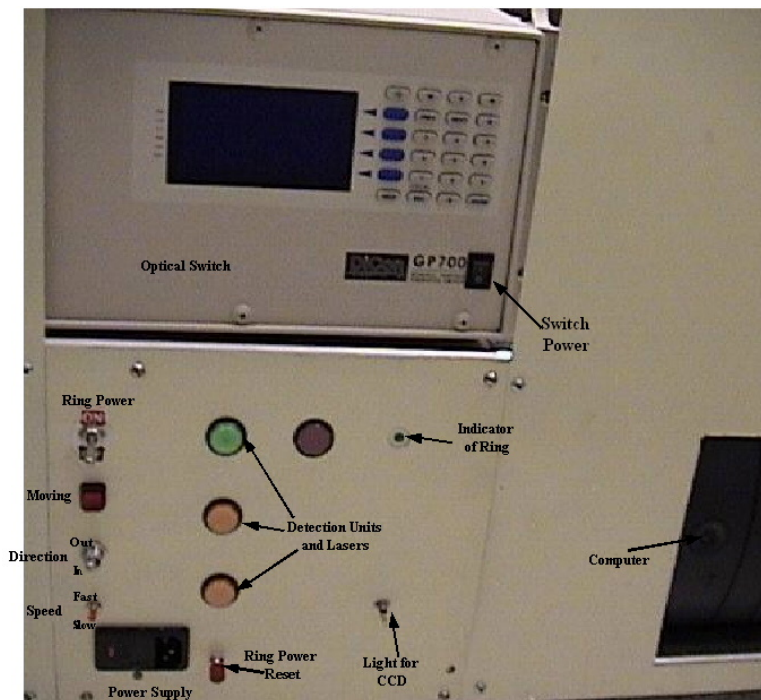


Figure 2-9. The control panel of the DOT imaging system.

DATA AQUISITION, PROCESSING and WRITING TO FILES

output file path (dialog if empty)

c:\clinic\test_dc.dat

function (open:0)

create or replace

gain file path (dialog if empty)

c:\clinic\test_gain.dat

function (open:0)

create or replace

append to file? (new file:F)

append to file

range1

1

gain of board1

0

output1

0.034

range2

1

gain of board2

0

output2

0.028

range3

1

gain of board3

0

output3

0.032

range4

1

gain of board4

0

output4

0.035

laser number

10 Wavelengths-----If diameter less than 10 cm or ruler number is less than -13.5mm

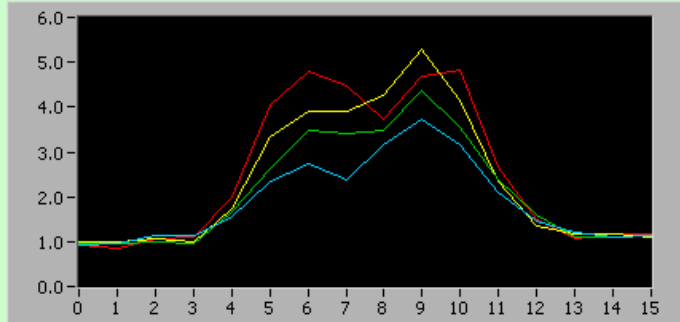
1

Source Points

64 source points

4

output waveform1



gain waveform1

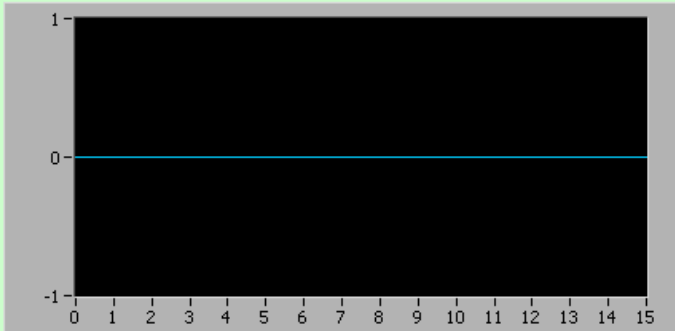


Figure 2-10. The LABVIEW control panel of the DOT imaging system.

CHAPTER 3
SYSTEM CALIBRATION AND DOT ALGORITHM REFINEMENTS

3.1 System Calibration

We describe a new calibration method that takes advantages of both the reference phantom based method and the data optimization scheme we developed. Various phantom experiments are performed using our newly developed silicon photodiodes-based DOT system in order to evaluate the calibration method. The dependence of the calibration method on phantom size and optical properties is also studied systemically. The results show that our new method can significantly improve the quality of quantitative absorption and scattering imaging even under the condition of very low absorption contrast.

3.1.1 Image Reconstruction Algorithm

An iterative finite element based algorithm, previously described in details elsewhere⁶⁹, is used for our image reconstruction of absorption and reduced scattering coefficients. Briefly, the steady-state photon diffuse equation

$$\nabla \cdot D(\mathbf{r})\nabla\Phi(\mathbf{r}) - \mu_a(\mathbf{r})\Phi(\mathbf{r}) = -S(\mathbf{r}) \quad (3.1)$$

coupled with Type III boundary conditions, $-D\nabla\Phi \cdot \hat{\mathbf{n}} = \alpha\Phi$, is transformed into the following matrix form of

$$[A]\{\Phi\} = \{b\}, \quad (3.2)$$

by the finite element discretization, where $\Phi(\mathbf{r})$ is the photon density, $\mu_a(\mathbf{r})$ is the absorption coefficient; $D(\mathbf{r})$ is the diffusion coefficient which can be written as $D(\mathbf{r}) = 1/3[\mu_a(\mathbf{r}) + \mu'_s(\mathbf{r})]$ where $\mu'_s(\mathbf{r})$ is the reduced scattering coefficient; $S = S_0\delta(\mathbf{r} - \mathbf{r}_0)$, is used where S_0 is the source strength and $\delta(\mathbf{r} - \mathbf{r}_0)$ is the Dirac delta function for a source at \mathbf{r}_0 ; $\hat{\mathbf{n}}$ is the unit normal vector for the boundary surface; α is the BC coefficient related to the internal reflection at the

boundary; the elements of matrix $[A]$ are $a_{ij} = \langle -D\nabla\phi_j \cdot \nabla\phi_i - \mu_a\phi_j\phi_i \rangle$, where $\langle \rangle$ indicates integration over the problem domain; $\{b\}$ is $-\langle S\phi_i \rangle + \alpha \sum_{j=1}^M \Phi_j \oint \phi_i\phi_j ds$; M is the number of boundary nodes; ϕ_i and ϕ_j are locally spatially varying Lagrangian basis functions at nodes i and j , respectively. Four critical parameters (the BC coefficient α , the source strength S_0 , and the initial guess of D and μ_a) can be accurately determined by a preprocessing data optimization scheme²⁸. Then a regularized Newton's method is used to update the initially guessed optical property (D and μ_a) distribution iteratively in order to minimize an object function composed of a weighted sum of the squared difference between computed and measured optical data at the medium surface.

The pre-processing data optimization scheme for determining the four initial parameters is discussed in detail elsewhere²⁸. Briefly, X-square errors, $X^2 = \sum_{i=1}^{M1} [\Phi_i^{(m)} - \tilde{\Phi}_i^{(c)}]^2$, are minimized as the function of the above four parameters, where $M1$ is the number of boundary measurements, $\Phi_i^{(m)}$ is the measured photon density from a given experimental heterogeneous medium, and $\tilde{\Phi}_i^{(c)}$ is the computed photon density from a numerical simulation of a homogeneous medium with the same geometry as the experimental medium. Given reasonable ranges for the four parameters, the minimum X^2 corresponds to the best initial guess of the four parameters.

3.1.2 Calibration Method

We present the calibration method here and provide further discussion about the method in subsection below. For a 2D imaging experiment, the calibration procedure is described by the following six steps:

A. Make a homogeneous phantom that has the same diameter as the heterogeneous phantom of interest.

B. Perform experiments with the homogeneous phantom. For 2D imaging experiments, there are 16 transmitters and 16 receivers. Obtain a set of measured data D_{ij} , where i is the transmitter number from 1 to 16 and j is the receiver number from 1 to 16. For each source i , light intensities from the 16 detectors are normalized.

C. Find the initial values of absorption coefficient μ_a , reduced scattering coefficient μ'_s and the boundary conditions coefficient α using D_{ij} . These initial parameters are required by our nonlinear iterative algorithm and can be found using the pre-processing method briefly described in Subsection 2.1 above.

D. Generate a 2D finite element mesh with the same diameter as the phantom. Using a unit source intensity for the 16 illuminated positions, the 2D photon propagation is simulated with the optical properties μ_a , μ'_s and the boundary conditions coefficient α identified in Step C. This creates a new set of data D_{ij}^* from the simulation.

E. Obtain a factor matrix f_{ij} using the following equation

$$f_{ij} = D_{ij}^* / D_{ij} \quad i, j = 1 \dots 16 \quad (3.3)$$

F. Multiply f_{ij} by the data set (E_{ij}) from the heterogeneous phantom to get the final data set for image reconstruction:

$$E_{ij}^* = f_{ij} E_{ij} \quad i, j = 1 \dots 16 \quad (3.4)$$

3.1.3 Experimental Methods and Materials

This system has been described in detail in subsection 2.1. The phantom materials used consisted of Intralipid as scatterer and India ink as absorber. Agar powder (1-2%) was used to solidify the Intralipid and Indian ink solutions. A single off-center target was embedded in a homogeneous background phantom in these imaging experiments. Figure 3-1 depicts the geometrical configuration for the test cases under study. One 14-mm-diameter cylindrical hole was drilled in the homogeneous background phantom for inclusions of the target with various optical contrasts. Three groups of experiments were performed to evaluate the calibration method. The three groups each contained three experiments with different phantom diameters and different levels of contrast in the target. The optical properties and geometry properties used in Groups 1 to 3 experiments are detailed in tables 3-1 to 3-3. The optical properties of the background phantoms for groups 1 to 3 are the same: $\mu_a = 0.005 \text{ mm}^{-1}$ and $\mu'_s = 1.0 \text{ mm}^{-1}$.

3.1.4 Results and Discussion

Figs. 3-2 to 3-4 present the reconstructed absorption and reduced scattering images from Groups 1, 2 and 3 experiments, respectively, where each set of imaging data was calibrated with the homogeneous phantom measurements from reference 1 (50mm diameter; left column), reference 2 (75mm diameter; middle column), and reference 3 (100mm diameter; right column), respectively. We can see that the best image quality is achieved when both the imaging and reference phantoms have the same dimension (see left column in Figure. 3-2, middle column in Figure. 3-3 and right column in Figure. 3-4). Under this situation, the recovered absorption and scattering images are quantitatively accurate in terms of the location, size and optical properties of the target. The reconstruction of the background is overall of high quality without any artifacts for smaller dimension cases and with minimal slight artifacts for larger dimension cases. In

particular, the very low absorption target is quantitatively resolved for all three background dimensions (Figure. 3-2a, Figure. 3-3b and Figure. 3-4c), which was impossible previously. Figure. 3-5 shows the one-dimensional (1D) profile of the absorption coefficient along the transect AB (see Figure. 3-1) for the images shown in Figs. 3-2a and 3-2d. This demonstrates a close quantitative examination of the selected images. Other cases have similar quality.

When the imaging data were calibrated using homogeneous phantom measurements having different dimension than the heterogeneous phantom of interest, the quality of the recovered images is clearly degraded (Figs. 3-2 to 3-4). These degradations are generally shown as a ring-pattern artifact (Figs. 3-2b and 3-2e; Figs. 3-4b, 4-4d and 3-4e) or a few millimeters shifting of the target toward the center of the background (Figs. 3-2c and 3-2f; Figs. 3-3a and 3-3d). It is interesting that there is no target shifting for all cases with the phantom of 100mm diameter. In general, the target is clearly detectable for most cases and the reconstruction is quantitative except for two cases with 100mm diameter phantom (Figs. 3-4j and 3-4k) where the recovered value of the reduced scattering coefficient is incorrect.

Quantitatively the improvement in image reconstruction with proper calibration is striking. For example, for the 1.4:1 absorption contrast experiments, when proper calibration was used, i.e., when the reference phantom had the same diameter as that of the heterogeneous phantom, the errors of the peak absorption coefficient recovered relative to the exact value were found to be 1.4% (Figure. 2-10a), 1.2% (Figure. 2-11b), and 2.8% (Figure. 2-12c) for the 50, 75 and 100mm diameter heterogeneous phantom cases, respectively. Whereas when improper calibration was performed, i.e., when the reference phantom had different diameter than that of the heterogeneous phantom, such errors are large as 110% and even the target cannot be detected for some of the cases (e.g., see Figs. 3-2b, 3-2c, 3-2e and 3-2f). For the 2:1 absorption and

scattering contrast experiments, the errors of the peak scattering coefficient compared to the exact value were calculated to be 5.5% (Figure. 3-2j) and 4.1% (Figure. 3-4l) for the 50 and 100mm diameter heterogeneous phantom cases, respectively, when proper calibration was applied. Whereas such errors are up to 60% when improper calibration was used.

Although the results shown above indicate the dependence of the image reconstruction on the size of reference phantom used, the calibration method described here will prove to be useful for clinical studies. For example, in the case of breast imaging, we can build a database based on a series of homogenous phantom measurements with a range of dimensions (e.g., from 4 to 11 cm with an increment of 5 mm). Whenever imaging measurements are performed on a particular size of breast, the imaging data obtained can be calibrated with one factor matrix from the database whose reference phantom diameter is equal or closest to that of the breast under measurement.

The calibration method described in this section is novel in that it takes advantages of both the pre-processing optimization scheme and the reference homogeneous phantom based method. The homogeneous phantom only based calibration method can remove systematic measurement errors while the pre-processing optimization scheme or model-based calibration methods can reduce the model mismatch errors due to the difference between the photon diffusion model and the physics involved. Thus the new calibration method can remove both types of errors which are resulted from the division of the measured data from the heterogeneous and reference homogeneous phantoms and multiplication of the computed data based on the pre-processing optimization scheme.

In sum, in this subsection a new calibration method is developed and evaluated by a series of phantom experiments with our newly developed diffuse optical tomography system. We

have shown that when the heterogeneous phantoms of interest and the reference homogeneous phantom have the same dimension, quantitative optical images can be obtained even under the conditions of very low absorption contrast. This study shows that this calibration method is sensitive to the reference phantom size.

3.2 Dual Mesh Method

As a finite element based reconstruction method, 3D DOT imaging needs a mesh with much more elements and nodes than 2D DOT imaging. For the nonlinear iterative DOT reconstruction, forward computation needs $O(n)$ multiplications (n is the node number), and the reverse computation needs $O(n^2)$ multiplications due to the full matrix property related with the Marquardt and Tikhonov regularization method⁶⁹. Therefore 3D DOT reconstruction computation burden is undesirable, especially for phantoms or tissues of large volumes. The dual mesh method utilizes two separate meshes: one fine mesh for the accurate photon density solution and a coarse mesh for the inverse process to update optical properties. It allows a significant reduction of computation burden for the problem with a big mesh, thus increasing the overall computational efficiency. In fact, the idea of dual meshing has been implemented in early works in both CW and frequency domains, where this method has been proved to significantly enhance the quality of reconstructed images³³. However, these early works did not exploit the potentials of this method in 3D DOT reconstruction. In this subsection, the dual mesh method is applied in the CW 3D DOT reconstruction. And the comparison with the single mesh method is made.

3.2.1 Dual Mesh Method

There are two meshes used for the dual mesh computation. One is the coarse mesh and the other is the fine mesh. For the cases in this section, the fine mesh is generated by splitting each coarse element into four fine mesh elements with equivalent volume for reducing the new mesh

singularity and for simplicity. And the new node i , is created at the centroid of each coarse mesh element, as shown in Figure. 3-6. For the single mesh method, both forward and inverse computations are performed in the coarse mesh. The coarse mesh contained 2,241 nodes corresponding to 10,368 linear tetrahedral elements. And the fine mesh, generated from coarse mesh, contains 12,609 nodes corresponding to 41,472 linear tetrahedral elements.

The dual mesh method for the 2D DOT reconstruction is described in detail elsewhere³³. The principle of dual mesh algorithm in 3D DOT reconstruction is similar. The forward computation is performed in the fine mesh. The local Lagrangian basis ϕ_i and ϕ_j , the optical properties D and μ_a in equation are defined in the fine mesh. The impact of the dual mesh method on the inverse process appears during the construction of the Jacobian matrix $[\mathfrak{J}]$, which is used to update the optical property values. The elements of $[\mathfrak{J}]$ are composed of the partial derivatives of the photon density at the observation sites with respect to the values of D and μ_a at each node within the coarse mesh. Considering the impact of the dual meshing, elements of the Jacobian matrix can be written as

$$\frac{\partial \alpha_{ij}}{\partial D_k} = \langle -\Psi_k \nabla \phi_i \cdot \nabla \phi_j \rangle, \quad (3.5)$$

$$\frac{\partial \alpha_{ij}}{\partial \mu_l} = \langle -\Psi_l \nabla \phi_i \cdot \nabla \phi_j \rangle, \quad (3.6)$$

where k and l are the nodes on the coarse mesh, Ψ_k and Ψ_l are the basis functions centered on nodes k and l in this mesh, and inner products are still performed over the elements in the fine mesh.

3.2.2 Experiments

The phantoms and targets were made of water, Intralipid (as scatterers), Indian Ink (as absorber) and agar (2%, used to solidify the phantom). Figure 3-7 describes the geometry of the phantom. A homogeneous background phantom ($\mu_a = 0.005 \text{ mm}^{-1}$ and $\mu'_s = 1.0 \text{ mm}^{-1}$) was made at first. Then a cylindrical hole with diameter of 14 mm was drilled at desired location in the background phantom and the target was put inside it. At last the hole with the target was refilled with background phantom materials. The location and the optical properties of the targets are shown in Table 3-4. For the three phantom experimental cases, the optical properties of the target are same ($\mu_a = 0.02 \text{ mm}^{-1}$ and $\mu'_s = 2.8 \text{ mm}^{-1}$) but with different off-center locations (15mm, 10mm, 5mm respectively). These three cases were performed to investigate lateral resolutions of the target.

3.2.3 Results and Discussion

For the dual mesh method, the reconstruction time was about 30 minutes per iteration on a 2.88 GHz PC with 1 Gb of RAM. For the single mesh method, the reconstruction time was about 15 minutes per iteration on the same PC. Reconstructed 3D μ_a and μ'_s images for each case are displayed at a series of transverse (coronal) sections perpendicular to axis Z and selected longitudinal (sagittal) sections perpendicular to axis X or axis Y. Quantitative one dimensional (1D) profiles of recovered optical properties along selected transects are also shown for all the cases.

Figure. 3-8, Figure. 3-9 and Figure. 3-10 plot the reconstructed μ_a images (a-d) and μ'_s images (e-h) for case 1 (4:1 μ_a , 2.8:1 μ'_s contrast, 15 mm off-center), case 2 (4:1 μ_a , 2.8:1 μ'_s contrast, 10 mm off-center) and case 3 (4:1 μ_a , 2.8:1 μ'_s contrast, 5 mm off-center) phantom experiments with the dual mesh method (left column) and the single mesh method (right

column), respectively. Rectangular figures plot recovered images at the sagittal cross section $y=0\text{mm}$ and circular figures plot recovered images at the coronal cross section $z=2\text{ mm}$ for each case. The color scale bar indicates values of μ_a (a-d) and μ'_s (e-h) in mm^{-1} . For all three cases, in the reconstructed μ_a images, the target is detected quantitatively, although there are some boundary artifacts in Figs. 3-8c, 3-8d, 3-9c, 9d, 10c and 10d. When the dual mesh method is used we see artifacts in the reconstructed μ_a images (Figs. 3-8c, 3-9c, 3-10c) are less than those in μ_a images (Figs. 3-8d, 3-9d, 3-10d) reconstructed with the single mesh method. In the reconstructed μ'_s images, with the dual mesh method, the target is differentiated quantitatively for all three cases, as shown in figures 3-8e and 3-8g for case 1, figures 3-9e and 3-9g for case 2, figures 3-10e and 3-10g for case 3, while with the single mesh method, we can see the target shape is deteriorated by artifacts although target μ'_s value is close to the exact value, as shown in Figure. 3-8h for case 1, Figure. 3-9h for case 2 and Figure. 3-10h for case 3.

Figure 3-11 plots the three-dimensional view of the reconstructed absorption coefficient images (Figs. 3-11a, c, e) in mm^{-1} and the reconstructed reduced scattering coefficient images (Figs. 3-11b, d, f) in mm^{-1} for case 1 (Figs. 3-11a, b, 15mm offset), case 2 (Figs. 3-11c, d, 10mm offset) and case 3 (Figs. 3-11e, f, 5mm offset) using dual mesh method. The showing slices in each figure are crossed at the center of the target. It is clear to see that the reconstructed targets are located in the expected positions.

Three-dimensional DOT reconstruction for tissue mimicking phantoms or tissues of large volumes, a mesh with thousands of elements is needed and the computational cost is high. The dual mesh method provides a way to reduce the computational burden without sacrificing the extracted image quality. The results shown in this section illustrate the feasibility and potential of the dual mesh method application in CW 3D DOT. We have reported that the dual mesh method

performed very well in two-dimensional DOT reconstruction for several coarse mesh and fine mesh combinations.³³ Here the coarse mesh and the fine mesh are fixed. It is not the purpose of this subsection to study the mesh effects on the 3D DOT reconstruction. One set of coarse mesh and fine mesh is enough to illustrate the dual mesh application in the CW 3D DOT.

To date, we have not found any resolution studies on CW 3D DOT. In frequency domain, Dehghani et. al. have investigated 3D DOT resolutions and localizations of property heterogeneity²⁴ and good accuracy in localization (within 7 mm of the true position in the worst case) was obtained. While the accuracy of quantitative imaging is almost 100% of the target values with *a priori* information regarding the anomaly location, the target absolute value of optical properties is 10% of the expected values without the information. In this section, the target localization error is less than 2 mm with the dual mesh method and less than 4 mm with the single mesh method. The target value errors from the reconstructed optical properties μ_a and μ'_s images are less than 2.5% and 10.7% with both methods without *a priori* information. The difference is possible due to more measurement of data pairs for our experiments (64 by 64), smaller background phantom size, different 3D DOT algorithm, compared with theirs.

In sum, an axial spatial resolution of 5 mm in the CW 3D DOT is achieved with a set of tissue mimicking phantom experiments by using both the dual mesh method and the single mesh method. In addition, for both the high and low contrast anomalies in the turbid media, the dual mesh method has the capability of detecting them with better image quality and more accurate maximum coefficient values than the single mesh method.

3.3 Source Intensity Optimization Method

We have previously demonstrated quantitative 3D image reconstruction of absorption and scattering images in CW domain using phantom and *in vivo* experiments.^{29, 37, 70} While our

results are promising, we intend to improve our 3D imaging capability by developing a method of source intensity optimization. Together with a pre-processing method previously developed for 2D imaging,²⁸ we experimentally show in this paper that the 3D imaging quality can be significantly enhanced for both absorption and scattering image reconstructions.

3.3.1 Source Intensity Optimization Methods

In our reconstruction algorithm, the diffusion equation is iteratively solved based on a regularized Newton's method in order to update an initially guessed optical property (D and μ_a) distribution. In addition to the initial optical properties, it is clear that the BC coefficient α and the source strength S_k must also be given for the entire solution procedure. In fact these initial parameters need to be accurately determined for quantitative image reconstructions as illustrated in [28] where we developed a preprocessing data optimization scheme for such a purpose. In the following we first describe two previous source calibration methods, uniform source intensity and normalized source intensity, and then introduce the new source optimization method.

Uniform source intensity method. In the uniform source intensity method, all the source terms, S_k ($k = 1, 2, \dots, 64$), are assumed to be the same, i.e., $S_k = S_o$. Thus there are only 4 parameters (α , S_o , and initial D and μ_a values) that need to be optimized before the

reconstruction. In our pre-processing data optimization scheme for determining the four initial

parameters, χ^2 -square errors, $\chi^2 = \sum_{i=1}^M [\Phi_i^{(m)} - \tilde{\Phi}_i^{(c)}]^2$, are minimized as a function of the above

four parameters, where M is the number of boundary measurements (in this study, $M=64 \times 64$),

$\Phi_i^{(m)}$ is the measured photon density from a given experimental heterogeneous medium, and

$\tilde{\Phi}_i^{(c)}$ is the computed photon density from a numerical simulation of a homogeneous medium

with the same geometry as the experimental medium. Given reasonable ranges for the four parameters, the minimum χ^2 corresponds to the best initial guess of the four parameters.

Normalized unit source intensity method. The second preprocessing method used previously is a normalized unit source calibration method. In this method, the source terms $S_k=1$ while the measured data at 64 measurement sites are normalized using the maximum of the 64 measured data for a given source location. Thus, using this method we only need to optimize three initial parameters (α and optical properties D and μ_a), and the normalized measured data

must be used for reconstructions. Similarly, square errors, $\chi^2 = \sum_{i=1}^M \left[(\Phi_i^{(m)})_{\text{norm}} - (\tilde{\Phi}_i^{(c)})_{\text{norm}} \right]^2$,

are minimized as a function of the above three parameters, where M is the number of boundary measurements (in this study, $M=64 \times 64$), $(\Phi_i^{(m)})_{\text{norm}}$ is the normalized measured photon density

from a given experimental heterogeneous medium, and $(\tilde{\Phi}_i^{(c)})_{\text{norm}}$ is the normalized computed photon density from a numerical simulation of a homogeneous medium with the same geometry

as the experimental medium. The minimum χ^2 gives the best initial guess of the three parameters.

Source intensity optimization method. In the source intensity optimization method, α and initial D and μ_a are optimized first using the normalized source intensity method described in the above subsection. Then for each of the 64 excitations, the corresponding source intensity, S_k , is obtained using the similar preprocessing procedure described in above two subsections. For

each of S_k (k from 1 to 64), square errors, $\chi_k^2 = \sum_{i=1}^{M1} \left[(\Phi_i^{(m)})_k - (\tilde{\Phi}_i^{(c)})_k \right]^2$, are minimized as a

function of S_k , where $M1$ is the number of measurement for each source excitations (in this

study, $M1=64$), $(\Phi_i^{(m)})_k$ indicates the original measured photon density from a given experimental heterogeneous medium for excitation at k , and $(\tilde{\Phi}_i^{(c)})_k$ is the computed photon density for excitation at k from a numerical simulation of a homogeneous medium with the same geometry as the experimental medium and with the α , D and μ_a obtained in the first step. The optimized source intensity S_k is obtained when χ_k^2 are minimized. Finally a total of 67 initial parameters are searched for full 3D image reconstructions.

3.3.2 Experiments

The phantom materials used consisted of Intralipid as scatterer and India ink as absorber. Agar powder (1-2%) was used to solidify the Intralipid and Indian ink solutions. A single off-center target was embedded in a homogeneous background phantom in these imaging experiments. Figure 3-12 depicts the geometrical configuration for the test cases under study. One 14 or 9-mm-diameter cylindrical hole was drilled in the homogeneous background phantom for inclusions of targets with various optical contrasts. A cylindrical target (14mm in diameter and 10 mm in height for cases 1-4 and 9 mm in diameter and 10 mm in height for cases 5-6) was placed into the hole where the rest of the hole was filled with phantom material that was the same as the background. Six experiments with different optical contrast levels between the target and background were performed to evaluate the three optimization methods discussed in Section 2. The geometrical information and optical properties used for the target in the 6 experiments are detailed in Table 3-5. The optical properties of the background were the same for all the experiments: $\mu_a=0.005 \text{ mm}^{-1}$ and $\mu'_s=1.0 \text{ mm}^{-1}$.

3.3.3 Results and Discussion

The results presented in this section were obtained using a 3D mesh with 10386 tetrahedron elements and 2241 nodes. Reconstructed 3D μ_a and μ'_s images for each case are displayed at a series of transverse (coronal) sections perpendicular to axis Z and selected longitudinal (sagittal) sections perpendicular to axis X or axis Y. Quantitative 1D profiles of recovered optical properties along selected transects are also shown for some cases.

Figure 3-13 shows the reconstructed μ_a images at a selected sagittal and coronal section for case 1 (2:1 μ_a contrast). From Figs. 3-13a and 3-13b, when the uniform source intensity method was used we see that boundary artifacts dominate the images and the target cannot be detected for this relatively low contrast case. The target is detectable with the normalization method (Figs. 3-13c and 3-13d), while we note relatively strong artifacts in the background. The detection of the target is clearly improved when the source optimization method was used (Figs. 3-13e and 3-13f), although there are still some small artifacts in the background region.

Reconstructed μ_a images at a series of coronal sections for case 2 (4:1 μ_a contrast) are plotted in Figure 3-14. As shown from column 3 in Figure. 3-14, when the uniform source method was used the target cannot be detected at most coronal sections except that at $z=-2\text{mm}$ the target was barely visible. For the images obtained by the normalization method (column 2 in Figure. 3-14), the target is resolvable, but with a marked circularly shaped artifact in the background. Again, when the source optimization method was utilized, the target is clearly detected with minimal artifacts, as shown from column 1 in Figure. 3-14.

Figure 3-15 plots the absorption and scattering images reconstructed for case 3. For the μ_a images in this case, the target is differentiated successfully from the background with all three methods (Figs. 3-15a-f). However, we can see that the quality of the extracted μ_a images

with the source intensity optimization method is still the best (Figs. 3-15a and 3-15d). For example, as shown in Figs. 3-15a and 3-15d, the shape and size of the target is better recovered and there are much less artifacts in the background. For the μ'_s images shown in Figs. 3-15g-o, we note that the uniform source intensity method basically fails to detect the target (Figs. 3-15i, l and o). The normalization method has the capability to detect the target, but with strong artifacts in the background (Figs. 3-15k and n). In addition, the recovered target position is shifted towards the center of the background (Figure. 3-15k). Figures 3-15g, j and m illustrate that the source intensity optimization method is capable of reconstructing μ'_s images with much better accuracy and with much less artifacts relative to the other two methods.

Figures 3-16 and 3-17, respectively, show the recovered absorption and scattering images at a selected sagittal section and a series of coronal sections for case 4. In this relatively high contrast case, we note that the target is detected for both the μ_a and μ'_s images with all three methods (e.g., see the images shown at $y=0$ and $z=2$ in Figs. 3-16 and 3-17). However, we can still see that the images with the source intensity optimization method have the best overall quality (column 1 in Figs. 3-16 and 3-17). For the absorption images, we observe that the normalization method (column 2 in Figure. 3-16) gives almost the same quality as the source optimization method, except that it generated more boundary artifacts (see the images at $z=-6$ in Figure. 3-10). The boundary artifacts in the images from the uniform source intensity method are clearly the strongest such that the target is invisible at several cut planes (e.g., see column 3 at $z=6$ mm in Figure. 3-16). For the scattering images shown in Figure. 3-17, we see that the recovered target position is shifted to the center of the background at several cut planes (see the images at $z=6$ mm in Figure. 3-17).

For a more quantitative assessment of the results, Figure 3-18 shows μ_a and μ'_s profiles along a transect through the centers of the target and background for the images at $y=0\text{mm}$ and $z=2\text{mm}$ for the cases 1-4 when the source intensity optimization method was used. The dotted line corresponds to the exact values and the solid line are referred to the extracted optical property values. From Figure.3-18, we calculated the relative errors of the recovered μ_a (maximum value) in the target to be 13.0%, 0.95%, 0.1% and 0.2% for cases 1-4, respectively. The relative errors of the extracted μ'_s (maximum value) in the target were found to be 2.0% and 8.8% for cases 3 and 4, respectively.

Figure 3-19 plots the absorption images (Figs. 3-19a and 3-19b) and scattering images (Figs. 3-19c and 3-19d) reconstructed with the source optimization method for case 5 (4:1 μ_a and μ'_s contrast) at the section $y=0\text{ mm}$ (Figs. 3-19a and 3-19c) and at the section $z=-3\text{ mm}$. The target is superficial and the closest distance between the target and one fiber bundle is 2 mm. The source intensity at the fiber bundle obtained with the source optimization method increased by 56% above the average. From figure 3-19 we see that both the scattering images and the absorption images were reconstructed successfully. The intensity increase did not appear to degrade the quality of image reconstruction.

Figure 3-20 shows the absorption images (Figs. 3-20a and 3-20b) and scattering images (Figs. 3-20c and 3-20d) reconstructed with the source optimization method for case 6 (4:1 μ_a and μ'_s contrast) at the section $y=4\text{ mm}$ (Figs. 3-20a and 3-20c) and at the section $z=-6\text{ mm}$. Again, the target is superficial and is embedded between two source fiber bundles. The source intensities at these two fiber bundles increased by 45% and 7.5%, respectively. Both the scattering images and the absorption images were reconstructed successfully while the shape of

the target (Fig 3-20c) was degraded because the target was close to the bottom of the background phantom.

Figures 3-21(a) and 3-21(b) plot the uniform source intensity obtained by the uniform source intensity method (dotted line) and the source intensity distribution obtained by the source intensity optimization method (solid line) from the original measurements of case 4 and the normalized measurements for case 4, respectively. Both the uniform source intensity method and the normalized unit source intensity method assume that all the 64 source intensities are the same. However, the real source intensity distributions are not uniform (the solid line in figure 3-21) due to the experimental and numerical errors. And for case 4, the maximum/minimum ratios are about 3.0 and 1.8 for the original and normalized data, respectively. The normalization reduced the source intensity maximum/minimum ratio from 3.0 to 1.8 and made the source intensity distribution more uniform. That may be the reason why the normalized unit source method is capable of obtaining better images than the uniform source intensity method.

Based on the results presented above, it is clearly seen that the source optimization method provides significantly improved image quality over the existing two source calibration methods. This is not surprising because both the uniform source intensity and the normalization methods assume that all the 64 source intensities are the same, while the real source intensity distributions are not uniform due to experimental errors. We believe that S_k 's (k from 1 to 64) represent real emitter intensities at the source locations around the phantom surface. The real emitter intensity at one location equals the multiplication of the corresponding laser module output intensity, the source fiber attenuation and the source fiber-phantom coupling coefficient.

While detailed evaluation to what extent 3D model can improve DOT imaging over 2D model is beyond the scope of this paper, it is interesting to initially compare the 3D results

presented here with our 2D results obtained previously. We have demonstrated that both μ_a and μ'_s images in heterogeneous media can be extracted quantitatively using 2D model with appropriate calibration and preprocess methods.^{31, 71} These 2D images gave similar quantitative accuracy as 3D images presented in this work. One expects that 3D model would provide better accuracy for image reconstruction than 2D model, however. A possible reason for explaining this contradiction is that the volume/amount of measured data available in the current 3D imaging system may not be enough relative to the number of unknown parameters involved in the 3D image reconstructions.

It is well known that the source intensity difference among the different source locations significantly degraded the DOT reconstructed image qualities. One way to calibrate the source intensity is that the optical source coupling coefficients and/or the optode positions are reconstructed simultaneously with the image extraction.⁷²⁻⁷⁴ Another way is to estimate the coupling coefficients with a homogenous and isotropic phantom before experiments.⁷⁵⁻⁷⁶ In this paper, our method estimated the source intensities at the different source locations by a fitting procedure with measured data from an inhomogeneous phantom and simulated data corresponding to a homogeneous model phantom. The presented results show that our proposed method can significantly improve the quality of reconstructed images. Combined the methods reported in Refs.72-74 with the source optimization method described here may result in further improvement. We plan to evaluate this combined method in future.

In sum, we have developed a new source optimization method in this paper. The imaging results shown indicate that this new method can quantitatively improve 3D image reconstructions.

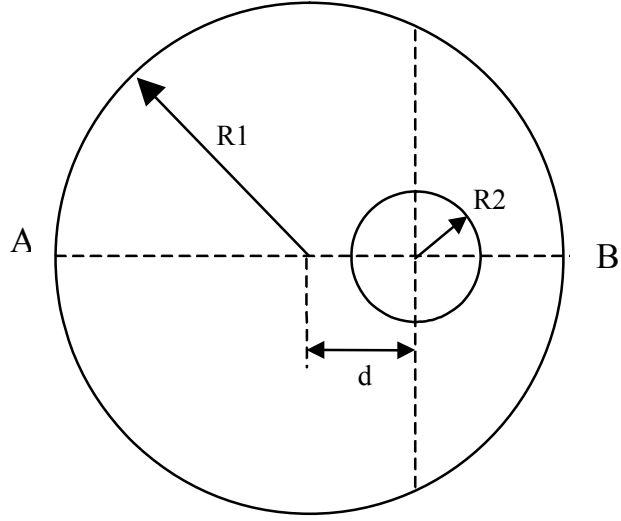


Figure 3-1. Geometry of the phantom configuration.

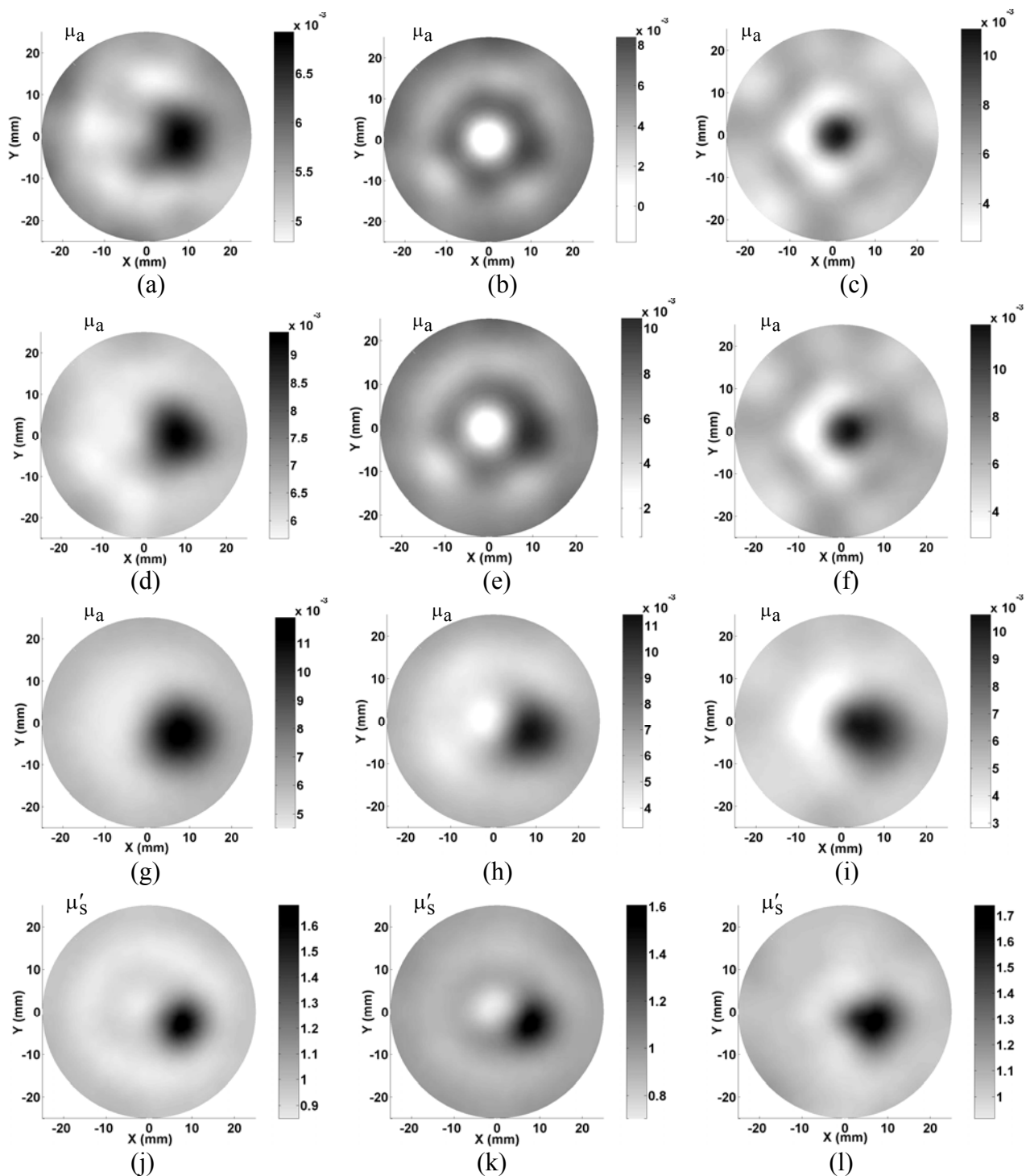


Figure 3-2. Reconstructed absorption and scattering images for the 3 cases in Group 1 when each set of imaging data was calibrated with 50mm diameter homogeneous phantom (left column), 75mm diameter phantom (middle column), and 100mm diameter phantom (right column), respectively. (a)-(c): absorption images from the case of target 1. (d)-(f): absorption images from the case of target 2. (g)-(i): absorption images from the case of target 3. (j)-(l): scattering images from the case of target3. The grey scale shows the absorption or reduced scattering coefficient value (mm^{-1}), while the axes indicate the spatial dimension (mm).

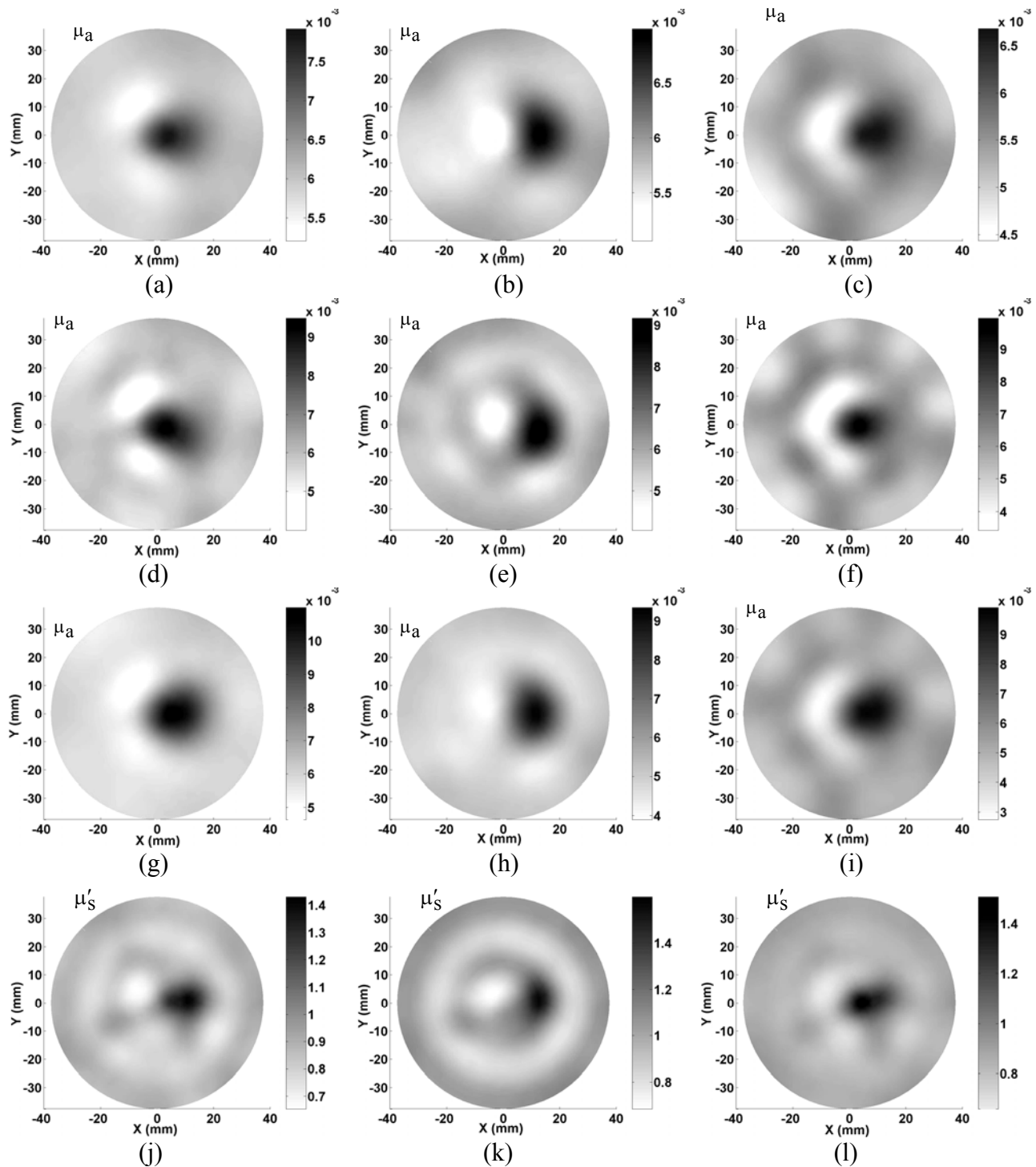


Figure 3-3. Reconstructed absorption and scattering images for the 3 cases in Group 2 when each set of imaging data was calibrated with 50mm diameter homogeneous phantom (left column), 75mm diameter phantom (middle column), and 100mm diameter phantom (right column), respectively. (a)-(c): absorption images from the case of target 1. (d)-(f): absorption images from the case of target 2. (g)-(i): absorption images from the case of target 3. (j)-(l): scattering images from the case of target 3. The grey scale shows the absorption or reduced scattering coefficient value (mm^{-1}), while the axes indicate the spatial dimension (mm).

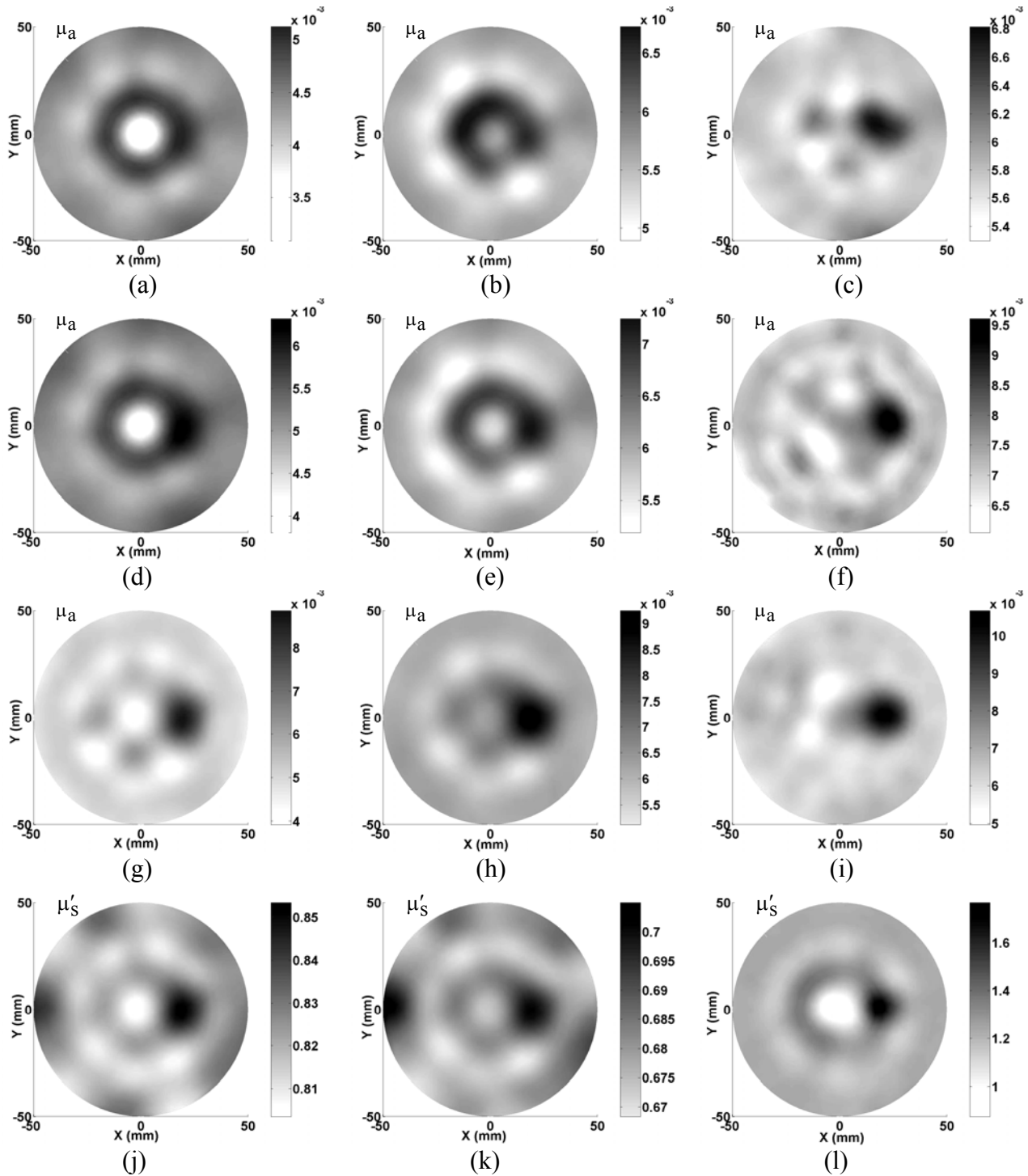


Figure 3-4. Reconstructed absorption and scattering images for the 3 cases in Group 3 when each set of imaging data was calibrated with 50mm diameter homogeneous phantom (left column), 75mm diameter phantom (middle column), and 100mm diameter phantom (right column), respectively. (a)-(c): absorption images from the case of target 1. (d)-(f): absorption images from the case of target 2. (g)-(i): absorption images from the case of target 3. (j)-(l): scattering images from the case of target 3. The grey scale shows the absorption or reduced scattering coefficient value (mm^{-1}), while the axes indicate the spatial dimension (mm).

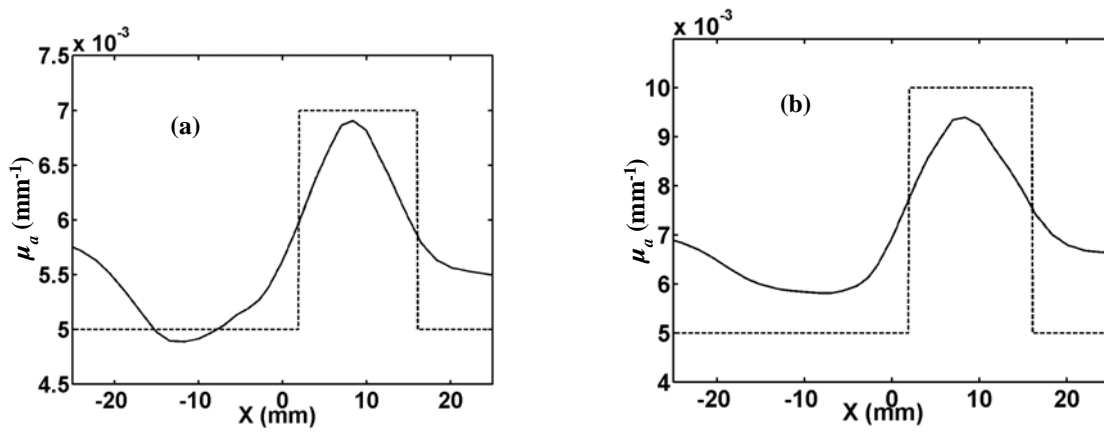


Figure 3-5. 1D profile of the absorption coefficient along the transect AB (see Figure. 3-1) for the image shown in Figure. 3-2a (a) and for image shown in Figure. 3-2d (b). The dotted and solid lines are, respectively, the exact and reconstructed absorption coefficient distributions.

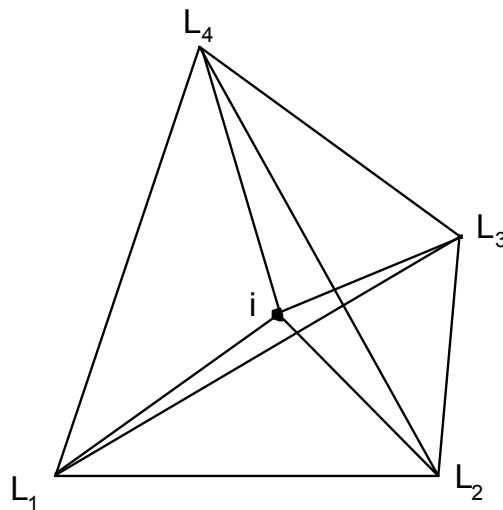


Figure 3-6. Four fine mesh elements generated from one coarse mesh element.

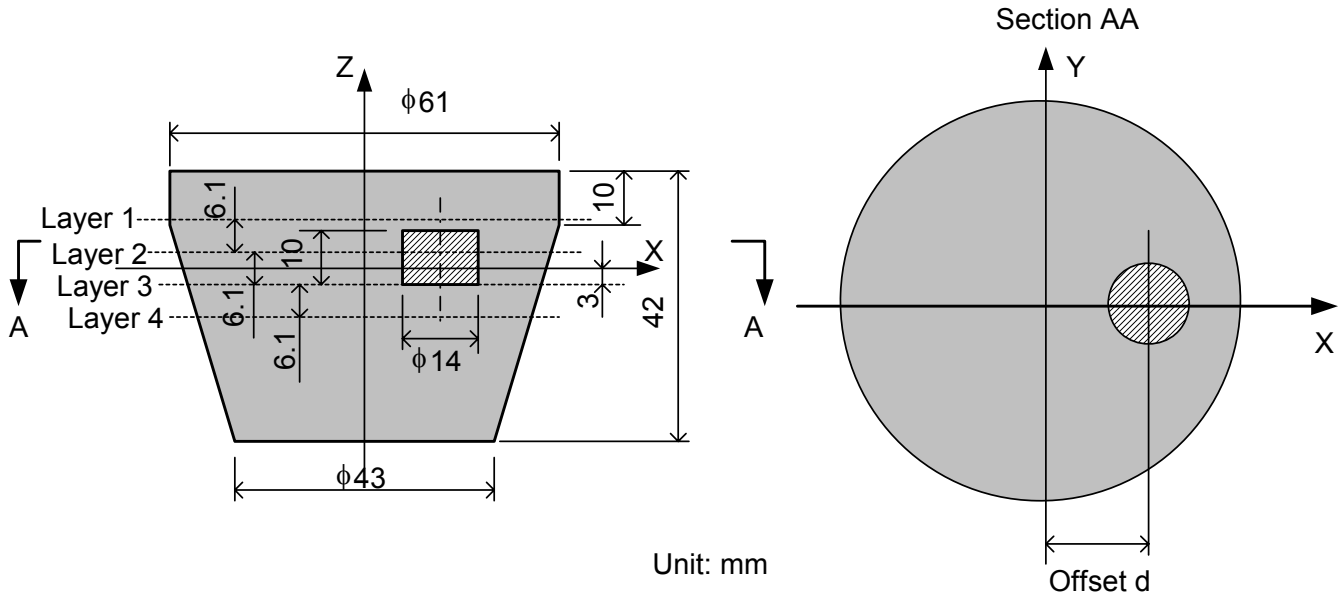


Figure 3-7. Geometry of the tissue mimicking phantom.

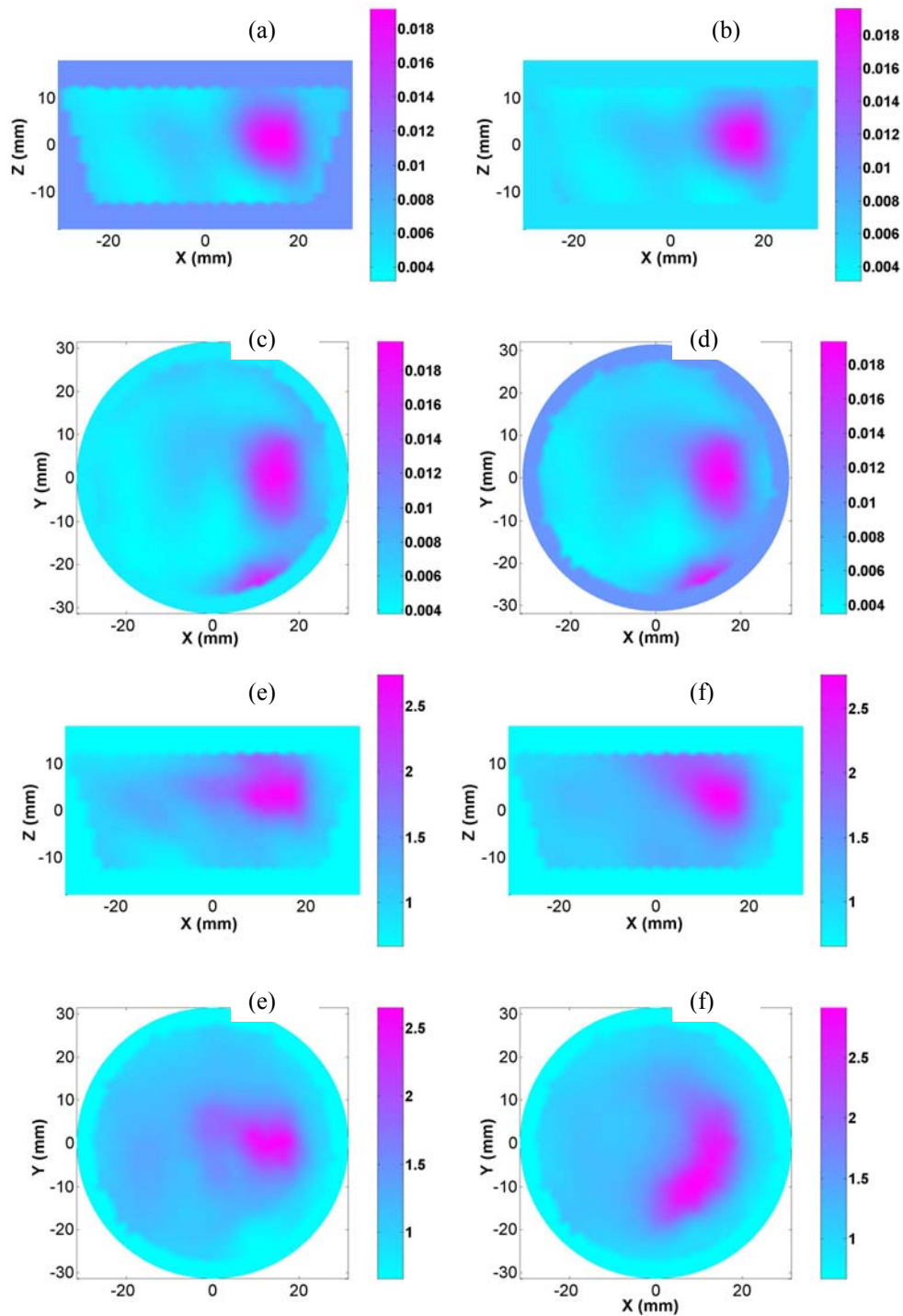


Figure 3-8. The μ_a images (a-d) and μ'_s images (e-h) reconstructed for case 1 (4:1 μ_a , 2.8:1 μ'_s contrast, 15 mm off-center) phantom experiment with the dual mesh method (left column) and the single mesh method (right column). The rectangular and circular figures are at the cross sections $y=0$ mm and $z=2$ mm respectively. The color scale bar indicates values of μ_a (a-d) and μ'_s (e-h).

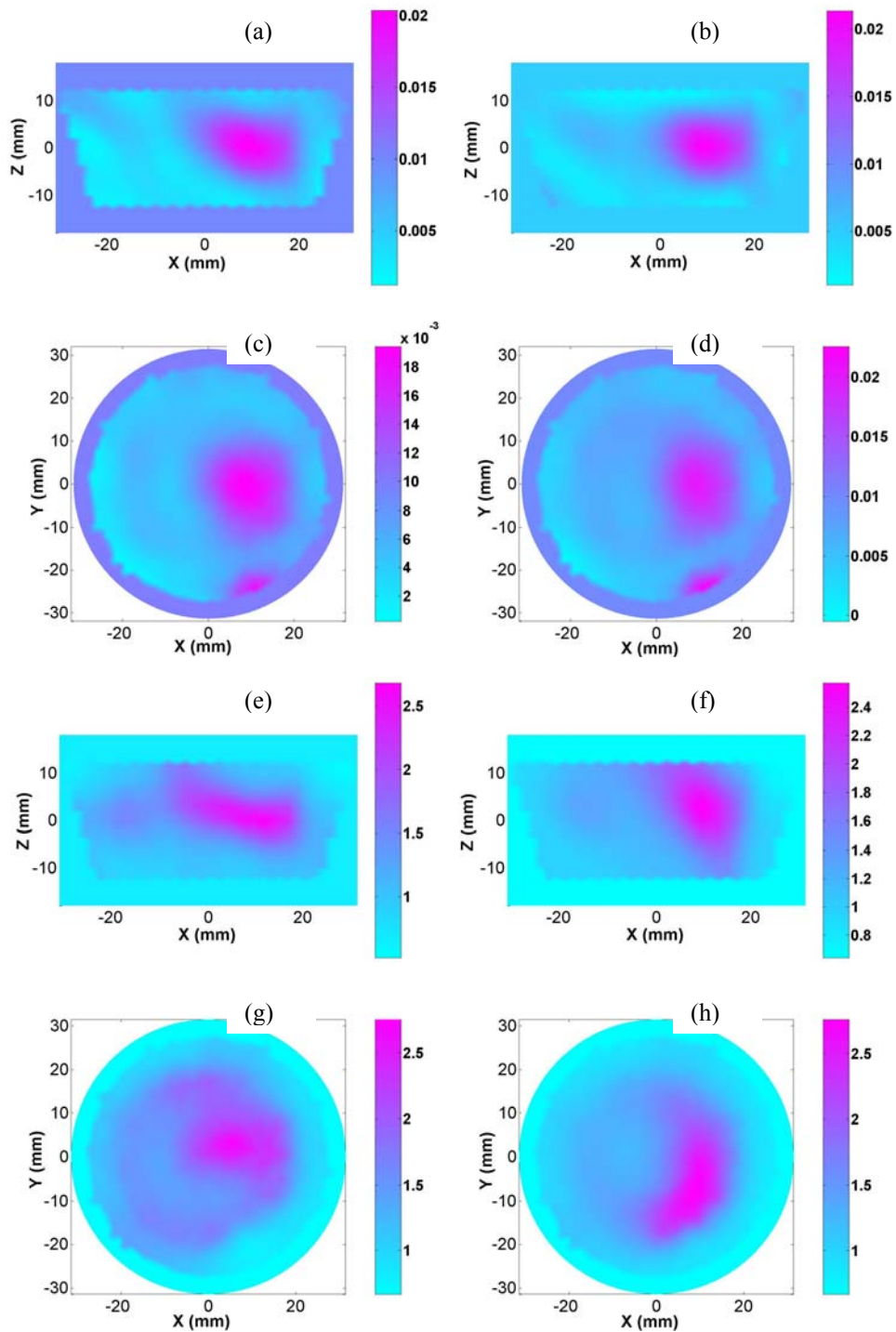


Figure 3-9. The μ_a images (a-d) and μ'_s images (e-h) reconstructed for case 2 (4:1 μ_a , 2.8:1 μ'_s contrast, 10 mm off-center) phantom experiment with the dual mesh method (left column) and the single mesh method (right column). The rectangular and circular figures are at the cross sections $y=0$ mm and $z=2$ mm respectively. The color scale bar indicates values of μ_a (a-d) and μ'_s (e-h).

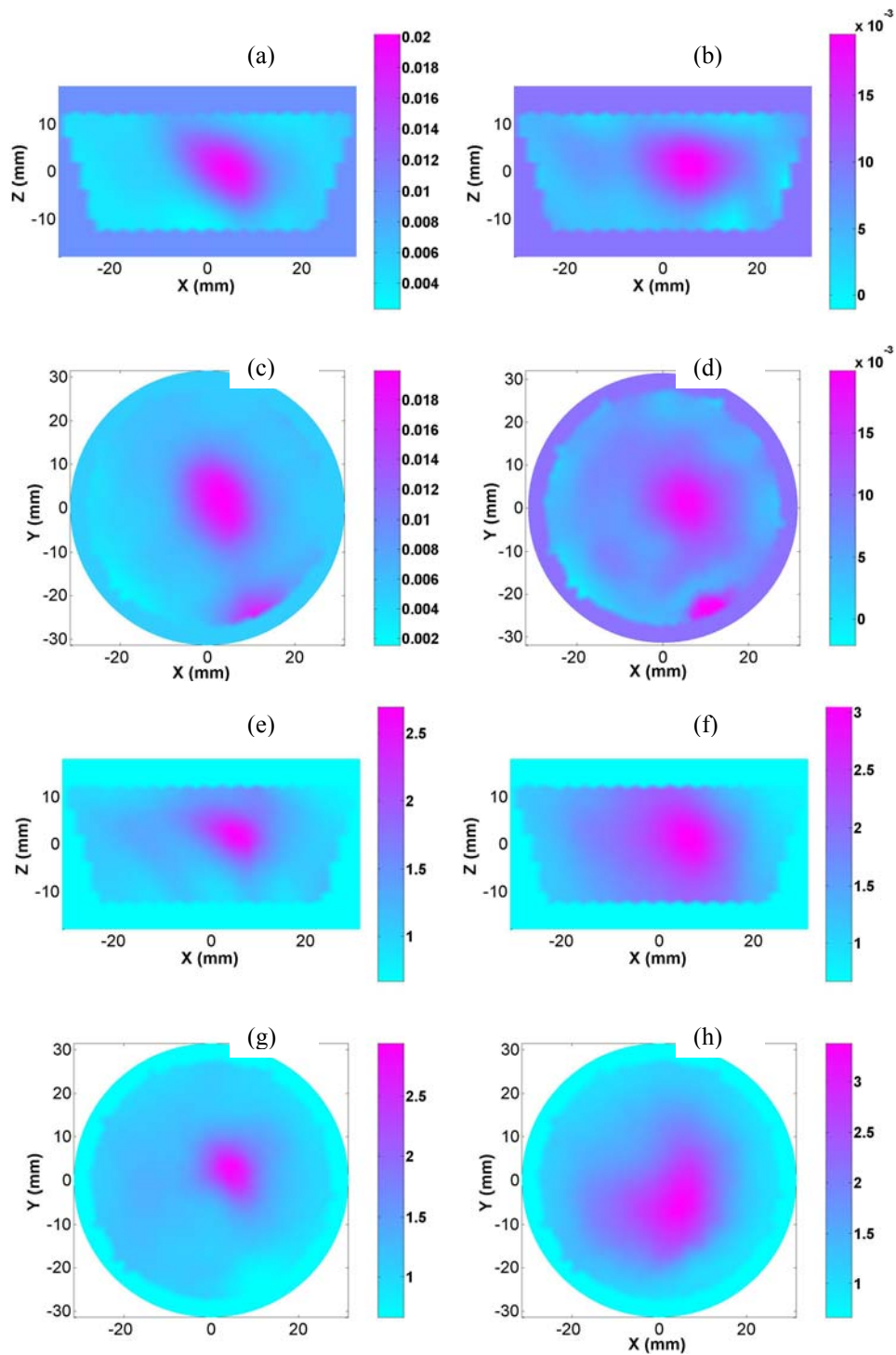


Figure 3-10. The μ_a images (a-d) and μ'_s images (e-h) reconstructed for case 3 (4:1 μ_a , 2.8:1 μ'_s contrast, 5 mm off-center) phantom experiment with the dual mesh method (left column) and the single mesh method (right column). The rectangular and circular figures are at the cross sections $y=0$ mm and $z=2$ mm respectively. The color scale bar indicates values of μ_a (a-d) and μ'_s (e-h).

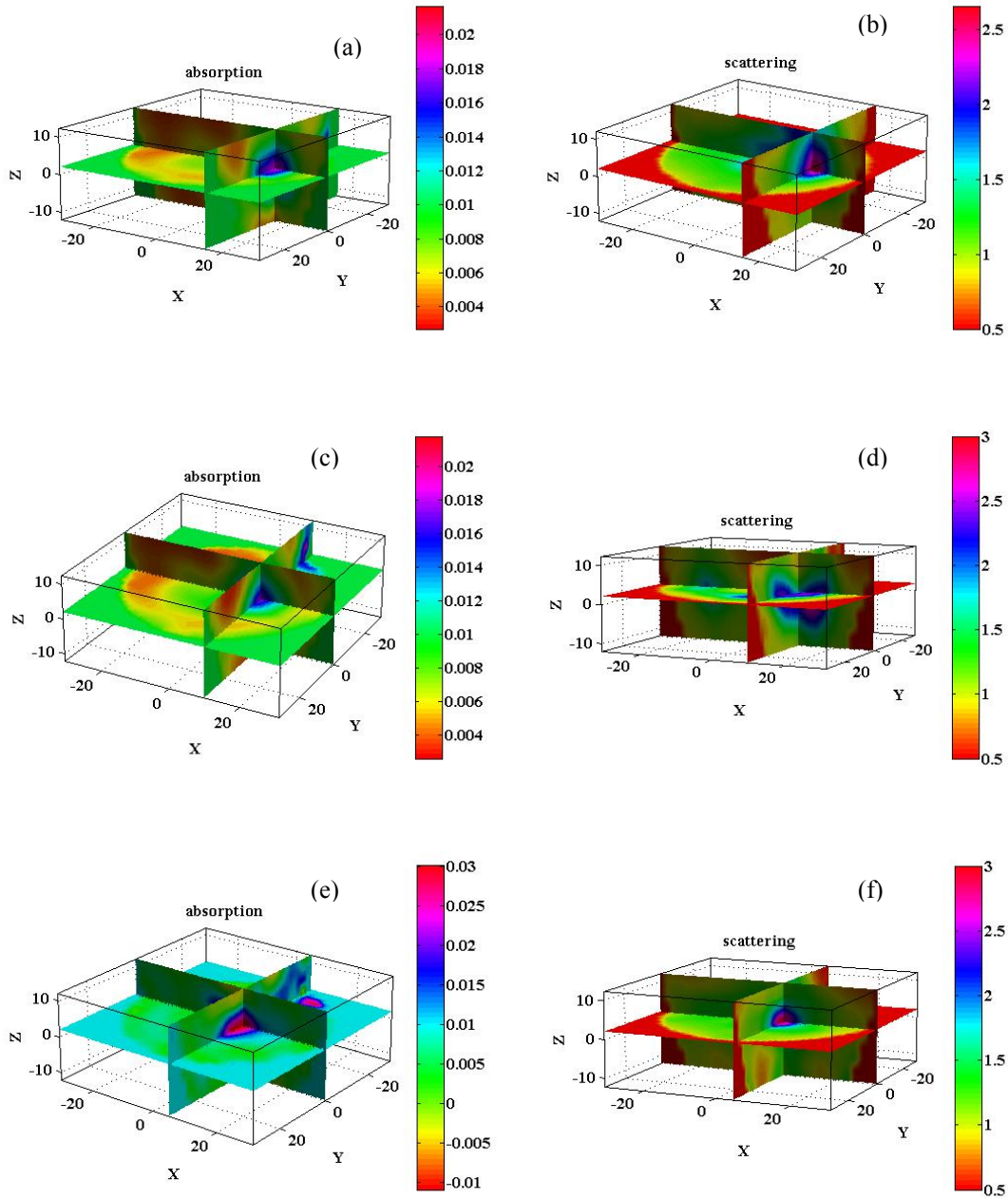
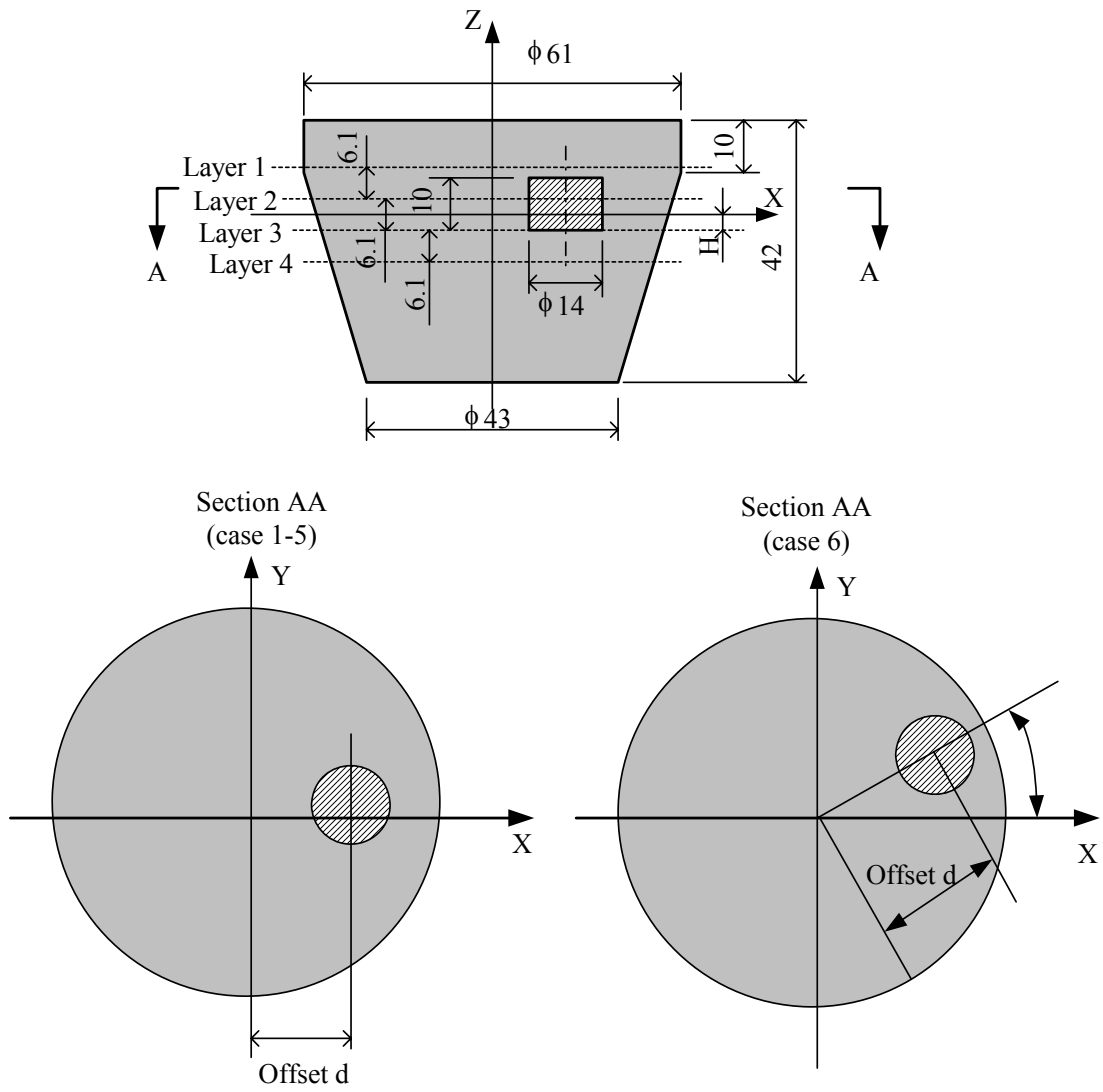


Figure 3-11. The three-dimensional views of the reconstructed absorption coefficient images (a, c, e) in mm^{-1} and the reconstructed reduced scattering coefficient images (b, d, f) in mm^{-1} for case 1 (a, b, 15 mm offset), case 2 (c, d, 10mm offset) and case 3 (e, f, 10mm offset) respectively using the dual mesh method. In each image, the showing slices are crossed at the center of the target.



Unit: mm

Figure 3-12. Geometry of the phantom under study.

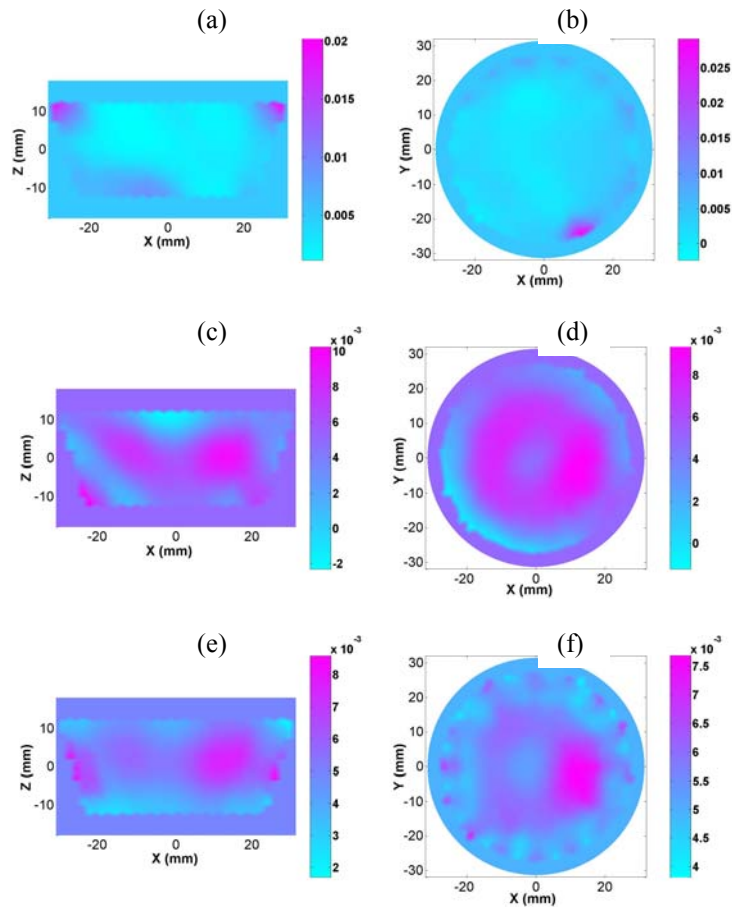


Figure 3-13. The absorption images reconstructed for case 1 (2:1 μ_a contrast) with the uniform source intensity method (a, b); the normalization method (c, d) and the source optimization method (e, f). Column 1 shows that images at $y=0$ mm plane and Column 2 gives the images at $z=0$ mm plane.

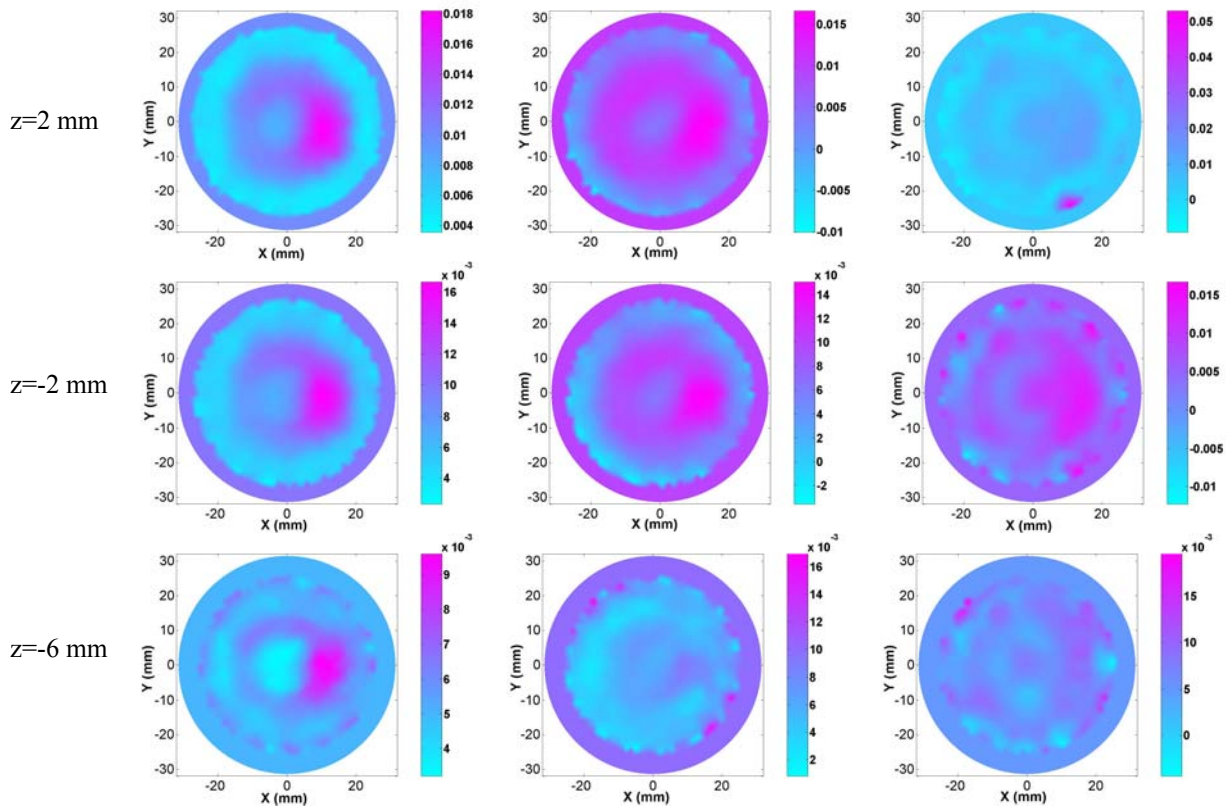
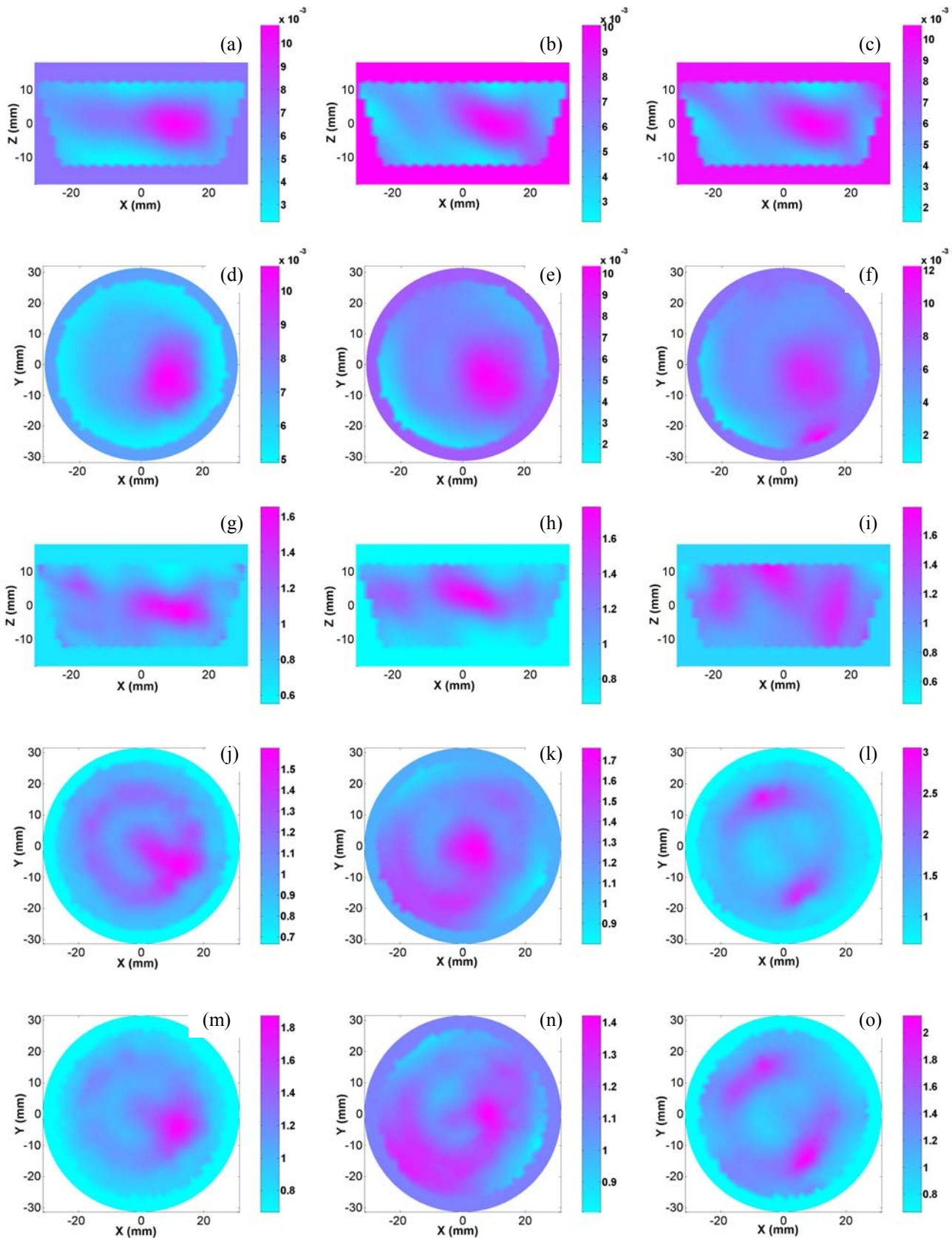


Figure 3-14. The absorption images reconstructed for case 2 ($4:1 \mu_a$ contrast) with the uniform source intensity (column 3); the normalization method (column 2) and the source optimization method (column 1).

Figure 3-15. Reconstructed absorption images (rows 1 and 2) and scattering images (rows 3-5) for case 3 (2:1 μ_a and μ'_s contrast) with the uniform source intensity (column 3); the normalization method (column 2) and the source optimization method (column 1)



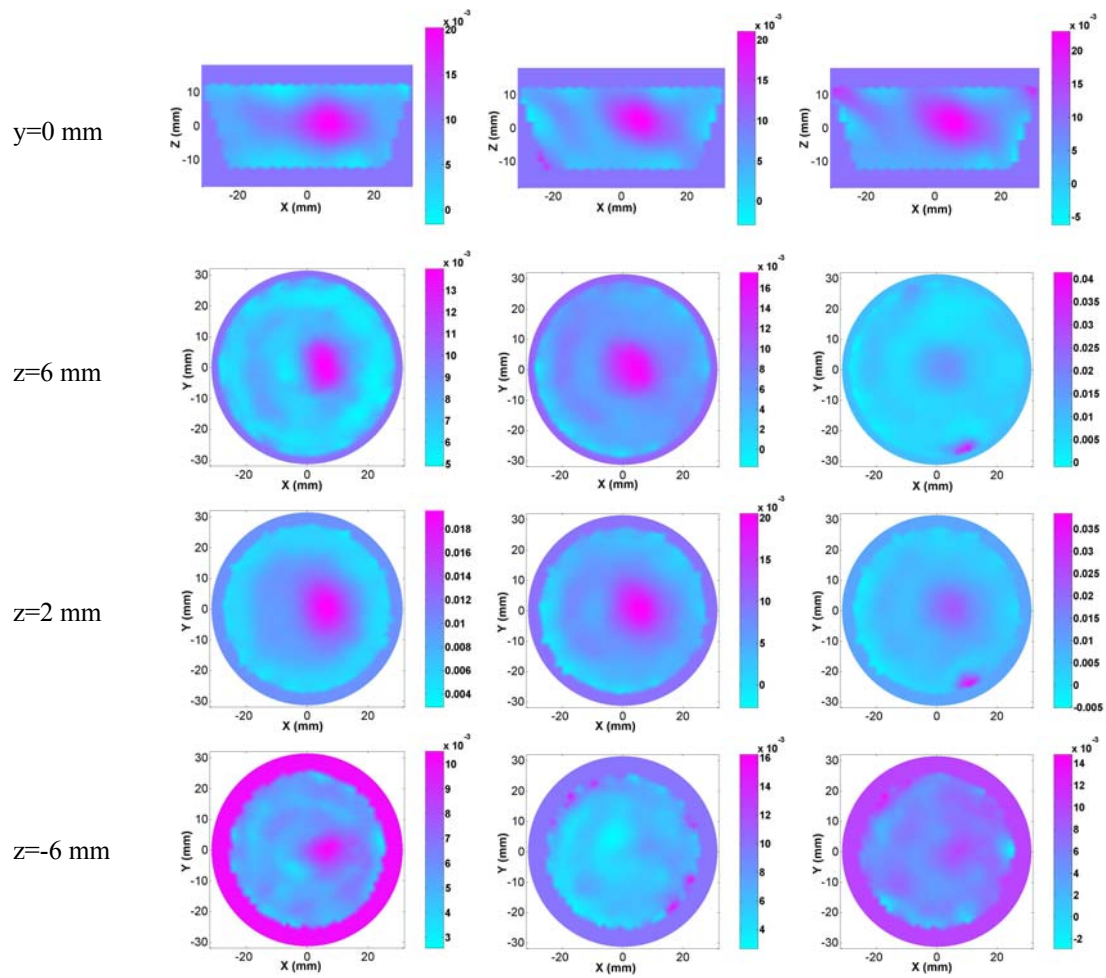


Figure 3-16. The absorption images reconstructed for case 4 ($4:1 \mu_a$ and μ'_s contrast) with the uniform source intensity (column 3); the normalization method (column 2) and the source optimization method (column 1).

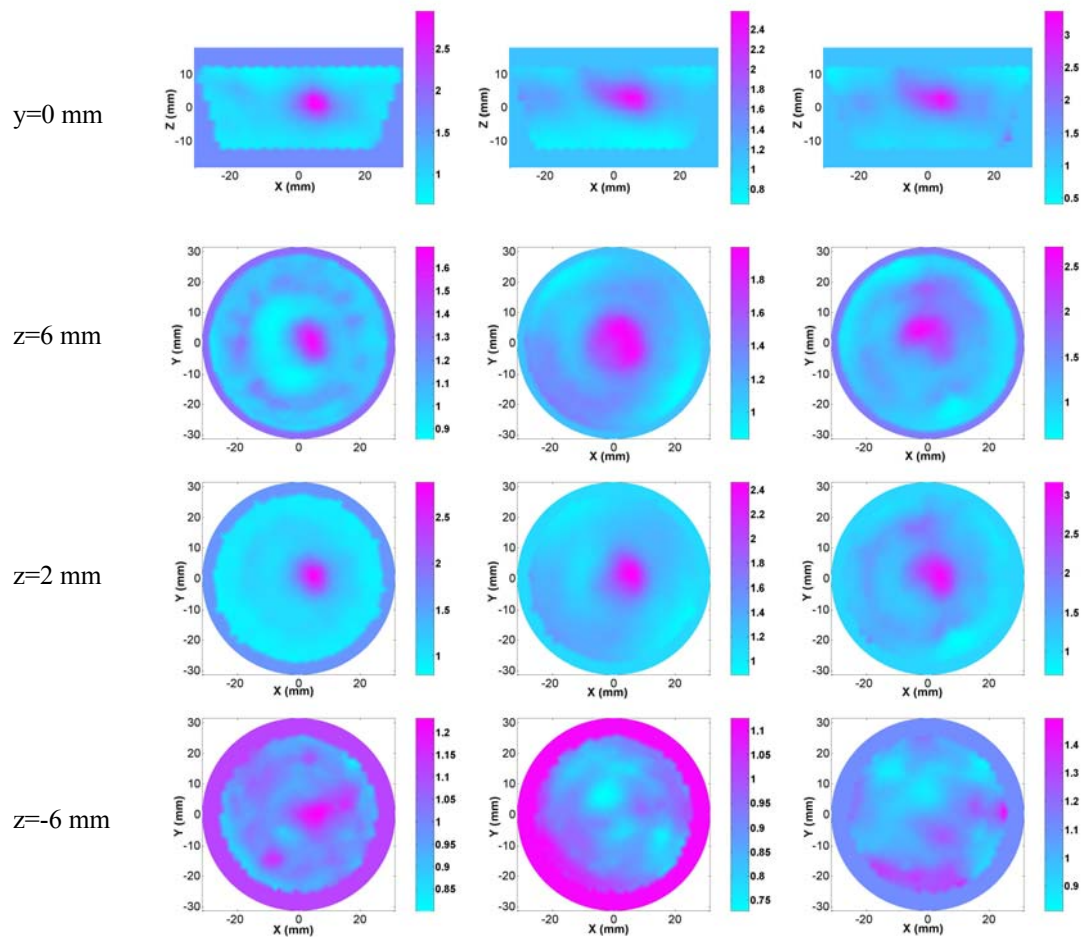


Figure 3-17. The scattering images reconstructed for case 4 (4:1 μ_a and μ'_s contrast) with the uniform source intensity (column 3); the normalization method (column 2) and the source optimization method (column 1).

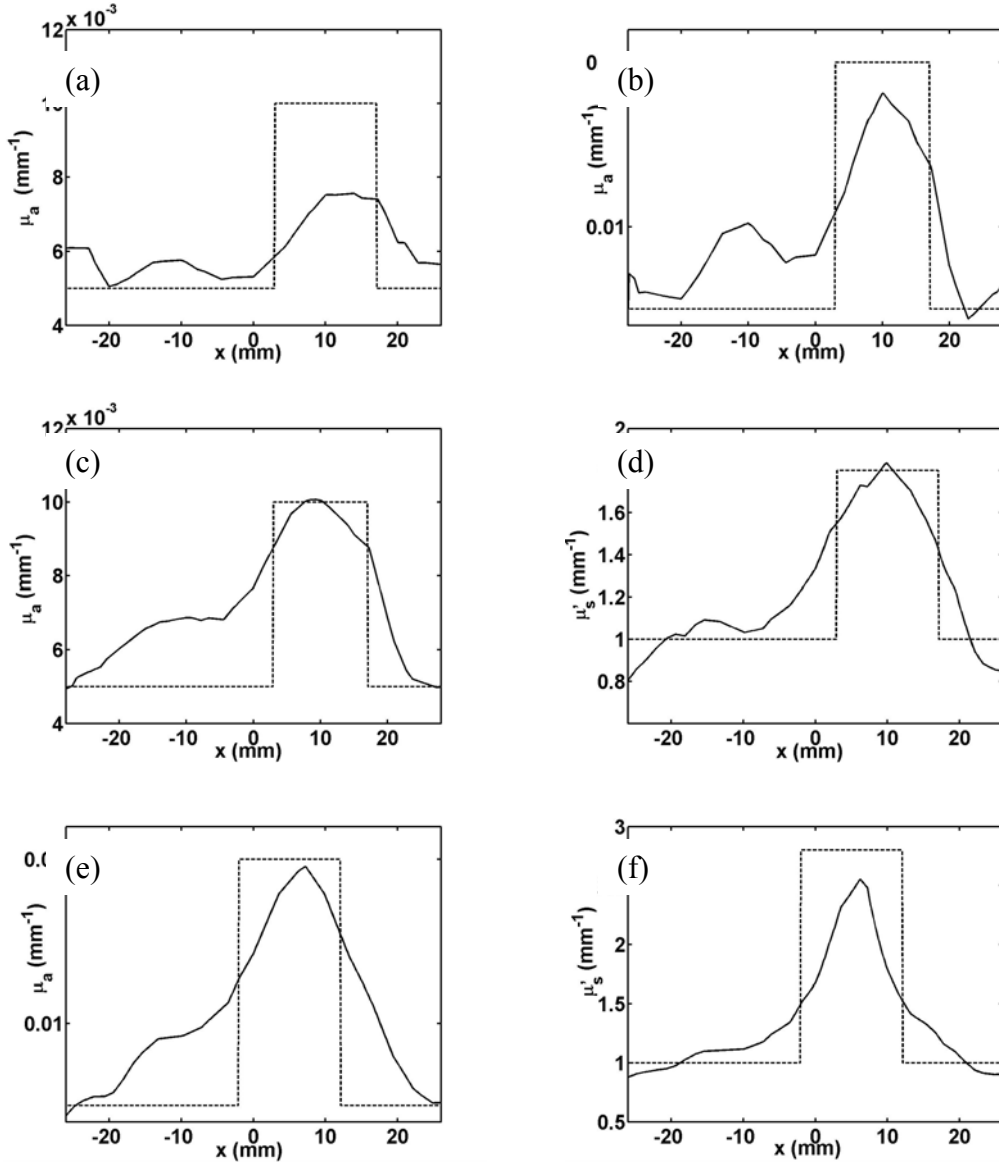


Figure 3-18. Recovered μ_a values along a transect through the centers of the target and background for the images at $y=0$ mm, $z=2$ mm for case 1 (a), case 2 (b), case 3 (c) and case 4 (e). Reconstructed μ'_s values along a transect through the centers of the target and background for the images at $y=0$ mm, $z=2$ mm for case 3 (d) and case 4 (f). Both the μ_a and μ'_s images were reconstructed using the source intensity optimization method. The dotted lines are the exact values and the solid lines indicate the extracted coefficients.

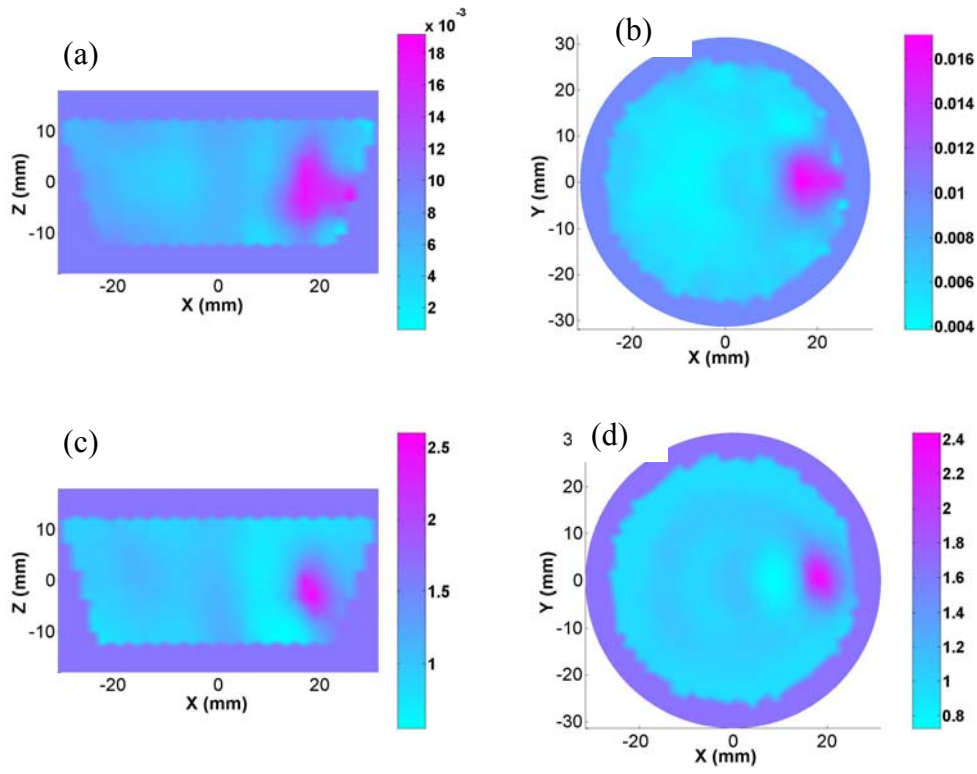


Figure 3-19. The absorption images (a and b) and scattering images (c and d) reconstructed with the source optimization method for case 5 (4:1 μ_a and μ'_s contrast) at the section $y=0$ mm (a and c) and at the section $z=-3$ mm.

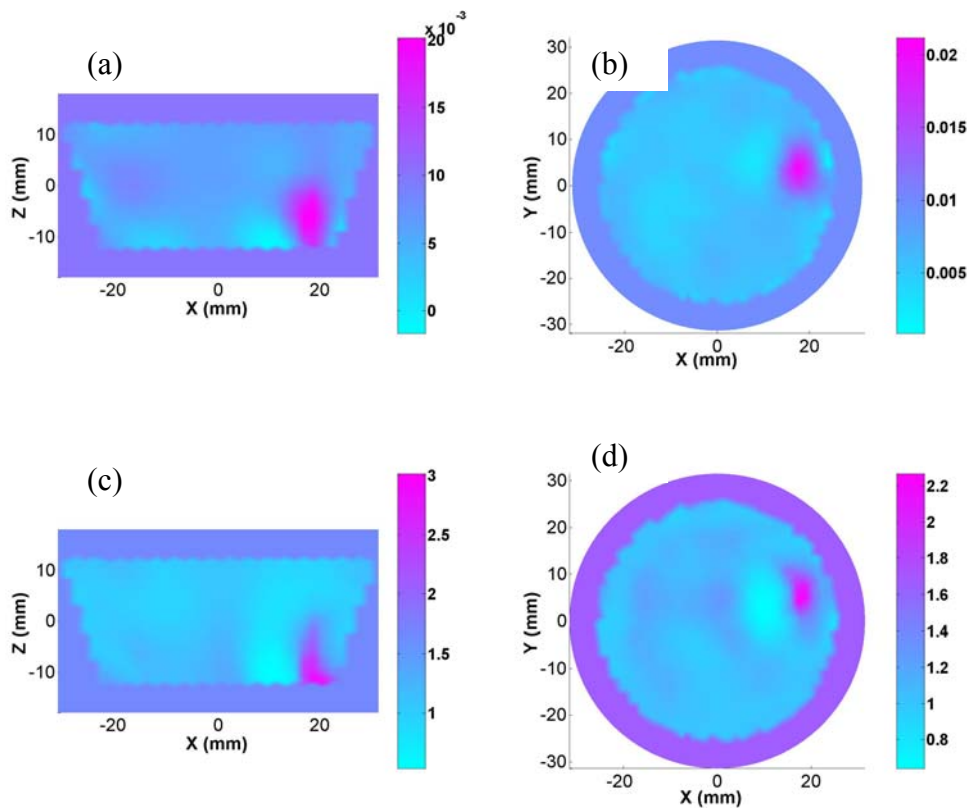


Figure 3-20. The absorption images (a and b) and scattering images (c and d) reconstructed with the source optimization method for case 6 (4:1 μ_a and μ'_s contrast) at the section $y=4$ mm (a and c) and at the section $z=-6$ mm.

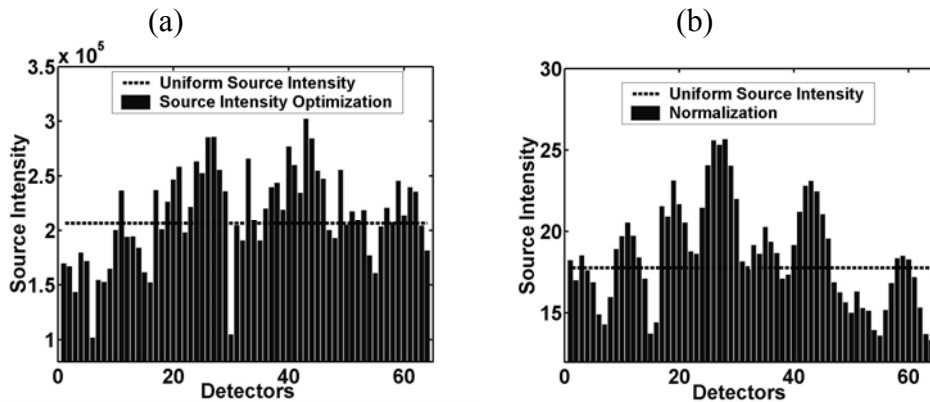


Figure 3-21. The source intensity obtained with the uniform source intensity method (dotted line) and the source intensity distribution obtained with the source intensity optimization method (solid line) from original measured data (a) and the normalized measured data (b) of experiment case 4.

Table 3-1 Optical and geometric parameters used for Group 1 experiments.

	R2 (mm)	D (mm)	μ_a (1/mm)	μ'_s (1/mm)		R1 (mm)
Target 1 (1.4:1 μ_a contrast)	7.0	9.0	0.007	1.0	Background ($\mu_a=0.005 \text{ mm}^{-1}$, $\mu'_s=1.0 \text{ mm}^{-1}$)	25.0
Target 2 (2:1 μ_a contrast)	7.0	9.0	0.01	1.0		
Target 3 (2:1 μ_a and μ'_s contrast)	7.0	9.0	0.01	1.8		

Table 3-2 Optical and geometric parameters used for Group 2 experiments.

	R2 (mm)	D (mm)	μ_a (1/mm)	μ'_s (1/mm)		R1 (mm)
Target 1 (1.4:1 μ_a contrast)	7.0	11.0	0.007	1.0	Background ($\mu_a=0.005 \text{ mm}^{-1}$, $\mu'_s=1.0 \text{ mm}^{-1}$)	37.5
Target 2 (2:1 μ_a contrast)	7.0	11.0	0.01	1.0		
Target 3 (2:1 μ_a and μ'_s contrast)	7.0	11.0	0.01	1.8		

Table 3-3 Optical and geometric parameters used for Group 3 experiments.

	R2 (mm)	D (mm)	μ_a (1/mm)	μ'_s (1/mm)		R1 (mm)
Target 1 (1.4:1 μ_a contrast)	7.0	21.0	0.007	1.0	Background ($\mu_a=0.005 \text{ mm}^{-1}$, $\mu'_s=1.0 \text{ mm}^{-1}$)	50.0
Target 2 (2:1 μ_a contrast)	7.0	21.0	0.01	1.0		
Target 3 (2:1 μ_a and μ'_s contrast)	7.0	21.0	0.01	1.8		

Table 3-4 Optical properties of the phantom background and the target for all 5 cases.

	d	μ_a (1/mm)	μ'_s (1/mm)	
case 1 (4:1 μ_a and μ'_s contrast)	15 mm	0.02	2.8	Background ($\mu_a=0.005 \text{ mm}^{-1}$, $\mu'_s=1.0 \text{ mm}^{-1}$)
case 2 (4:1 μ_a and μ'_s contrast)	10 mm	0.02	2.8	
case 3 (4:1 μ_a and μ'_s contrast)	5 mm	0.02	2.8	

Table 3-5 Optical properties of the target and background used in the six experiments performed.

	d	H	μ_a (1/mm)	μ'_s (1/mm)	
case 1 (2:1 μ_a contrast)	10 mm	3 mm	0.01	1.0	Background ($\mu_a=0.005 \text{ mm}^{-1}$, $\mu'_s=1.0 \text{ mm}^{-1}$)
case 2 (4:1 μ_a contrast)	10 mm	3 mm	0.02	1.0	
case 3 (2:1 μ_a and μ'_s contrast)	10 mm	3 mm	0.01	1.8	
case 4 (4:1 μ_a and μ'_s contrast)	5 mm	3 mm	0.02	2.8	
case 5 (4:1 μ_a and μ'_s contrast)	19 mm	9 mm	0.02	2.8	
case 6 (4:1 μ_a and μ'_s contrast)	19 mm	12 mm	0.02	2.8	

CHAPTER 4
PARTICLE SIZE IMAGING: PHANTOM EXPERIMENTAL STUDIES

4.1 Measurement of Particle Size Distribution and Concentration in Heterogeneous Turbid Media

In this section we attempt to establish a method directly based on more rigorous Mie scattering theory for the reconstruction of particle size distribution and concentration without the limitations existing in the use of the power law. We use both simulations and phantom experiments to validate our method. We also describe a new scheme for optimizing the initial parameters needed for reconstructions in MSDOT and a method for calibrating the scattering spectra obtained from phantom experiments.

4.1.1 Materials and Methods

Two inverse algorithms are required in order to obtain particle size distribution and concentration with MSDOT. The first is a DOT algorithm for the recovery of spectroscopic scattering images in heterogeneous turbid media. Our DOT algorithm, described in detail elsewhere, uses a regularized Newton's method to update an initial optical property distribution iteratively in order to minimize an object function composed of a weighted sum of the squared difference between computed and measured optical data at the medium surface. The computed optical data (i.e., photon intensity) is obtained by solving the photon diffusion equation with finite element method. The second algorithm is one that extracts the particle morphological information using the scattering spectra obtained from the first algorithm described above. It casts the reconstruction as an optimization problem in which the optimization parameters are coefficients in a probability function such as Gaussian distribution function using *a priori* assumptions. This inverse algorithm is based on a least squares optimization, where the difference between measured and computed scattering spectra is iteratively minimized by adjusting the optimization parameters under Mie scattering theory.

It is known that an optimized initial optical property distribution is critical for quality image reconstruction using DOT algorithm. We reported an effective preprocessing scheme for such purpose previously; however, it requires time-consuming computational procedures to obtain the initial parameters needed for image reconstruction at a single wavelength. Clearly this would not be efficient for image reconstruction at multiple wavelengths in MSDOT. Thus we implemented an algorithm for optimizing initial optical properties based on the following core relationship:

$$(J^T J + \beta I) \Delta \chi = J^T (\Phi^o - \Phi^c) \quad (4.1)$$

where

$$J = \begin{Bmatrix} \frac{\partial \Phi_1}{\partial D} & \frac{\partial \Phi_1}{\partial \mu_a} \\ \frac{\partial \Phi_2}{\partial D} & \frac{\partial \Phi_2}{\partial \mu_a} \\ \vdots & \vdots \\ \frac{\partial \Phi_N}{\partial D} & \frac{\partial \Phi_N}{\partial \mu_a} \end{Bmatrix}, \Delta \chi = (\Delta D, \Delta \mu_a), \Phi^o = \begin{Bmatrix} \Phi_1^o \\ \Phi_2^o \\ \vdots \\ \Phi_N^o \end{Bmatrix}, \Phi^c = \begin{Bmatrix} \Phi_1^c \\ \Phi_2^c \\ \vdots \\ \Phi_N^c \end{Bmatrix},$$

Φ^o and Φ^c are the observed and calculated photon density; D and μ_a are the diffusion and absorption coefficients, respectively; $\Delta \chi$ is the update of optical properties; N is the number of nodes used in the finite element mesh used; β is a regularization parameter and I is an identical matrix. In this algorithm, optimized initial optical properties are obtained by iteratively solving Eq. (4-1). Since there exist only two variables, it is very fast to reach convergence.

Once $D(\lambda)$ is recovered using DOT algorithm, the reduced scattering spectra can be obtained by the following relationship for turbid media:

$$(1 - g)\mu_s(\lambda) \approx \frac{1}{3D(\lambda)} \quad (4.2)$$

where $(1 - g)\mu_s$ is the reduced scattering coefficient and g is the average cosine of scattering angles. Following Jiang et al.⁷⁷⁻⁸⁰, the scattering spectra are correlated with particle size distribution and concentration through the following relationship under Mie Theory:

$$(1 - g)\mu_s(\lambda) = \mu'_s(\lambda) = \int_0^\infty \frac{3Q_{\text{scat}}(x, n, \lambda)[1 - g(x, n, \lambda)]}{2x} \phi f(x) dx \quad (4.3)$$

where Q_{scat} is the scattering efficiency; x is the particle size; n is the refractive index of particles; ϕ is the particle concentration/volume fraction; $f(x)$ is the particle size distribution. Both Q_{scat} and g can be computed with Mie Theory.⁸¹ In Equation (4.3) we have assumed that particles act as independent scatterers without particle-particle interaction. In order to solve for $f(x)$ and ϕ from measured scattering spectra, an inversion of Eq. (4.3) must be obtained. Our numerical inversion is based on a Newton-type iterative scheme through least-squares minimization of the objective functional:

$$\chi^2 = \sum_{j=\lambda_1}^{\lambda_{10}} [(\mu'_s)_j^o - (\mu'_s)_j^c]^2 \quad (4.4)$$

where $(\mu'_s)_j^o$ and $(\mu'_s)_j^c$ are the observed and computed reduced scattering coefficients at ten wavelengths, $j = \lambda_1, \lambda_2, \dots, \lambda_{10}$ (more wavelengths can be used, depending on the number of wavelength available from the experimental system). In the reconstruction, we have assumed a Gaussian particle size distribution in this study (a priori knowledge about the mode and distribution form of the particle size are usually available in a practical situation),

$$f(x) = \frac{1}{\sqrt{2\pi}b} e^{-\frac{(x-a)^2}{2b^2}}, \text{ where } a \text{ is the average size of particles and } b \text{ is the standard deviation.}$$

Substituting above $f(x)$ into Eq. (4.3), we obtain

$$(1 - g)\mu_s(\lambda) = \mu'_s(\lambda) = \int_0^\infty \frac{3Q_{\text{scat}}(x, n, \lambda)[1 - g(x, n, \lambda)]}{2x} \phi \frac{1}{\sqrt{2\pi b^2}} e^{-\frac{(x-a)^2}{2b^2}} dx \quad (4.5)$$

Now the particle sizing task becomes to recover three parameters a , b and ϕ . As described in detail in Refs. 77-78, we have used a combined Marquardt-Tikhonov regularization scheme to stabilize the reconstruction procedure.

4.1.2 Simulations and experiments

Simulations are used to test the sensitivity of particle sizing algorithm to noise effect with reduced scattering coefficients at ten wavelengths (This is the number of wavelength available from our imaging system). Simulated scattering spectra were generated using Eq. (4.5) when the particle size distribution and concentration were given. Particle size distribution and concentration were reconstructed using the particle sizing algorithm when 0%, 1%, 5%, 10%, and 20% noise was added to the “measured” scattering spectra, respectively.

Phantom experiments were conducted using our ten-wavelength DOT system (638, 673, 690, 733, 775, 808, 840, 915, 922 and 960nm). This newly developed imaging system and its calibration were described in detail elsewhere. Briefly, light from one of the ten laser modules is transmitted to an optical switch, which sequentially passes it to 16 pre-selected points at the surface of the phantom for 2D imaging experiments. 16x16 measured data is then input into our DOT reconstruction algorithm to generate a 2D cross-sectional image of the phantom. Three sets of phantom experiments were conducted to validate the overall approach for extracting particle size distribution and concentration using MSDOT. The background phantom materials used consisted of Intralipid as scatterer and India ink as absorber. Agar powder (1-2%) was used to solidify the Intralipid and India ink solutions. The cylindrical background phantom had a radius of 25mm, an absorption coefficient of 0.005/mm and a reduced scattering coefficient of 1.0/mm. A thin glass tube (9mm in inner diameter, 0.4mm in thickness) containing polystyrene

suspensions (Polysciences, Warrington, PA) was embedded off-center in the background solid phantom. Three different types of polystyrene spheres were used in the three experiments: 2.06 μm in diameter, 0.02 μm in standard deviation and 0.52% in concentration for Case 1; 2.85 μm in diameter, 0.14 μm in standard deviation and 1.02% in concentration for Case 2; 5.66 μm in diameter, 0.30 μm in standard deviation and 2.62% in concentration for Case 3. The refractive index of the spheres and their surrounding aqueous medium are 1.59 and 1.33, respectively.

4.1.3 Results

Results from two simulations are displayed in Tables 4-1 and 4-2. From simulation 1 for a particle diameter of 2.855 μm , we can see that both the mean size and concentration of particles can be recovered accurately with up to 20% noise; the relative errors of reconstruction of these two parameters were calculated to be within 3.0 ~ 44.9% and 2.9 ~ 33.3%, respectively, given the noise levels used. We also note that the recovery of the standard deviation is quite sensitive to noise effect: the relative error is as large as 100%. From simulation 2 for a particle diameter of 10.0 μm , the relative errors of reconstructed parameters a and ϕ are within 0.5 ~ 20.2% and 0.4 ~ 21.8%, respectively, given the noise levels used. Similarly we see that the standard deviation recovery is sensitive to the noise levels and the relative errors is up to 96.6%. Overall the extraction of particle concentration is least sensitive to noise effect. Using these reconstructed parameters at different noise levels, we calculated the scattering spectra using Eq. (5) for simulation 1 and present them in Figure. 4-1.

Phantom data at 10 wavelengths for all three cases were collected, and both absorption and scattering images were recovered at each wavelength using our DOT algorithm (only the scattering images are needed here for particle sizing). Figure 4-2 shows the reconstructed μ'_s

images for Case 2 at 10 different wavelengths. In particle sizing, both peak and average μ'_s values of the target area were used to recover the particle size distribution (PSD), $f(x)$, and concentration, ϕ .

We found that best particle sizing was achieved when the reconstructed peak or average μ'_s values calibrated using the optimized initial μ'_s values. In this calibration, the subtractions of the mean initial μ'_s at 10 wavelengths from each individual initial μ'_s value are defined as calibration factors. Then a calibrated μ'_s spectrum was obtained by subtracting the calibration factors from the peak or average μ'_s values. For all three experimental cases studied, the calibrated μ'_s spectra were used to reconstruct the particle size parameters.

The mean particle diameter (a), the standard deviation (b) and the concentration (ϕ) reconstructed from both the peak and average μ'_s values for the three cases are listed in Table 4-3 where the exact parameters from the manufacture are also given for comparison. We immediately note that both the mean size and concentration are recovered with good quality, consistent with the simulations. We found the relative error of the reconstructed mean particle size is within 8.4% for the three cases examined, while the relative error of the recovered concentration is 33.3%, 0.8% and 11.1% for Cases 1, 2 and 3, respectively. Similar to the simulations, the standard deviations were recovered with errors as large as 86.6% (Case 3). When the average μ'_s spectra were used, we see that the reconstructed results are generally similar to that with the peak μ'_s spectra; however, overall the peak spectra-based reconstruction has better quality. Figure. 4-3 presents the exact and recovered PSD (normalized) for the three different polystyrene suspensions when the peak spectra were used for reconstruction. In Figure. 4-4, scattering spectra obtained with different methods for Cases 1 and 3 are shown, in which we

can see that the calibrated spectra match well with the Mie theory fittings using the recovered particle parameters.

4.1.4 Discussion and Conclusions

The ultimate goal of our work is to see if we can extract cellular morphological information of breast tissue using MSDOT. The simulations and phantom study presented here represent our first step toward that goal. In our simulations and phantom experiments, the choices of 2, 3, 6 and 10 μm polystyrene scatterers were intended to mimic mitochondria and nuclei, the two primary contributors to tissue scattering reported in the literature to date.^{42, 82-83} We have used Mie theory to recover the particle size distribution and concentration from the scattering spectra obtained using MSDOT at 10 different wavelengths. It is known that Mie theory assumes spherical particles without particle-particle interactions. While these assumptions do not pose problems in our phantom study, they may do so in real tissue where scatterers generally are not spherical. Interestingly, Mourant et al.⁸² presented Mie calculations of μ'_s in cultured cell suspensions which showed excellent agreement between the Mie theory and diffusion approximation. In a prior study, we have shown that accurate PSD can be recovered in concentrated TiO_2 suspensions where TiO_2 particles are not spherical.⁷⁸⁻⁷⁹ In another study, we have demonstrated that the PSD in KCl suspensions can still be well reconstructed when the concentration of KCl particles is as high as 40%.^{78,80} Thus it is reasonable to believe that the approach described here for particle sizing would provide quality results from in vivo data particularly if we focus on the reconstruction of only particle mean size and concentration.

In our particle sizing, the refractive indices of the polystyrene suspensions and the surrounding medium (water) are important parameters and have been assumed known a priori. In a clinical situation, we can obtain these information empirically from the literature, or we can

ultimately recover the refractive indices of scatterers as we reconstruct the PSD and concentration. Our phantom results have shown that the calibration method developed for correcting the initial scattering values is able to provide quality reconstruction of PSD and concentration. However, there is no clear physical explanation about the spectra subtraction used in the calibration. We suspect that the spectra subtraction might have reduced the scattering impact of the background medium on the particle suspensions in the target. In addition, we have set the boundary conditions (BC) coefficient as constant for all 10 wavelengths in the calibration. We plan to implement a method that can provide optimized wavelength-dependant BC coefficient, which should give better initial scattering spectra.

In summary, we have presented an approach for reconstruction of PSD and concentration in heterogeneous turbid media from scattering spectra measured using MSDOT. Both simulations and phantom results have shown that the PSD and concentration of polystyrene spheres contained in the target can be reconstructed with 10-wavelength data available from our current MSDOT system. We expect to apply the approach described in this section to in vivo clinical data obtained from tumor-bearing breasts in the near future.

4.2 Imaging of Particle Size Distribution and Concentration in Heterogeneous Turbid Media

In this section, we present for the first time images of particle size and concentration using tissue phantom experiments where a target is embedded in a scattering medium. The recovered images obtained are quantitative in terms of the target size and shape, and the particle size and concentration in both the target and background media.

4.2.1 Methods and materials

The methods were described in above subsection. Phantom experiments were conducted using our ten-wavelength DOT system (638, 673, 690, 733, 775, 808, 840, 915, 922 and 960nm).

Two sets of phantom experiments were conducted to demonstrate the overall approach for imaging particle size and concentration using MSDOT. The cylindrical background phantom had a radius of 25mm, an absorption coefficient of 0.005/mm (India ink as absorber) and a reduced scattering coefficient of 1.0/mm (Intralipid as scatterer). A thin glass tube (9mm in inner diameter, 0.4mm in thickness) containing polystyrene suspensions (Polysciences, Warrington, PA) was embedded off-center in the background solid phantom. Two different types of polystyrene spheres were used in the experiments: one had a diameter of 2.06 μm and a concentration of 0.52%, and the other had a diameter 5.66 μm and a concentration of 2.62%. The refractive index of the spheres and their surrounding aqueous medium are 1.59 and 1.33, respectively.

4.2.2 Results and discussion

We first performed simulations to evaluate the sensitivity of particle sizing on the number of wavelengths used. “Measured” μ'_s spectra were generated using Eq. (8) with $a=2.86 \mu\text{m}$, $b=0.145 \mu\text{m}$ and $\phi=1.02\%$ for 10, 20 and 50 wavelengths between 600 and 1000nm, respectively. When 5% noise was added to each set of “measured” μ'_s spectra, we found that the relative errors of recovering the particle parameters were within 14% using the 10-wavelength spectra, while such errors were as low as 4% when 50-wavelength spectra were used. The Mie theory fittings using the extracted parameters at 10, 20 and 50 wavelengths are shown in Figure. 4-5(a) where the exact spectra are also presented for comparison. We see that the 10-wavelength spectra are able to provide quantitatively accurate reconstruction. We also performed simulations to test the noise sensitivity when 1, 5, or 10% random noise was added to the 10-wavelength spectra. The relative errors of the recovered parameters (a and ϕ) were calculated to be 3, 14, and 17% for parameter a and 3, 11 and 14% for the parameter ϕ . However, the recovery of the

standard deviation was sensitive to noise, which had a relative error of 93% when 10% noise was added.

A finite element mesh with 634 nodes was used for the DOT reconstructions. To show the accuracy of the DOT reconstruction, Figure. 4-5(b) depicts the recovered μ'_s spectra at a typical node location in the target area for the 2.06 μm polystyrene case, in comparison with the corresponding Mie theory fitting using the extracted particle parameters. And the DOT reconstructed absorption and reduced scattering images for the 2.06 μm polystyrene case for all ten wavelengths are shown in the Figure. 4-6. The recovered mean size and concentration at each node are used for imaging display. Figure. 4-7 presents the reconstructed images of particle size and concentration for the 2.06 and 5.66 μm polystyrene cases. We immediately note that the particle size and concentration of both the target and background are quantitatively imaged. The reconstructed mean particle size and concentration in the background were found to be within 154.7~155.1nm and 0.92~1.21% for the 2.06 μm polystyrene case, and 155.3~155.5nm and 1.17~1.95% for the 5.66 μm polystyrene case, compared to 150nm and 1%, the equivalent mean particle size and concentration of the actual Intralipid/Ink background. In the target region, the recovered mean particle sizes are in the range of 1.31 to 2.25 μm with average value of 1.72 μm for the 2.06 μm polystyrene case and 3.48 to 5.97 μm with average value of 4.62 μm for the 5.66 μm polystyrene case, while the reconstructed concentrations are in the range of 0.48 to 0.87% with average value of 0.65% for the 2.06 μm polystyrene case and 1.76 to 2.70% with average value of 2.25% for the 5.66 μm polystyrene case. Similar to the simulations, we see that the standard deviation recovery is sensitive to the noise. The maximum relative errors of the extracted standard deviation are up to 67.9% and 84.9% for the 2.06 μm and 5.66 μm polystyrene case respectively.

It should be noted that while only the recovered μ'_s spectra were needed for particle sizing, the absorption images were quantitatively reconstructed for the experimental two cases studied [see Figs. 4-7(a1)-4-7(a10); note that the absorption contrast between the target and background was extremely low in both cases, resulting in strong artifacts along the boundary]. Others and we have recently shown repeated experimental evidence that the cross-talk between μ_a and μ'_s images can be minimized using CW based DOT reconstructions, suggesting that future work involving phantom studies with different levels of absorption in the target are feasible and worthy.

In our particle sizing, the refractive indices of the polystyrene suspensions and the surrounding medium are important parameters and have been assumed known a priori. In a clinical situation, we can obtain these information empirically from the literature, or we can ultimately recover the refractive indices of scatterers as we reconstruct the PSD and concentration. In response to the possible perturbation of the glass tube used in the experiments, we have previously shown that such perturbation was insignificant in the image reconstruction⁸⁴. In this work, we assumed that the scatterers are spherical. But in tissues, while larger scatterers such as nuclei are spherical, the smaller scatterers such as mitochondria are ellipsoidal. A possible solution to this is to consider a modified Wentzel-Kramers-Brillouin model (WKB) theory for non-spherical particles as described in [63]. Compared with the diffuse reflectance spectroscopy (DRS), our method can image the particle size and concentration in heterogeneous media whereas DRS can only deal with homogeneous media. In addition, we believe our method can provide more accurate particle sizes and concentrations than DRS, because DRS often is based on analytical solutions to the diffusion equation with the assumption of infinite or semi-infinite media.

In conclusions, we have demonstrated quantitative imaging of particle size and concentration of heterogeneous turbid media using MSDOT. The choices of the 2.06 and 5.66 μm polystyrene particles were intended to simulate typical mitochondria and nuclei, respectively. The phantom results presented suggest that the method described in this section may be applied for in vivo imaging of tissue morphology, adding more parameters for clinical decision-making.

4.3 Experimental Results from Concentrated Suspensions with Bi-modal Particle Size Distribution

A method directly based on more rigorous Mie scattering theory for the reconstruction of particle size distribution and volume fraction has already been proposed and validated by a set of phantom experiments in the above sections. A single particle size distribution was assumed and the only one kind of particles was used in the phantom studies. In pure optical spectroscopy studies, it has been shown that scattering spectra are correlated with tissue morphology.^{42, 82-83, 85} These experimental studies had suggested that both nuclei and mitochondria contributed to tissue scattering significantly. But it remained unclear how much the contribution of nuclei and mitochondria was to the scattering.

In this section, two kinds of particles with different diameters and volume fractions were mixed together and their contributions to the scattering were studied experimentally. This section was organized as follows. Subsection 4.3.1 discussed the experiment system and phantom materials. The experimental results and discussion were in subsection 4.3.2. Finally, the subsection 4.3.3 was about the conclusions.

4.3.1 Experimental system and materials

The ten wavelength (638, 673, 690, 733, 775, 808, 840, 915, 922 and 965 nm), the experimental system and its calibration have already been described in detail elsewhere.^{40, 71} In

this section, two dimensional images were reconstructed. Only fiber probes of 16 sources and 16 detectors located in one layer were used for the 256 measurements at each wavelength.

The cylindrical background phantom had a radius of 25mm, an absorption coefficient of 0.005/mm (India ink as absorber) and a reduced scattering coefficient of 1.0/mm (Intralipid as scatterer) at wavelength of 808nm. A thin glass tube (9mm in inner diameter, 0.4mm in thickness) containing polystyrene suspensions (Polysciences, Warrington, PA) was embedded off-center in the background solid phantom. Three sets of experiments were performed. The targets were composed of two kinds of polystyrene suspensions and water, as shown in Tables 4-4, 4-5, and 4-6, respectively. For experiment set 1, there were 5 cases, with fixed volume fraction 1.255% of polystyrene with diameter of 6 μ m and decreased volume fraction from 1.255% to 0.05% for polystyrene with diameter of 1 μ m. For experiment set 2, there were four cases, with fixed volume fraction 0.77% of 1 μ m polystyrene spheres and volume fraction of 6 μ m polystyrene spheres reduced from 0.7% to 0.1%. In the 3 cases of experiment set 3, the volume fraction of 6 μ m polystyrene spheres was fixed on 1.255% and other kind of polystyrenes spheres had different diameters and volume fraction concentrations for each of 3 cases, as shown in Table 4-6.

4.3.2 Experimental results and discussion

For all the 11 experimental cases in the three sets, the absorption coefficient image and the reduced scattering coefficient image at each of ten wavelengths were reconstructed using our CW DOT algorithm although only the reduced scattering coefficient images were used for the further particle size and volume fraction extraction. For each case at each wavelength, the preprocess method for searching initial value of absorption coefficient μ_a , $\mu'_s(\lambda)$ and α was implemented and the initial values corresponding to the global minimum error, which was the

square sum of the difference between the computed and measured photon density, resulted in the best reconstruction image quality³¹. Figure. 4-8 plotted the reconstructed scattering images at nine wavelengths for case 1 in experiment set 1, using the initial values at the global minimum error. However, the boundary coupling coefficient α was supposed to be same approximately at all wavelengths due to their same boundary conditions. Because of the system noise, the values of α corresponding to the global minimum error at the nine wavelengths were not the same.

To see how much influences of the values of α at different wavelengths on the reconstructed results, we assume the values of α at all wavelengths were same and the initial values were chosen when the total initial searching error, which was the sum of the initial searching error of all wavelengths, reached the minimum. For the case1 in experiment set 1 (denoted as case1_1 or set1_1), the value of α was found to be 0.29 and the reconstructed reduced scattering coefficient images were plotted in Figure. 4-9. One may see that the image quality was worse than that of Figure. 4-8 since there were more artifacts in Figure. 4-9 because the initial value at each wavelength was not corresponding to the one at the global minimum error.

The target region in the scattering images was segmented and the reduced scattering coefficient values of all nodes in the target were averaged. The average values at 10 wavelengths for 5 cases of experiment set 1 were plotted in Figure. 4-10 and Figure. 4-11 The average values in Figure. 4-10 were calculated from the images reconstructed with initial values at global minimum error and in Figure. 4-11 from the images reconstructed with the fixed value of α at different wavelengths. The point at wavelength 965 nm was ignored due to the worst image quality. Only scattering values at nine wavelengths were used for further particle size and volume fraction extraction. The extracted scattering spectra in Figure. 4-11 were used for the

further process because they resulted in more stable results than the spectra in Figure. 4-10. It means that the same α value assumption at different wavelengths was critical for particle size and volume fraction extraction. From both Figure. 4-10 and Figure.4-11, the scattering decreased from case 1 to case 5 as the total particle volume fraction decreased. The slopes of the five scattering spectra in Figure.4-11 decreased from case1 to case5 as well.

Figure. 4-13 and Figure. 4-14 plotted the average values of reduced scattering coefficient in the target at 10 wavelengths for experiment set 2 and set 3, respectively. All these values were calculated from the images reconstructed with the initial values when the values of α at different wavelengths were assumed to be the same. Once again, one could see that the scattering at the tenth wavelength in Figure. 4-12 turned out to be abnormal due to the low signal noise ratio at that wavelength and the values at that wavelength were ignored for the further process. In Figure. 4-12, the slope differences among the four scattering spectra were easy to see but the scattering level differences were not.

One particle size distribution was assumed when the particle size and volume fraction were extracted, although we mixed two different kinds of particles into the target. The extracted particle size and volume fraction based on the scattering spectra from Figs. 4-11, 4-12 and 4-13 were shown in Tables 4-7, 4-8 and 4-9 for experiment set 1, set 2 and set 3, respectively. In Table 4-7, the calculated scattering ratio was the ratio of the calculated reduced scattering coefficient of 1 μm particles in the glass tube to the total calculated reduced scattering coefficient from both kinds of particles. The volume fraction and the particle size distribution were known so that the scattering coefficient was able to be calculated by Eq. (4-3). The volume fraction was referred to as the volume concentration of 1 μm particles in the target. Similarly, in Table 4-8, the calculated scattering ratio was the ratio of the calculated reduced scattering coefficient of

6 μm particles to the total calculated scattering. The volume fraction was referred to as the volume concentration of 6 μm particles. In Table 4-9, the calculated scattering ratio was the division of the calculated reduced scattering coefficient of 0.75 μm , 0.11 μm , 0.075 μm particles by the total calculated scattering in the target for each case. And the volume fraction was the volume fraction of 0.75 μm , 0.11 μm , 0.075 μm particles in the glass tube.

Figure. 4-14a and 4-15a plotted the extracted equivalent mean particle diameter versus the calculated reduced scattering coefficient ratio of 1 μm particles and of 6 μm particles for experiment set 1 and set 2, respectively. In both sets, the extracted particle diameter increased almost proportionally as the calculated reduced scattering coefficient ratio of 6 μm particles (the larger particles) increased. In contrary, the extracted particle diameter decreased almost proportionally as the calculated reduced scattering coefficient ratio of 1 μm particles (the smaller particles) decreased. The extracted equivalent particle diameters with respect to the volume fraction of 1 μm particles for set1 and the volume fraction of 6 μm particles for set 2 were plotted in Figure. 4-14b and 4-15b, respectively. For set1, the volume fraction of 6 μm particles remains 1.255%. When the volume fraction of 1 μm particles increased from 0.05% to 1.255%, the extracted diameter decreased from 3.4 μm to 0.7 μm . For set 2, the volume fraction of 1 μm particles remained 0.77% and when the volume fraction of 6 μm increased from 0.1% to 0.7%, the extracted diameter increased from 0.6 μm to 1.3 μm . For both set1 and set2, the minimum extracted diameter values, such as 0.7 μm in case1_1 and 0.6 μm in case2_4, were less than the smaller particle diameter 1 μm . The possible reason was that the background particle (Intralipid) diameter around 150 nm may affect the extracted diameter in the target.

In the set1 and set2, only two kinds of particles with different diameters of 1 μm and 6 μm were used. To see how the particle diameters effected on the extracted equivalent mean

diameter, experiment set 3 was performed. For cases 1_4, 3_1 and 3_2, all of them had one kind of particles with diameter of 6 μm , volume fraction of 1.255% and very close calculated scattering ratio of the smaller particle, 0.24 for case1_4, 0.297 for case3_1 and 0.299 for case3_2. Another kind of particles (with smaller diameter) for them had diameter of 1 μm , 0.75 μm and 0.11 μm and the extracted diameters were 3.2 μm , 3.2 μm and 1.8 μm , respectively. The extracted diameters decreased from 3.2 μm to 1.8 μm when the smaller particles diameter reduced from 1 μm to 0.11 μm , provided other conditions were same. Compared the case3_3 with case1_5, one might obtain the similar conclusion. These two cases had very close calculated scattering ratio and had the same volume fraction of particles with diameter of 6 μm . Another kind of particles had diameter of 1.0 μm for case1_5 and 0.064 μm for case3_3 and the extracted diameters were 3.4 μm and 2.4 μm , respectively.

For all cases, the equivalent particle volume fraction could not be extracted quantitatively, but it could be obtained qualitatively. For experiment set1, the true total particle volume fraction was from 1.26% to 2.51% and the extracted volume fraction was around 0.9%. For experiment set2, the true total particle volume fraction was from 0.87% to 1.47% and the extracted volume fraction was around 0.5%. One might see that the extracted total volume fraction was larger when the true value was bigger.

The particles were assumed to be spherical. It was true for the experiments. But the nucleus and the mitochondria in tissues are elliptical not spherical. Our ultimate goal is the clinical applications. How the spherical assumption affects on the clinical results will be our next research study.

In this section, we have assumed that the particle size distribution was Gaussian distribution although we intended to put two different kinds of particles into the target. It was our

goal to study how each kind of particle affected the extracted results. Currently, there are only 10 wavelengths available. It is not feasible to assume no size distribution mode, as described in reference [78]. We may do so in the future when there are more wavelength measurements available.

4.3.3 Conclusions

When there were two kinds of particles with different diameters in the target and only one particle size distribution was assumed in the particle size extraction calculation, the extracted equivalent particle diameter increased almost proportionally as the calculated scattering ratio of the bigger particles increased and the calculated scattering ratio of the smaller particles decreased. The extracted diameter was also increased with the increment of the volume fraction of bigger particles and the decrement of the volume fraction of the smaller particles, but not proportionally. The extracted diameter decreased when the diameter of one kind of particle in the target decreased and another kind of particle diameter remained same. The equivalent particle volume fraction could be reconstructed qualitatively, but not quantitatively. Finally, the reduced scattering coefficient spectra, obtained when the boundary coupling coefficient α was assumed to be constant for each wavelength, resulted in better results than the spectra obtained from the initial values corresponding to the global minimum error.

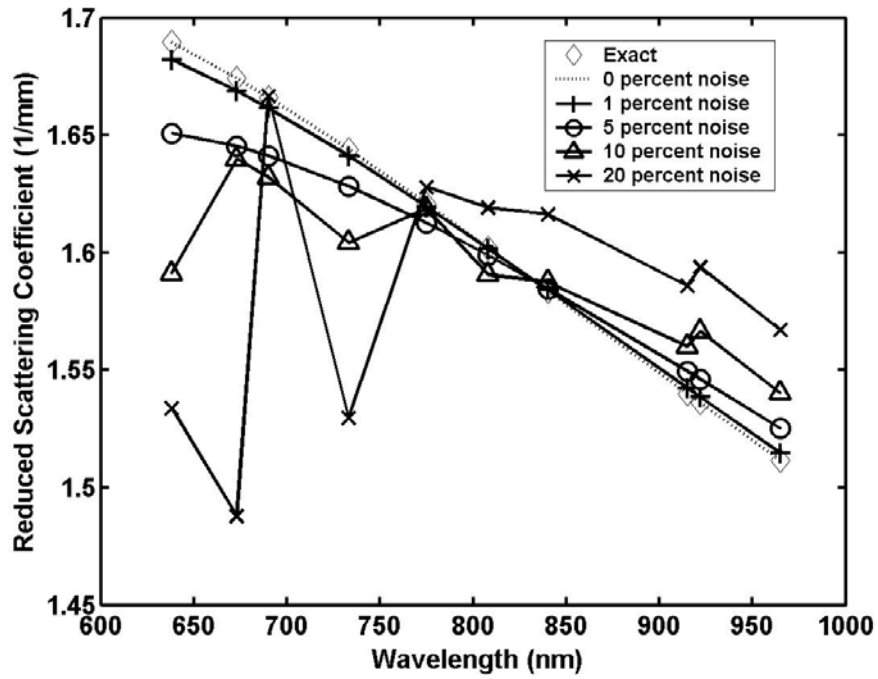


Figure 4-1. Simulated scattering spectra obtained from Mie calculation and the fittings based on the recovered particle size distribution and concentration at different noise levels. 10 wavelengths were used in the simulations.

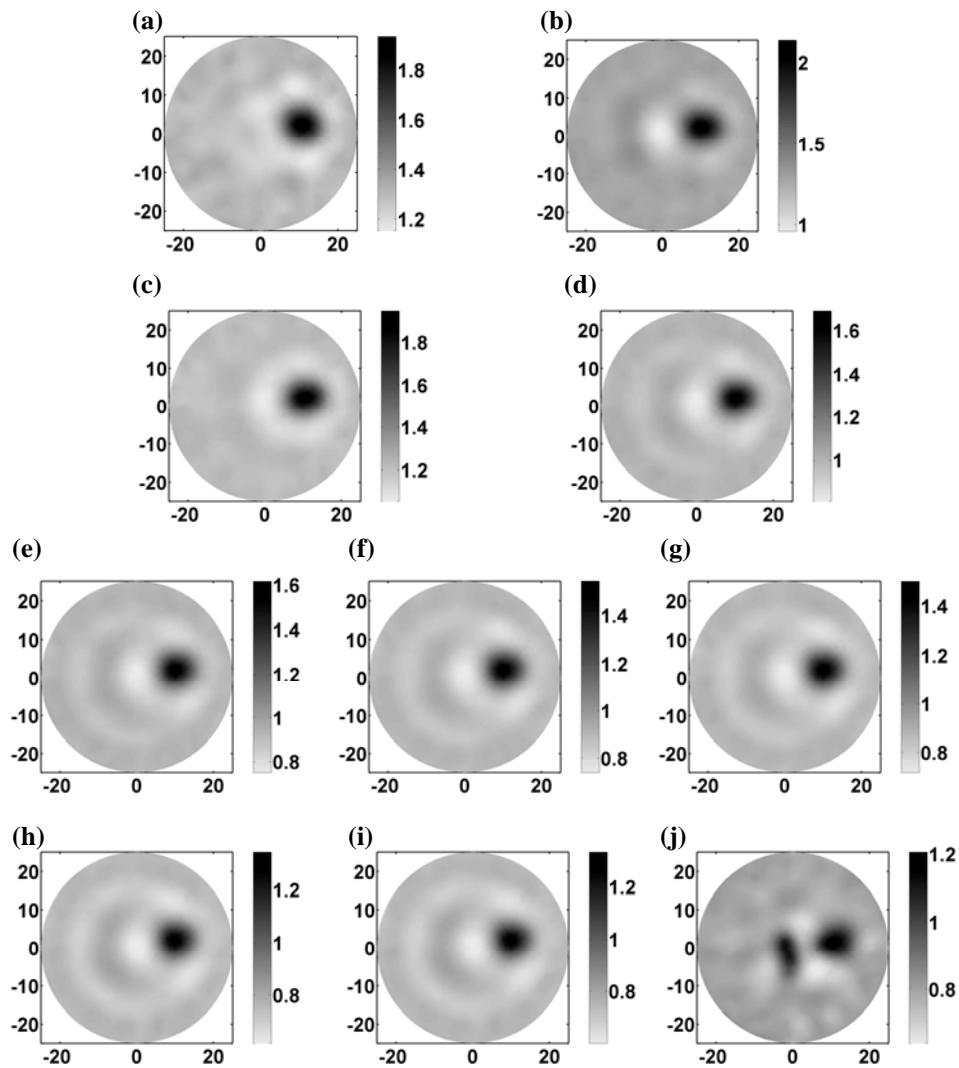


Figure 4-2. Reconstructed scattering images for Case 2 at 10 different wavelengths. (a) at 638 nm (b) at 673 nm, (c) at 690 nm (d) at 733 nm, (e) at 775 nm, (f) at 808 nm, (g) 840 nm, (h) at 915 nm, (i) at 922 nm and (j) at 965 nm.

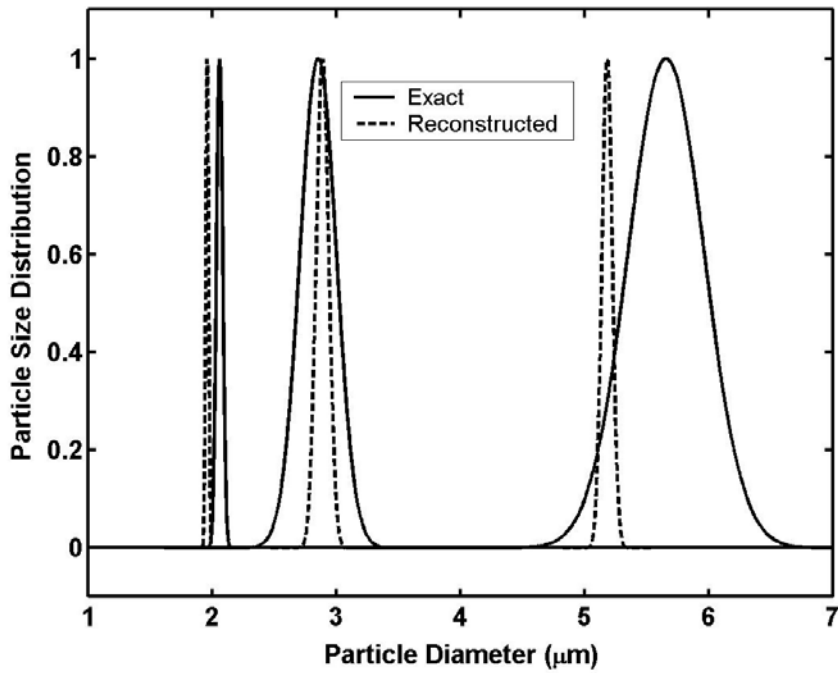


Figure 4-3. Normalized exact (solid lines) and reconstructed (dashed lines) particle size distribution from phantom measurements for Cases 1, 2 and 3.

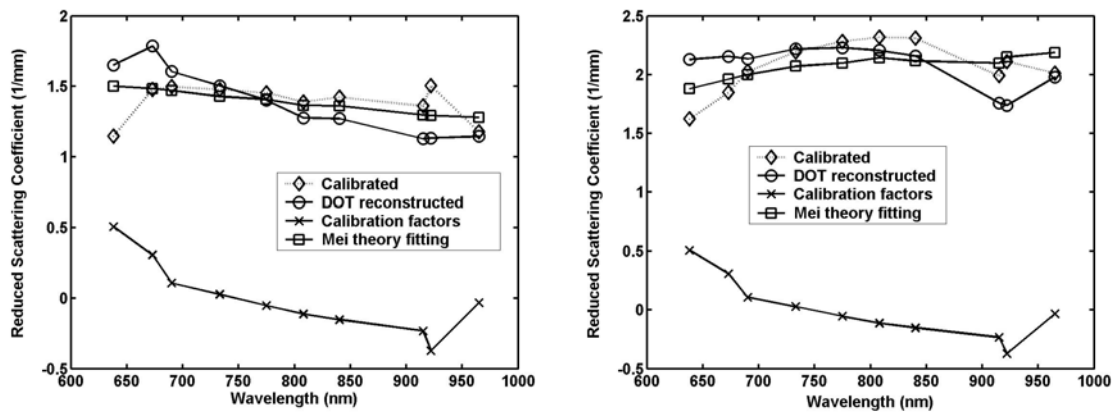


Figure 4-4. Experimental scattering spectra obtained with different methods for Case 1 (left) and Case 3 (right). Circles: spectra from the DOT reconstruction. Diamonds: spectra after calibration. Squares: Mie fitting using the recovered particle parameters. Crosses: calibration factors/spectra.

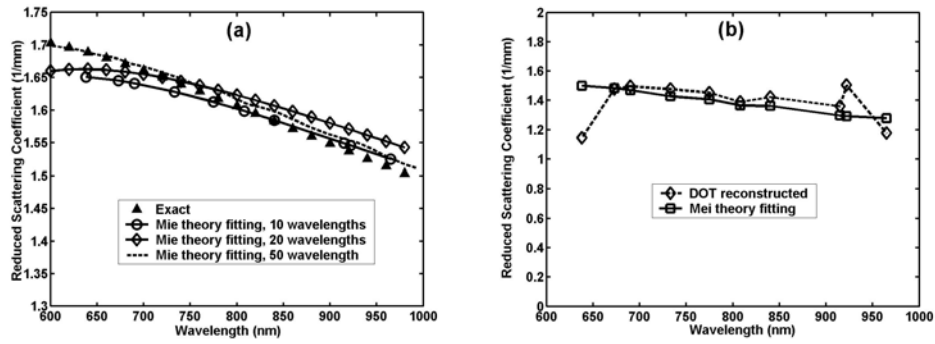


Figure 4-5. Scattering spectra: (a) The spectra generated by Eq. (5) and the Mie fittings using recovered particle parameters from simulated data (5% noise) with 10, 20, and 50 wavelengths, respectively. (b) Experimental spectra DOT reconstructed at a typical node in the target area and the corresponding Mie fitting using recovered particle parameters for the $2.06\ \mu\text{m}$ polystyrene case.

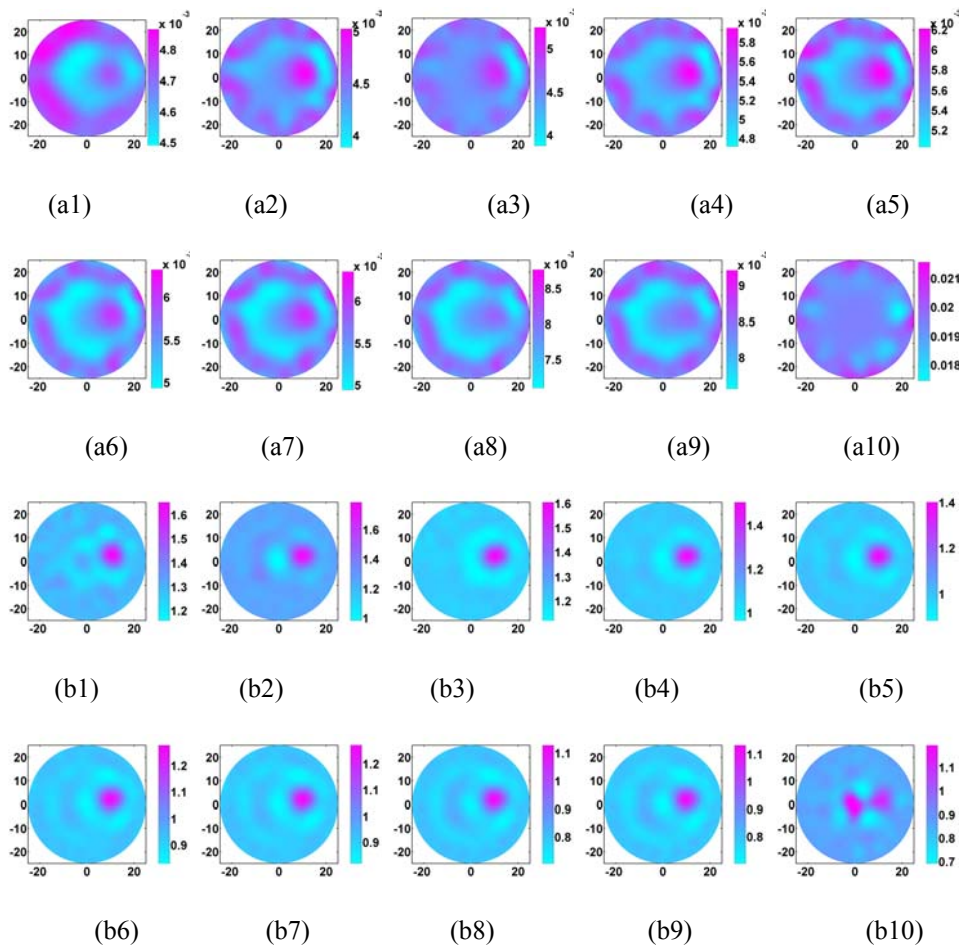


Figure 4-6. The DOT reconstructed absorption images (a1 to a10) and reduced scattering images (b1 to b10) at 10 different wavelengths: a1/b1 at 638nm; a2/b2 at 673nm; a3/b3 at 690nm; a4/b4 at 733nm; a5/b5 at 775nm; a6/b6 at 808nm; a7/b7 at 840nm; a8/b8 at 915nm; a9/b9 at 922nm and a10/b10 at 965nm for the 2.06 μm polystyrene case for all ten wavelengths.

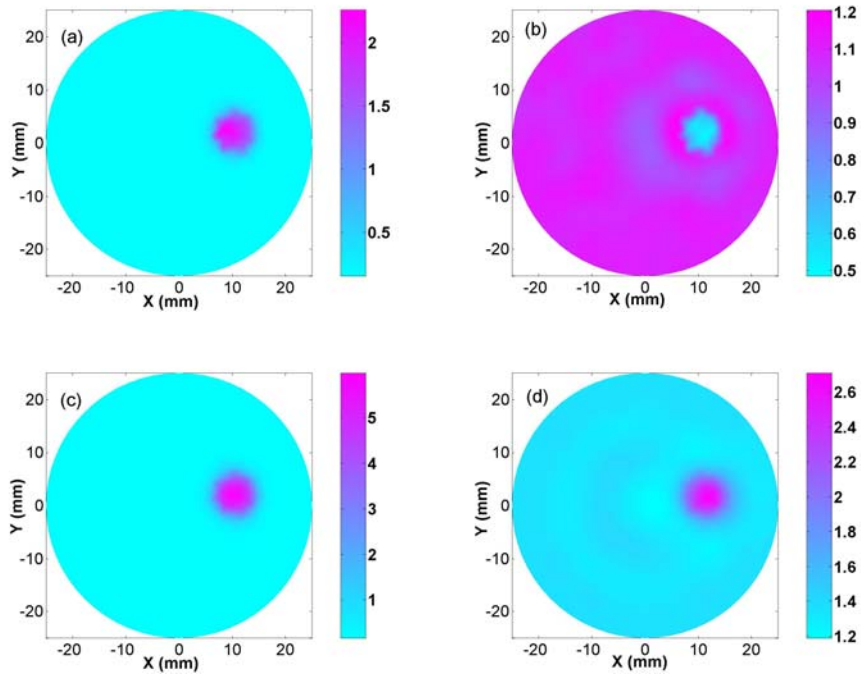


Figure 4-7. Reconstructed images of mean particle size (a, c) and concentration (b, d) for the 2.06 μm (a, b) and 5.66 μm (c, d) polystyrene cases, respectively. The axes (left and bottom) indicate the spatial scale, in millimeters, whereas the colorful scale (right) records the mean particle size or concentration, in micrometers or percentage.

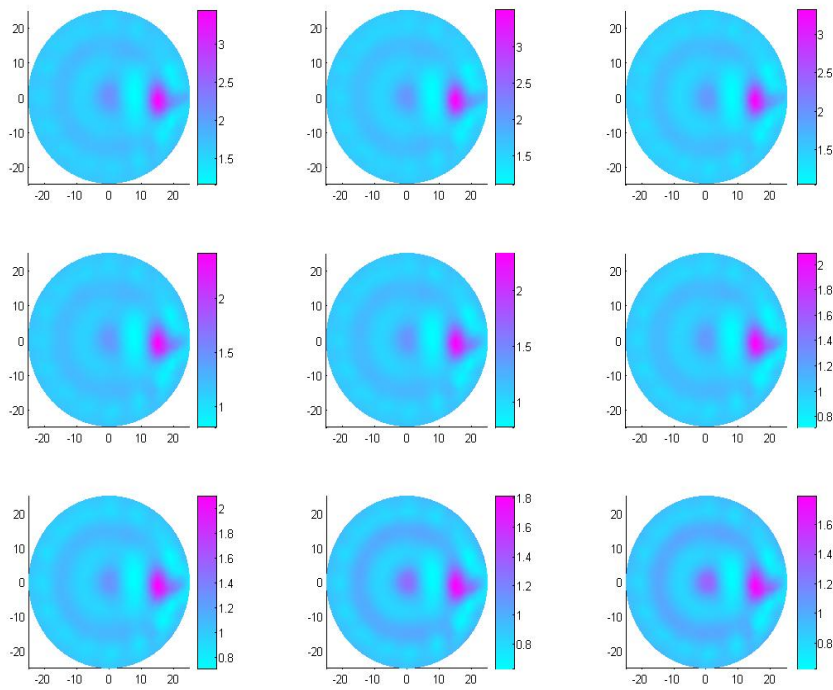


Figure 4-8. The reduced scattering coefficient images at 9 different wavelengths for experiment set1_1 (top row, left) 638 nm, (top row, middle) 673 nm, (top row, right) 690 nm, (middle row, left) 733 nm, (middle row, middle) 775 nm, (middle row, right) 808 nm, (bottom row, left) 840 nm, (bottom row, middle) 915 nm and (bottom row, right) 922 nm. The α values were same for all 9 wavelengths.

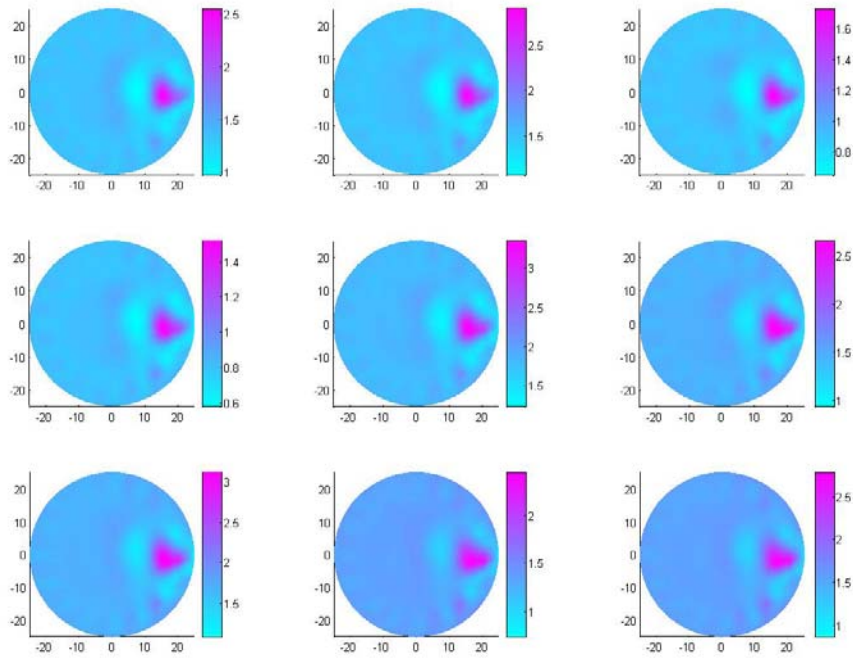


Figure 4-9. The reduced scattering coefficient images at 9 different wavelengths for experiment set1_1: (top row, left) 638 nm, (top row, middle) 673 nm, (top row, right) 690 nm, (middle row, left) 733 nm, (middle row, middle) 775 nm, (middle row, right) 808 nm, (bottom row, left) 840 nm, (bottom row, middle) 915 nm and (bottom row, right) 922 nm. The α value for each wavelength is different, obtained from the initial value search program. The global minimum error initial value is selected.

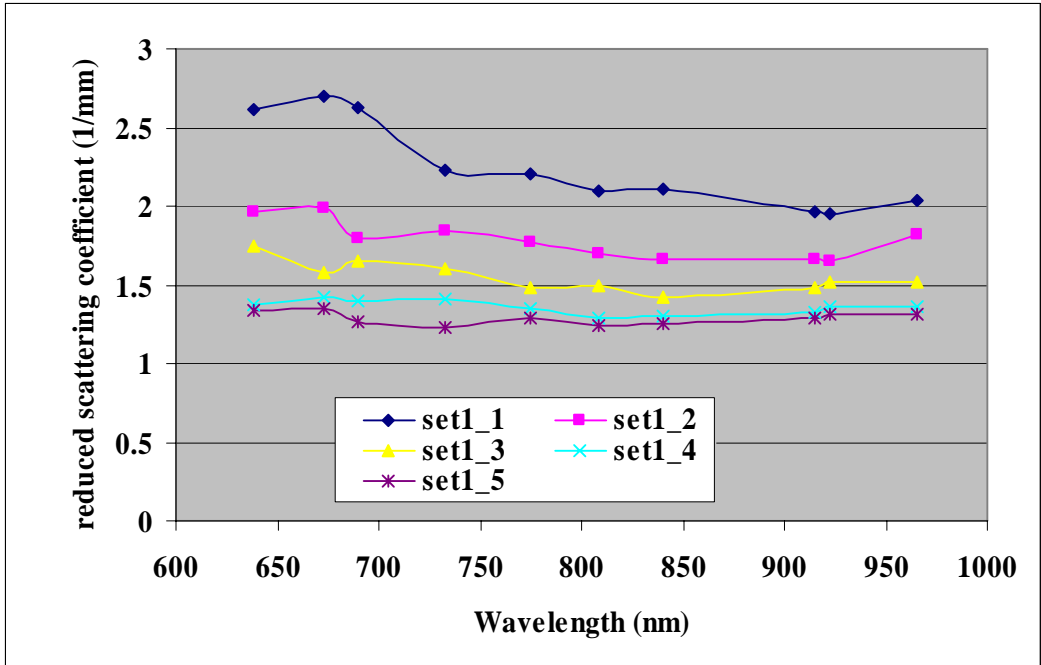


Figure 4-10. Reduced scattering coefficient at 10 wavelengths for 5 cases of experiment set1. Fixed α value was applied for each case.

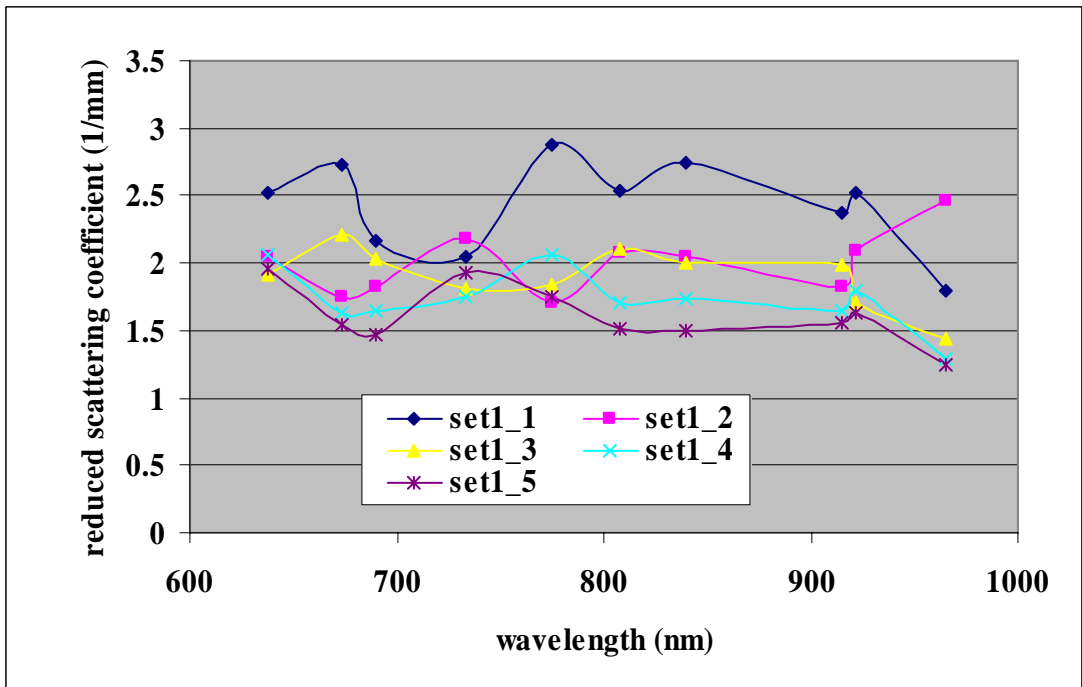


Figure 4-11. Reduced scattering coefficient at 10 wavelengths for 5 cases of experiment set1. The value of α corresponding to the global minimum error was applied for each case.

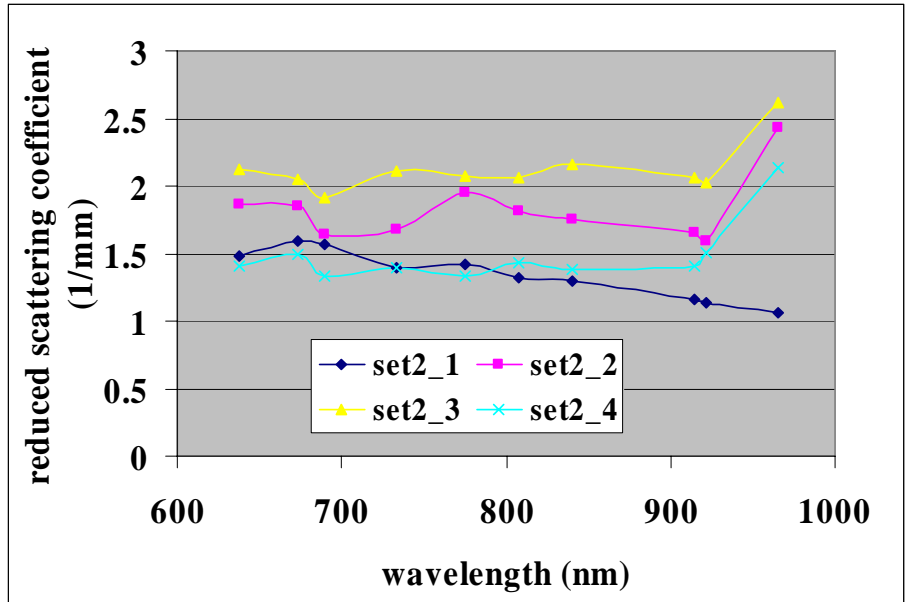


Figure 4-12. Reduced scattering coefficient at 10 wavelengths for 4 cases of experiment set2. Fixed α value was applied for each case.

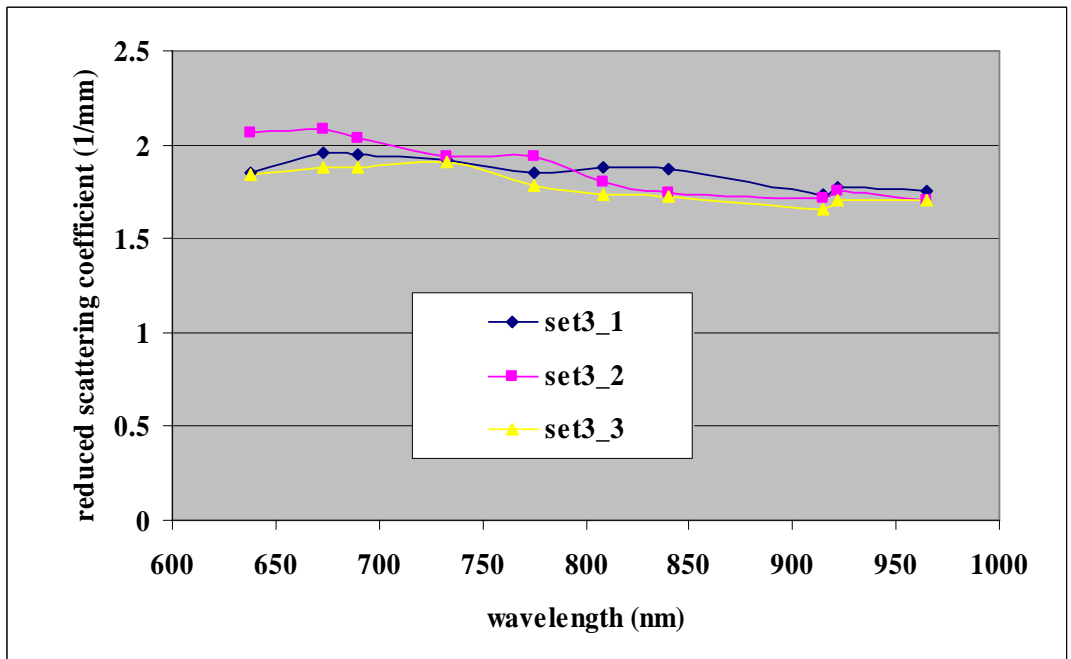
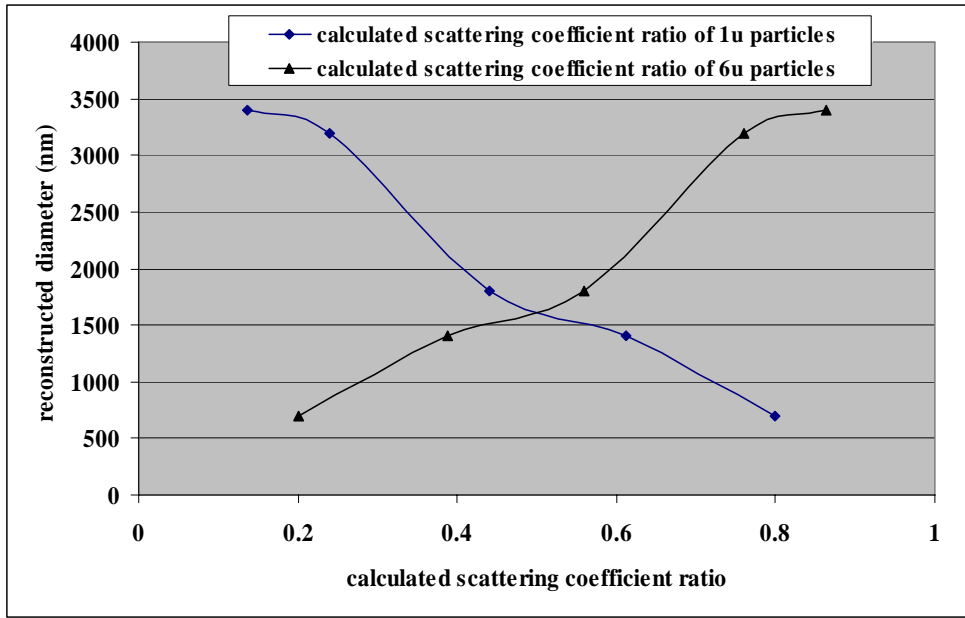
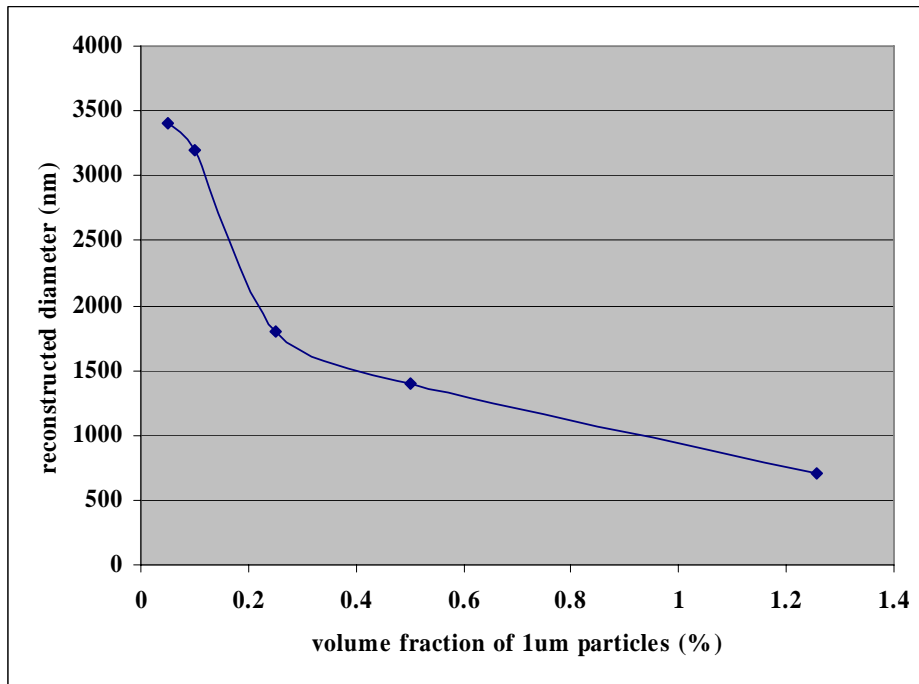


Figure 4-13. Reduced scattering coefficient at 10 wavelengths for 3 cases of experiment set 3. Fixed α value was applied for each case.

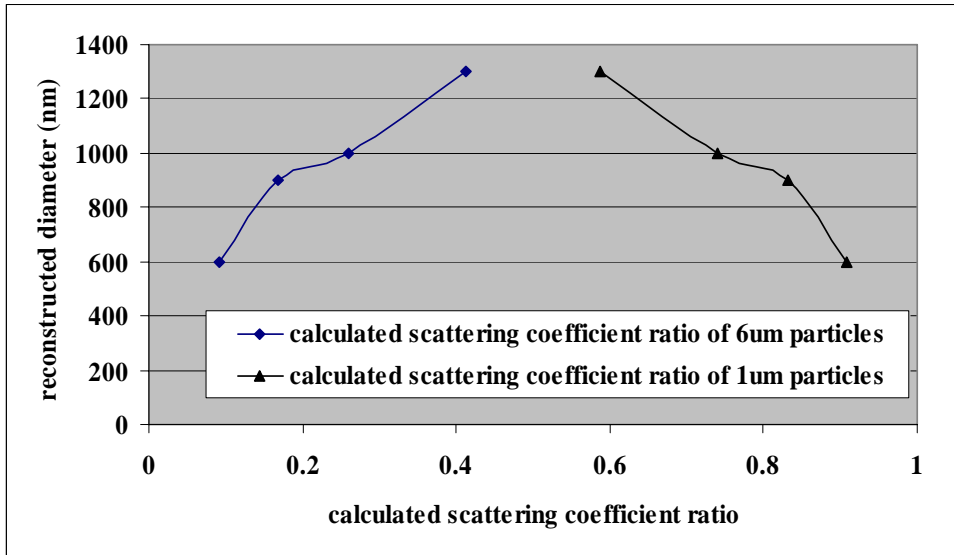


(a)

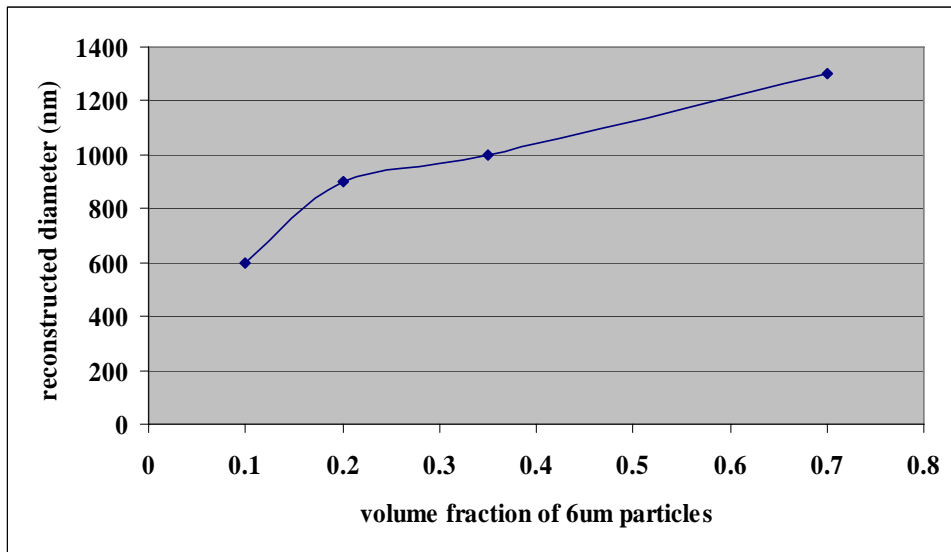


(b)

Figure 4-14. The reconstructed diameter versus (a) the calculated scattering coefficient ratio of 1 μm particles and 6 μm particles and (b) the volume fraction of 1 μm particles for experiment set 1.



(a)



(b)

Figure 4-15. The reconstructed diameter versus (a) the calculated scattering coefficient ratio of 1 μm particles and 6 μm particles and (b) the volume fraction of 1 μm particles for experiment set 2.

Table 4-1 Reconstructed parameters from simulated data at different noise levels for simulation 1.

Parameters	Exact	Reconstructed results and errors	Noise Levels				
			0%	1%	5%	10%	20%
Φ	1.02%	Reconstructed	1.02%	1.05%	1.13%	1.16%	1.36%
		Error	0.0%	2.9%	10.8%	13.7%	33.3%
a	2.855	Reconstructed	2.85	2.94	3.27	3.36	4.14
		Error	0.03%	3.0%	14.6%	17.6%	44.9%
b	0.145	Reconstructed	0.14	0.17	0.29	0.01	0.01
		Error	0.7%	17.9%	100%	93.1%	93.1%

Table 4-2 Reconstructed parameters from simulated data at different noise levels for simulation 2.

Parameters	Exact	Reconstructed results and errors	Noise Levels				
			0%	1%	5%	10%	20%
Φ	5.0%	Reconstructed	5.0%	5.02%	4.89%	5.37%	26.4%
		Error	0.0%	0.40%	2.20%	7.40%	21.8%
a	10.0	Reconstructed	10.0	10.05	10.07	10.74	7.98
		Error	0.0%	0.50%	0.70%	7.40%	20.2%
b	0.3	Reconstructed	0.30	0.44	0.59	0.043	0.023
		Error	0.0%	46.7%	96.6%	85.7%	92.3%

Table 4-3 Reconstructed parameters from experimental data using the peak and average scattering spectra of the target area.

Cases	Parameters	Exact	Reconstructed (Peak)	Error (Peak)	Reconstructed (Average)	Error (Average)
Case 1	Φ	0.52%	0.69%	33.3%	0.75%	44.2%
	a (um)	2.06	1.96	4.9%	2.40	16.4%
	b (um)	0.02	0.01	50.0%	0.01	67.9%
Case 2	Φ	1.02%	1.01%	0.8%	0.85%	16.6%
	a (um)	2.85	2.89	1.2%	2.73	4.5%
	b (um)	0.14	0.05	65.6%	0.12	15.2%
Case 3	Φ	2.62%	2.33%	11.1%	2.18%	16.8%
	a (um)	5.66	5.18	8.4%	5.19	8.2%
	b (um)	0.31	0.04	86.6%	0.05	84.9%

Table 4-4 Target materials of experiment set 1. The unit of volume is mL.

Experiment Sets	Targets					Total Volume
	6 μ m, 2.51%		1 μ m, 2.60%		water	
	volume	particle volume percent	volume	particle volume percent	volume	
set1-1	4.0	1.255	3.86	1.255	0.14	8.0
set1-2	4.0	1.255	1.54	0.5	2.46	8.0
set1-3	4.0	1.255	0.77	0.25	3.23	8.0
set1-4	4.0	1.255	0.31	0.1	3.69	8.0
set1-5	4.0	1.255	0.15	0.05	3.8	8.0

Table 4-5 Target materials of experiment set 2. The unit of volume is mL.

Experiment Sets	Targets					Total Volume
	1 μ m, 2.60%		6 μ m, 2.51%		water	
	volume	Particle volume percent	volume	Particle volume percent	volume	
set2-1	0.77	0.25	2.23	0.7	5.0	8.0
set2-2	0.77	0.25	1.12	0.35	6.11	8.0
set2-3	0.77	0.25	0.64	0.2	6.59	8.0
set2-4	0.77	0.25	0.32	0.1	6.91	8.0

Table 4-6 Target materials of experiment set 3. The unit of volume is mL.

Experiment Set3	Targets						Total Volume
	6 μ m, 2.51%		varied diameter			water	
	volume	Particle volume percent	diameter	Volume	Particle volume percent	volume	
set3-1	4.0	1.255	0.75 μ m	0.62	0.2	3.38	8.0
set3-2	4.0	1.255	0.11 μ m	2.96	1.0	1.04	8.0
set3-3	4.0	1.255	0.064 μ m	3.95	1.3	0.045	8.0

Table 4-7 Reconstructed results of set1.

cases	Calculated Scattering ratio	Volume ratio (percentage)	Extracted total volume percentage	Extracted mean diameter (μ m)
set1_1	0.798	1.255	0.8	700
set1_2	0.613	0.5	0.8	1400
set1_3	0.441	0.25	0.8	1800
set1_4	0.240	0.1	1	3200
set1_5	0.136	0.05	1	3400

Table 4-8 Reconstructed results of set2.

cases	Calculated Scattering ratio	Volume ratio (percentage)	Extracted total volume percentage	Extracted mean diameter (μm)
set2_1	0.414	0.7	0.6	1300
set2_2	0.261	0.35	0.5	1000
set2_3	0.168	0.2	0.5	900
set2_4	0.092	0.1	0.4	600

Table 4-9 Reconstructed results of set3.

cases	Calculated Scattering ratio	Volume ratio (percentage)	Extracted total volume percentage	Extracted mean diameter (μm)
set3_1	0.297	0.2	1.3	3200
set3_2	0.299	1.0	0.9	1800
set3_3	0.156	1.3	1	2400

CHAPTER 5
EX VIVO AND IN VIVO STUDY OF TUMOR CELL SIZING

5.1 Ex Vivo Study of Tumor Cells

The cellular architecture of early cancer cells changes⁵³. These morphological alterations typically include enlargement of the nuclei and increased nuclear density or nuclear crowding. Early tumors are readily treatable if these cellular alterations can be detected. These early warning signs, however, are thus far detectable only by histological examination of tissues taken out by biopsy. Here we describe a non-invasive imaging technique based on multi-spectral diffuse optical tomography (MSDOT) that can image cellular size and crowding.

We have tested the potential of this technique for imaging cellular size and crowding in *ex vivo* breast tissue. Immediately after the mastectomy of the right breast of a 62 years old female with a biopsy confirmed infiltrating ductal carcinoma ($\approx 3.3 \times 1.7 \times 3.0$ cm), a portion of the breast with the tumors was sectioned transversely into an approximately 1.5 cm thick section using a tissue slicer. From the section, a 3x2cm fresh tissue slice with both tumor and normal tissues was obtained. We then placed this tissue slice in the hole (4x6 cm) of a 7x10 cm cylindrical solid background phantom composed of agar powder, Intralipid solution and India ink for mimicking tissue scattering and absorption (Figure. 5-1a). We further poured liquid phantom (at 39°C) with the same optical properties as the solid phantom into the hole/breast tissue and then cooled down the liquid phantom to 20°C to obtain a full tissue-containing solid phantom for imaging (center in Figure. 5-1b). In Figure. 1b we also see that the multi-channel optic fibers (16 transmitters and 16 receivers) are in gentle contact with the phantom. After the optical measurement, a tissue sample from the same tissue slice was taken for histological examination. The microscopic sections of both tumor and normal tissues are shown in Figs. 5-2a and 5-2b, respectively.

Figs. 5-3a and 5-3b show the recovered cellular size and crowding or volume fraction images, respectively, where we immediately note that the tumor, normal tissue and background phantom are readily differentiated. The recovered average size of the scatterers in the tumor area was calculated to be 5.1 μm relative to the average nuclear size of 8.9 μm in the tumor region measured from the microscopic sections. This relatively large difference in size makes us to believe that what we reconstructed is most likely an effective size of combined nuclear and mitochondria (normally 1~2 μm) structure, which gives an expected effective size of approximately 5.0~5.5 μm from the microscopic sections. From Figure. 5-3b, we found that the extracted average cellular volume fraction or crowding in the tumor is 17% which is close to the nuclear crowding of 19% estimated from the microscopic sections.

Our results show that multi-spectral diffuse optical tomography has the potential to image cellular alterations, making it possible for detecting precancerous abnormal tissues.

5.2 Morphological Characteristics of Breast Tumors: In-Vivo Study with Multispectral Diffuse Optical Tomography

5.2.1 Methods

The three dimensional multispectral (10 wavelengths) imaging system and its calibration were described in chapter 2 and 3. Here only two-dimensional image was discussed. And 256 measurement data at 16 detection positions for each of 16 source locations were used for further image reconstruction. Chapter 4 detailed the algorithm of particle size imaging and its validations with numerical simulations and phantom experiments. Briefly, the tissue-mimicking phantom/clinical measurement data at each wavelength were used to obtain the absorption coefficient and reduced scattering coefficient images using our finite element based DOT reconstruction algorithm introduced in subsection 1.5. Then the reconstructed reduced scattering coefficient images at all wavelengths were utilized to extract the morphological images such as

the mean diameter image and the volume fraction image of the scattering particles using a Levenberg-Marquat inverse procedure.

Our clinical trial experiments, performed in the biomedical engineering department of University of Florida, were approved and monitored by the Institute Review Board of University of Florida Health Center. And our clinical trial experiments, performed in physics department, Clemson University, were approved and monitored by the Institute Review Board of Clemson University. All the patients, taking part in the clinical trial experiments, signed the consent forms. Since the imaging system could only cover 2 cm slice of a breast, the clinical trial experiments were conducted after the radiologists showed us which breast was abnormal and the approximate location of the abnormality from the mammogram films. The imaging results were compared with the mammogram report recorded by the radiologist and the biopsy report recorded by the pathologist. All the cases had the mammogram reports. Some clinical cases conducted in Clemson University did not have the biopsy report and all cases conducted in biomedical engineering department of university of Florida had the biopsy report.

5.2.2 Results

5.2.2.1 Case studies: #1, 2 and 3: Infiltrating ductal carcinomas

The NIR diffuse optical tomography imaging was conducted for the right breast of a 52 years old female volunteer with patient ID #G1. The right craniocaudal (CC) and mediolateral oblique (MLO) mammograms for the patient were shown in Figs. 5-4a and 5-4b, respectively. From the mammogram, an ill-defined speculated mass was found in the center lateral portion of the right breast, which lay under a marker for the palpable abnormality. BI-RADS category was 4. Sonographic images of the right breast also demonstrated an ill-defined hypoechoic mass with lobular margins measuring approximately $1.0 \times 1.6 \times 1.0$ cm in the 9 o'clock position corresponding to the abnormality noted in the mammogram. After biopsy, mastectomy was

performed and the surgery confirmed that the patient had an invasive ductal carcinoma in the right breast. Cut surfaces revealed a $1.2 \times 1.2 \times$ approximately 1.3 cm retracted and firm nodule of pink-tan tumor tissue in the lower outer quadrant subject to the biopsy site on the skin.

The DOT imaging was conducted one week before the biopsy and the mastectomy surgery. The reconstructed reduced scattering coefficient images at 9 wavelengths from 638nm to 922nm of the examined breast for the patient were shown in Figs. 5-5a to 5-5i, respectively. The horizontal and vertical axis represented x and y in mm. The color bar indicated values of reduced scattering coefficients in 1/mm. From all the scattering images, one target was detected around 6 o'clock while the surgery report indicated the tumor was in the lower outer quadrant, which means the tumor was around 7 o'clock.

The reduced scattering images at 9 wavelengths were used to extract the scattering particle mean diameter image in micrometer (shown in Figure.5-6a) and the scattering particle volume fraction image in percentage (shown in Figure. 5-6b). From Figure. 5-6a, the maximum diameter in the tumor region was found to be $3.1 \mu\text{m}$ and the average diameters in the tumor and the background were $2.18\mu\text{m}$ and $0.45\mu\text{m}$, respectively. The ratio of the average diameter in the tumor to that in the background was calculated to be 4.84. Similarly, from Figure. 5-6b, the maximum volume fraction in the tumor region was found to be 1.6% and the average volume fractions in the tumor and in the background were 1.32% and 0.48%. The ratio of the average volume fraction in the tumor to that in the background was calculated to be 2.75. The target and the background were segmented by the criteria of full width at half maximum (FWHM) at each figure. From both the diameter image and the volume fraction image, the suspicious tumor was located in a small region. This observation was consistent with the surgery report which revealed

a $1.2 \times 1.2 \times$ approximately 1.3 cm retracted and firm nodule of pink-tan tumor tissue in which the tumor was limited in.

The second patient (patient ID #G2) was a 50 years old female volunteer with palpable abnormality in the right breast. The right craniocaudal mammogram and the right mediolateral mammogram of the patient were shown in Figure. 5-7a and 5-7b respectively. From these mammograms, an extremely dense pattern of fibroglandular tissue, which limits the sensitivity, was identified. There was a 4-5 cm mass-like area in the upper-outer quadrant of the right breast, which correlated to the palpable abnormality. There was no architectural distortion or suspicious calcification. No skin thickening or adenopathy was noted. The ultrasonography of the right breast showed a 3×1.9 cm heterogeneous hypoechoic mass with some posterior shadowing corresponding to the palpable abnormality located at 10 o'clock. And there was an adjacent 9×6 mm similar hypoechoic solid nodule, as well as other small nodules. After biopsy, mastectomy surgery was conducted. From the surgery, a white, semi-cystic, semi-solid tumor mass with infiltrative borders was located in the lateral inferior quadrant (6-9 o'clock) and measured 4.0 cm from lateral to medial, 4.5 cm from inferior to superior, and 2.4 cm from anterior to deep. The breast parenchyma revealed fibrocystic change beneath the areola and nipple, which created a solid tan-white portion of breast tissue, measuring $2.2 \times 3.0 \times 2.5$ cm.

The NIR DOT imaging of the second patient was conducted two days before the biopsy and surgery. The reconstructed reduced scattering coefficient images at 9 wavelengths from 638nm to 922nm were shown in Figs 5-8a to 5-8i. These images were then used to extract the scattering particle mean diameter and volume fraction images, which were shown in Figs. 5-9a and 5-9b respectively. From the scattering images, one saw that the detected target was not limited in one region. The detected targets were located either in the center or around 10 o'clock

of the breast. From the mean diameter image and the volume fraction image shown in Figure. 5-9, one saw that the detected target were a big one located around the center and around 10 o'clock. These findings were consistent with the surgery report.

From Figure. 5-9a, the maximum diameter in the tumor region was found to be 5.3 μm and the average diameters in the tumor and in the background were 4.14 μm and 0.48 μm respectively. The ratio of the average diameter in the tumor to that in the background was calculated to be 8.62. Similarly, from Figure. 5-9b, the maximum volume fraction in the tumor region was found to be 1.9% and the average volume fractions in the tumor and in the background were 1.7% and 0.56%. The ratio of the average volume fraction in the tumor to that in the background was calculated to be 3.03.

The third patient was 50 years old female volunteer, with patient ID #G8. Unfortunately, we could not obtain the mammogram films because the patient moved to other hospital after the mammogram screening and biopsy were conducted in Shands Hospital where our CO-PI works. The reports of mediolateral oblique mammogram and craniocaudal mammogram of both breasts were obtained. The breasts were composed of very dense fibroglandular tissues, which can limit mammogram sensitivity. In the mammograms, there were no masses or areas of distortion. The mammograms' conclusion was "Probably benign right mammogram. Benign left mammogram." However, the biopsy report indicated that a ductal carcinoma in situ, non-comedo type, of breast, nuclear grade III is found. The biopsy found there were 2 masses in the left breast, one in the 11 o'clock position and one in the retroareolar region. Only the 11 o'clock lesion was biopsied. Surgical excision was recommended.

Before the biopsy, the NIR DOT imaging experiments of the patient left breast were conducted. Because the patient felt pain in the neck during the NIR imaging experiment,

measurements stopped at 7th wavelength. And because the dense breast tissue resulted in low SNR at the shorter wavelengths, the reduced scattering coefficient images at 4 wavelengths from 733 nm to 840 nm were reconstructed and shown in Figure. 5-10. Based on the scattering images at 4 wavelengths, the scattering particle mean diameter and volume fraction images were reconstructed and shown in Figs. 5-11a and 5-11b respectively. From both the scattering images and the morphological images, the detected targets were located around 12 o'clock and 3 o'clock. There was more than one target, which was consistent with the biopsy report, while the mammogram report indicated that there were no suspicious masses or lesions in the left breast.

From Figure. 5-11a, the maximum diameter in the tumor region was found to be 4.8 μm and the average diameters in the tumor and in the background were 3.65 μm and 0.31 μm respectively. The ratio of the average diameter in the tumor to that in the background was calculated to be 11.77. Similarly, from Figure. 5-11b, the maximum volume fraction in the tumor region was found to be 1.84% and the average volume fractions in the tumor and in the background were 1.61% and 0.64%. The ratio of the average volume fraction in the tumor to that in the background was calculated to be 2.51.

5.2.2.2 Case studies: #4, 5 and 6: Benign nodule or mass

The fourth patient was a 69 years old female volunteer with patient ID #S5. Figure. 5-12 represented the right breast mediolateral oblique mammogram (a) and the right breast craniocaudal mammogram (b). In the mammogram, a stellate area of architectural distortion and asymmetric density had developed in the superior lateral quadrant, where the patient felt a palpable mass. But the right breast ultrasound examination report indicated that in the area of the known mammographic abnormality, no discrete mass was identified. There was some slight shadowing in this area. No biopsy report was available for this patient.

The reconstructed absorption coefficient images for the right breast of the patient at 9 wavelengths from 638nm to 922nm (a to i) were shown in Fig 5-13. Horizontal and vertical axis represented x and y in mm, respectively. The color bar indicated the value of absorption coefficient in 1/mm. And the reconstructed reduced scattering coefficient images at the right breast of the patient at 9 wavelengths from 638nm to 965nm (a to i) were shown in Figure. 5-14. The color bar indicated the value of the reduced scattering coefficient in 1/mm. Only the reduced scattering coefficient images at 9 wavelengths were used to extract the scattering particle mean diameter image (shown in Figure. 5-15a) and volume fraction image (shown in Figure. 5-15b). In all the absorption coefficient images, the reduced scattering coefficient images and morphological images, only one target around 8 o'clock is identified, while in the mammogram the abnormality was located around 9 o'clock.

As shown in Figure. 5-15, the scattering particle mean diameter increased in the target region while the volume fraction in the target region decreased. From Figure. 5-15a, the maximum diameter in the tumor region was found to be $0.65\ \mu\text{m}$ and the average diameters in the tumor and the background were found to be $0.53\ \mu\text{m}$ and $0.11\ \mu\text{m}$, respectively. The ratio of the average diameter in the tumor to that in the background was calculated to be 4.82. Similarly, from Figure. 5-15b, the minimum volume fraction in the tumor region was found to be 0.2% and the average volume fractions in the tumor and in the background were found to be 0.42% and 0.93%. The ratio of the average volume fraction in the tumor to that in the background is calculated to be 0.45.

The fifth patient was a 42 years old female volunteer with patient ID #S7. Figure. 5-16 showed the left breast craniocaudal mammogram (a) and the left breast mediolateral oblique mammogram (b). The mammogram report indicated that the nodular density below the scar

marker appeared to press out on the spot compression CC view and no persisted nodular density was seen on the roll views. There was reportedly no palpable mass. The ultrasound report indicated that two smooth lobulated solid nodules were presented in the medial aspect of the left breast at 9:30 o'clock. The more anterior nodule measured $5.8 \times 4.8 \times 8.3$ mm and the mid left breast nodule measured $6.9 \times 3.6 \times 9.1$ mm. The BI-RADS category is 3.

The NIR DOT imaging experiment was conducted after the mammogram examination. The reconstructed reduced scattering coefficient images at 9 wavelengths for the left breast of the patient #S7 were shown in Figure. 5-17. Horizontal and vertical axis represented x and y in mm, respectively. The color bar indicated the value of reduced scattering coefficient in 1/mm. In the scattering images, there were two targets located around 6:00 o'clock and 8 o'clock respectively, while the mammogram could not identify any target and the ultrasound detected two separate nodules positioned around 9:30 o'clock.

Using the reduced scattering coefficient images, the scattering particle mean diameter image (shown in Figure. 5-18a) and volume fraction image (shown in Figure. 5-18b) were reconstructed. The mean diameter image (shown in Figure. 5-18a) had a big artifact in the center that was possibly resulted in from the center artifacts in the scattering images 5-17h and 5-17i. The volume fraction image (shown in Figure. 5-18b) identified the targets at the right positions. From Figure. 5-17a, the maximum diameter in the tumor region was found to be $4.7\mu\text{m}$ and the average diameters in the tumor and the background were $4.15\mu\text{m}$ and $1.33\mu\text{m}$, respectively. The ratio of the average diameter in the tumor to that in the background was calculated to be 3.12. Similarly, from Figure. 5-17b, the maximum volume fraction in the tumor region was found to be 1.7% and the average volume fractions in the tumor and in the background were calculated to

be 1.41% and 0.29%. The ratio of the average volume fraction in the tumor to that in the background is calculated to be 4.86.

The sixth patient was a 60 years old female volunteer with patient ID #S9. Figure. 5-19 showed the mediolateral oblique mammogram (a) and the mediolateral mammogram (b) of the right breast. The mammogram report indicated that small nodular opacity in outer aspect was seen only in single projection on the exaggerated craniocaudal view of the right breast (the film of the exaggerated CC mammogram was not available) and it had an identical appearance to study one year ago. And a large dominant opacity was re-demonstrated also unchanged. It measured approximately 1.4 cm in diameter and sit more medially within the lateral aspect of the right breast. The BI-RADS category was 2, benign findings. Ultrasound imaging was not conducted.

The NIR DOT imaging experiment was conducted two days after the mammogram screening. The reconstructed reduced scattering coefficient images at 9 wavelengths were shown in Figure. 5-20. Two targets, one at 5 o'clock and the other at 11 o'clock, were identified in almost all the scattering images, which was consistent with the mammogram report indicating two targets, one 4mm in diameter in the outer aspect and the other 1.4 cm in diameter within the lateral aspect. Using these reduced scattering coefficient images, the scattering particle mean diameter image (shown in Figure. 5-21a) and volume fraction image (shown in Figure. 5-21b) were reconstructed. The morphological images also identified two targets. From Figure. 5-21a, the maximum diameter in the tumor region was found to be $0.64\mu\text{m}$ and the average diameters in the tumor and the background were calculated to be $0.53\mu\text{m}$ and $0.12\mu\text{m}$, respectively. The ratio of the average diameter in the tumor to that in the background was calculated to be 4.41. Similarly, from Figure. 5-21b, the maximum volume fraction in the tumor region was found to

be 1.42% and the average volume fractions in the tumor and in the background were found to be 0.53% and 1.05%. The ratio of the average volume fraction in the tumor to that in the background was calculated to be 0.505.

5.2.2.3 Statistical analysis and pathological co-registration

Besides the 6 clinical cases, the clinical experimental measurements of 7 more benign cases and 1 more malignant tumor case were processed. The scattering particle mean diameter and volume fraction for each case were reconstructed. There were 10 benign cases and 4 malignant cases available for the statistical analysis. The peak values of the recovered scattering particle mean diameter and volume fraction in the target region were found in the reconstructed mean diameter image and volume fraction image for each case. The average values and the standard deviations of the mean diameter and volume fraction for the 10 benign cases and 4 malignant cases were calculated, respectively. The calculated results were shown in Figure. 5-22, where the solid bar indicated the malignant cases and the bar with cross pattern represented the benign cases. The average diameter for the malignant tumors was calculated to be $4.325 \mu\text{m}$ with deviation of $1.34 \mu\text{m}$. And the average volume fraction for malignant tumors was calculated to be 1.7375% with standard deviation of 0.65%. Similarly, the average diameter for the benign abnormalities was calculated to be $1.3455 \mu\text{m}$ with deviation of $1.43 \mu\text{m}$. And the average volume fraction for the benign abnormalities was calculated to be 0.658% with standard deviation of 0.51%. The ratio of the average diameter of malignant tumors to that of benign abnormalities was $4.352/1.345=3.23$. Similarly, the ratio of the average volume fraction of malignant tumors to that of benign abnormalities was $1.7375\%/0.658\%=2.64$.

For each case, the recovered volume fraction versus the recovered diameter was plotted in Figure. 5-23. The square dots indicated the malignant cases and the diamond dots represented the benign cases. It was clear that all the malignant cases were located in the upright quadrant

and all the benign cases except one were located in the downleft quadrant. The exception case was from the patient ID #S7, discussed in above subsection. The center artifact dominated the reconstructed mean diameter image and the result of that case was deteriorated. The preliminary result showed that the recovered scattering particle mean diameter and volume fraction could be the new criteria to differentiate the malignant tumors from the benign abnormalities.

The microscopic pictures of the tumor cells for patient #G1, #G2 and #G3 were obtained from our cooperated pathologist in the Shands hospital and they were shown in figure 5-24. All these three pictures were magnified by 400 times. From these pictures, we could find the average diameter and the approximate volume fraction of the cancer cell nucleus and nucleolus. Please note that the nucleus and nucleolus were not spherical. The diameter of one nucleus was the average of the length and the width. The diameter of nucleolus was approximated as 0.2 times the corresponding the nucleus. The volume fraction of the nucleus was 0.667 multiplying the ratio of the area occupied by the nucleus to the whole area of the section, where 0.667 was the factor considering that we calculated the 3D volume fraction not the 2D area fraction. The found values were shown in table 5-1. The volume fraction of nucleolus was calculated as $(0.2)^3=0.008$ times the corresponding nucleus volume fraction. And these values were compared with average value calculated from the reconstructed diameter images and volume fraction images for corresponding cases. From the Table 5-1, we found that the relative errors of the reconstructed average diameters for #G1, #G2 and #G8, compared to the values of nucleus found from pathological pictures, are 55.3%, 6.5% and 31.9%, respectively. Similarly, we found that the extracted average volume fraction, compared to the values found from pathological pictures, are 77.9%, 60.3% and 76.4%, respectively. From the table, we saw that the reconstructed diameters were about 2 times less than the diameters of nucleus for case #G1 and #G8 and the

reconstructed volume fractions were about 3 times less than those of nucleus for all three cases. The reconstructed diameters and volume fraction were larger than those of the nucleolus and less than those of the nucleus. We could conclude that the scattering particles were including both the nucleus and the small particles such as the nucleolus, mitochondria. We could not see mitochondria in these pictures but their sizes were close to that of nucleolus.

In sum, in this subsection, we have studies 14 clinical cases including 10 benign cases and 4 malignant cases and detailed 6 clinical cases, in which the tumors were identified successfully in both the reconstructed diameter and volume fraction images. The statistical analysis showed that the reconstructed diameter and volume fraction may provide new parameters to differentiate the malignant breast tumors from the benign abnormalities while more clinical results were needed to prove it further. By comparison with the pathological pictures, we found that the scattering particles were not only the nucleus but also the smaller particles such as nucleolus and the mitochondria.

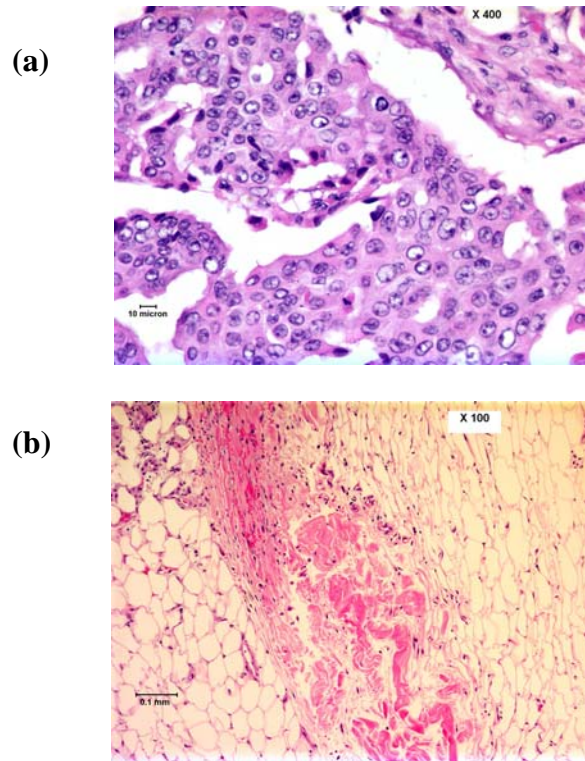


Figure 5-1. The microscopic picture of (a) the tumor tissue (400 time magnificent) and (b) the normal tissue (100 time magnificent).

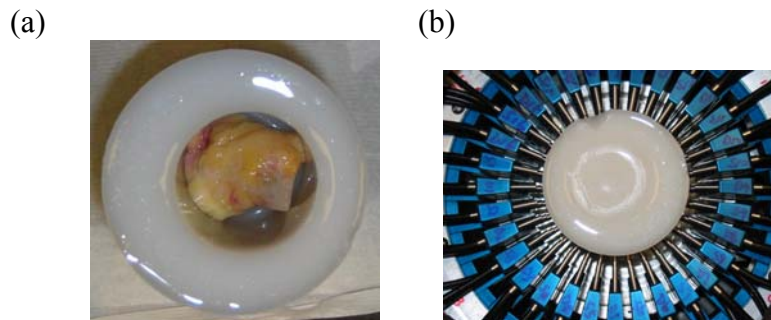


Figure 5-2. Experiment preparation: (a) the removed tissue was put inside the background phantom; (b) The tissue was covered with background phantom and examined by the system.

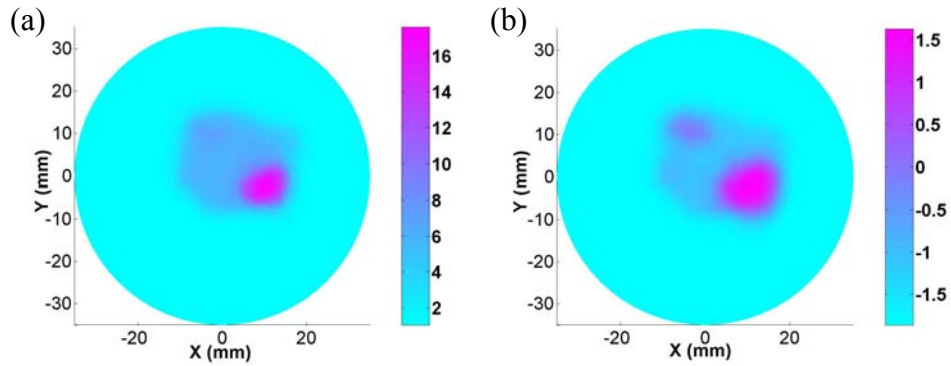


Figure 5-3. Ex-vivo results: (a) The extracted nucleus concentration distribution in the tissue region and the intralipid concentration distribution in the background region (percentage), where the color bar indicates the percentage number; (b) The logarithm of extracted nucleus size distribution in the tissue region and the intralipid size distribution in the background region, where the color bar responses to the logarithm of the diameter in micrometer.

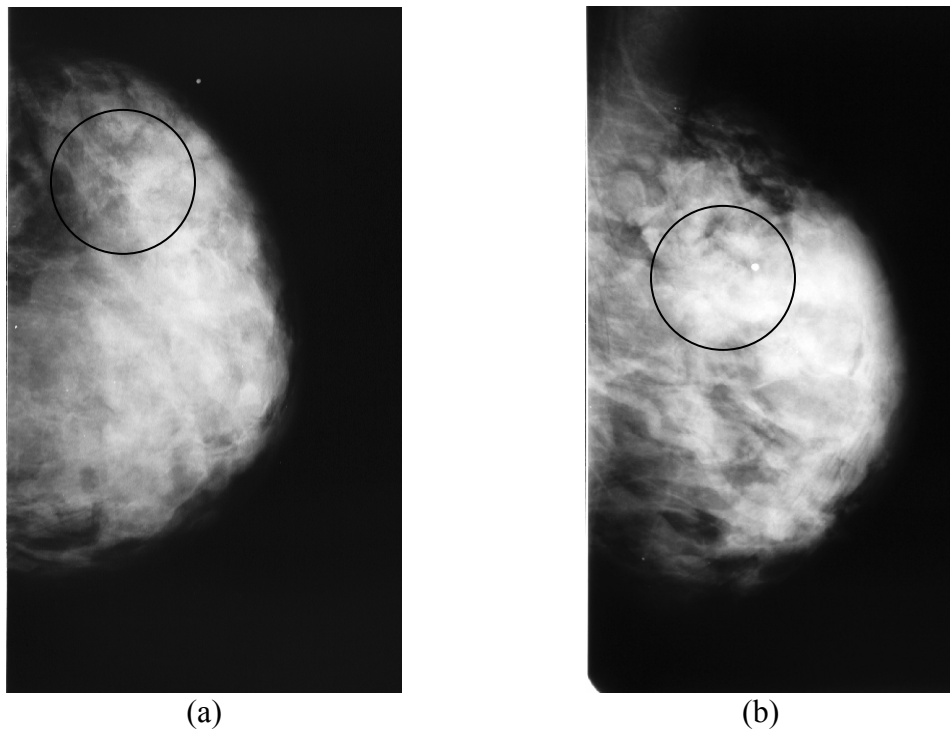


Figure 5-4. Mammogram films: (a) Right CC mammogram, (b) Right MLO mammogram for the right breast of a 52 years old patient (patient ID #G1).

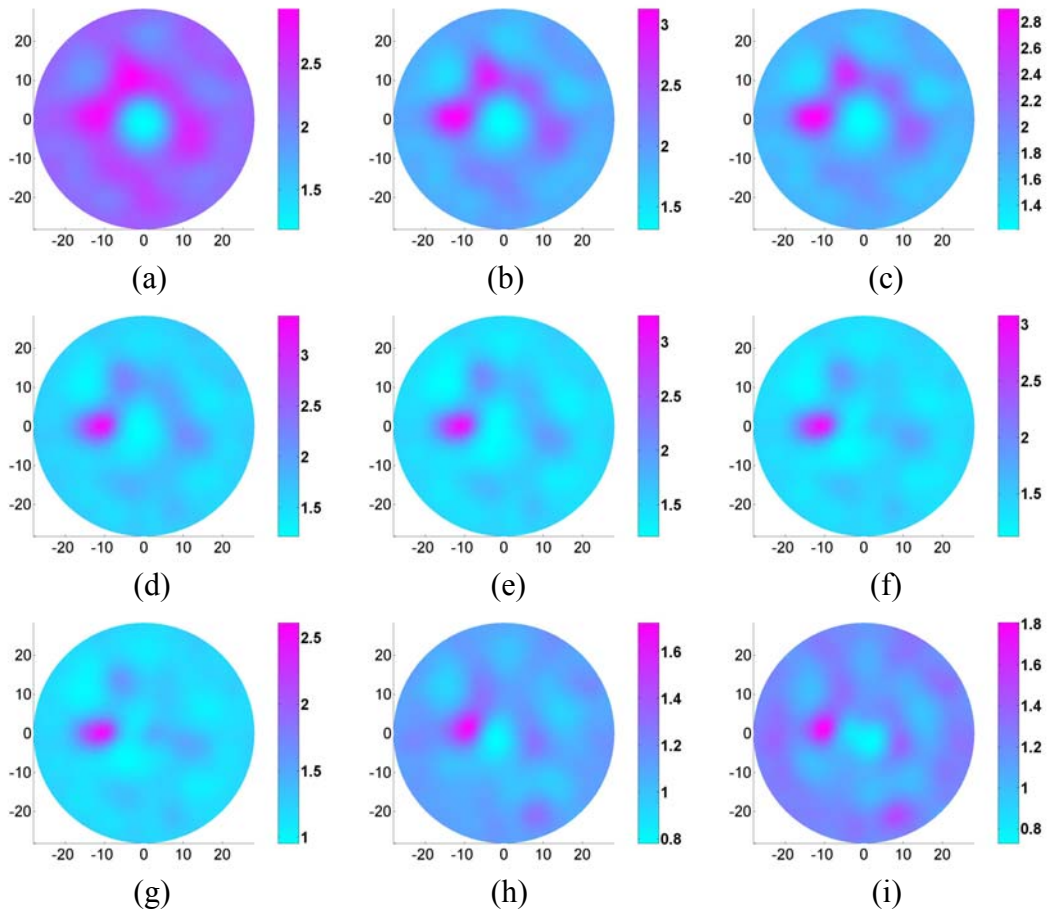


Figure 5-5. The constructed scattering images at 9 wavelengths from 638nm to 922nm (figs. a to i) of the examined breast for patient G1. Horizontal and vertical axis represent x and y respectively. The color bar indicated the value of the reduced scattering coefficient in 1/mm.

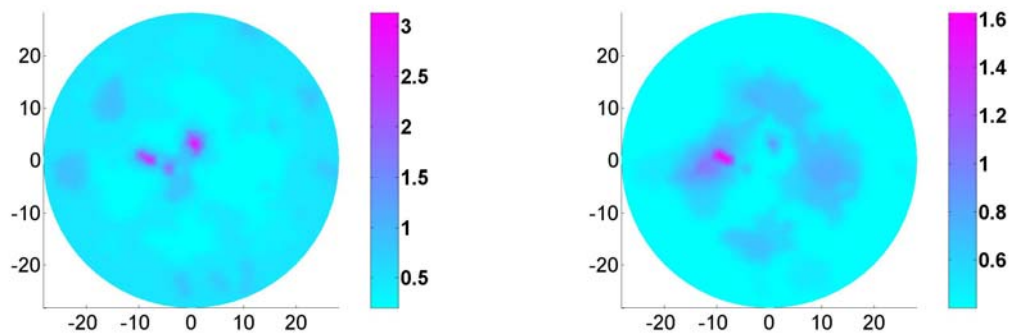
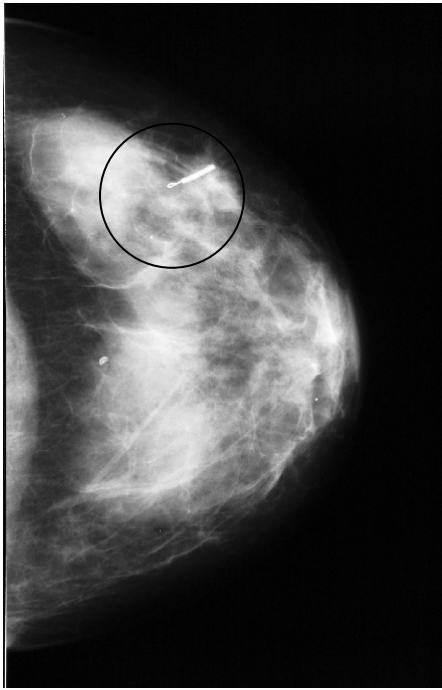
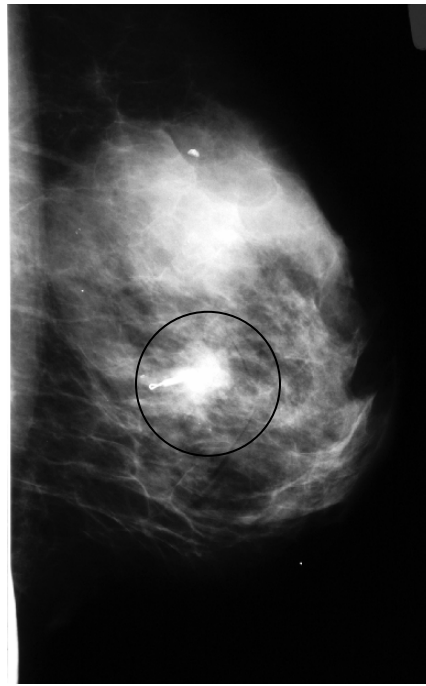


Figure 5-6. The extracted images of particle diameters (a) and particle volume fraction (b) of the examined breast for patient G1. The colorful bar in (a) represents the value of particle diameters in micrometer. And the colorful bar in (b) represents the value of particle volume fraction of percentage. Horizontal and vertical axis represent x and y respectively.



cc



MLO

Figure 5-7. Mammogram films: (a) CC mammogram, (b) MLO mammogram for the right breast of a 50 years old patient.

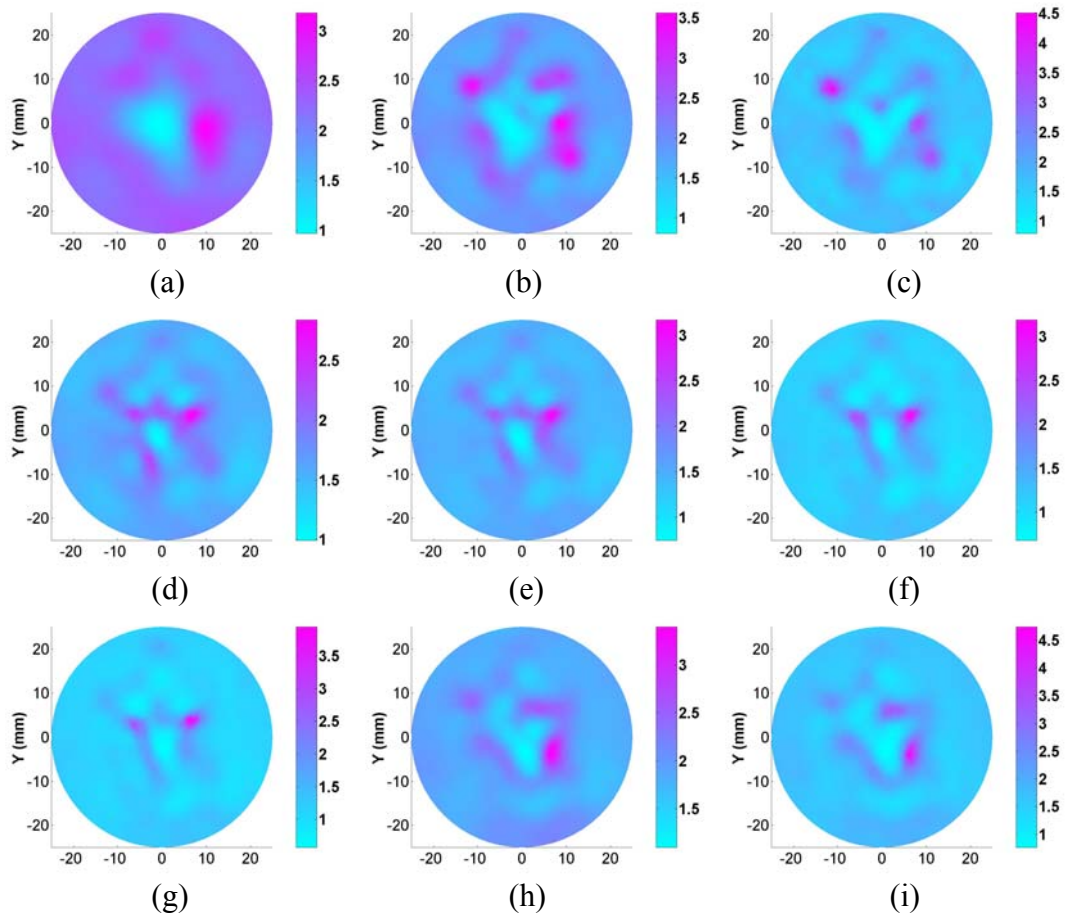


Figure 5-8. The reconstructed scattering images at 9 wavelengths from 638nm to 922nm (Figs. a to i) of the examined breast for patient #G2. Horizontal axis represents x. The colorful bar indicated the value of the reduced scattering coefficient in 1/mm.

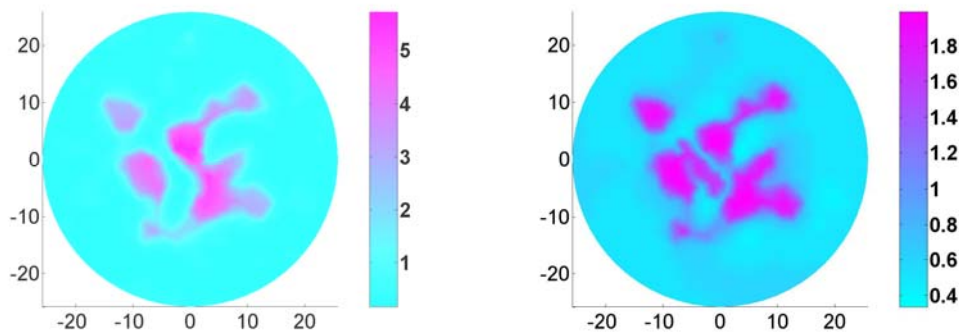


Figure 5-9. The extracted images of particle diameters (a) and particle volume fraction (b) of the examined breast for patient #G2. The colorful bar in (a) represents the value of particle diameters in micrometer. And the colorful bar in (b) represents the value of particle volume fraction of percentage. Horizontal and vertical axis represent x and y respectively.

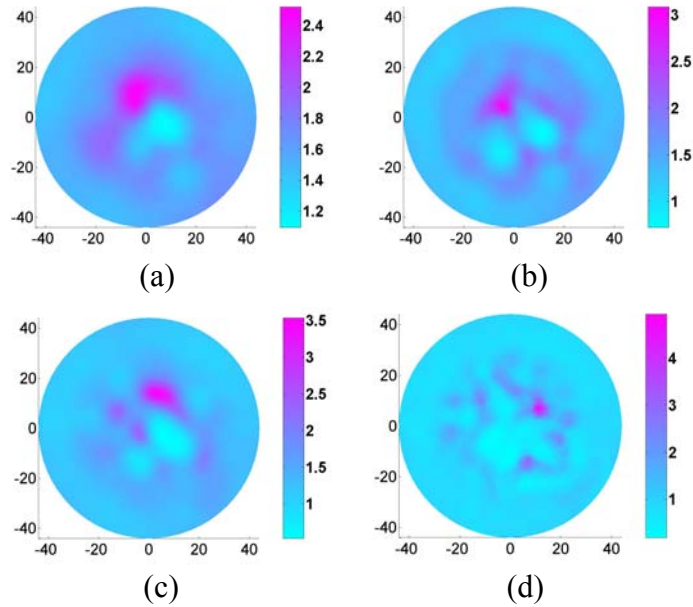


Figure 5-10. The reconstructed scattering images at 4 wavelengths from 733nm to 840nm (Figs. a to d) of the examined breast for patient G8. Horizontal and vertical axis represent x and y respectively. The colorful bar indicated the value of the reduced scattering coefficient in 1/mm.

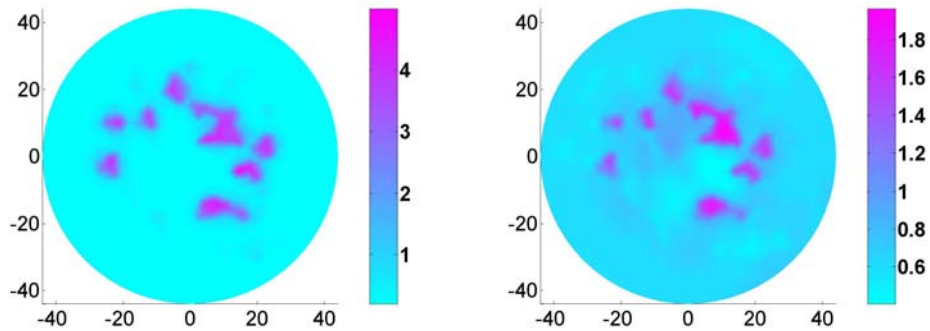


Figure 5-11. The extracted images of particle diameters (a) and particle volume fraction (b) of the examined breast for patient G8. The colorful bar in (a) represents the value of particle diameters in unit of micrometer. And the colorful bar in (b) represents the value of particle volume fraction of percentage. Horizontal and vertical axis represent x and y respectively.

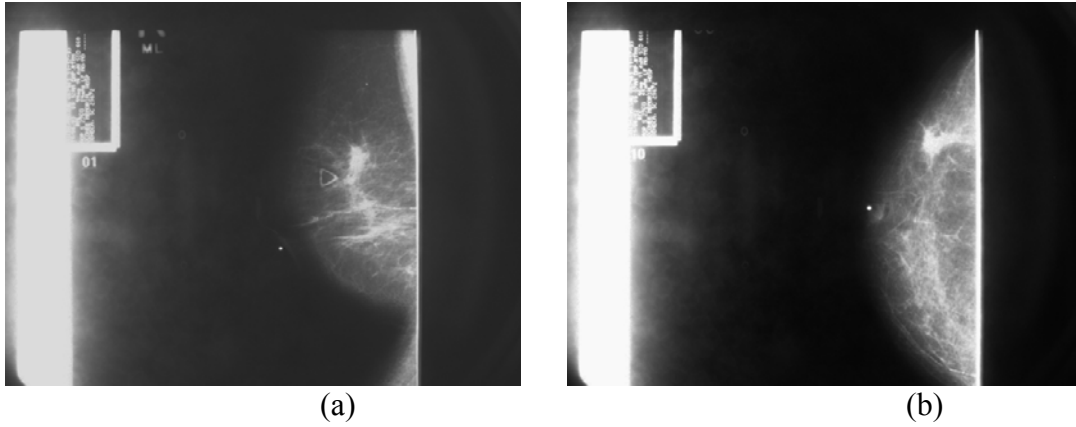


Figure 5-12. Mammogram films: (a) MLO and (b) CC mammography of the right breast for patient #S5.

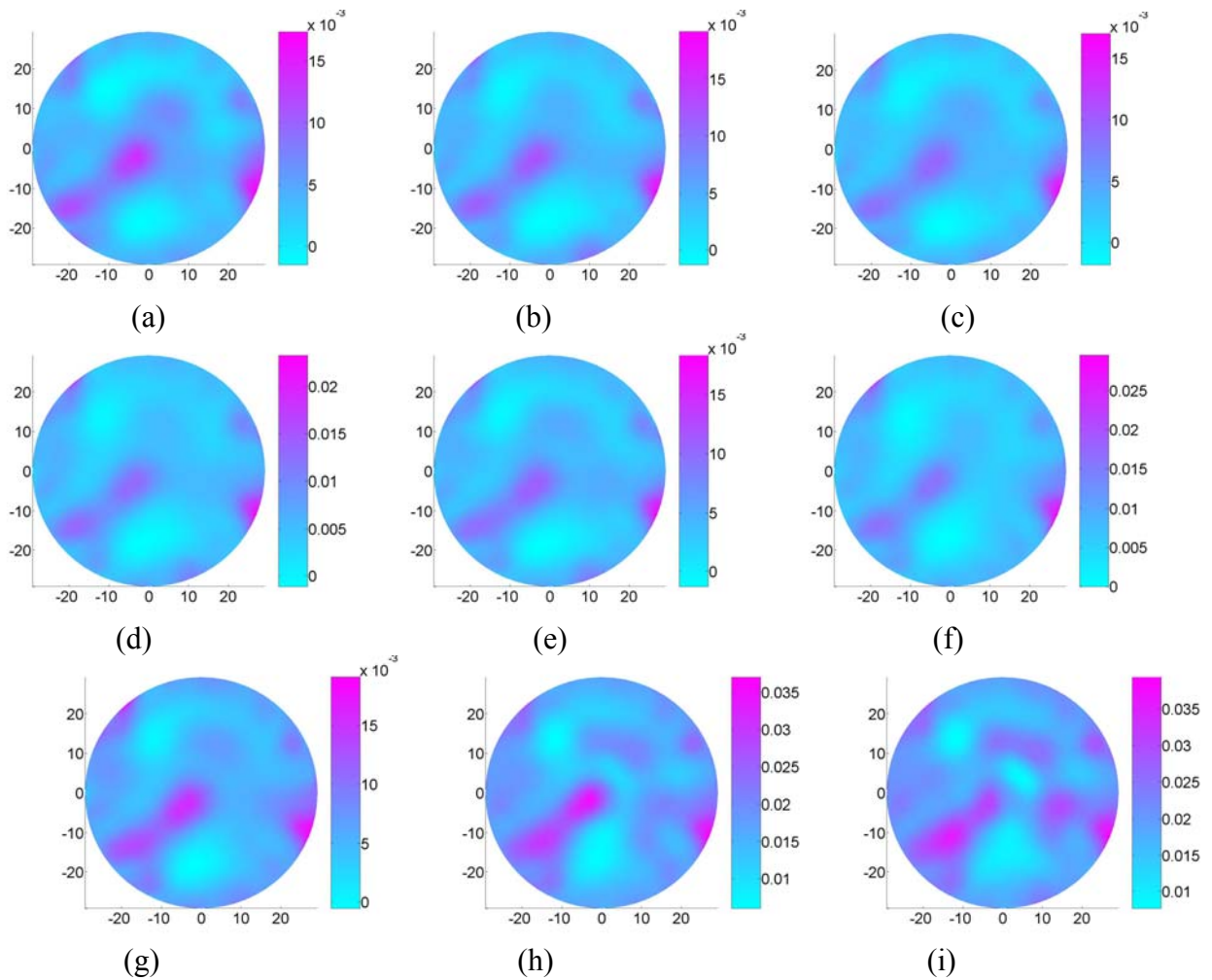


Figure 5-13. The reconstructed absorption coefficient images for the right breast of the patient #S5 at 9 wavelengths from 638nm to 922nm (a to i). Horizontal and vertical axis represent x and y in mm, respectively. The color bar indicates the value of the absorption coefficient in 1/mm.

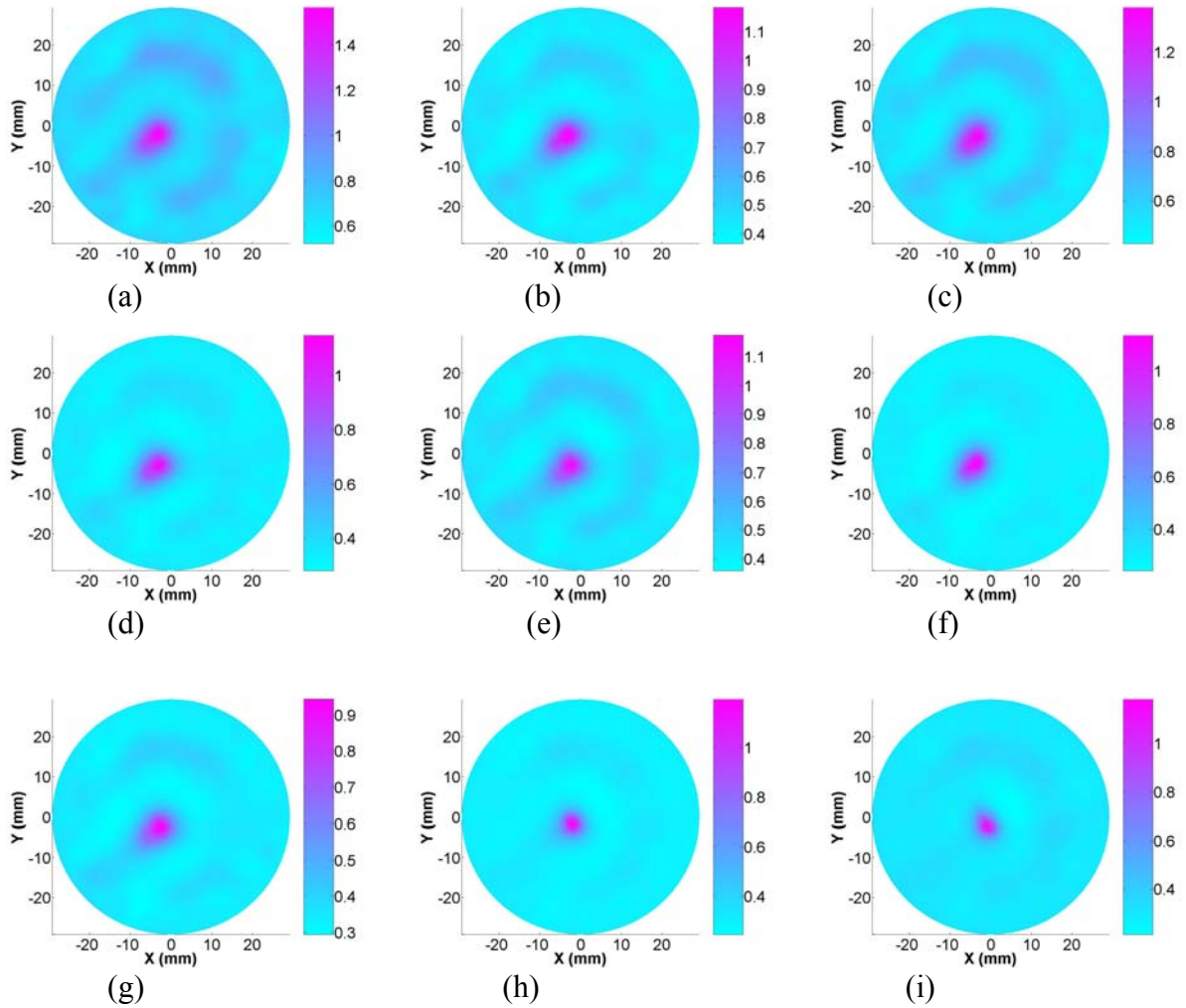


Figure 5-14. The reconstructed scattering images at the right breast of the patient #S5 at 9 wavelengths from 638nm to 965nm (a to i). The color bar indicated the value of the reduced scattering coefficient in 1/mm.

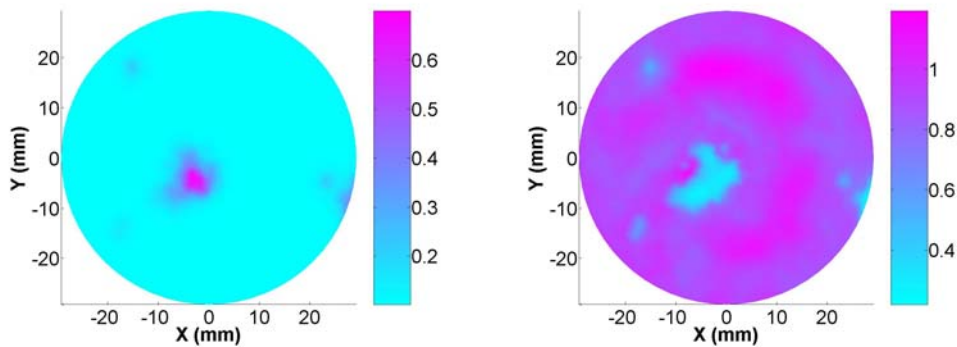


Figure 5-15. The reconstructed particle diameter image (a) and the particle volume fraction image (b) of the right breast for patient #S5. The colorful bar in (a) represents the value of particle diameters in micrometer. And the colorful bar in (b) represents the value of particle volume fraction in percentage.



Figure 5-16. Mammogram films: (a) CC and (b) MLO mammography of the left breast for patient #S7.

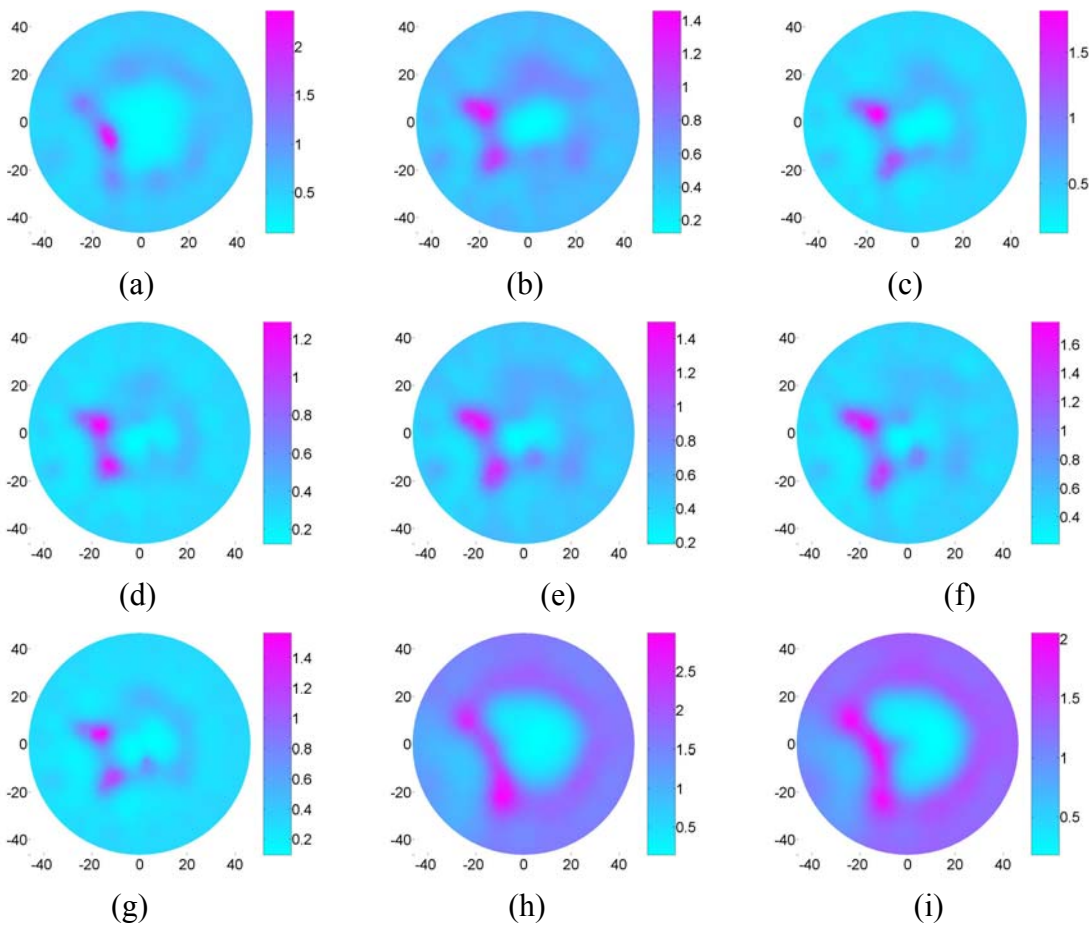


Figure 5-17. The reconstructed scattering images of the examined breast at 9 wavelengths from 638nm to 965nm (a to i) for patient #S7. The color bar indicated the value of the reduced scattering coefficient in 1/mm. Horizontal and vertical axis represent x and y in mm. respectively.

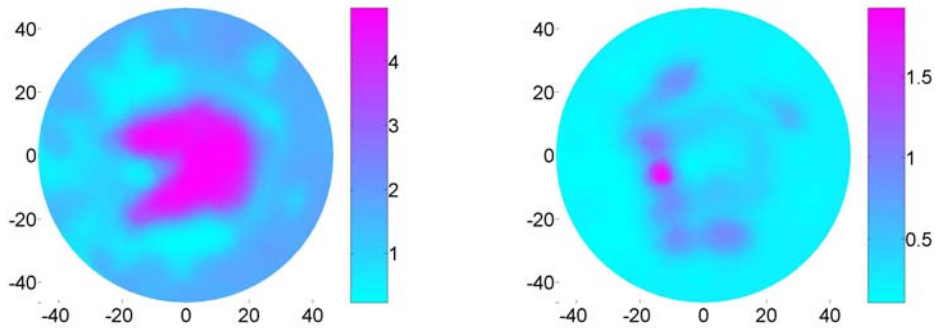


Figure 5-18. The reconstructed particle diameter image (a) and the particle volume fraction image (b) of the examined breast for patient #S7. The colorful bar in (a) represents the value of particle diameters in micrometer. And the colorful bar in (b) represents the value of particle volume fraction in percentage.

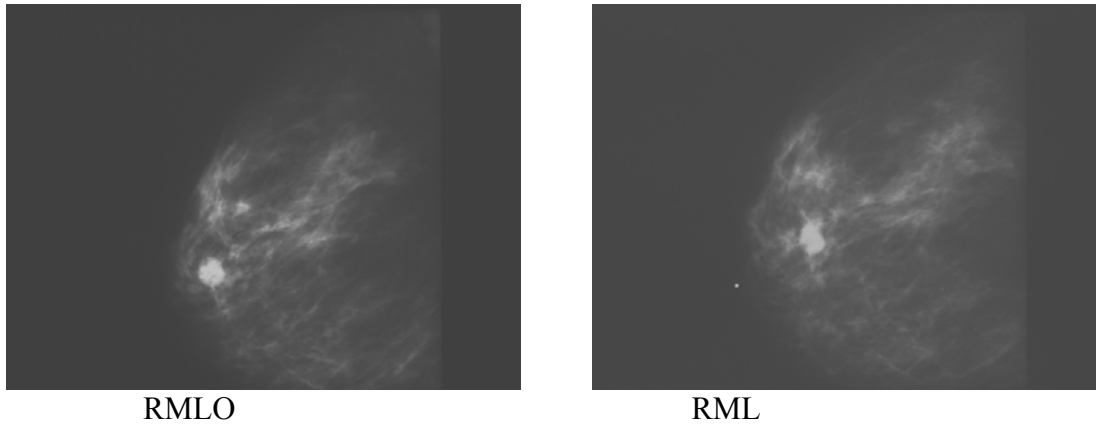


Figure 5-19. Mammogram films: (a)RMLO, (b)RML images of the patient #S9.

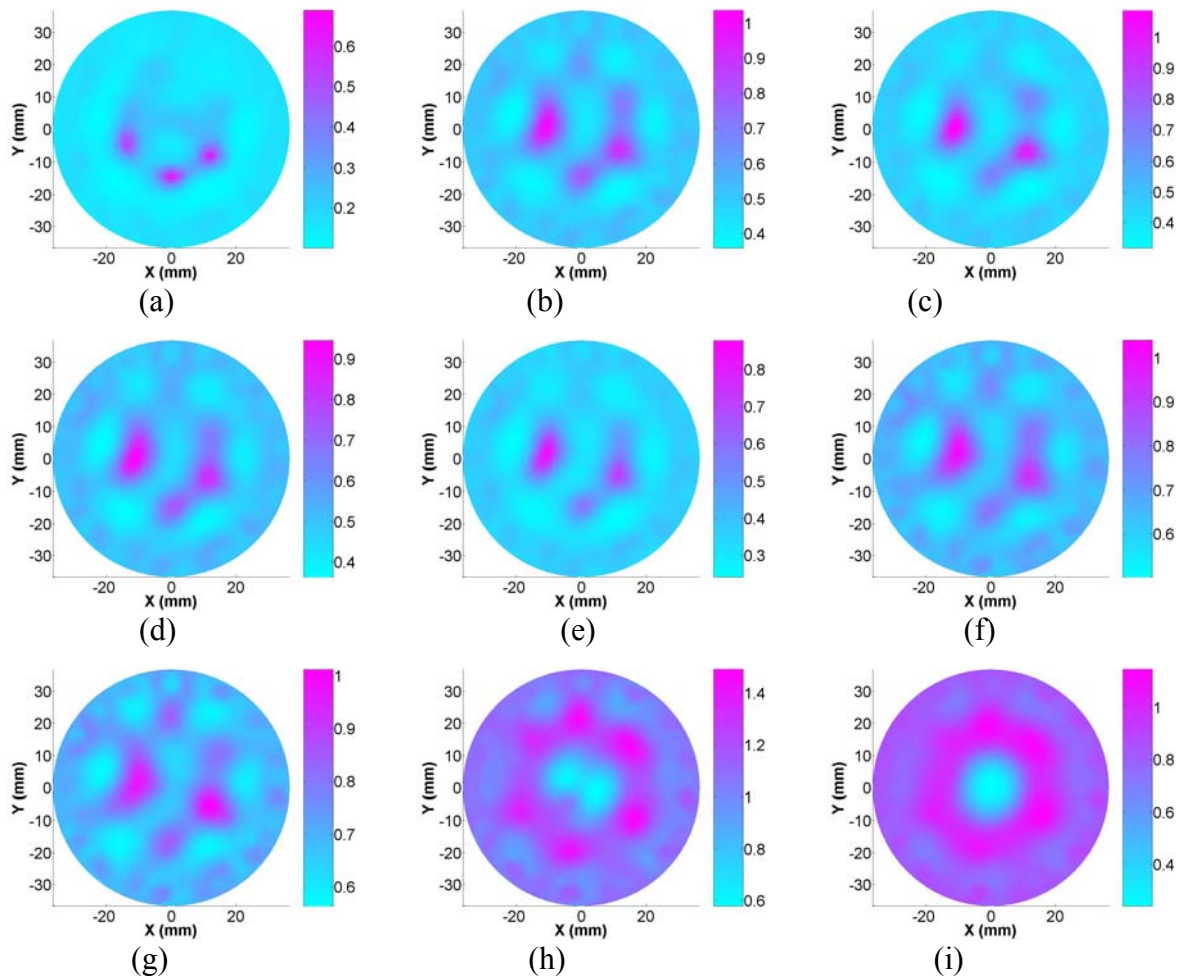


Figure 5-20. The reconstructed scattering images of the right breast for patient #S9 at 9 wavelengths from 638nm to 965nm (a to i). The color bar indicated the value of the reduced scattering coefficient in 1/mm.

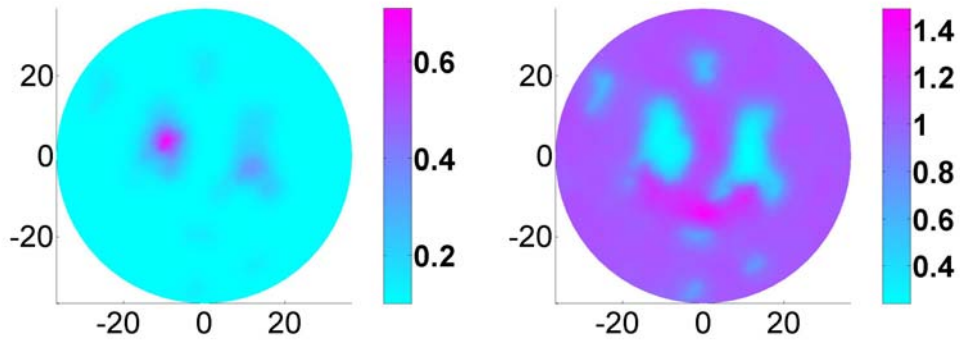


Figure 5-21. The reconstructed particle diameter image (a) and the particle volume fraction image (b) of the right breast for patient #S9. The colorful bar in (a) represents the value of particle diameters in micrometer. And the colorful bar in (b) represents the value of particle volume fraction in percentage.

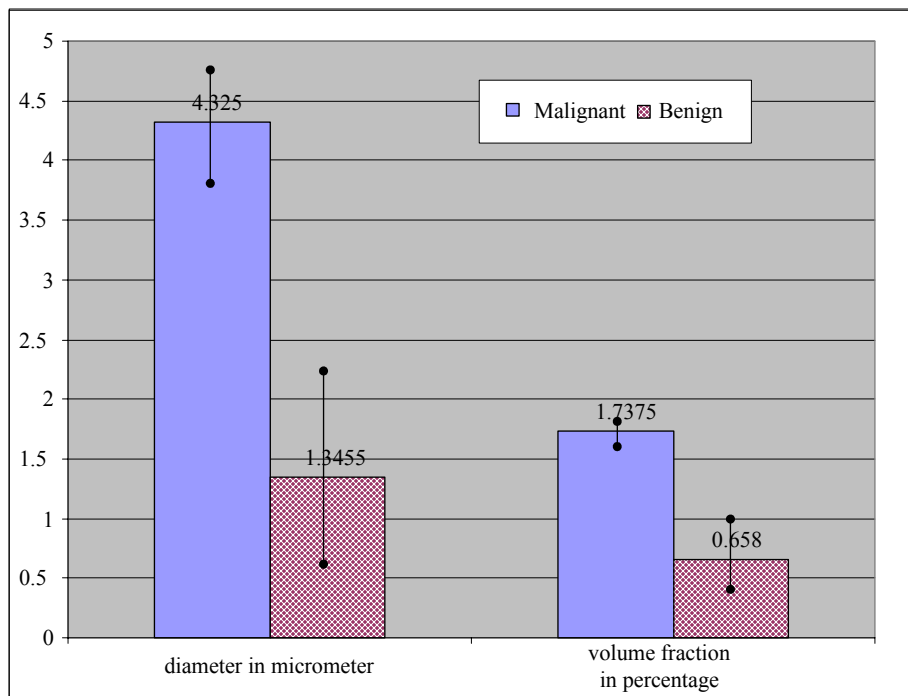


Figure 5-22. Average values of recovered mean diameter and volume fraction of scattering particles for 8 benign cases and 4 malignant cases, respectively. The deviations are shown in the corresponding bars.

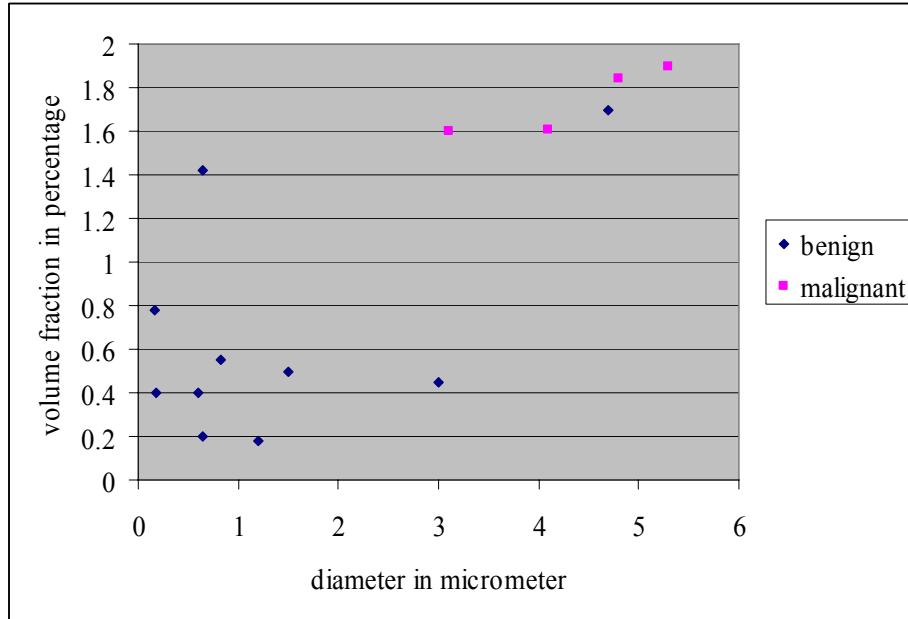
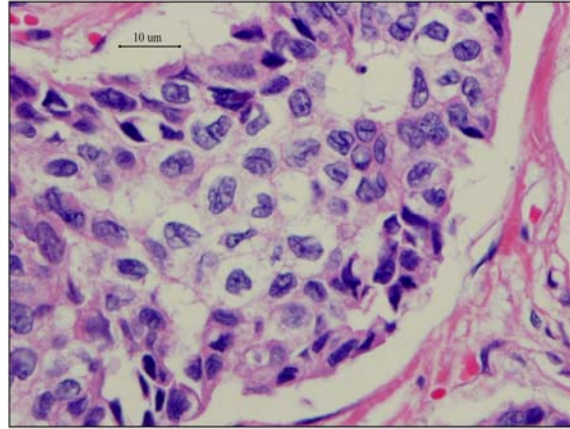
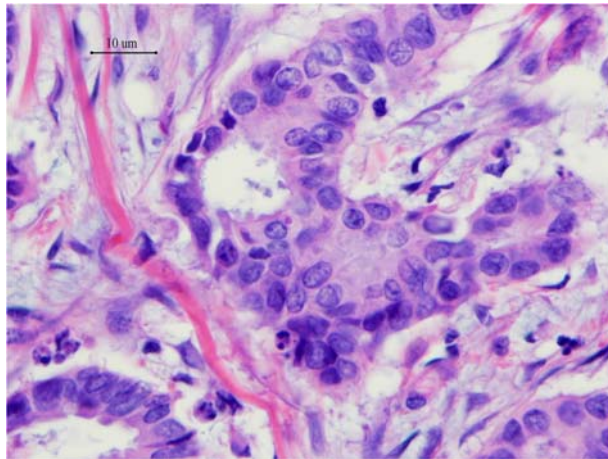


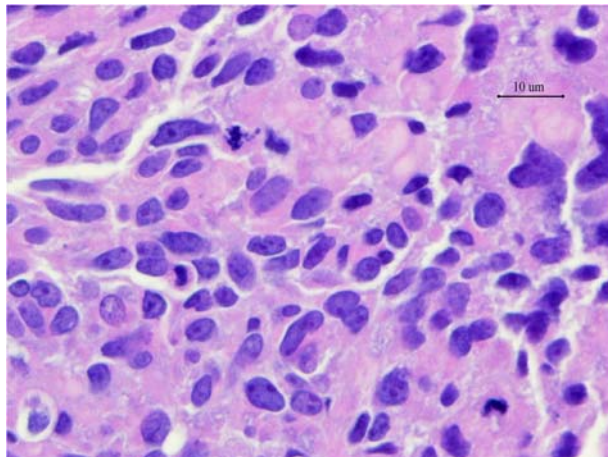
Figure 5-23. The peak value of the recovered volume fraction in the target region versus the peak value of mean diameter in the target region. The diamond dots indicate the benign cases and the square dots indicate the malignant cases.



(a)



(b)



(c)

Figure 5-24. The pathological microscopic pictures of tumor cells for patient #G1 (shown in a), #G2 (shown in b) and #G3 (shown in c).

Table 5-1 Mean diameters and volume fraction of the nucleus and nucleolus found from the microscopic pictures and those of scattering particles calculated from the reconstructed images.

cases	from microscopic pictures				reconstructed	
	nucleus		nucleolus		diameter (μm)	volume fraction
	diameter (μm)	volume fraction	diameter (μm)	volume fraction		
#G1	4.88	5.89%	0.97	0.047 %	2.18	1.32%
#G2	4.43	4.29%	0.88	0.034 %	4.14	1.70%
#G8	5.36	6.84%	1.07	0.054 %	3.65	1.61%

CHAPTER 6
SPECTRALLY CONSTRAINED IMAGING OF ABSORPTION CHROMOPHORES AND
SCATTERING CONCENTRATION

6.1 Introduction

For breast tissue, the major absorption chromophores are oxy-hemoglobin (HbO₂), deoxy-hemoglobin (Hb), water and lipid.⁸⁶ Breast tumors have been found to have higher HbO₂ and Hb concentrations than the normal tissues.¹⁵ The scattering is modeled with a simple power law, which is reasonably accurate for most cases.^{14, 55} However, the parameters in the power law do not have a clear relationship to the scatterer size and concentration inside tissues. A new model based on Mie theory was proposed for describing the scattering inside the tissues.⁶² Previously, the absorption coefficient and the reduced scattering coefficient at each wavelength were calculated with DOT and sequentially, the absorption coefficients at all wavelengths were mapped into the concentrations of HbO₂, Hb, water, and lipid using their absorption spectra. The scattering spectra were optimized to find the parameters of power law or the scatterers' size distribution and volume fractions. Recently, Corlu A., et. al., proposed to couple the absorption spectra and the power law into the CW DOT reconstruction algorithm to calculate the chromophore concentrations and the power law parameters directly using the measurements at several optimized wavelength simultaneously.⁵⁵ These authors found that measurements at optimal wavelengths yielded better separation of scattering from absorption and superior separation of one chromophore from the others.⁵⁵ Srinivasan S. et al.⁸⁷ have proven that the spectral constraints in the frequency domain DOT could provide better robustness and stability in the presence of higher level of noise and reduce cross talk between chromophore and scattering parameters.

Corlu A. et. al. found that the scattering prefactor a and the scattering power b in the power law were difficult to be separated and that the scattering power b was fixed and only the

prefactor a was reconstructed when the clinical data were processed³⁹. Instead of the power law, we used the relatively rigorous algorithm in form of an integral for scattering based on Mie theory and we found that it was even more difficult to separate the scatterers' size distribution and volume fraction when spectral constraint was applied and the chromophore concentrations, scatterers' size and volume fraction were reconstructed simultaneously. In this chapter, we presented a new method to separate the scatterers' size and volume fraction easily and the method was validated by numerical simulation and *in vivo* clinical experiments.

The remainder of this chapter was organized as follows. In section 6.2, the multi-spectral DOT reconstruction algorithms with constraint were introduced, in which there were two different methods, one was the traditional method as described in subsection 6.2.1 and the other was our new proposed method described in subsection 6.2.2. In section 6.3, several numerical simulations were performed to validate our new method. In section 6.4, two *in vivo* clinical experiments were reported and the imaging results were discussed.

6.2 Algorithms

6.2.1 Spectrally Constrained Reconstruction with the Method from Literature

In this method, we assume that the tissue absorption was contributed by L absorption chromophores with the concentration of C_l for l^{th} chromophore. And the absorption coefficient μ_a could be expressed by

$$\mu_a(\lambda) = \sum_{l=1}^L C_l \cdot \varepsilon_l(\lambda) \quad (6.1)$$

where $\varepsilon_l(\lambda)$ indicates the absorption extinction coefficient of the l^{th} chromophore at wavelength λ . Following Jiang et al.⁷⁷⁻⁷⁸, the scattering spectra were correlated with particle size distribution and concentration through the following relationship under Mie Theory:

$$\mu'_s(\lambda) = \int_0^\infty \frac{3Q_{\text{scat}}(x, n, \lambda)[1 - g(x, n, \lambda)]}{2x} \phi f(x) dx \quad (6.2)$$

where Q_{scat} was the scattering efficiency; x was the particle size; n was the refractive index of particles; ϕ was the particle concentration/volume fraction; $f(x)$ was the particle size distribution. Both Q_{scat} and g could be computed with Mie Theory⁸¹. We have assumed a Gaussian particle size distribution in this study (a priori knowledge about the mode and distribution form of the particle size were usually available in a practical situation),

$$f(x) = \frac{1}{\sqrt{2\pi}b} e^{-\frac{(x-a)^2}{2b^2}}, \text{ where } a \text{ was the average size of particles and } b \text{ was the standard}$$

deviation, which was fixed to be 1% of a in this study (the influence of b was relatively small). Instead of reconstructing μ_a and μ'_s at each wavelength and sequentially obtaining C_1 , a and ϕ using the absorption and scattering spectra, μ_a and μ'_s were substituted with C_1 , a and ϕ in the diffusion equation and C_1 , a and ϕ were reconstructed simultaneously with multi-spectral measurement data using the following equation:

$$\partial\Phi_\lambda = \mathfrak{I}_{C_1, \lambda} \cdot \partial C_1 + \dots + \mathfrak{I}_{C_M, \lambda} \cdot \partial C_M + \mathfrak{I}_{\phi, \lambda} \cdot \partial\phi + \mathfrak{I}_{a, \lambda} \cdot \partial a \quad (6.3)$$

where Φ_λ was the boundary measurements at wavelength λ , \mathfrak{I} was the Jacobian matrix and could be calculated with the following equations:

$$\begin{aligned} \mathfrak{I}_{C_1, \lambda} &= \left(\frac{\partial\Phi}{\partial\mu_a} \cdot \frac{\partial\mu_a}{\partial C_1} \right)_\lambda = \left(\mathfrak{I}_{\mu_a} \varepsilon_1 \right)_\lambda, \text{ for } 1=1\dots L \\ \mathfrak{I}_{\phi, \lambda} &= \left(\frac{\partial\Phi}{\partial\mu'_s} \cdot \frac{\partial\mu'_s}{\partial\phi} \right)_\lambda = \left(\mathfrak{I}_\kappa (-3\kappa^2) \frac{\partial\mu'_s}{\partial\phi} \right)_\lambda \\ \mathfrak{I}_{a, \lambda} &= \left(\frac{\partial\Phi}{\partial\mu'_s} \cdot \frac{\partial\mu'_s}{\partial a} \right)_\lambda = \left(\mathfrak{I}_\kappa (-3\kappa^2) \frac{\partial\mu'_s}{\partial a} \right)_\lambda \end{aligned} \quad (6.4)$$

where \mathfrak{J}_{μ_a} and \mathfrak{J}_{κ} were the Jacobian matrix at each wavelength which could be calculated with the method described by the reference [Paulsen and Jiang, 1995], κ was the diffusion coefficient.

From Eq. (6.2), we could obtain

$$\left(\frac{\partial \mu_s'}{\partial \phi} \right)_{\lambda} = \int_0^{\infty} \frac{3Q_{\text{scat}}(x, n, \lambda)[1-g(x, n, \lambda)]}{2x} \frac{1}{\sqrt{2\pi b^2}} e^{-\frac{(x-a)^2}{2b^2}} dx \quad (6.5)$$

and

$$\left(\frac{\partial \mu_s'}{\partial a} \right)_{\lambda} = \phi \frac{\partial \left(\int_0^{\infty} \frac{3Q_{\text{scat}}(x, n, \lambda)[1-g(x, n, \lambda)]}{2x} \frac{1}{\sqrt{2\pi b^2}} e^{-\frac{(x-a)^2}{2b^2}} dx \right)}{\partial a}. \quad (6.6)$$

Finally, the total system could be expressed as

$$\begin{pmatrix} \partial \Phi_{\lambda_1} \\ \partial \Phi_{\lambda_2} \\ \vdots \\ \partial \Phi_{\lambda_W} \end{pmatrix} = \begin{bmatrix} \mathfrak{J}_{C_1, \lambda_1} & \cdots & \mathfrak{J}_{C_L, \lambda_1} & \mathfrak{J}_{\phi, \lambda_1} & \mathfrak{J}_{a, \lambda_1} \\ \mathfrak{J}_{C_1, \lambda_2} & \cdots & \mathfrak{J}_{C_L, \lambda_2} & \mathfrak{J}_{\phi, \lambda_2} & \mathfrak{J}_{a, \lambda_2} \\ \vdots & \ddots & \vdots & \vdots & \vdots \\ \mathfrak{J}_{C_1, \lambda_W} & \cdots & \mathfrak{J}_{C_L, \lambda_W} & \mathfrak{J}_{\phi, \lambda_W} & \mathfrak{J}_{a, \lambda_W} \end{bmatrix} \bullet \begin{pmatrix} \partial C_1 \\ \vdots \\ \partial C_L \\ \partial \phi \\ \partial a \end{pmatrix} \quad (6.7)$$

where W was the wavelength number of measurements.

6.2.2 Spectrally Constrained Reconstruction with Scatterer's Volume Fraction Method

In this method, we assume that there were M kinds of particles with different size or diameters inside tissues. For each of them, the corresponding contributed scattering could be obtained by

$$\mu'_{sm}(\lambda) = \int_0^\infty \frac{3Q_{scat}(x, n, \lambda)[1 - g(x, n, \lambda)]}{2x} \frac{1}{\sqrt{2\pi b^2}} e^{-\frac{(x-a_m)^2}{2b^2}} dx, \text{ for } m = 1, \dots, M \quad (6.8)$$

where b was fixed to be 1% of a_m . The total scattering can be calculated by the summation

$$\mu'_s(\lambda) = \sum_{m=1}^M \phi_m \cdot \mu'_{sm}(\lambda) \quad (6.9)$$

where ϕ_m was the volume fraction of the m^{th} kind of particles. Now it was the ϕ_m and C_l needed to be reconstructed simultaneously with the following new equation

$$\partial\Phi_\lambda = \mathfrak{I}_{C_1, \lambda} \cdot \partial C_1 + \dots + \mathfrak{I}_{C_M, \lambda} \cdot \partial C_M + \mathfrak{I}_{\phi_1, \lambda} \cdot \partial \phi_1 + \dots + \mathfrak{I}_{\phi_M, \lambda} \cdot \partial \phi_M \quad (6.10)$$

where the Jacobian matrix could be obtained by

$$\begin{aligned} \mathfrak{I}_{C_l, \lambda} &= \left(\frac{\partial\Phi}{\partial\mu_a} \cdot \frac{\partial\mu_a}{\partial C_l} \right)_\lambda = \left(\mathfrak{I}_{\mu_a} \varepsilon_l \right)_\lambda, \text{ for } l = 1 \dots L \\ \mathfrak{I}_{\phi_m, \lambda} &= \left(\frac{\partial\Phi}{\partial\mu_s} \cdot \frac{\partial\mu_s}{\partial\phi_m} \right)_\lambda = \left(\mathfrak{I}_\kappa (-3\kappa^2) \mu'_{sm} \right)_\lambda, \text{ for } m = 1 \dots M \end{aligned} \quad (6.11)$$

Finally, substitute Eq. (6.1) into Eq. (6.9), the system equation at all wavelengths could be expressed as

$$\begin{pmatrix} \partial\Phi_{\lambda_1} \\ \partial\Phi_{\lambda_2} \\ \vdots \\ \partial\Phi_{\lambda_W} \end{pmatrix} = \begin{bmatrix} \mathfrak{I}_{C_1, \lambda_1} & \dots & \mathfrak{I}_{C_L, \lambda_1} & \mathfrak{I}_{\phi_1, \lambda_1} & \dots & \mathfrak{I}_{\phi_M, \lambda_1} \\ \mathfrak{I}_{C_1, \lambda_2} & \dots & \mathfrak{I}_{C_L, \lambda_2} & \mathfrak{I}_{\phi_1, \lambda_2} & \dots & \mathfrak{I}_{\phi_M, \lambda_2} \\ \vdots & \ddots & \vdots & \vdots & \ddots & \vdots \\ \mathfrak{I}_{C_1, \lambda_W} & \dots & \mathfrak{I}_{C_L, \lambda_W} & \mathfrak{I}_{\phi_1, \lambda_W} & \dots & \mathfrak{I}_{\phi_M, \lambda_W} \end{bmatrix} \cdot \begin{pmatrix} \partial C_1 \\ \vdots \\ \partial C_L \\ \partial \phi_1 \\ \vdots \\ \partial \phi_M \end{pmatrix} \quad (6.12)$$

In the above equation, the size of $\partial\Phi_{\lambda,w}$ is $M1 \times 1$, each of Jacobain matrix $\mathfrak{J}_{C_1,\lambda_1}$ and $\mathfrak{J}_{\phi_m,\lambda_m}$ had size of $M1 \times N$, and each of ∂C_1 and $\partial\phi_m$ had size of $N \times 1$, where N is the node number and $M1$ was the measurements per wavelength.

6.3 Numerical Simulations

For the following numerical simulation cases, the absorption coefficient and reduced scattering coefficient were calculated with Eq. (6.1) and Eq. (6.2) provided the given concentrations of HbO₂, Hb and water (ignored the lipid) and the given diameter and volume fraction of particles. The “experimental measurements” used for the reconstruction were calculated with the diffusion equation using the finite element method, as described in [69].

6.3.1 Reconstruction with the Method from Literature

For simulation case 1, the cylindrical background had a diameter of 50mm with an offset target of 10mm in diameter. The concentration of HbO₂, Hb and water, the diameter and the volume fraction of particles are 10 μM , 8 μM , 10 μM , 1000 nm and 0.2% in the background and 20 μM , 16 μM , 20 μM , 5000 nm and 2.0% in the target. With the reconstruction method described in section 6.2.1 and “measurements” at 5 wavelengths (673, 733, 775, 840 and 922), the reconstructed results were shown in Figure. 6-1. There was no noise added to the “measurement” data. The concentration of HbO₂, Hb and water were extracted quantitatively. But the particle diameter image and the particle volume fraction image failed to be reconstructed. In Figure. 6-1d, the volume fraction of the target was reconstructed to be 0.36%, much less than the true value 2.0%. And in Figure. 6-1e, the particle diameter of the target was found to be 900 nm, much less than the true value 5000 nm.

In the numerical simulation case 2, we assume the concentration of H₂O₂, Hb and water are same in the background and the targets and only the volume fraction and the diameter of scattering particles were reconstructed. Figs. 6-2a and 6-2b plotted the exact values of the particle volume fraction and the particle diameter for both the background and the three targets. These figures also indicated the geometry of the background and the targets. Using the reconstruction method described in section 6.2.1 and five wavelengths data (673, 733, 775, 840 and 922 nm), the reconstructed particle volume fraction image and the particle diameter image were shown in Figure. 6-2c and 6-2d, respectively. There was a significant amount of cross-talks between the reconstructed volume fraction image and diameter image, and the reconstructed values in the targets were far away from the true values.

6.3.2 Reconstruction with the Scattering Volume Fraction Method

In the numerical simulation case 3, the absorption coefficients at all wavelengths were set to be 0.005mm^{-1} and only the particle size volume fractions were reconstructed. The geometry of the background and the three targets were shown in Figure. 6-3a. There were three kinds of particles (150 nm, 1000 nm, 6000 nm in diameters) in both the background and the three targets. The exact particle volume fractions for the background and the targets were shown in Table 6-1. The particle size volume fraction images were reconstructed with the method described in subsection 6.2.2. And the reconstructed volume fraction images for the particles with diameters of 150 nm, 1000 nm and 6000 nm were shown in Figs. 6-4a, 6-4b and 6-4c by using “measurements” at 8 wavelengths and in Figs. 6-4d, 6-4e and 6-4f by using “measurements” at 20 wavelengths, respectively. The 8 wavelengths were 638, 673, 690, 733, 775, 808, 840 and 915 nm and the 20 wavelengths were distributed uniformly in the range from 600 nm to 900 nm. With 8 wavelengths, the errors of extracted value of the volume fraction were 2.0 % for target1, 10.0% for target2 and 10.0% for target3. And the reconstructed results were slightly better when

using data at 20 wavelengths. There were slight cross-talks between volume fraction images of 1000 nm particles and 6000 nm particles. That was why there was 10% error in the extracted volume fraction values in target 2 and target 3.

For the numerical simulation case 4, the geometry were shown in Figure. 6-3b and the concentrations of Hbo2, Hb and water, the volume fraction for 1000 nm particles and 6000 nm particles were shown in Table 6-2 for the background and 5 targets. With the reconstruction method described in subsection 6.2.2 and using “measurement” data at 5 wavelengths (673, 733, 775, 840 and 922 nm), the reconstructed concentration and volume fraction images were shown in Figs. 6-5a, 6-5b, 6-5c, 6-5d, 6-5e without noise added in the data and shown in Figs. 6-5f, 6-5g, 6-5h, 6-5i, 6-5j when 1.0% random noise added. These images indicate that the concentrations and the volume fractions were reconstructed quantitatively for both with and without noise. Without noise, the errors of the extracted concentration of Hbo2, Hb and water, the volume fractions of 1000 nm particles and 6000 nm particles were about 2.5%, 2.0%, 1.5%, 3.0% and 5.0%. The cross-talk between the reconstructed volume fraction images (Figs. 6-5d and 6-5e) was very slight. The added 1.0% random noise introduced artifacts into the reconstructed images, especially the water concentration image (Figure. 6-5h) and the volume fraction image of 6000nm particles (Figure. 6-5j). The noise made the cross-talk between the volume fraction images worse. The accuracy of the reconstructed water concentration and the reconstructed volume fraction of 6000 nm particles was reduced approximately 20% by the noise. In contrary, the reconstructed concentration images of Hbo2, Hb and the volume fraction image of 1000 nm particles were not deteriorated by the noise.

To see how the selection of $\mu'_{sm}(\lambda)$ in Eq. 6.9 affected the reconstructed image quality, numerical simulation case 5 was performed, in which we assumed that targets 4 and 5 were

composed of 150 nm and 5000 nm particles but use the $\mu'_{sm}(\lambda)$ from 1000 nm and 6000 nm particles, not from 150 nm and 5000 nm particles, in the reconstruction. The images at the bottom row in Figure. 6-5 showed the reconstructed results. The water concentration image and the 6000 nm particles volume fraction image were deteriorated by the intentional wrong-selection of particle diameters in the reconstruction but they were reconstructed quantitatively although there were some artifacts. The concentration images of Hbo2 and Hb and the volume fraction image of 1000 nm particles were reconstructed quantitatively.

In sum, the numerical simulation results validated the new method, the scattering volume fraction method, with which both the absorption chromophore concentrations and the volume fraction of the scattering particles were reconstructed successfully and simultaneously while the water concentration image was sensitive to the noise.

6.4 In-Vivo Imaging with the Molar Absorption from References

The experimental system for the clinical study and the system calibration were described in reference [40, 71]. The measurement data at five wavelengths of 673, 733, 775, 840 and 922 nm were used for the image reconstructions. Here we assumed that the absorption chromophores were Hbo2, Hb and water and the scattering particle diameters were 1000 nm (simulating the small particles such as mitochondria) and 6000nm (simulating the larger particles such as nucleus) in the breast tissue. For the clinical studies here, the concentrations of Hbo2, Hb and water, the volume fractions of 1000 nm and 6000 nm diameter particles were reconstructed using the method described in section 6.2.2.

The first patient, with patient Id #S28, was 58 years old female with a biopsy confirmed multicentric invasive ductal carcinoma at 3 and 9 o'clock. The second patient, with patient ID #S5, was a 69 years old female with a benign nodule at 8 o'clock. The second patient

mammogram films and report were discussed in subsection 5.2.2.2. The concentration images of Hbo2, Hb and water, and the volume fraction images of 1000 nm particles and 6000 nm particles were shown in Figs. 6-6a, 6-6b, 6-6c, 6-6d and 6-6e for patient1 and in Figs. 6-6f, 6-6g, 6-6h, 6-6i and 6-6j for patient2, respectively. For patient1, the Hbo2 and water concentration images had two targets at correct positions but Hb concentration image only identified one target around 3 o'clock. For patient2, the Hbo2 and Hb concentration images identified the target at the correct position but water concentration image failed to detect the target and only got a circular artifacts. Both of the volume fraction images for patient 1 obtained the targets at 3 and 9 o'clock, as shown in Figs. 6-6d and 6-6e. For patient 2, the target around 8 o'clock was obvious in both of the reconstructed volume fraction images. Consistent with the numerical simulation case 4, the water concentration image was vulnerable to noise and there was a circular artifact, as shown in Figs. 6-6c and 6-6h. And the volume fraction image of 6000 nm particles had more artifact than the volume fraction image of 1000 nm particles. The absolute values of the volume fraction of 1000 nm and 6000 nm particles in the target for patient 1 (malignant tumor) were found to be 1.6% and 4.4%, larger than 0.98% and 2.2% for patient 2 (benign tumor). The ratio of the extracted volume fraction of 1000 nm particles to that of 6000 nm particles for patient1 was calculated to be 2.75, larger than 2.24 for patient 2.

In sum, for both clinical cases, both the absorption chromophore concentration images except the water concentration image and scattering particle volume fraction images were reconstructed successfully and the tumors were identified in the correction locations.

6.5 Measurements of Molar Extinction Coefficients

In the above sections, the molar extinction coefficients of Hbo2, Hb and water, used for absorption chromophores' reconstruction, were from the literature⁸⁸⁻⁹². However, the system measurement mismatches resulted in the errors and were the possible reasons why the water

images failed to be reconstructed. The molar extinction coefficients' measurements were necessary for accurate chromophore imaging. Here we used the human being whole blood (Innovative Research Inc, Southfield, MI 48034, USA) solution with blood concentration of 0.6%, 0.8% and 1.0% and Intralipid concentration 1.0% to measure the molar extinction coefficients of HbO₂ and Hb. The whole blood hemoglobin concentration was measured to be 11.3 g/dL using a hemoglobin meter. The hemoglobin concentrations of 0.6%, 0.8% and 1.0% blood solution were calculated to be 45.8 μ M, 61.7 μ M and 76.33 μ M, respectively. The water absorption coefficients at each wavelength were measured using the 1.0% Intralipid solution. The top part of the home-made liquid solution container was the top part of a drinking water bottle, which helded the bottom part made of Cling Wrap (The glad products company, Oakland, CA 94612), as shown in Figure. 6-7. The liquid solution container was hung in the center of the ring with a mechanical frame and the fiber probes touched the bottom part of the container, as shown in Figure. 6-8. The Cling Wrap was so thin that its interferences on light propagation could be ignored.

When the liquid solution was exposed to air, the hemoglobin was totally oxygenized. The absorption chromophores were HbO₂ and water. After measurements, several grams yeasts were put into the solution and the container was sealed. One hour later, the oxy-hemoglobin was deoxygenized. The absorption chromophores became Hb and water. Then measurements at each wavelength were made for molar absorption calculation of Hb.

Measurements for 1.0% Intralipid solution, HbO₂ and Hb solutions were processed by the algorithms described before. Briefly, for the data at each wavelength of each liquid solution, a preprocessing method was utilized for searching the initial values (boundary coefficient α , optical properties μ_a and μ_s'). The boundary coefficient α for all the data were selected as 0.49

for consistency. With the initial values, the reconstructions of absorption and scattering coefficients were performed. The average values of the reconstructed absorption coefficients of all finite element nodes were the solution absorption coefficients at the corresponding wavelengths. The tenth wavelength measurements were ignored due to its lowest SNR.

The water absorption was calculated at first. The measurement results (the diamond line) were shown in Figure. 6-9. At wavelengths shorter than 700nm, the measured absorption values were much larger than the values from the literature (indicated by the triangle line). At the longer wavelengths, the measured absorption coefficients were close to the values from the literature.⁸⁸⁻

89

The molar extinction coefficients of Hbo2 and Hb were calculated by the following equation:

$$\varepsilon_M(\lambda) = (\mu_{\text{soltution}}(\lambda) - \mu_{\text{water}}(\lambda)) / C \quad (6.13)$$

where $\varepsilon_M(\lambda)$ was the molar extinction coefficient of Hbo2 or Hb in unit of 1/(mm.M) at wavelength λ , $\mu_{\text{soltution}}(\lambda)$ was the average value of the reconstructed absorption coefficients of Hbo2 or Hb solution at wavelength λ in unit of 1/mm, $\mu_{\text{water}}(\lambda)$ was the average value of the reconstructed absorption coefficients of water at wavelength λ in unit of 1/mm and C was the molar concentration of the Hbo2 or Hb in unit of M. The measured molar extinction coefficients of Hbo2 and Hb from the solution of three different concentrations were shown in Figure. 6-10 and Figure. 6-11, respectively. The solid line indicates the values from the reference [90-92].

For the Hbo2, the measured molar absorptions at shorter wavelengths were the same as the values from the references, while the largest deviation of the measured value at the longer wavelengths from the reference value was about 25%. From Figure. 6-11, one could see that the measured molar absorptions at shorter wavelengths were 2 to 3 times smaller than the values

from literature. At longer wavelengths, the measured values were close to the values from literature. The measurements for the solutions with different concentrations were very consistent. Finally, the average values of the measured molar absorptions at three different concentrations were adopted for further image reconstructions.

6.6 Phantom Experiments

Four cases of phantom experiments were performed to evaluate the measured water absorption coefficients and the measured molar extinction coefficients of Hbo2 and Hb. The background of the phantom was made of 0.5% human blood, saline water as absorption chromophores, 1.0% Intralipid as scatterers and 1% agar used to solidify the cylindrical phantom with diameter of 50 mm. An offset through hole with diameter of 9mm was drilled to hold a very thin glass tube, inside which the target liquid solution for each case was put. The target liquid solution was composed of 1.0% Intralipid, saline water and human blood with concentrations of 1.5%, 1.25%, 1.0% and 0.75% for cases 1-4. The blood solution with concentrations of 1.5%, 1.25%, 1.0% and 0.75% was calculated to have hemoglobin concentrations of 114.5 μ M,, 95.41 μ M, 76.33 μ M and 57.25 μ M, respectively.

The total hemoglobin concentration C_{HbT} was defined as the sum of the concentrations of Hbo2 and Hb. And oxygen saturation was referred to as the ratio of C_{Hbo2} to C_{HbT} , where C_{Hbo2} represented the concentration of Hbo2. Using the measured molar extinction coefficient spectra of Hbo2 and Hb, the measured water absorption spectra and the algorithm described in section 6.2.2, the reconstructed images of total hemoglobin concentration, oxygen saturation, the water concentration and scattering particle volume fraction for the 4 phantom experimental cases were shown in Figure. 6-12. Only one scattering particle size was assumed. So there was one particle volume fraction ϕ image for each case, as shown in Figs. 16m-p. Figs. 6-12a-d plotted the

images of C_{HbT} for cases 1-4. The maximum values in the target were found to be 111.0 μM , 89.0 μM , 80.5 μM and 55.5 μM and the relative errors were calculated to be 3.9%, 6.8%, 5.4% and 3.1% for cases 1-4, respectively. The oxygen saturation images, the water concentration images and the volume fraction images for 4 cases were plotted in the second row, third row and fourth row in Figure. 6-12. The exact value of oxygen saturation was 1.0 or 100% since the blood solution was exposed to the air. The water concentration was about 99% and the volume fraction of scattering particles was set to be 1.0%. The oxygen saturation images were deteriorated by the boundary artifacts. The scattering particle volume fraction images were also deteriorated by artifacts located in the image center. The accuracy of the reconstructed water concentration images were worse compared with other images.

In sum, four cases of phantom experiments with different total hemoglobin concentrations in the target were performed. The reconstructed images demonstrated that the total hemoglobin concentrations were extracted accurately, while the oxygen saturation images were deteriorated by the boundary artifacts.

6.7 In-Vivo Imaging with the Measured Molar Extinction Coefficients

In this section, five clinical cases were studied and the clinical experimental data were processed using the measured molar extinction coefficient spectra of HbO₂ and Hb, the measured water absorption spectra and three different reconstruction methods described in the following paragraphs.

In method 1, we assume that the scattering inside the breast tissues were homogeneous and the scattering coefficients at each wavelength were selected from the preprocessing method described in section 3.2 and the scattering coefficient at each wavelength was fixed as initial values. Only the concentrations of absorption chromophores HbO₂, Hb and water were reconstructed. The system equation 6.12 is modified to be

$$\begin{pmatrix} \partial\Phi_{\lambda_1} \\ \partial\Phi_{\lambda_2} \\ \vdots \\ \partial\Phi_{\lambda_W} \end{pmatrix} = \begin{pmatrix} \mathfrak{S}_{C_1,\lambda_1} & \cdots & \mathfrak{S}_{C_L,\lambda_1} \\ \mathfrak{S}_{C_1,\lambda_2} & \cdots & \mathfrak{S}_{C_L,\lambda_2} \\ \vdots & \ddots & \vdots \\ \mathfrak{S}_{C_1,\lambda_W} & \cdots & \mathfrak{S}_{C_L,\lambda_W} \end{pmatrix} \begin{pmatrix} \partial C_1 \\ \vdots \\ \partial C_L \end{pmatrix} \quad (6.14)$$

In method 2, we assume that the scattering inside the breast tissues were uniform homogeneous as well. But the uniform scattering coefficient at each wavelength, only one value for all the nodes at one wavelength, was updated as the absorption chromophores Hb_{o2}, Hb and water concentrations at each node were updated in the reconstruction procedure. The system equation was modified to be

$$\begin{pmatrix} \partial\Phi_{\lambda_1} \\ \partial\Phi_{\lambda_2} \\ \vdots \\ \partial\Phi_{\lambda_W} \end{pmatrix} = \begin{pmatrix} \mathfrak{S}_{C_1,\lambda_1} & \cdots & \mathfrak{S}_{C_L,\lambda_1} & \sum_{i=1}^N \mathfrak{S}_{D_i,\lambda_1} & 0 & 0 & 0 \\ \mathfrak{S}_{C_1,\lambda_2} & \cdots & \mathfrak{S}_{C_L,\lambda_2} & 0 & \sum_{i=1}^N \mathfrak{S}_{D_i,\lambda_2} & 0 & 0 \\ \vdots & \ddots & \vdots & \vdots & \vdots & \vdots & \vdots \\ \mathfrak{S}_{C_1,\lambda_W} & \cdots & \mathfrak{S}_{C_L,\lambda_W} & 0 & 0 & 0 & \sum_{i=1}^N \mathfrak{S}_{D_i,\lambda_W} \end{pmatrix} \begin{pmatrix} \partial C_1 \\ \vdots \\ \partial C_L \\ \partial D_0(\lambda_1) \\ \partial D_0(\lambda_2) \\ \vdots \\ \partial D_0(\lambda_W) \end{pmatrix} \quad (6.15)$$

where $D_0(\lambda_W)$ was the diffusion coefficient initial value at wavelength λ_W and was updated

each iteration, $\sum_{i=1}^N \mathfrak{J}_{D_i, \lambda_W}$ was the summation of N Jacobian vectors $\mathfrak{J}_{D_i, \lambda_W}$ at wavelength

λ_W , ∂C_L was a vector with size of $N \times 1$ and $\partial D_0(\lambda_W)$ was a scalar.

In method 3, we assume that there was only one kind of scattering particles and the scattering spectra were calculated with equation 6.8. Please see the detailed description in subsection 6.2.2. The system equation was written as

$$\begin{pmatrix} \partial \Phi_{\lambda_1} \\ \partial \Phi_{\lambda_2} \\ \vdots \\ \partial \Phi_{\lambda_W} \end{pmatrix} = \begin{bmatrix} \mathfrak{J}_{C_1, \lambda_1} & \cdots & \mathfrak{J}_{C_L, \lambda_1} & \mathfrak{J}_{\phi_1, \lambda_1} \\ \mathfrak{J}_{C_1, \lambda_2} & \cdots & \mathfrak{J}_{C_L, \lambda_2} & \mathfrak{J}_{\phi_1, \lambda_2} \\ \vdots & \ddots & \vdots & \vdots \\ \mathfrak{J}_{C_1, \lambda_W} & \cdots & \mathfrak{J}_{C_L, \lambda_W} & \mathfrak{J}_{\phi_1, \lambda_W} \end{bmatrix} \bullet \begin{pmatrix} \partial C_1 \\ \vdots \\ \partial C_L \\ \partial \phi_1 \end{pmatrix} \quad (6.16)$$

where both ∂C_L and $\partial \phi_1$ are vector with size of $N \times 1$.

CASE S5. The patient, with ID #S5, was a 69 years old female with a benign nodule at 8 o'clock and is the second patient discussed in section 6.4. Her mammogram films and report were discussed in subsection 5.2.2.2. With the measured molar extinction coefficient spectra of Hbo2, Hb and water absorption spectra, the reconstructed absorption chromophore concentration images (a, d, g for Hbo2 concentrations in μM , b, e, h for Hb concentrations in μM and c, f, I for water concentration in percentage) and scatterers' volume fraction image in percentage (j) were shown in Figure. 6-13, using method 1 (1st row), method 2 (2nd row) and method 3 (3rd row). With the molar extinction coefficient spectra of Hbo2, Hb and the water absorption spectra from literature, the reconstructed images of Hbo2, Hb concentrations and water concentration were shown in Figure. 6-14.

When the molar extinction coefficients from literature were used, the reconstructed water concentration images (Figure. 6-14c with method 1, Figure. 6-14.f with method 2) had maximum value larger than 100%. And the Hb concentration images (Figure. 6-14b with method 1, Figure. 6-14e with method 2) had more artifacts than the Hb concentration images (Figure. 6-13b with method 1, Figure. 6-13e with method 2) reconstructed with the measured extinction coefficient spectra. The measured molar extinction coefficient spectra utilization improved the reconstructed image quality substantially.

In Figure. 6-13, with all three methods, the target was able to be detected in each of concentration images and the scattering particle volume fraction image. With method 1, the reconstructed Hbo2, Hb and water concentrations shown in Figs. 6-13a, 6-13b and 6-13c were larger than the concentrations reconstructed with method 2 shown in Figs. 6-13d, 6-13e and 6-13f. Especially the Hbo2 concentration reconstructed with method 1 was almost 2 times larger than that reconstructed with method 2. Compared with method 2 and method 3, the reconstructed Hbo2 and Hb concentrations were very close. But the water concentration (Figure. 6-13i) with method 3 was two times less than the water concentration (Figure. 6-13f) reconstructed with method 2.

CASE S7. The mammogram films and report for patient S7 were discussed in subsection 5.2.2.2. Using the measured molar extinction coefficient spectra of Hbo2, Hb and the measured water absorption spectra, the reconstructed concentration images of Hbo2 (Figs. 6-15a, d, g in μM), Hb (Figs. 6-15b, e, h in μM) and water (Figs. 6-15c, f, I in percentage) were shown in Figure. 6-15 with method 1 (1st row), method 2 (2nd row) and method 3 (3rd row) for clinical case S7. Figure. 6-16 plotted the concentration images with method 1 (1st row) and method 2 (2nd row) using the molar extinction coefficient spectra from literature. When the molar extinction

coefficient spectra from literature were used, the reconstructed water concentrations (shown in Figs. 6-16c and 6-16f) were larger than 100% and the reconstructed HbO₂ concentrations (shown in Figs. 6-16a and 6-16d) were almost two times larger than the HbO₂ concentrations (shown in Figs. 6-15a and 6-15d) reconstructed using measured absorption spectra. The detected target in the images reconstructed with method 2 using the absorption spectra from reference was shifted to the image center, as shown in Figs. 6-16d, e, f. One could see that the measured absorption spectra utilization improve the reconstructed image quality substantially as well.

As shown in Figure. 6-15, the concentration images reconstructed with method 1 and method 2 were similar in terms of the target position and the concentration values. When method 3 was applied, the concentration images of HbO₂ and Hb were similar to the images extracted with other two methods. But the water concentration was much less than that extracted with method 1 and 2.

CASE S28. Figure. 6-17 plotted the reconstructed chromophore concentration images (Figs. 6-17a-6-17i) and the scattering particle volume fraction image (Figs. 6-17j) with method 1 (1st row), method 2 (2nd row) and method 3 (3rd row) using the measured extinction coefficient spectra for clinical case S28. With method 1, the target in Hb concentration image (Figure. 6-17b) was shifted to the image center and the water concentration image (Figure. 6-17c) failed to detect the target and was dominated by the boundary artifacts. With method 3, the water concentration image (Figure. 6-17i) also failed to detect the target and dominated by the boundary artifacts. With method 2, it was easy to see all the reconstructed concentration images identified the target successfully.

CASE G1. The mammogram films and report for patient case G1 are discussed in subsection 5.2.2.1. Figure. 6-17 plotted the reconstructed chromophore concentration images

(Figs. 6-18a-6-18i) and the scattering particle volume fraction image (Figs. 6-18j) with method 1 (1st row), method 2 (2nd row) and method 3 (3rd row) using the measured extinction coefficient spectra for clinical case G1. The reconstructed concentration images with method 1 (Figs. 6-18a-c) and method 2 (Figure. 6-18d-f) were similar in terms of target locations, concentration values and artifacts. With method 3, the reconstructed Hbo2 concentration image (Figure. 6-18g) and water concentration image (6-18i) have a little bit more artifacts than the images (Figs. 6-18a, c, d and f) extracted with other two methods.

CASE G14. Figure. 6-18 plots the reconstructed chromophore concentration images (Figs. 6-19a-6-19i) and the scattering particle volume fraction image (Figs. 6-19j) with method 1 (1st row), method 2 (2nd row) and method 3 (3rd row) using the measured molar extinction coefficient spectra for clinical case G14. With all three methods, the reconstructed concentration images and scattering particle volume fraction identified the target successfully, while the reconstructed images with method 3 (Figs. 6-19g and 6-19i) had a little bit more artifacts than the images extracted with other two methods.

In sum, 5 clinical cases are studied with three methods in this section. Method 2 is best among the three methods, while all 3 methods can reconstruct the concentration images and scattering particle volume fraction image successfully. And the measured molar extinction coefficient spectra of Hbo2, Hb and the measured water absorption spectra were critical to the image reconstructions and had improved the image quality substantially.

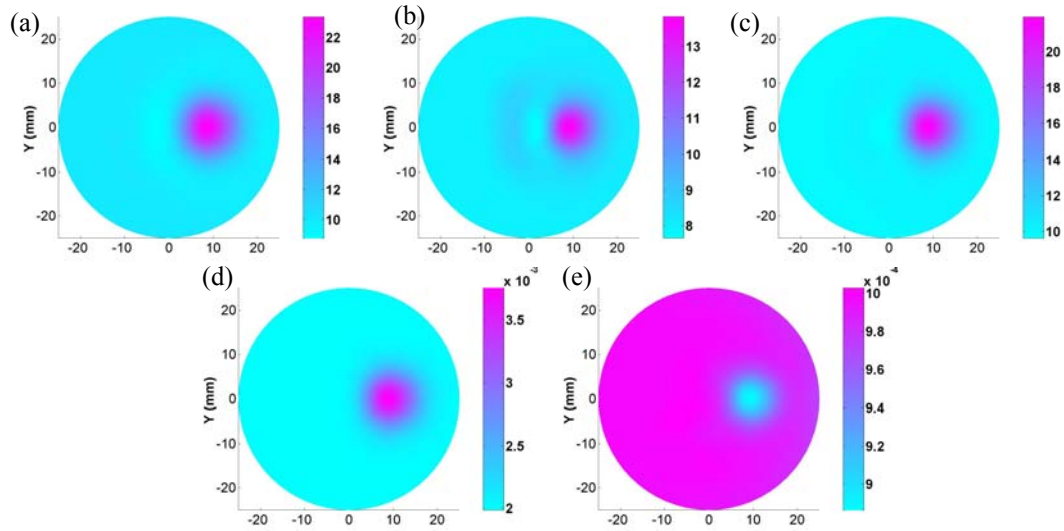


Figure 6-1. Reconstructed concentration images of Hbo2 (a), Hb (b) and water (c) and images of equivalent diameters (d) and volume fraction (e) with the method described in subsection 6.2.1.

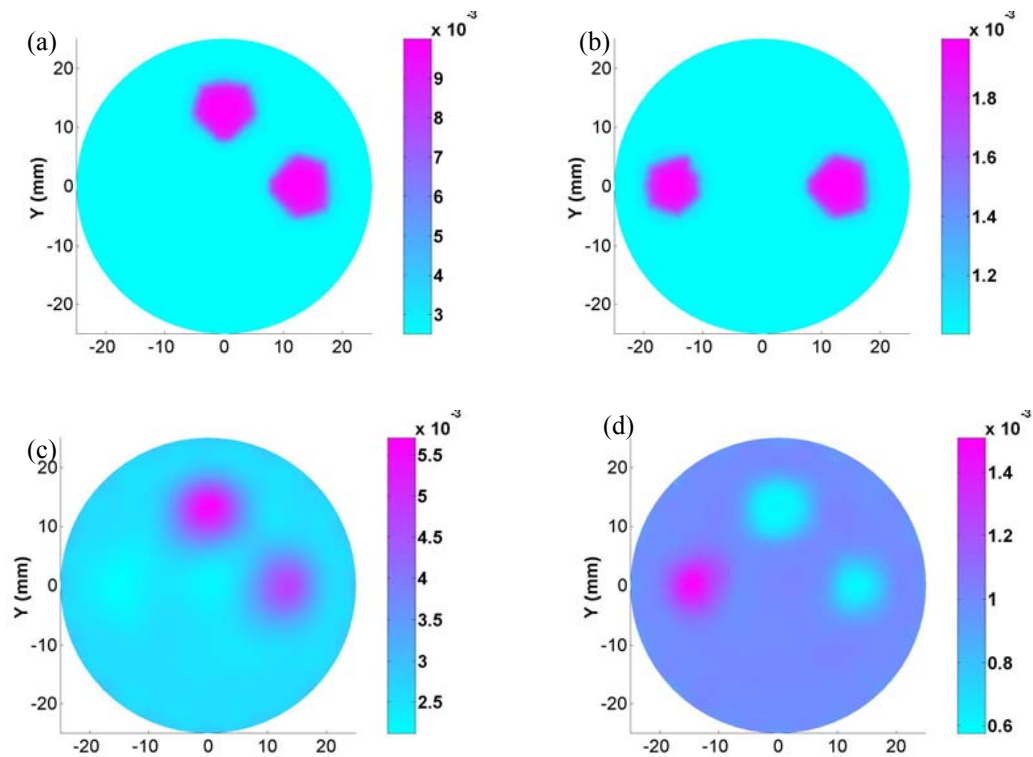


Figure 6-2. The exact images of volume fraction (a) and diameters (b) and the reconstructed images of volume fraction (c) and diameters (d) with the method described in subsection 6.2.1 when only the volume fraction and diameters are reconstructed.

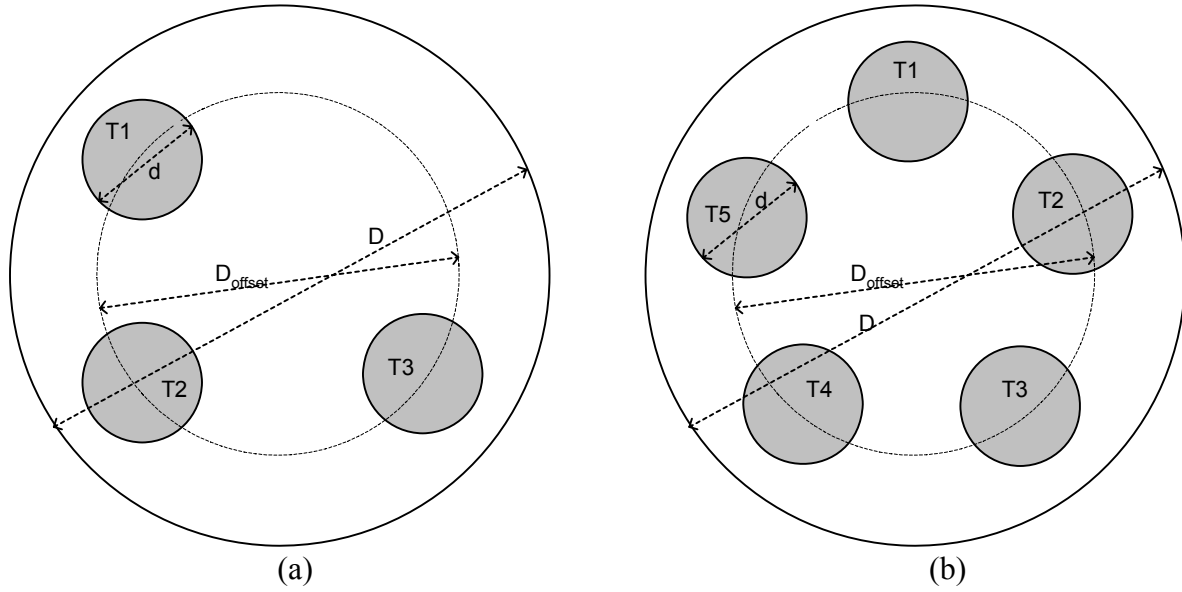


Figure 6-3. The geometry of the numerical simulations for case 3 (a) and case 4 (b), where $D=70$ mm, $d=20$ mm and $D_{\text{offset}}=40$ mm.

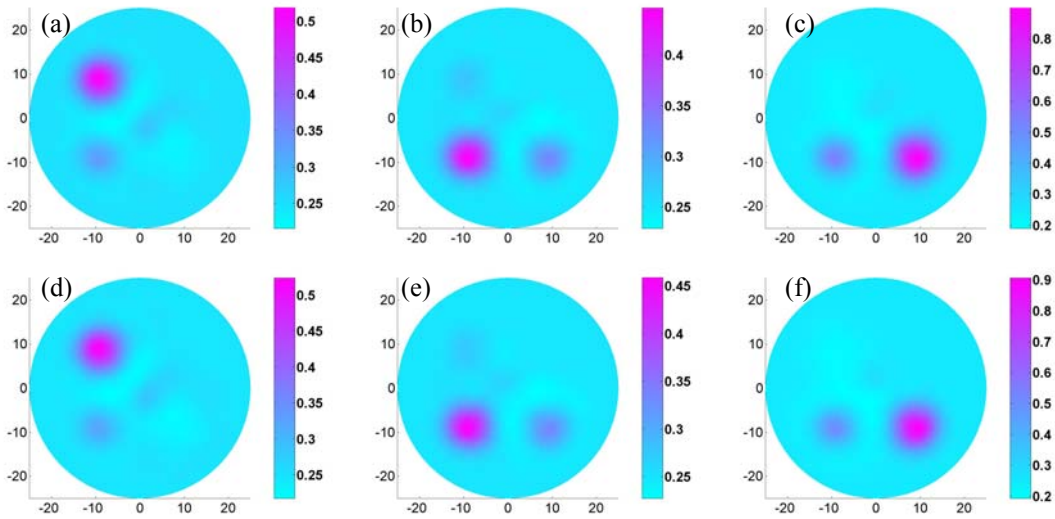


Figure 6-4. The reconstructed volume fractions images for 150 nm particles (a, d), 1000 nm particles (b, e) and 6000 nm particles (c, f) with data of 8 wavelengths (images from a to c) and with data of 20 wavelengths (from d to f) when only the volume fraction images are reconstructed using the method described in subsection 6.2.2.

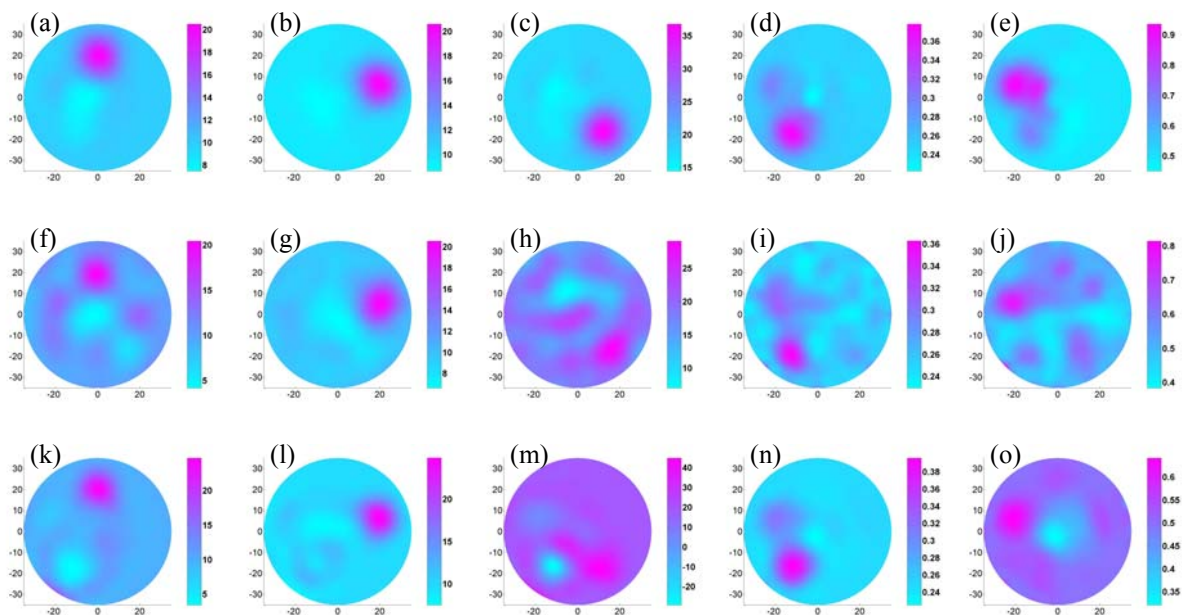


Figure 6-5. The reconstructed images of concentrations of Hbo2, Hb, water and volume fractions of 1000 nm particles and 6000 nm particles from leftmost column to rightmost column. The images at the top row and the middle row were reconstructed without adding noise in the numerical “measurement” data and with 1% random noise added, respectively. The images at the bottom row were reconstructed with intended wrong-selected sizes of particles in the targets.

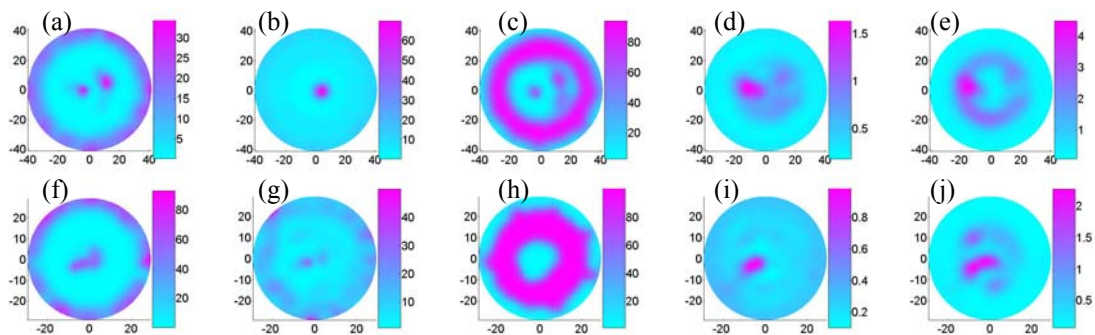


Figure 6-6. The reconstructed concentration images of Hbo2 (a, f), Hb (b, g), water (c, h) and volume fraction images of 1000 nm particles (d, i) and 6000 nm particles (e, j) for patient 1 (the top row images from a to e) and for patient 2 (the bottom row images from f to j).



Figure 6-7. The container for molar absorption measurements. The upper part is the drinking water bottle and the bottom part is composed of Cling Wrap, with 1.0% Intralipid solution inside.

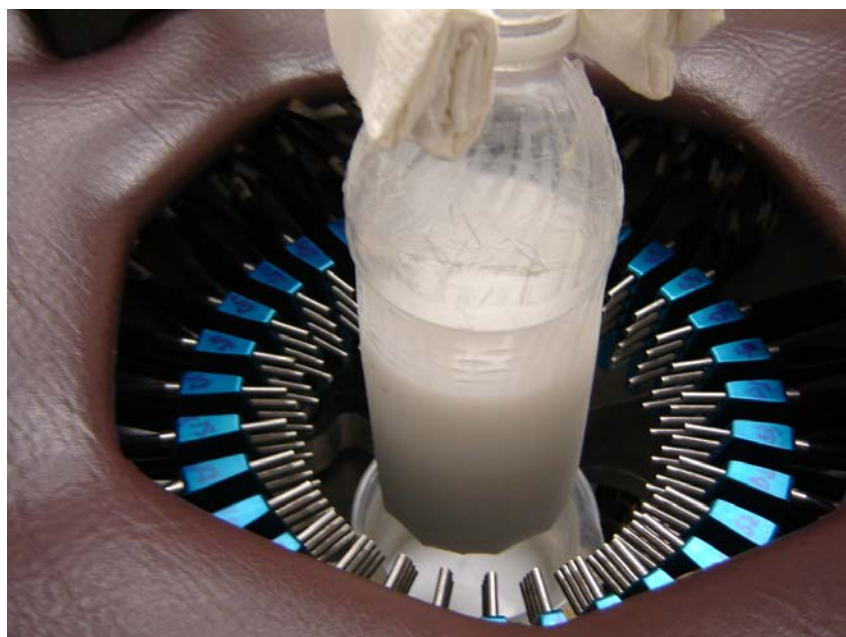


Figure 6-8. The liquid solution inside the container is ready for the measurements. The Cling Wrap contacts with fiber probes.

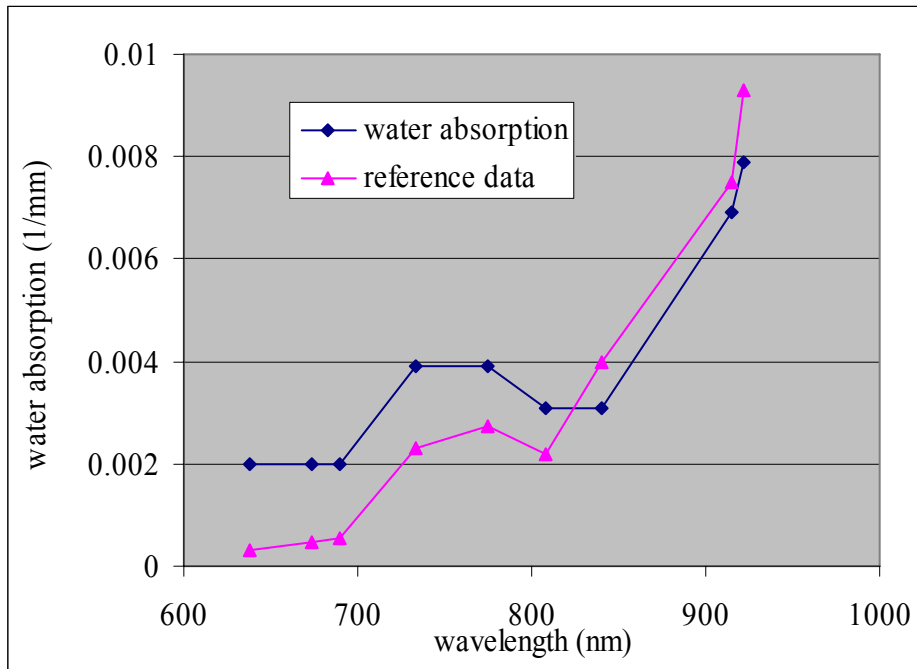


Figure 6-9. The absorption coefficients of water from the reference (triangle) and measurements of Intralipid solution (diamonds).

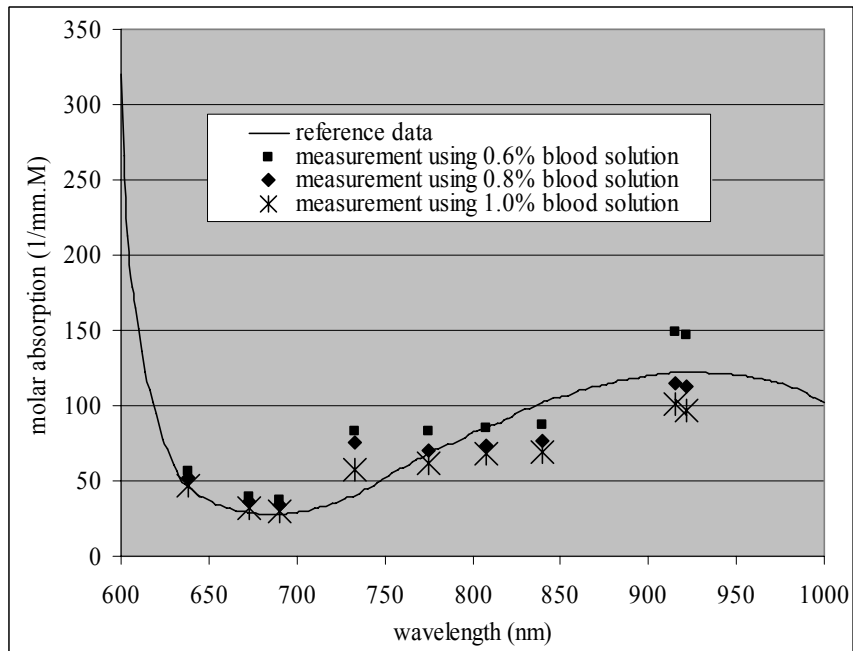


Figure 6-10. The molar absorption of oxy-hemoglobin from the reference (solid line) and measurements of blood solution with different concentrations (squares, diamonds, stars).

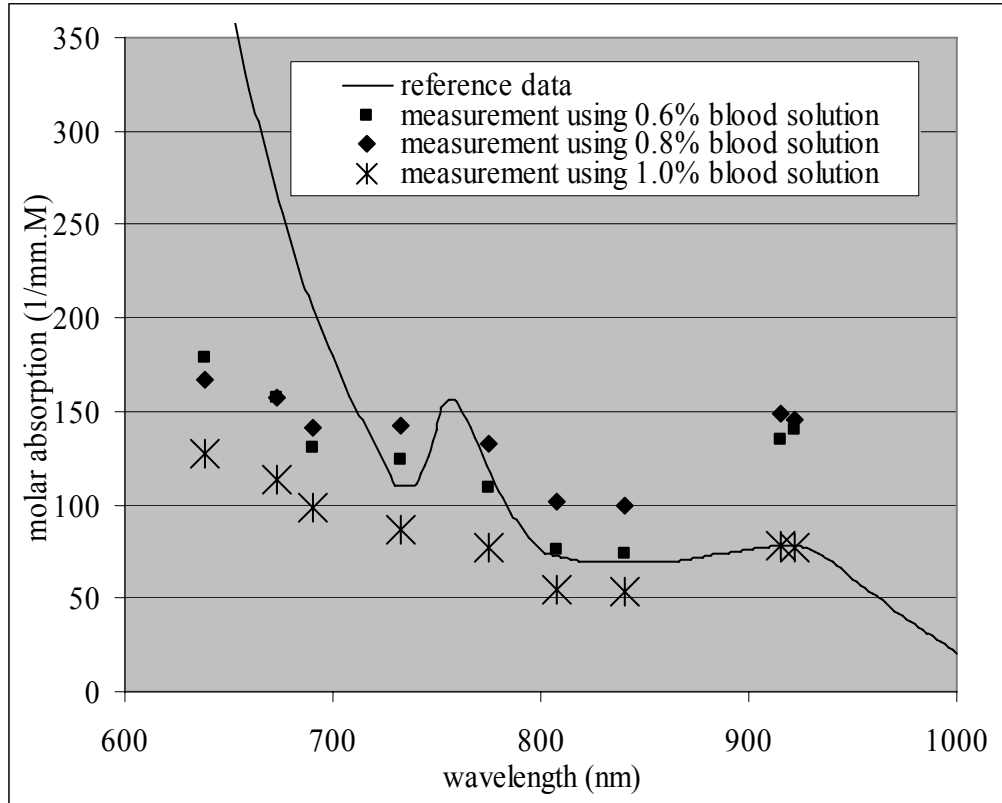


Figure 6-11. The molar absorption of deoxy-hemoglobin from the reference (solid line) and measurements of blood solution with different concentrations (squares, diamonds, stars).

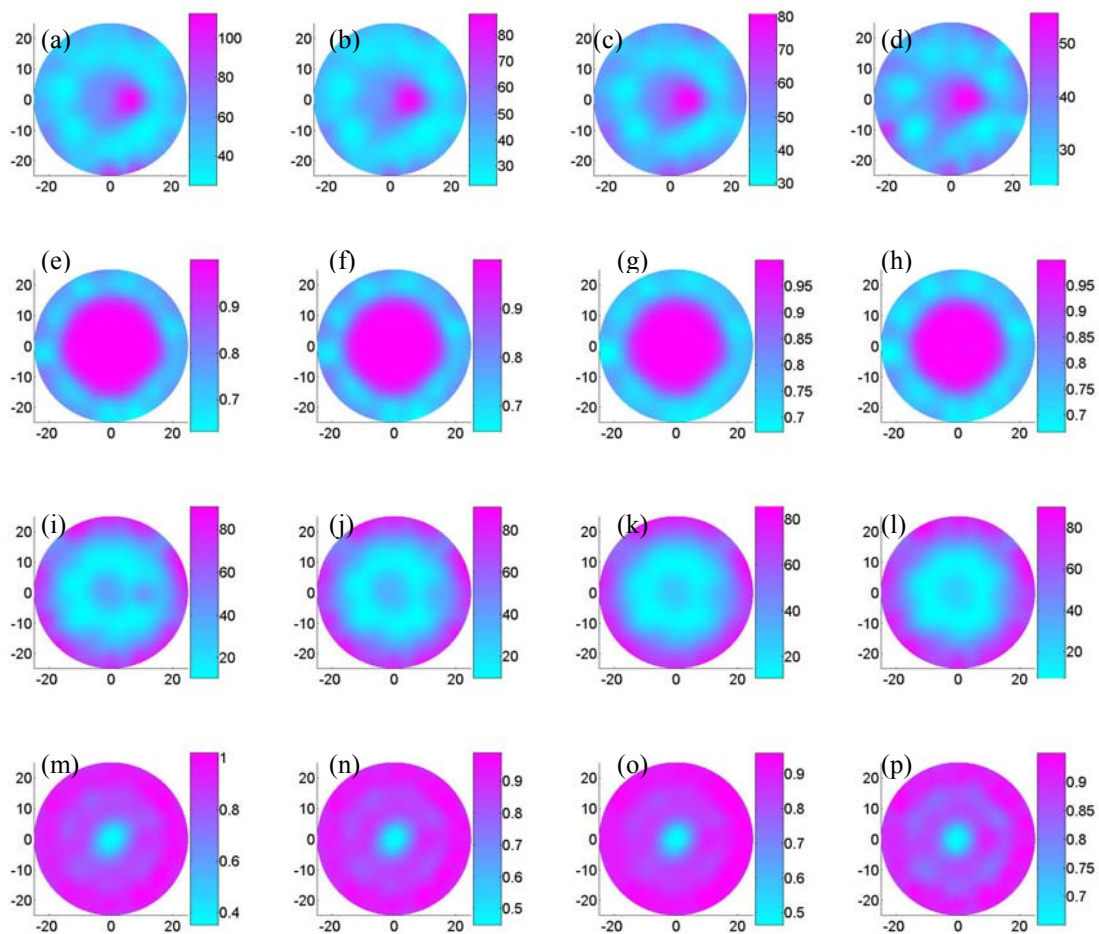


Figure 6-12. Reconstructed images of total hemoglobin concentrations (1st row) in unit of μM , oxygen saturation (2nd row), water concentration (3rd row) in percentage and scatterers volume fraction (4th row) in percentage of phantom experiments case 1 (1st column from left to right), case 2 (2nd column), case 3 (3rd column) and case 4 (4th column).

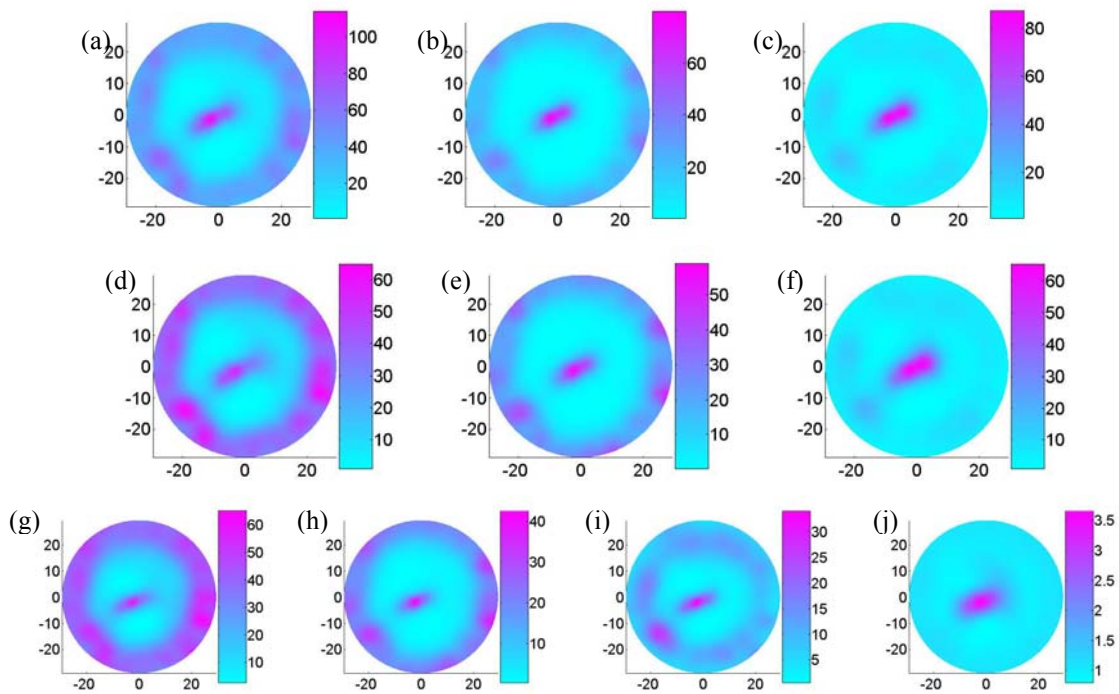


Figure 6-13. Chromophores concentration images (a, d, g for Hbo2 concentrations in μM , b, e, h for Hb concentrations in μM and c, f, I for water concentration in percentage) and scatterers' volume fraction image in percentage (j) reconstructed with the measured molar spectra, using method 1 (1st row), method 2 (2nd row) and method 3 (3rd row) for clinical case S5.

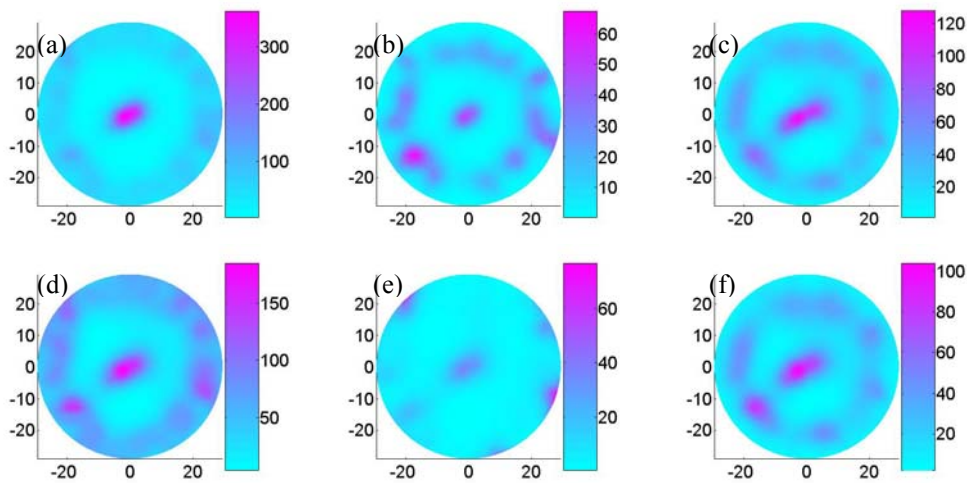


Figure 6-14. For clinical case S5, chromophores concentration images (a, d for Hbo2 concentrations in μM , b, e for Hb concentrations in μM and c, f for water concentration in percentage) reconstructed with the molar spectra from reference, using method 1 (1st row) and method 2 (2nd row) for clinical case S5.

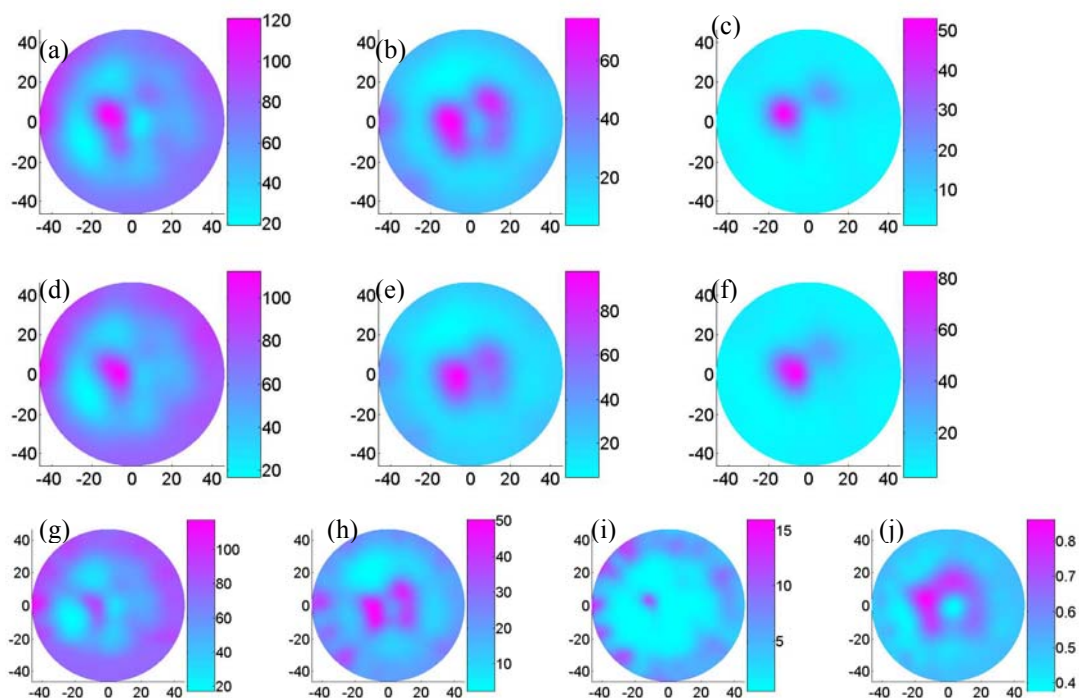


Figure 6-15. For clinical case S7, chromophores concentration images (a, d, g for HbO₂ concentrations in μM , b, e, h for Hb concentrations in μM and c, f, I for water concentration in percentage) and scatterers' volume fraction image in percentage (j) reconstructed with the measured molar spectra, using method 1 (1st row), method 2 (2nd row) and method 3 (3rd row).

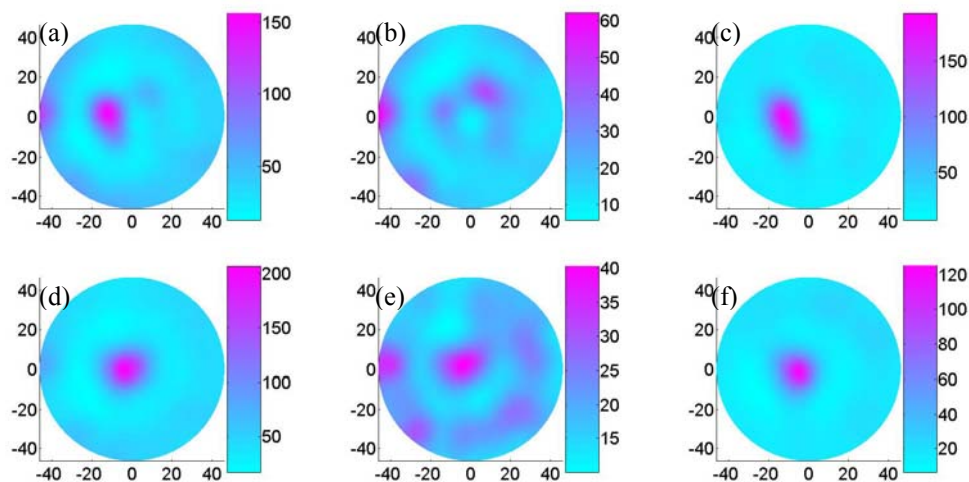


Figure 6-16. For clinical case S7, chromophores concentration images (a, d for HbO₂ concentrations in μM , b, e for Hb concentrations in μM and c, f for water concentration in percentage) reconstructed with the molar spectra from reference, using method 1 (1st row) and method 2 (2nd row).

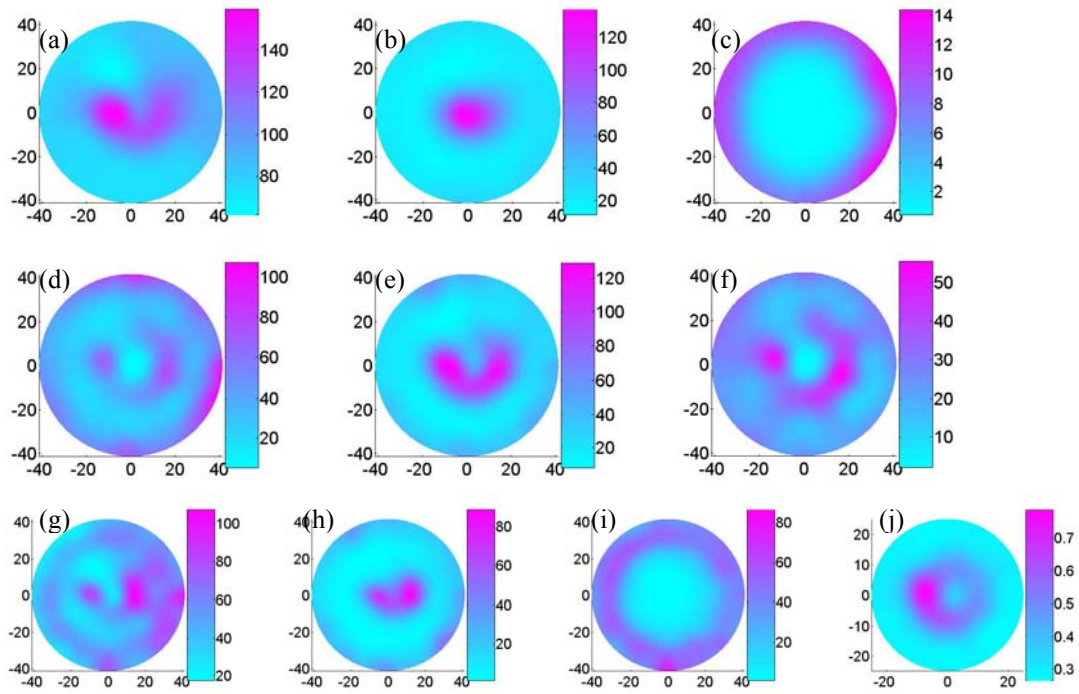


Figure 6-17. For clinical case S28, chromophores concentration images (a, d, g for HbO₂ concentrations in μM , b, e, h for Hb concentrations in μM and c, f, i for water concentration in percentage) and scatterers' volume fraction image in percentage (j) reconstructed with the measured molar spectra, using method 1 (1st row), method 2 (2nd row) and method 3 (3rd row).

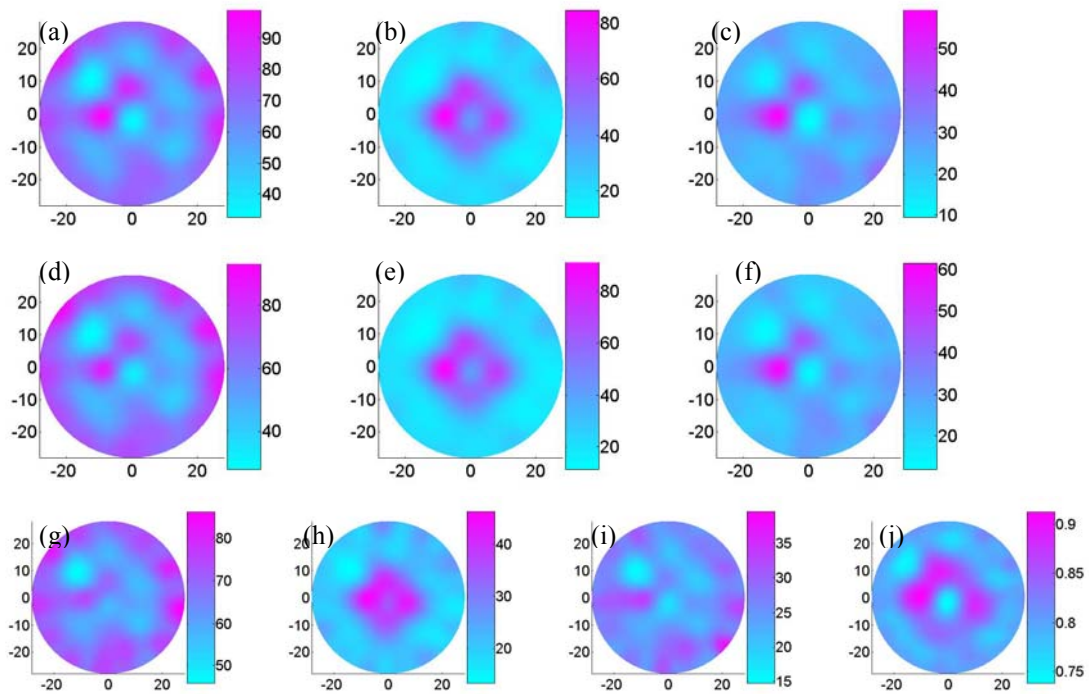


Figure 6-18. For clinical case G1, chromophores concentration images (a, d, g for HbO₂ concentrations in μM , b, e, h for Hb concentrations in μM and c, f, I for water concentration in percentage) and scatterers' volume fraction image in percentage (j) reconstructed with the measured molar spectra, using method 1 (1st row), method 2 (2nd row) and method 3 (3rd row).

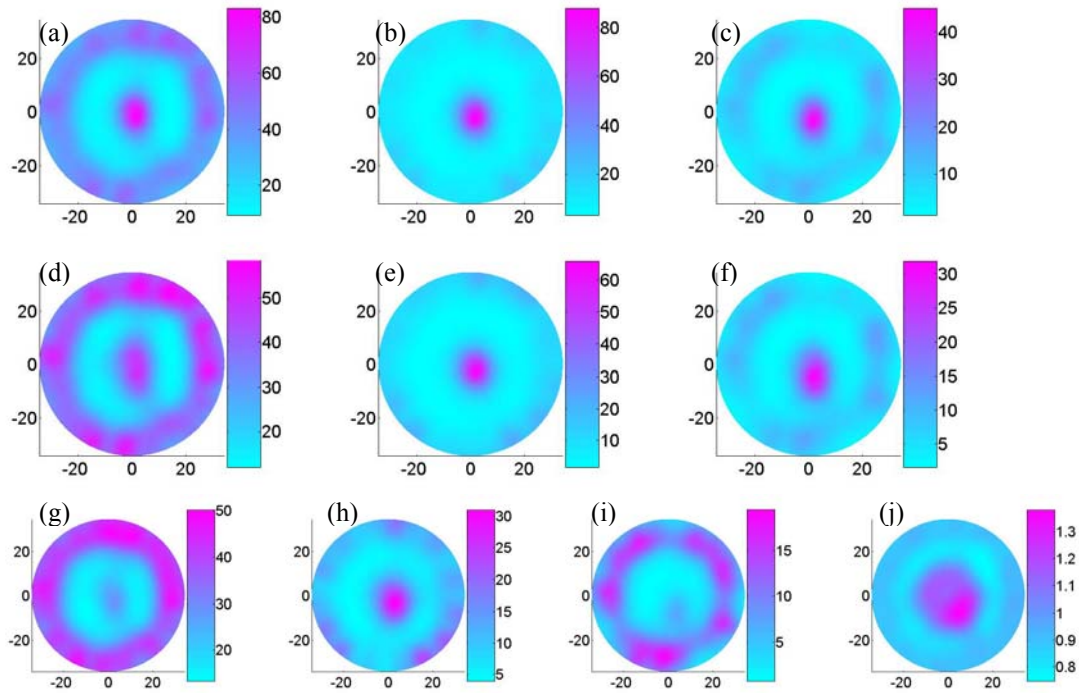


Figure 6-19. For clinical case G14, Chromophores concentration images (a, d, g for HbO₂ concentrations in μM , b, e, h for Hb concentrations in μM and c, f, I for water concentration in percentage) and scatterers' volume fraction image in percentage (j) reconstructed with the measured molar spectra, using method 1 (1st row), method 2 (2nd row) and method 3 (3rd row).

Table 6-1 Volume fraction of different particles in the background and the three targets for numerical simulation case 3.

Regions	Volume fraction of different particles		
	Diameter of 150 nm	Diameter of 1000 nm	Diameter of 60000 nm
Background	0.25%	0.25%	0.5%
Target 1	0.5%	0.5%	1.0%
Target 2	0.5%	0.5%	1.0%
Target 3	0.5%	0.5%	1.0%

Table 6-2 Concentrations of the absorption chromophores and Volume fractions particles for numerical simulation case4.

Regions	Concentrations of absorption chromophores (μM)			Volume fraction of different particles	
	Hbo2	Hb	water	Diameter of 1000 nm	Diameter of 60000 nm
Background	10.0	10.0	18.0	0.25%	0.5%
Target 1	20.0	10.0	18.0	0.25%	0.5%
Target 2	10.0	20.0	18.0	0.25%	0.5%
Target 3	10.0	10.0	36.0	0.25%	0.5%
Target 4	10.0	10.0	18.0	0.375%	0.5%
Target 5	10.0	10.0	18.0	0.25%	1.0%

CHAPTER 7 CONCLUSIONS AND FUTURE STUDIES

7.1 Conclusions

This dissertation has explored the abilities of diffuse optical tomography to detect the breast tumors from both the hardware and the algorithm aspects. In general, both the tissue-like phantom experimental results and the clinical trial experimental results show that DOT is very promising to identify the breast abnormalities. The unique features of DOT, functional imaging and morphological imaging, allows DOT to detect the tumors when the tumors are at early stages.

The continue-wave imaging system played a key role in this study. All the tissue-like phantom experiments and clinical trial experiments are conducted with the system. The quantitative imaging results proved that the system is very robust. Furthermore, the LABVIEW controller provides a very friendly interface and makes the instrument easy to be operated. Especially the application of gain controller and optical switch make the instrument running automatically whenever the patient breast is in good position.

Both the dual mesh method and the source intensity optimization method can improve the 3D DOT image quality substantially, as shown by the tissue-like phantom experimental results in chapter 3. These results also show the robustness and the accuracy of our 3D DOT algorithm. The target with absorption contrast as low as 1.4 times can be identified. The spatial resolution of 5mm in the lateral direction is achieved. Smaller spatial resolution may be obtained if higher contrast targets are used.

The morphological imaging, including the scattering particle mean diameter imaging and the scattering particle volume fraction imaging, is first proposed by us. The morphological images are extracted from the reduced scattering images at different wavelengths. The

morphological imaging has the possibilities to prove doctors with nucleus size and nucleus crowding non-invasively. The tissue-like phantom results in chapter 4 show that the reconstructed diameter is larger if there are relative more scattering particles with larger diameters. This conclusion may serve as criteria for our further clinical results of morphological images. Experimental data for 10 benign clinical cases and 4 malignant cases are processed to obtain the morphological images. These preliminary results show that the estimated maximum diameter and volume fraction in the malignant tumor region are 3.23 and 2.64 times as large as that in the benign abnormality region, respectively. The reconstructed diameter and volume fraction could be the new criteria to differentiate the malignant tumors from the benign abnormalities, although more clinical results are needed to further prove the ratio number. By comparison with the pathological pictures, we find that the scattering particles are not only the nucleus but also the smaller particles such as nucleolus and the mitochondria.

Spectrally constrained DOT imaging is supposed to provide better accuracy compared with the two steps imaging method, in which the absorption coefficients and scattering coefficients are obtained at first and then these coefficients are fitting to extract the absorption chromophore concentrations and scattering parameters. The spectrally constrained DOT imaging method is proposed by Corlu et al. at first. However, the scattering parameter a and b in the power law are difficult to be obtained simultaneously. A new method, namely scatterers' volume fraction method, is proposed, in which the scattering equation is linearized. With this new method, both the concentration images of HbO₂, Hb and water and the volume fraction images of scattering particles with different diameters can be imaged simultaneously. The method is validated by numerical simulations and clinical results.

The measured molar absorption extinction coefficients of HbO₂ and Hb and the absorption spectra of water are different with those in the literature at some wavelengths. When the measured absorption spectra for HbO₂, Hb and water are utilized, the reconstructed image quality is improved substantially in terms of target locations, concentration values and artifacts, especially for the water concentration image.

7.2 Future Studies

7.2.1 Imaging System and Calibrations

The potentials of DOT imaging are deteriorated by the artifacts. The artifacts are caused by many reasons, such as experimental system noise, computational errors, modeling errors, detection and source fiber coupling errors, etc. The calibration method, source intensity optimization method, dual mesh method and spectrally constraint reconstruction method discussed in the above chapters are used to reduce the reconstructed image artifacts. Computational calibration method,⁷²⁻⁷⁵ in which the coupling coefficients are updated at the same time as the optical properties are updated in the reconstruction, may further eliminate the artifacts. A recent study show that the difference in data for multiple wavelength pairs, instead of the absolute measurements at the wavelengths, is used to reconstruct absolute absorption chromophore concentrations and the image quality is improved substantially.⁹³ While the DOT image quality, especially for clinical cases, is acceptable, more efforts are needed to further eliminate the artifacts because the artifacts may result in unnecessary biopsy if one day the optical imaging modality serves as the routine breast cancer screening.

There are only 10 laser modules with different wavelengths from 638 nm to 965 nm in our experimental system. The measurements at more wavelengths should provide more robust and more accurate results of morphological and functional imaging using the multi-spectral

DOT. Next generation of our experimental system should have more laser modules or have a laser with the adjustable wavelengths.

The current system can not image the whole breast one time and only cover 2 cm slice each imaging time, while the whole breast can be imaged one slice after another by adjusting the patient vertical positions using the hydraulic pump in the system. Further modifications of the fiber bundle interface are needed to image the whole breast one imaging time.

7.2.2 Multi-modality Imaging

One of the major drawbacks of the DOT imaging is its low spatial resolution. One way to overcome the drawback is using other imaging modality such as MRI, ultrasound, X-ray to enhance the spatial resolution. This technology is called multi-modality imaging. The combination of high spatial resolution MRI imaging and high contrast DOT imaging in frequency domain has been investigated and the DOT imaging quality has been improved using the co-registered MRI imaging guided structural information.⁹⁴ The study of coregistered tomographic x-ray and optical breast imaging has been performed recently and the pilot clinical results have been shown.⁹⁵ A study has shown that targets of 2-3mm in diameter embedded inside a cylindrical background phantom with 5cm in diameter could be reconstructed quantitatively in terms of the positions and optical properties using the ultrasound guided finite element based DOT imaging modality.⁹⁶ Combination of two imaging modalities could integrate their strengths and avoid one or two weakness of an individual modality.⁹⁷

7.2.3 Scattering Theory

We have assumed that the scattering particles such as nucleus or mitochondria inside the breast are spherical due to the utilization of MIE theory. But the real shape of the scattering particles is nonspherical. Advanced scattering theories are needed to describe the scattering behaviors of the nonspherical particles. So far, there are no accurate and robust mathematical

models to describe the light scattering properties of complex structures.⁹⁸ Recent progress in reduced-order expressions for the total scattering cross section spectra of nonspherical particles provides a possible way to solve the problem.⁹⁹ Another method to study the scattering of complex structures is finite-difference time-domain modeling.¹⁰⁰

7.2.4 Clinical Studies

The ultimate goal of this dissertation and our study is to detect the breast tumors and differentiate the malignant tumors from the benign abnormalities. The hardware improvements, system calibration methods and new algorithms introduced in this dissertation serve the goal. The clinical trial experiments play a key role to validate our methods

The phantom experiments of 3D DOT has been done. However, clinical results of 3D DOT imaging are needed to further show the abilities and promises of our 3D DOT for breast cancer detection since the real breast cancer imaging is a 3D problem.

The preliminary clinical studies in chapter 5 shows that the reconstructed diameter and volume fraction could be the new criteria to differentiate the malignant tumors from the benign abnormalities based on the results of 14 clinical cases. However, more clinical results are needed to further prove the conclusion.

The co-registration of optical imaging with other methods such as biopsy and surgery is important but difficult. We have compared our reconstructed diameter imaging and volume fraction with the pathological pictures taken from the tumor samples in the target area. But we don't know the exact location of the samples corresponding to the reconstructed images because there are no good ways to record sample locations in the real breast during the surgery (we only know the approximate location) and the breasts are soft and easy to deform. A better way to do the co-registration should be proposed in the future clinical studies.

LIST OF REFERENCES

1. Breast Cancer Facts & Figures 2005-2006, Ries LAG 2005.
2. Cutler M, Transillumination as an aid to diagnosis of breast lesions, *Surg. Gynaecol. Obstet.* 48, 721-727 (1929).
3. Jones C H, Methods of breast imaging, *Phys. Med. Biol.*, 27, 463-499 (1982).
4. Jarlman O, Balldin G and Larsson A S, Diagnostic accuracy of light scanning and mammography in women with dense breasts, *ACTA Radiol.* 33, 69-71 (1992).
5. Jarlman O, Balldin G, Andersson I, Lofgre M, Larsson A S and Linell F, Relation between lightscanning and the histologic and mammographic appearance of malignant breast tumors, *ACTA Radiol.* 33, 63-68 (1992).
6. Cheong WF, Prael SA and Welch AJ, A review of the optical properties of biological tissues, *IEEE J. Quantum Electron.* 26, 2166-2185 (1990).
7. Troy O. McBride, Brian W. Pogue, Ellen D. Gerety, Steven B. Poplack, Ulf L. Osterberg, Keith D. Paulsen, Spectroscopic diffuse optical tomography for the quantitative assessment of hemoglobin concentration and oxygen saturation in breast tissue, *Appl. Opt.* 38, 5480-5490 (1999).
8. Peters VG, Wyman DR, Patterson MS, Frank GL, Optical-properties of normal and diseased human breast tissues in the visible and near-infrared, *Phys. Med. Biol.* 35, 1317-1334 (1990).
9. Gayen SK and Alfano RR, Sensing lesions in tissues with light, *Opt. Express.* 4, 475-480 (1999).
10. Key H, Davies ER, Jackson PC, Wells PNT, Optical attenuation characteristics of breast tissues at visible and near-infrared wavelengths, *Phys. Med. Biol.* 36, 579-590 (1991).
11. Profio AE, Navarro GA and Sartorius OW, Scientific basis of breast diaphanography, *Med. Phys.* 16, 60-65 (1989).
12. Gu XJ, Zhang QZ, Bartlett M, Schutz L, Fajardo LL, Jiang HB, Differentiation of cysts from solid tumors in the breast with diffuse optical tomography, *Acad. Radiol.* 11, 53-60 (2004).
13. Jiang H, Iftimia N, Xu Y, Eggert JA, Fajardo LL, Klove KL, Near-infrared optical imaging of the breast with model-based reconstruction, *Acad. Radiol.* 9, 186-194 (2002).

14. Pogue B.W., Jiang S., Dehghani H., Kogel C., Soho S., Srinivasan S., Song X., Tosteson T.D., Poplack S.P., Paulsen K.D., Characterization of hemoglobin, water, and NIR scattering in breast tissue: analysis of intersubject variability and menstrual cycle changes, *J. Biomed. Opt.* 9, 541-552 (2004).
15. Srinivasan, S., Pogue, B. W., Jiang, S., Dehghani, H., Kogel, C., Soho, S., Gibson, J. J., Tosteson, T. D., Poplack, S. P., Paulsen, K. D., Interpreting hemoglobin and water concentration, oxygen saturation, and scattering measured by near-infrared tomography of normal breast in vivo, *Proc. Natl. Acad. Sci. USA* 100, 12349-12354 (2003).
16. Chance B, Near-infrared images using continuous, phase-modulated, and pulsed light with quantitation of blood and blood oxygenation, *Ann. NY Acad. Sci.* 838, 29-45 (1998).
17. Kang KA, Chance B, Zhao S, Srinivasan S, Patterson E and Trouping R, Breast tumor characterization using near infrared spectroscopy, photon migration and imaging in random media and tissue, Vol 1888, ed. Alfano RR and Chance B (Bellingham, WA: SPIE) 487-499.
18. Suzuki K, Yamashita Y, Ohta K, Kaneko M, Yoshida M and Chance B, Quantitative measurement of optical parameters in normal breasts using time-resolved spectroscopy: in vivo results of 30 Japanese women, *J. Biomed. Opt.* 1, 330-334 (1996).
19. McBride T.O., Pogue B.W., Jiang S., Sterberg U.L., Paulsen K.D., Poplack S.P., Initial studies of in vivo absorbing and scattering heterogeneity in near-infrared tomographic breast imaging, *Opt. Lett.* 26, 822-824 (2001).
20. Tromberg BJ, Coquoz O, Fishkin J, Pham T, Anderson ER, Butler J, Cahn M, Gross JD, Venugopalan V, Pham D, Non-invasive measurements of breast tissue optical properties using frequency-domain photon migration, *Philos. T. Roy. Soc. B.* 352, 661-668 (1997).
21. Sickles EA, Breast-cancer detection with trans-illumination and mammography, *Am. J. Roentgenol.* 142, 841-844 (1984).
22. Ntziachristos V, Ma XH, Chance B, Time-correlated single photon counting imager for simultaneous magnetic resonance and near-infrared mammography, *Rev. Sci. Instrum.* 69, 4221-4233 (1998).
23. Ntziachristos V, Yodh AG, Schnall M, Chance B, Concurrent MRI and diffuse optical tomography of breast after indocyanine green enhancement, *Proc. Natl. Acad. Sci. USA* 97, 2767-2772 (2000).
24. Dehghani H., Pogue BW, Jiang SD, Brooksby B, Paulsen KD, Three-dimensional optical tomography: resolution in small-object imaging, *Appl. Opt.* 42, 3117-3128 (2003).

25. Dehghani H, Pogue BW, Poplack SP, Paulsen KD, Multiwavelength three-dimensional near-infrared tomography of the breast: initial simulation, phantom, and clinical results, *Appl. Opt.* 42, 135-145 (2003).
26. Dehghani H, Doyley MM, Pogue BW, Jiang SD, Geng J and Paulsen KD, Breast deformation modelling for image reconstruction in near infrared optical tomography, *Phys. Med. Biol.* 49, 1131-1145 (2004).
27. Hebden JC, Veenstra H, Dehghani H, Hillman EMC, Schweiger M, Arridge SR and Delpy DT, hree-dimensional time-resolved optical tomography of a conical breast phantom, *Appl. Opt.* 40, 3278-3287 (2001).
28. Iftimia N, Jiang HB, Quantitative optical image reconstruction of turbid media by use of direct-current measurements, *Appl. Opt.* 39, 5256-5261(2000).
29. Xu Y, Iftimia N, Jiang HB, Key LL, Bolster MB, Three-dimensional diffuse optical tomography of bones and joints, *J. Biomed. Opt.* 7, 88-92 (2002).
30. Xu Y, Iftimia N, Jiang HB, Key LL, Bolster MB, Imaging of in vitro and in vivo bones and joints with continuous-wave diffuse optical tomography, *Opt. Express.* 8, 447-451 (2001).
31. Xu Y, Gu X, Khan T, Jiang HB, Absorption and scattering images of heterogeneous scattering media can be simultaneously reconstructed by use of dc data, *Appl. Opt.* 41, 5427-5437 (2002).
32. Culver JP, Choe R, Holboke MJ, Zubkov L, Durduran T, Slemple A, Ntziachristos V, Chance B, Yodh AG, Three-dimensional diffuse optical tomography in the parallel plane transmission geometry: Evaluation of a hybrid frequency domain/continuous wave clinical system for breast imaging, *Med. Phys.* 30, 235-247 (2003).
33. Gu X, Xu Y, Jiang HB, Mesh-based enhancement scheme in diffuse optical tomography, *Med. Phys.* 30, 861-869 (2003).
34. Li CQ, Jiang HB, Three dimensional diffuse optical tomography: resolution and contrast studies with dual mesh method, (ready to be submitted, 2006).
35. Li CQ, Jiang HB, Source intensity optimization in quantitative three-dimensional diffuse optical tomography, accepted by *Journal of X-ray science and technology* (2006).
36. Jiang HB, Iftimia N, Xu Y, Eggert JA, Fajardo LL, Klove KL, Near-infrared optical imaging of the breast with model-based reconstruction, *Acad. Radiol.* 9, 186-194 (2002).
37. Jiang HB, Xu Y, Iftimia N, Eggert J, Klove K, Baron L, Fajardo L, Three-dimensional optical tomographic Imaging of breast in a human subject, *IEEE Trans. Med. Imaging* 20, 1334-1340 (2001).

38. Iftimia N, Gu X, Xu Y, Jiang HB, A compact, parallel-detection diffuse optical mammography system, *Rev. Sci. Instrum.* 74, 2836-2842 (2003).
39. Corlu A, Choe R, Durduran T, Lee K, Schweiger M, Arridge SR, Hillman EMC, Yodh AG, Diffuse optical tomography with spectral constraints and wavelength optimization, *Appl. Opt.* 44, 2082-2093 (2005).
40. Li CQ, Zhang HZ, Anderson B, Jiang HB, Multispectral breast imaging using a ten-wavelength, 64*64 source/detector channels silicon photodiode-based diffuse optical tomography system, *Med. Phys.* 33, 627-636 (2006).
41. Brunsting A, Mullaney P., Differential light scattering from spherical mammalian cells, *Biophys. J.* 14, 439-453 (1974).
42. Perelman LT, Backman V, Wallace M, Zonios G, Manoharan R, Nusrat A, Shields S, Seiler M, Lima C, Hamano T, Itzkan I, J Van Dam, Crawford JM, Feld MS, Observation of periodic fine structure in reflectance from biological tissue: a new technique for measuring nuclear size distribution, *Phys. Rev. Lett.* 80, 627-630 (1998).
43. Backman V, Gurjar R, Badizadegan K, Itzkan L, Dasari RR, Perelman LT, Feld MS, Polarized light scattering spectroscopy for quantitative measurement of epithelial cellular structures in situ, *IEEE J. Sel. Top. Quant.* 5, 1019-1026 (1999).
44. Anderson RR, Polarized-light examination and photography of the skin, *Arch. Dermatol.* 127, 1000-1005 (1991).
45. Demos SG, Alfano RR, Temporal gating in highly scattering media by the degree of optical polarization, *Opt. Lett.* 21, 161-163 (1996).
46. Yoo KM, Alfano RR, Time resolved depolarization of multiple backscattered light from random-media, *Phys. Lett. A* 142, 531-536 (1989).
47. Demos SG, Alfano RR, and Dmons SJ, Optical polarization imaging, *Appl. Opt.* 36, 150-155 (1997).
48. Amelink A, Bard MPL, Burgers SA, Sterenborg HJCM, Single-scattering spectroscopy for the endoscopic analysis of particle size in superficial layers of turbid media, *Appl. Opt.* 42, 4095-4101 (2003).
49. Mourant, J.R., Johnson, T.M., Freyer, J.P. , Characterizing mammalian cells and cell phantoms by polarized backscattering fiber-optic measurements, *Appl. Opt.* 40, 5114-5123 (2001).
50. Bartlett M, Huang G, Larcom L, Jiang HB, Measurement of particle size distribution in mammalian cells in vitro by use of polarized light spectroscopy, *Appl. Opt.* 43, 1296-1307 (2004).

51. Gurjar RS, Backman V, Perelman LT, Georgakoudi I, Badizadegan K, Itzkan I, Dasari RR, Feld MS, Imaging human epithelial properties with polarized light-scattering spectroscopy, *Nat. Med.* 7, 1245-1248 (2001).
52. McBride TO, Pogue BW, Jiang S, Sterberg UL, Paulsen KD, Poplack SP, Initial studies of in vivo absorbing and scattering heterogeneity in near-infrared tomographic breast imaging, *Opt. Lett.* 26, 822-824 (2001).
53. Cotran RS, Robbins S, Kumar V, Robbins Pathological basis of disease (W.B. Saunders, Philadelphia, Pennsylvania, 1994).
54. Pogue BW, Jiang S, Dehghani H, Kogel C, Soho S, Srinivasan S, Song X, Tosteson TD, Poplack SP, Paulsen KD, Characterization of hemoglobin, water, and NIR scattering in breast tissue: analysis of intersubject variability and menstrual cycle changes, *J. Biomed. Opt.* 9, 541-552 (2004).
55. Corlu A, Durduran T, Choe R, Schweiger M, Hillman EMC, Arridge SR, Yodh AG, Uniqueness and wavelength optimization in continuous-wave multispectral diffuse optical tomography, *Opt. Lett.* 28, 2339-2341(2003).
56. Graaff R, Aarnoudse JG, Zijp JR, Sloot PMA, de Mul FFM, Greve J, Koelink MH, Reduced light-scattering properties for mixtures of spherical particles: a simple approximation derived from Mie calculations, *Appl. Opt.* 31, 1370-1376 (1992).
57. Mourant JR, Fuselier T, Boyer J, Johnson TM, Bigio IJ, Predictions and measurements of scattering and absorption over broad wavelength ranges in tissue phantoms, *Appl. Opt.* 36, 949-957 (1997)
58. Nilsson AMK., Sturesson C, Liu DL, Andersson-Engels S, Changes in spectral shape of tissue optical properties in conjunction with laser-induced thermotherapy, *Appl. Opt.* 37, 1256-1267 (1998).
59. Johns M, Liu H, Limited Possibility for Quantifying Mean Particle Size by Logarithmic Light-Scattering Spectroscopy, *Appl. Opt.* 42, 2968-2671 (2003).
60. Backman V, Wallace MB, Perelman LT, Arendt JT, Gurjar R, Muller MG, Zhang Q, Zonios G, Kline E, McGillican T, Shapshay S, Valdez T, Badizadegan K, Crawford JM, Fitzmaurice M, Kabani S, Levin HS, Seiler M, Dasari RR, Itzkan I, Van Dam J, Feld MS, Detection of preinvasive cancer cells, *Nature.* 406, 35-36 (2000).
61. Li CQ, Jiang HB, Imaging of particle size and concentration in heterogeneous turbid media with multispectral diffuse optical tomography, *Opt. Express.* 12, 6313-6318 (2004).
62. Li CQ, Jiang HB, Measurement of particle-size distribution and concentration in heterogeneous turbid media with multispectral diffuse optical tomography, *Appl. Opt.* 44, 1838-1844 (2005).

63. Li X, Chen Z, Gong J, Taflove A, Backman V, Analytical techniques for addressing forward and inverse problems of light scattering by irregularly shaped particles, *Opt. Lett.* 29, 1239-11241 (2004).
64. Hielscher AH, Klose AD, Scheel Ak, Moa-Anderson B, Backhaus M, Netz U and Beuthan J, Sagittal laser optical tomography for imaging in turbid media, *Phys. Med. Biol.* 49, 1147-63 (2004).
65. Ren K, Abdoulaev G, Bal G, and Hielscher A, Algorithm for solving the equation of radiative transfer in the frequency domain, *Opt. Lett.* 29, 578-580 (2004).
66. Ripoll J and Ntziachristos V, Iterative boundary method for diffuse optical tomography, *J. Opt. Soc. Am. A.* 20, 1103-1110 (2003).
67. Paulsen KD, Jiang HB, Spatially varying optical property reconstruction using a finite-element diffusion equation approximation, *Med. Phys.* 22, 691-701 (1995).
68. Arridge SR, Schweiger M, Hiraoka M, Delpy DT, A finite-element approach for modeling photon transport in tissue, *Med. Phys.* 20, 299-309 (1993).
69. Paulsen KD, Jiang HB, Spatially varying optical property reconstruction using a finite-element diffusion equation approximation, *Med. Phys.* 22, 691-701 (1995).
70. Jiang HB, Xu Y, Iftimia N, Experimental three-dimensional optical image reconstruction of heterogeneous turbid media from continuous-wave data, *Opt. Express* 7, 204-209 (2000).
71. Li CQ, Jiang HB, A calibration method in diffuse optical tomography, *J. Opt. A: Pure Appl. Opt.* 6, 844-852 (2004).
72. Boas DA, Gaudette T, Arridge SR, Simultaneous imaging and optode calibration with diffuse optical tomography, *Opt. Express.* 8, 263-270 (2001).
73. Scott JJ, Culver JP, Arridge SR, Boas DA, Optode positional calibration in diffuse optical tomography, *Appl. Opt.* 42, 3154-3162 (2003).
74. Oh S, Milstein AB, Millane RP, Bouman CA, Webb KJ, Source-detector calibration in three-dimensional Bayesian optical diffusion tomography, *J. Opt. Soc. Am. A.* 19, 1983-1993 (2002).
75. Tarvainen T, Kolehmainen V, Vauhkonen M, Vanne A, Gibson AP, Schweiger M, Arridge SR, Kaipio JP, Computational calibration method for optical tomography, *Appl. Opt.* 44, 1879-1888 (2005).
76. Schmitz CH, Graber HL, Luo HB, Arifl I, Hira J, Pei YL, Bluestone A, Zhong S, Andronica R, Soller I, Ramirez N, Barbour SLS, Barbour RL, Instrumentation and calibration protocol for imaging dynamic features in dense-scattering media by optical tomography, *Appl. Opt.* 39, 6466-6486 (2000).

77. Jiang HB, Pierce J, Kao J, Sevick-Muraca E, Measurement of particle-size distribution and volume fraction in concentrated suspensions with photon migration techniques, *Appl. Opt.* 36, 3310-3318 (1997).
78. Jiang HB, Enhanced photon migration methods for particle sizing in concentrated suspensions, *AIChE J.* 44, 1740-1744 (1998).
79. Jiang HB, Marquez G, Wang L, Particle sizing in concentrated suspensions using steady-state, continuous-wave photon migration techniques, *Opt. Lett.* 23, 394-396 (1998).
80. Bartlett M, Jiang HB, Measurement of particle size distribution in concentrated, rapidly flowing potassium chloride (KCl) suspensions using continuous-wave photon migration techniques, *AIChE J.* 47, 60-65 (2001).
81. Bohren GF and Hoffman DR, *Absorption and scattering of light by small particles* (Wiley, New York, 1983).
82. Mourant JR, Hielscher AH, Eick AA, Johnson TM, and Freyer JP, Evidence of intrinsic differences in the light scattering properties of tumorigenic and nontumorigenic cells, *Cancer Cytopathol.* 84, 366-374 (1998).
83. Beauvoit B, Liu H, Kang K, Kaplan PD, Miwa M, Chance B, Characterization of absorption and scattering properties of various yeast strains by time-resolved spectroscopy, *Cell Biophys.* 23, 91-109 (1993).
84. Shives E, Xu Y, Jiang HB, Fluorescence lifetime tomography of turbid media based on an oxygen-sensitive dye, *Opt. Express.* 10, 1557-1562 (2002), <http://www.opticsexpress.org/abstract.cfm?URI=OPEX-10-26-1557>.
85. Cerussi AE, Jakubowski D, Shah N, Bevilacqua F, Lanning R, Berger AJ, Hsiang D, Butler J, Holcombe RF, Tromberg BJ, Spectroscopy enhances the information content of optical mammography, *J. Biomed. Opt.* 7, 60-71 (2002).
86. Yodanis and B. Chance, Spectroscopy and imaging with diffusing light, *Phys. Today*, 48, 34-40 (1995).
87. Srinivasan S, Pogue BW, Jiang SD, Dehghani H, Paulsen KD, Spectrally constrained chromophore and scattering near-infrared tomography provides quantitative and robust reconstruction, *Appl. Opt.* 44, 1858-1869 (2005).
88. Kou L, Labrie D, Chylek P, Refractive indices of water and ice in the 0.65-2.5 μm spectral range, *Appl. Opt.* 32, 3531-3540 (1993).
89. Buiteveld H, Hakvoort JMH, Donze M, The optical properties of pure water, in *SPIE Proceedings on Ocean Optics XII*, edited by J. S. Jaffe, 2258, 174-183 (1994).

90. Gratzer WB, Tabulated molar extinction coefficient for hemoglobin in water, Med. Res. Council Labs, Holly Hill, London.
<http://omlc.ogi.edu/spectra/hemoglobin/summary.html>.
91. Kollias N, Tabulated molar extinction coefficient for hemoglobin in water, Wellman Laboratores, Harvard Medical School, Boston.
<http://omlc.ogi.edu/spectra/hemoglobin/summary.html>.
92. Takatani S, Graham MD, Theoretical analysis of diffuse reflectance from a two-layer tissue model, *IEEE Trans. Biomed. Eng. BME.* 26, 656--664 (1987).
93. Xu H, Pogue BW, Springett R, Dehghani H, Spectral derivative based image reconstruction provides inherent insensitivity to coupling and geometric errors, *Opt. Lett.* 30, 2912-2914 (2005).
94. Brooksby B, Jiang SD, Dehghani H, Pogue BW, Paulsen KD, Kogel C, Doyley M, Weaver JB, Poplack SP, Magnetic resonance-guided near-infrared tomography of the breast, *Rev. Sci. Instrum.* 75, 5262-5270 (2004).
95. Zhang Q, Brukilacchio TJ, Li A, Stott JJ, Chaves T, Wu T, Chorlton M, Rafferty E, Moore RH, Kopans DB, Boas DA, Coregistered tomographic x-ray and optical breast imaging: initial results, *J. Biomed. Opt.* 10, Art. No. 024033 (2005).
96. Zhao HZ, Gu XJ, Jiang HB, Imaging small absorbing and scattering objects in turbid media using diffuse optical tomography structurally guided by reconstructive ultrasound tomography, *Opt. Communicat.* 238, 51-55 (2004).
97. Cherry SR, Multimodality in vivo imaging systems: Twice the power or double the trouble? *Ann. Rew. Biomed. Eng.* 8, 35-62 (2006).
98. Li X, Taflove A, Backman V, Recent progress in exact and reduced-order modeling of light-scattering properties of complex structures, *IEEE J. Sel. Top. Quant.* 11 (4): 759-765 (2005).
99. Li X, Chen ZG, Taflove A, Backman V, Euphase-sphere approximation for analysis of light scattering by arbitrarily shaped nonspherical particles, *Appl. Opt.* 43, 4497-4505 (2004).
100. Li X, Taflove A, Backman V, Quantitative analysis of depolarization of backscattered light by stochastically inhomogeneous dielectric particles, *Opt. Lett.* 30, 902-904 (2005).

BIOGRAPHICAL SKETCH

Changqing Li was born on August 21, 1973 in Xingyang, Henan Province, China. He earned his B.S. in the Mechanical and Electrical Engineering from the Northwestern Polytechnic University, Xi'an China in 1995. He earned his M.E. in Engineering Mechanics from the Tsinghua University, Beijing, China in 1998. And he earned his M.S. in Electrical Engineering from Clemson University, SC in 2002. He entered the PhD program in the physics department, Clemson in 2002 and transferred to the biomedical engineering department, University of Florida at the beginning of 2005.